Non-perturbative approaches to Scattering Amplitudes

by

Lucía Gómez Córdova

A thesis
presented to the University of Waterloo
in fulfillment of the
thesis requirement for the degree of
Doctor of Philosophy
in
Physics

Waterloo, Ontario, Canada, 2019

Examining Committee Membership

The following served on the Examining Committee for this thesis. The decision of the Examining Committee is by majority vote.

External Examiner: Simon Caron-Huot
Canada Research Chair in High-Energy Physics
Assistant Professor of Physics,
McGill University

Supervisor: Pedro Vieira
Faculty, Perimeter Institute for Theoretical Physics
Adjunct Professor, Dept. of Physics and Astronomy,
University of Waterloo

Co-supervisor: Rob Myers
Faculty, Perimeter Institute for Theoretical Physics
Adjunct Professor, Dept. of Physics and Astronomy,
University of Waterloo

Internal Member: Niayesh Afshordi
Associate Faculty, Perimeter Institute for Theoretical Physics
Associate Professor, Dept. of Physics and Astronomy,
University of Waterloo

Internal Member: Freddy Cachazo
Faculty, Perimeter Institute for Theoretical Physics
Adjunct Professor, Dept. of Physics and Astronomy,
University of Waterloo

Internal-External Member: Benoit Charbonneau
Associate Professor, Dept. of Pure Mathematics,
University of Waterloo

Author's Declaration

I hereby declare that I am the sole author of this thesis. This is a true copy of the thesis, including any required final revisions, as accepted by my examiners.

I understand that my thesis may be made electronically available to the public.

Abstract

This thesis is devoted to the study of scattering amplitudes using two non-perturbative approaches. In Part I we focus on a particular theory known as $\mathcal{N} = 4$ Super-Yang-Mills in four spacetime dimensions. The scattering amplitudes in this theory are dual to the expectation value of null polygonal Wilson loops which can be computed non-perturbatively using integrability. The Wilson loop is decomposed into smaller polygons and computed as an evolution of the color flux tube of the theory, summing over all intermediate flux tube states. By a suitable generalization of the building blocks called pentagons we describe how this program can describe all helicity configurations of the amplitude. We also show how the contribution from all flux tube excitations can be resummed to reproduce the general kinematics result at weak coupling. In Part II we take a different approach and study the space of Quantum Field Theories (QFTs). We focus on two-dimensional theories with a mass gap and a global symmetry. By studying the consequences of unitarity, crossing symmetry and analyticity of the $2 \to 2$ scattering matrix element we are able to constrain the space of allowed QFTs. At the boundary of this space we find several interesting features of the S-matrices and identify various integrable points.

Acknowledgements

A mis hermanos Rodrigo y Sofía.

Table of Contents

Chapter 1

Introduction

Quantum Field Theory (QFT) has successfully provided a framework to describe a wide range of physical phenomena from condensed matter systems to high energy physics. However, most of its success lies in describing weakly coupled systems where we can use perturbation theory. Taming strongly coupled theories like Quantum Chromodynamics (QCD) outside the lattice has proven much more challenging. Given the difficult situation, one can follow different strategies to understand aspects of strongly coupled QFTs.

One possibility is to study first simpler theories that can serve as toy models. The hope is that by understanding how to compute observables in these simpler models one would be able to export techniques and ideas to more complicated theories. Examples of these toy models might enjoy a large number of symmetries or live in less spacetime dimensions.

Another possible strategy is to constrain the space of consistent quantum field theories by imposing general principles. That is, instead of starting with the details of the theory (like a specific Lagrangian), one can get access to non-perturbative observables by asking the right type of questions. This is known as the bootstrap philosophy and has proven incredibly powerful, particularly for conformal field theories.

In the present thesis we use the above two strategies to study strongly coupled QFT. The observables we focus on are scattering amplitudes. In Part I we follow the first approach and turn our attention to a specific theory known as $\mathcal{N} = 4$ Super-Yang-Mills. In Part II we take the second strategy and constrain the space S-matrices for two-dimensional massive QFTs with a global symmetry. In the following we give a brief introduction to the problems studied in parts I and II of the thesis.

Part I: Pentagons in N=4 in SYM

A well known example of a toy model for QCD is $\mathcal{N} = 4$ Super-Yang-Mills (SYM). This is a superconformal four-dimensional theory which is also integrable. Although the usual integrable theories are two-dimensional, $\mathcal{N} = 4$ SYM gets around this problem by means of holography, which states that there is a dual description in terms of the world-sheet of a string in a higher dimensional target space. With the help of integrability, notable progress has been made in computing physical observables at finite coupling.

Scattering amplitudes in this theory are dual to the expectation value of null polygonal Wilson loops and can be computed at finite coupling using the Pentagon Operator Product Expansion (POPE) approach [1]. A key object in this construction is the flux-tube stretching between two null Wilson lines. Surprisingly, the four-dimensional amplitudes can be described in terms of the integrable dynamics of the flux-tube excitations.

The scattering amplitude is computed as a sequence of transitions between different flux-tube states called *pentagon transitions*, summing over all possible flux-tube excitations [1]. The pentagon transitions –the main dynamical object in the problem– can be in turn bootstrapped from the S-matrices between flux-tube excitations. With the power of integrability, these objects were computed at finite coupling.

It was first understood in [1] how to compute scattering amplitudes where the external particles have a particular configuration of helicities known as *maximally helicity violating*. The first problem we tackle on the thesis is the inclusion of all possible helicity configurations. As we shall see in chapters 3 and 4, this requires the generalization of the pentagon transitions to *superpentagons*. These chapters have an overlap with the publications [2, 3] which I co-authored.

Although this approach provides a remarkable finite coupling formulation of scattering amplitudes, the explicit sum over all possible flux-tube excitations is difficult to perform. Therefore in practice the scattering amplitudes are given as an expansion over a particular limit where only the lightest flux-tube excitations dominate. By studying the analytic structure of the pentagon transitions, in chapter 5 –based on the article [4]– we will show how the contribution of all flux-tube excitations can be taken into account in order to reproduce the tree-level six-point amplitudes.

Part II: S-matrix Bootstrap

Concerning the second approach alluded to at the beginning of this introduction, it is natural to ask if bootstrap techniques can also be applied to massive QFTs, in particular if these techniques can be useful in constraining scattering amplitudes. The idea of finding an S-matrix from general principles like unitarity and crossing was very popular in the 1960s but fell out of fashion with the formulation of Quantum Chromodynamics and the development of perturbative tools. Drawing inspiration from AdS/CFT and the conformal bootstrap, the program was recently revived in [5, 6].

In this approach, a useful question to ask is: what are the maximum couplings allowed for a given spectrum (masses of particles and bound states) of the theory? The answer gives rise to bounds that carve out the space of consistent quantum field theories. The physical intuition for the existence of these bounds is that by increasing a given coupling the bound state mass would be smaller or more bound states could be created, thus changing the originally fixed spectrum.

The first problem studied in this revival [6] was the two-dimensional scattering of theories with a single type of particles. Bounds on possible cubic couplings were obtained along with the S-matrices saturating those bounds. At special points in this boundary (i.e. particular spectra), known integrable theories like the sine-Gordon model and critical Ising model with magnetic field were found. Part of these results are reviewed in chapter 6 as an introduction to the subject.

In this thesis we add another ingredient to the problem and study two-dimensional theories with a global symmetry. This is a richer situation where we have different particles that can scatter and form bound states in various representations of the symmetry group. In chapter 7 we will establish various bounds for theories with $O(N)$ symmetry through both numerical and analytic studies. Furthermore, we will rediscover known integrable theories like the Gross-Neveu and non-linear sigma models as well as an integrable solution whose corresponding physical model is yet to be determined. The content of this chapter is based on our publication [7].

In chapter 8 we will restrict to theories without bound states and explore the associated space of S-matrices. We will consider various subsections of this space and find that some of the integrable theories mentioned above appear at special points on its boundary. Moreover, we will unveil very interesting structures of the S-matrices at the boundary of this space. The material of this chapter is based on investigations with Yifei He, Martín Krusczenski and Pedro Vieira which resulted in the article [8].

Part I

Pentagons in $\mathcal{N} = 4$ SYM

Chapter 2

Preliminary notions

2.1 $\mathcal{N} = 4$ Super-Yang-Mills

In this first part of the thesis we focus on a particular theory known as $\mathcal{N} = 4$ Super-Yang-Mills (SYM). It is a gauge theory in four spacetime dimensions whose Lagrangian takes the form (for clarity we are ommiting indices)

$$\mathcal{L} = \text{Tr}\ \left[-\frac{1}{4}F^2 - \frac{1}{2}(D\phi)^2 + \frac{i}{2}\bar{\psi}\slashed{D}\psi + \frac{g_{\text{YM}}}{2}\bar{\psi}\,\Gamma\,[\phi, \psi] + \frac{g_{\text{YM}}^2}{4}[\phi, \phi]^2 \right] \tag{2.1}$$

where g_{YM} is the coupling constant, Γ are the ten-dimensional Dirac matrices[1] and all fields transform in the adjoint representation of the $SU(N)$ gauge group. The field content of the theory is: the gauge field A_μ (with its associated field strength $F_{\mu\nu}$), four Weyl fermions (antifermions) $\psi_A(\bar{\psi}^A)$ and six real scalars $\phi^{AB} = -\phi^{BA}$, where $A, B = 1, ..., 4$ are indices for the SU(4) R-symmetry rotating the different supercharges.

This theory has several features that have made possible to achieve substancial progress in the computation of different observables. It is conformal, has $\mathcal{N} = 4$ supersymmetry, and is integrable. It is also the prototypical example of the AdS/CFT correspondence.

In this work we restrict to the planar limit of the theory where the number of colors is taken to infinity $N \to \infty$ and focus on two particular observables: scattering amplitudes and null polygonal Wilson loops which we describe below.

---

[1]The Lagrangian (2.1) was first computed in [9] from the dimensional reduction of $\mathcal{N} = 1$ SYM in ten spacetime dimensions, which provides a simple explanation for the appearence of the ten-dimensional Dirac matrices.

2.2 Scattering Amplitudes

In this section we review some basic aspects of scattering amplitudes in $\mathcal{N} = 4$ SYM, for a nice review see e.g. [10].

The observable we study in next chapters is the color-ordered amplitude, which is found by stripping out the color structure

$$\mathrm{A}_n = [\mathrm{Tr}\ (T^{a_1}T^{a_2}\ldots T^{a_n})A_n + \mathrm{permutations}] + \mathrm{multi\text{-}traces} \qquad (2.2)$$

where T^a are the gauge group generators and the color ordered amplitude is a function of the Yang-Mills coupling and number of colors as well as the external momenta $A_n = A_n(p_1, ..., p_n; g_{\mathrm{YM}}, N)$. If we take the planar limit where $N \to \infty$ we can ignore the contribution from the multi-traces. The leading term of the single-trace is referred to as planar amplitude $\mathcal{A}_n$ and admits an expansion in terms of the 't Hooft coupling $\lambda = g_{\mathrm{YM}}^2 N$. This is the observable we focus on henceforth.

The fields we are scattering are massless and can be packed into a single superfield:

$$\Phi = g^+ \tilde{\eta}^A \psi_A + \frac{1}{2!}\tilde{\eta}^A\tilde{\eta}^B \phi_{AB} + \frac{1}{3!}\epsilon_{ABCD}\tilde{\eta}^A\tilde{\eta}^B\tilde{\eta}^C\bar{\psi}^D + \frac{1}{4!}\epsilon_{ABCD}\tilde{\eta}^A\tilde{\eta}^B\tilde{\eta}^C\tilde{\eta}^D g^-\,, \qquad (2.3)$$

where $\tilde{\eta}^A$ are Grassmann variables carrying an index $A = 1, ..., 4$ for the SU(4) R-symmetry and the fields are: two gluons $g^\pm$ with helicity ± 1, four fermions (antifermions) ψ_A $(\bar{\psi}^A)$ with helicity $+\frac{1}{2}$ $(-\frac{1}{2})$ and six scalars $\phi_{[AB]}$.

Similarly, one can write a single superamplitude where different powers of $\tilde{\eta}$ encode the information of which particles are being scattered. The superamplitude takes the form

$$\mathcal{A}_n = \delta^{(4)}(p)\delta^{(8)}(\bar{q})\left[\mathcal{A}_n^{\mathrm{MHV}} + \tilde{\eta}^4 \mathcal{A}_n^{\mathrm{NMHV}} + \ldots + \tilde{\eta}^{4(n-4)}\mathcal{A}_n^{\mathrm{N}^{4(n-4)}\mathrm{MHV}}\right]\,, \qquad (2.4)$$

where we have used the notation $\delta^{(4)}(p) = \delta^{(4)}\left(\sum_{i=1}^n p_i^\mu\right)$, $\delta^{(8)}(\bar{q}) = \prod_{A=1}^4 \sum_{i<j}^n \langle ij\rangle\tilde{\eta}_i^A\tilde{\eta}_j^A$ and $(\tilde{\eta})^4 = \epsilon_{ABCD}\tilde{\eta}^A\tilde{\eta}^B\tilde{\eta}^C\tilde{\eta}^D$ [2]. To give an example, if we want the amplitude $\mathcal{A}_4(\psi, \bar{\psi}, \phi, \phi)$ we would pick the term with $\tilde{\eta}_1^1\,\tilde{\eta}_2^2\tilde{\eta}_2^3\tilde{\eta}_2^4\,\tilde{\eta}_3^1\tilde{\eta}_3^2\,\tilde{\eta}_4^3\tilde{\eta}_4^4$ in (2.4). In order to have a an SU(4) singlet, each term in the superamplitude comes with a multiple of four $\tilde{\eta}$s. As a consequence of supersymmetry, the smallest and largest powers of $\tilde{\eta}$ in the expansion (2.4) are respectively $4(2)$ and $4(n-2)$. The first one is referred to as Maximally Helicity Violating (MHV) and

---

[2]We are using the spinor helicity formalism and on-shell supercharges $q_A = [p|\,\partial_{\tilde{\eta}^A}$ $\bar{q}^A = |p\rangle\tilde{\eta}^A$ as reviewed in [10].

includes the gluon amplitude $\mathcal{A}_n^{\text{MHV}} \supset \mathcal{A}_n \left(g^- g^- g^+ \dots g^+ \right)$ [3]. The next terms are known as (next-to)^k maximally helicity violating (N^kMHV) and will play an important role in the next chapters.

2.3 Wilson loop duality

Another observable we will work with is the expectation value of Wilson loops. First introduced in the study of strong interactions, they are a probe of confinement in a given theory. The Wilson loops are non-local observables defined by

$$W[\mathcal{C}] = \text{Tr} \, \mathcal{P} \exp \int_{\mathcal{C}} A \,, \tag{2.5}$$

where A is the gauge field of the theory, $\mathcal{P}$ denotes path ordering and the Wilson loop depends on the contour of integration $\mathcal{C}$.

Remarkably, in $\mathcal{N} = 4$ SYM the scattering amplitudes reviewed in the previous section are dual to the expectation value of Wilson loops with a null polygonal contour. The (lightlike) edges of the contour are identified with the momenta of the scattered (massless) particles and close into a polygon because of momentum conservation. Schematically, we have

$$\mathcal{A}_n(p_1, \dots, p_n) = W_n(x_1, \dots, x_n) \tag{2.6}$$

where the dual variables x_i parametrizing the vertices of the polygon are related to the external momenta as $p_i = x_i - x_{i+1}$.

The duality was first observed at strong coupling in [11]. In the context of the AdS/CFT correspondence, the computation of gluon scattering amplitudes at strong coupling amounts to finding a minimal area in AdS$_5$ ending in the polygonal contour described above[4]. The duality was then checked at weak coupling (up to two loops and six external particles) in [12–15].

So far we have referred to the usual bosonic Wilson loops which map to MHV amplitudes. The duality is also valid for general helicity configurations once we consider the proper generalization to a supersymmetric Wilson loop. For the case of null polygonal

---

[3]The name comes from thinking of $2 \to (n-2)$ scattering; from supersymmetry $\mathcal{A}_n(g^+ g^+ \to g^- \dots g^-)$ and $\mathcal{A}_n(g^+ g^+ \to g^+ g^- \dots g^-)$ are zero, so that $\mathcal{A}_n(g^+ g^+ \to g^+ g^+ g^- \dots g^-)$ is the maximally helicity violating amplitude which in our all incoming notation translates to $\mathcal{A}_n \left(g^- g^- g^+ \dots g^+ \right)$.

[4]To reach this conclusion, the authors of [11] perform a T-duality under which AdS$_5$ maps to itself.

contours, the idea is to introduce edge $\mathcal{E}$ and vertex $\mathcal{V}$ terms which have the schematic form[5] $\mathcal{E} = A + \eta\bar{\psi} + \mathcal{O}(\eta^2)$ and $\mathcal{V} = 1 + (\eta)^2\phi + \mathcal{O}(\eta^3)$. (For the clarity in the present discussion we have omitted writting the explicit expressions which can be found in Appendix B of [16].) The supersymmetric Wilson loop is given by

$$W_n^{\text{super}} = \text{Tr} \ (E_1\mathcal{V}_{12}E_2\ldots E_n\mathcal{V}_{n1}) \ , \quad E_i = \mathcal{P}\exp\int_{\mathcal{C}} \mathcal{E}_i \, . \tag{2.7}$$

The bottom component in the η expansion of (2.7) matches the bosonic Wilson loop described above.

As a final remark for this section, let us point out that the amplitude/Wilson loop duality clarifies the origin of a hidden symmetry in the scattering amplitudes side. In [17] it was discovered that the amplitudes possess an extra *dual superconformal symmetry* which under the duality simply maps to the ordinary superconformal invariance in the Wilson loop picture. It is worth noting that at loop level the scattering amplitudes/Wilson loops have are infrarred/ultraviolet divergences that naively break some of the symmetries. The problem can be solved by considering finite ratios of the observables and corrected generators as in [18]. The dual and ordinary superconformal symmetries together generate an infinite dimensional Yangian symmetry which encodes the integrability of the theory [18–20].

2.4   Pentagon Operator Product Expansion

Now we introduce the final and main ingredient of Part I: the Pentagon Operator Product Expansion (POPE). As first put forward in [21] and then refined in [1, 22–24], the idea of the POPE program is to compute the expectation value of theWilson loops described in the previous section as an evolution of the color flux tube supported by two null Wilson lines. The program takes its name from the Operator Product Expansion (OPE) used in conformal field theories where one sums over the states generated by fusing the local operators inside a correlation function. In the Pentagon program, the sum is over the possible flux tube excitations.

In any conformal field theory, the polygonal Wilson loops can be decomposed into a sequence of smaller polygons, the building blocks being squares and pentagons. The squares encode the evolution of a given flux tube state and the pentagons the transition between

---

[5]The Grassmann variables for the supersymmetric Wilson loop are related to the ones introduced in (2.3) for the amplitudes via $\tilde{\eta}_i = [\langle i-1, i\rangle\langle i, i+1\rangle]^{-1} [\langle i, i+1\rangle\eta_{i-1} - \langle i-1, i+1\rangle\eta_i + \langle i-1, i\rangle\eta_{i+1}]$.
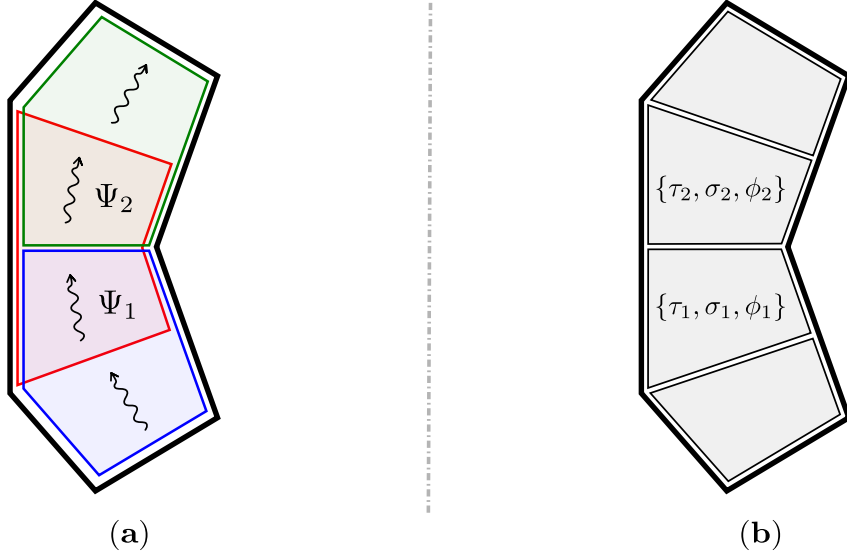
Figure 2.1: **(a)** Pentagon decomposition for the heptagon Wilson loop. We start at the bottom of the polygon and follow the evolution of the flux tube to the top. The transitions between the flux tube states vacuum $\to \Psi_1 \to \Psi_2 \to$ vacuum is encoded in the pentagon transitions: $P(0|\Psi_1)P(\Psi_1|\Psi_2)P(\Psi_2|0)$. **(b)** In each middle square $\{\tau_i, \sigma_i, \phi_i\}$ play the role of time, space and angle; they parametrize the cross ratios of the polygon.

different flux tube states. In figure 2.1 we show such decomposition for a heptagon Wilson loop.

The kinematical data given by the cross ratios of the n-polygon is related to $\{\tau_i, \sigma_i, \phi_i\}$ which play the role of time, space and angle in each of the $(n-5)$ middle squares[6]. On the other hand, the dynamics is carried by the pentagon transitions, in analogy to the structure constants in the regular OPE. In sum, the Wilson loop can be written as[7]:

$$\mathcal{W}_n = \sum_{\psi_i} P(0|\psi_1)P(\psi_1|\psi_2)\dots P(\psi_{n-6}|\psi_{n-5})P(\psi_{n-5}|0)\, e^{\sum_j (-E_j\tau_j + ip_j\sigma_j + im_j\phi_j)}, \qquad (2.8)$$

where $P(\psi_i|\psi_j)$ are the pentagon transitions and ψ_i are flux tube states with energy E_i, momentum p_i and angular momentum m_i defined in the i-th middle square. Notice that in the limit $\tau_i \to \infty$ the main contribution comes from the lightest flux tube excitations. This

---

[6]For the specific relation between cross ratios and flux tube parameters see for instance appendix A of [22].

[7]Here, $\mathcal{W}$ refers to a finite ratio described in the following chapter.

limit is known as collinear limit since in the scattering amplitude picture it amounts to having a particular kinematic regime where two adjacent momenta are collinear ($p_{i+1} \approx p_i$) whereas in the polygonal Wilson loop it correspondons to flattening two of its edges. As we shall see in the next chapters, this is the natural expansion in the POPE program.

So far the discussion has been for a general conformal field theory. What makes $\mathcal{N} = 4$ SYM special is that, thanks to integrability, the different ingredients in the decomposition (2.8) can be bootstrapped at finite coupling. It is indeed because of the integrability friendly two-dimensional auxiliary problem of the flux tube dynamics that we can compute the non-perturbative four-dimensional scattering amplitudes in this theory.

There are various descriptions of the color flux tube in $\mathcal{N} = 4$ SYM. The first one alluded to in the discussion above is a square null Wilson loop. The flux tube can also be viewed as a large spin operator of the form $\mathcal{O} = \mathrm{Tr} \ [\Phi(D_-)^s\Phi]$ (where the derivative is along a null direction x^-). At strong coupling it is useful to think of the dual description as a folded string rotating in AdS_5 known as the Gubser-Klebanov-Polyakov (GKP) string [25]. The flux tube excitations can then be viewed as field insertions along a null Wilson line or inside the sea of null derivatives of $\mathcal{O}$ or as ripples on the GKP string [22].

Using integrability, the finite coupling dispersion relations for the fundamental excitations were worked out in [26]. The lightest flux tube excitations are: six real scalar fields ϕ^{AB}, four fermions (antifermions) $\psi_A(\bar{\psi}^A)$ and two gluons $F, \bar{F}$. As explained in the next chapters, they can form bound states and effective excitations.

The pentagon transitions appearing in the decomposition (2.8) can be bootsrapped following a modified version of the form factor axioms in integrability [1, 22]. Keeping the details to chapter 4, one of the axioms is called the *fundamental relation* $P(\psi_i|\psi_j) = S(\psi_i|\psi_j)P(\psi_j|\psi_i)$ and gives an explicit relation between the pentagon transitions and the S-matrices for flux tube excitations.

Let us summarize the main points presented in this section. The decomposition (2.8) shows how the expectation value of null polygonal Wilson loops can be computed as an evolution of the color flux tube of the theory, summing over all intermediate flux tube states. Through the duality between Wilson loops and scattering amplitudes described in the previous section, the same decomposition also provides a fully non-perturbative representation of the Maximal Helicity Violating (MHV) gluon scattering amplitudes in planar $\mathcal{N} = 4$ SYM theory.

In the following chapters we describe how we can include different helicity configurations in this program and obtain the amplitudes away from the collinear limit at weak coupling. The outline is the following: in chapter 3 we present the map between charged pentagons and different components of the superamplitudes; in chapter 4 we introduce the different

building blocks of the POPE integrand and in chapter 5 we explain how we can resum the contribution from all flux tube excitations at weak coupling.

Chapter 3

POPE for all helicities I

3.1   Introduction

In this chapter we will argue that a suitable generalization of the pentagon transitions into super or *charged* pentagon transitions allows one to describe all amplitudes, for any number of external particles with arbitrary helicities and at any value of the 't Hooft coupling.

While the key ingredient in having an OPE expansion such as (2.8) is conformal symmetry, a central ingredient in the charged pentagon approach will be supersymmetry.

The idea of charging the pentagons is not entirely new, and already appeared in [22] where certain charged transitions were introduced and successfully compared against N^kMHV amplitudes. More recently, further charged transitions were bootstrapped and matched with amplitudes in [24, 27, 28].

The aim of this chapter is to complete this picture by proposing a simple map between all possible helicity amplitudes and all the ways charged pentagons can be patched together into an OPE series like (2.8). An interesting outcome of this charged pentagons analysis is a simple proposal for how parity acts at the level of the super Wilson loop, which, as far as we are aware, was not known before.

3.2   The Charged Pentagon Program

In the dual Wilson loop picture, N^kMHV amplitudes are computed by a super Wilson loop decorated by adjoint fields inserted on the edges and cusps [16, 29]. It is this super loop
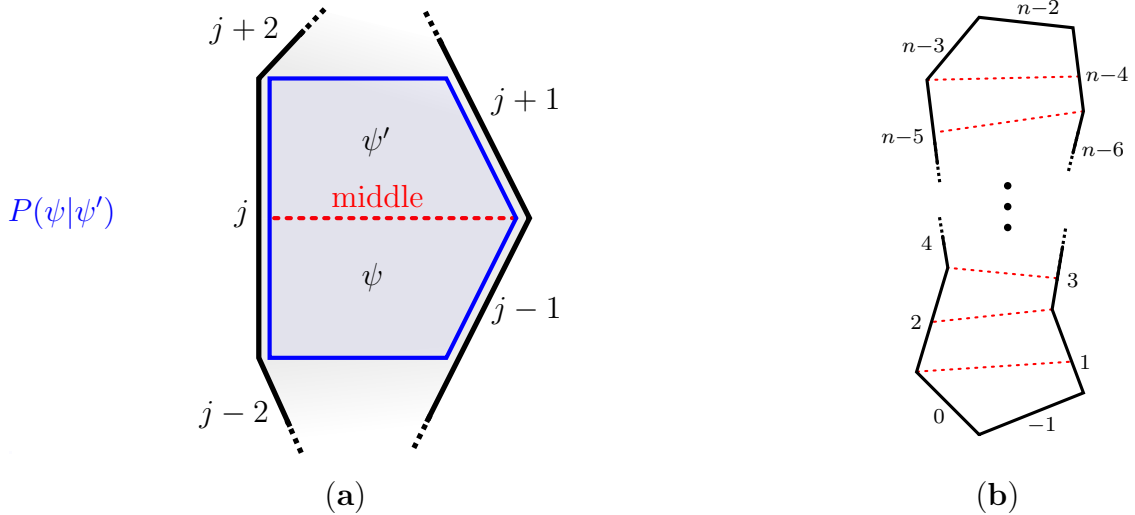
Figure 3.1: **a**) The pentagon transitions are the building blocks of null polygonal Wilson loops. They represent the transition $\psi \to \psi'$ undergone by the flux-tube state as we move from one square to the next in the OPE decomposition. This breaking into squares is univocally defined by specifying the middle (or inner dashed) edge of the pentagon to be $Z_{\mathrm{middle}} \propto \langle j-2, j, j+2, j-1 \rangle Z_{j+1} - \langle j-2, j, j+2, j+1 \rangle Z_{j-1}$. **b**) In the OPE-friendly labelling of edges, adopted in this chapter, the middle edge of the j-th pentagon ends on the j-th edge. As a result, the very bottom edge is edge -1 while the very top one is edge $n-2$. The map between the OPE index j and the more common cyclic index j_{cyc} reads $j_{\mathrm{cyc}} = \frac{3}{4} - \frac{1}{4}(-1)^j(2j+3) \bmod n$.

that we want to describe within the pentagon approach.

At first, let us first ask ourselves what would be a natural extension of (2.8) that allows for some regions of the loop to be *charged* due to the insertion of these extra fields. The minimal modification one could envisage is to generalize the pentagon transitions to super pentagon transitions or *charged* transitions, in which $P(\psi|\psi')$ stands as the bottom component. As for the $\mathcal{N} = 4$ on-shell super field, a pentagon would naturally come in multiple of five components

$$\mathbb{P} = P + \chi^A P_A + \chi^A \chi^B P_{AB} + \chi^A \chi^B \chi^C P_{ABC} + \chi^A \chi^B \chi^C \chi^D P_{ABCD} , \qquad (3.1)$$

where χ is a Grassmann parameter, $A = 1, 2, 3, 4$ an R-charge index, and where, for sake of clarity, we have suppressed the states ψ and ψ'. With these charged transitions at hand,

13

we could now imagine building up charged polygons such as

$$\mathcal{P}_A \circ \mathcal{P}^A \equiv \sum_{\psi_1} P_A(0|\psi_1) P^A(\psi_1|0) e^{-E_1\tau_1 + \cdots},$$

$$\mathcal{P}_{AB} \circ \mathcal{P} \circ \mathcal{P}^{AB} \equiv \sum_{\psi_1,\psi_2} P_{AB}(0|\psi_1) P(\psi_1|\psi_2) P^{AB}(\psi_2|0) e^{-E_1\tau_1 + \cdots}, \qquad (3.2)$$

$$\mathcal{P}_{AB} \circ \mathcal{P}_{CD} \circ \mathcal{P}^{AB} \circ \mathcal{P}^{CD} \equiv \sum_{\psi_1,\psi_2,\psi_3} P_{AB}(0|\psi_1) P_{CD}(\psi_1|\psi_2) P^{AB}(\psi_2|\psi_3) P^{CD}(\psi_3|0) e^{-E_1\tau_1 + \cdots}$$

and so on. Here, an upper index represents a contraction with an epsilon tensor. Namely, we use $P^A = \epsilon^{ABCD} P_{BCD}$, $P^{AB} = \epsilon^{ABCD} P_{CD}$ and $P^{ABC} = \epsilon^{ABCD} P_D$ to compress the expressions above.

The most obvious change with respect to the MHV case is that R-charge conservation now forbids some of the processes which were previously allowed and vice-versa. For instance, in the creation amplitude $P_{AB}(0|...)$ we can produce a scalar ϕ_{AB} out of the vacuum, since this excitation has quantum numbers that match those of the charged pentagon. At the same time, neutral states such as the vacuum or purely gluonic states – which appeared in the non-charged transitions – can no longer be produced by this charged pentagon.

What stays the same is that all these charged transitions can be bootstrapped using integrability – as much as their bosonic counterparts. The *scalar* charged transition P_{AB} and the *gluon* charged transition P_{ABCD}, for instance, already received analysis of this sort in [22, 24].[1] The fermionic charged transitions, P_A and P_{ABC}, were more recently constructed in [27, 28].

The super pentagon hypothesis (3.1) and its OPE corollary (3.2) are the two main inputs in the charged pentagon program for helicity amplitudes. In the rest of this section we present a simple counting argument supporting the equivalence between super OPE series and super amplitudes.

The important point is that not all the N^{k}MHV amplitudes are independent. Because of supersymmetry, many of them get linked together by means of so-called SUSY Ward identities. At given number n of particles, there is a basis of $\mathcal{N}(k,n)$ amplitudes in terms of which one can linearly express all the remaining ones.

The problem of eliminating this redundancy, such as to count the $\mathcal{N}(k,n)$ independent amplitudes, was beautifully analyzed in [30]. As explained below, the very same counting applies to inequivalent super OPE series like (3.2).

---

[1]Both were denoted by P_* in these works.

Counting the number of super OPE series is relatively easy:

At first, one notices that the R-charge of a polygon is always a multiple of four, as a consequence of $SU(4)$ symmetry. The first two cases in (3.2), for instance, involve charged pentagons with a total of 4 units, as for NMHV amplitudes, while the last example in (3.2) has a total of 8 units of charge, and should thus be related to N^2MHV amplitudes.

In the NMHV case, the amount of charge in each of the $n-4$ pentagons uniquely specifies the super OPE series and there is clearly $(n-1)(n-2)(n-3)(n-4)/4!$ ways of distributing four units of charge between the $n-4$ pentagons in our tessellation. Precisely this number is reported for $\mathcal{N}(1,n)$ in [30], see discussion below (3.12) therein.

This kind of partitions no longer enumerate all cases starting with N^2MHV amplitudes. For instance, there are three independent ways of charging all the four pentagons of an octagon with two units of charge,

$$\mathcal{P}_{AB} \circ \mathcal{P}_{CD} \circ \mathcal{P}^{AB} \circ \mathcal{P}^{CD}\,, \quad \mathcal{P}_{AB} \circ \mathcal{P}^{AB} \circ \mathcal{P}_{CD} \circ \mathcal{P}^{CD}\,, \quad \mathcal{P}_{AB} \circ \mathcal{P}_{CD} \circ \mathcal{P}^{CD} \circ \mathcal{P}^{AB}\,, \quad (3.3)$$

with the last line in (3.2) being one of them. (We can understand this as coming from the three possible irreducible representations in $\mathbf{6} \otimes \mathbf{6}$ or, equivalently, as the three inequivalent ways of forming singlets in $\mathbf{6} \otimes \mathbf{6} \otimes \mathbf{6} \otimes \mathbf{6}$.) Therefore, to count the number of N^2MHV charged polygons we have to consider not only the number of ways of distributing eight units of charge within four pentagons but also to weight that counting by the number of inequivalent contractions of all the R-charge indices. Remarkably, this counting is identical to the one found in [30] based on analysis of the SUSY Ward identities. This is particularly obvious when looking at Table 1 in [30] where the number of independent N^2MHV components for 8 and 9 particles is considered. [2] In sum, our construction in (3.2) generates precisely $\mathcal{N}(2,8) = 105$, $\mathcal{N}(2,9) = 490, \ldots$ different N^2MHV objects, in perfect agreement with the number of independent components arising from the study of the SUSY Ward identities.

It is quite amusing that the notation in [30] with a partition vector $\lambda = [\lambda_1, \ldots, \lambda_{n-4}]$ seems perfectly tailored to describe the charged pentagon approach where we have $n-4$ pentagons with charges $\lambda_i \in \{0, 1, 2, 3, 4\}$. It also guarantees that the most general N^kMHV counting works the same for both amplitudes and OPE series, and concludes this analysis. The next step is to endow the charged pentagon construction with a precise dictionary between charged polygons and helicity configurations of scattering amplitudes.

---

[2] The weight $3 = \mathcal{S}_{\lambda=[2,2,2,2]}$ in their table is precisely the one explained in our above discussion.
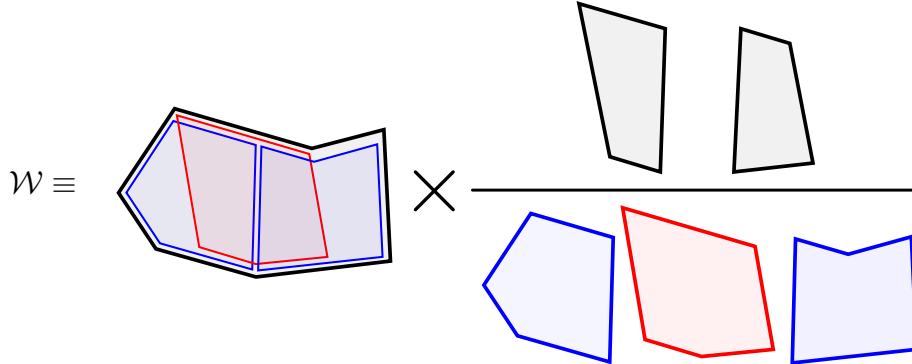
Figure 3.2: We study the conformally invariant and finite ratio $\mathcal{W}$ introduced in [1]. It is obtained by dividing the expectation value of the super Wilson loop by all the pentagons in the decomposition and by multiplying it by all the middle squares. The twistors that define these smaller pentagons are either the twistors of the original polygon (an heptagon in this figure) or the middle twistors described in figure 3.1.a (in the above figure there are three distinct middle twistors, for instance).

3.3 The Map

A compact way of packaging together all helicity amplitudes is through a generating function, also known as the super Wilson loop [16, 29]

$$W_{\text{super}} = W_{\text{MHV}} + \eta_i^1 \eta_j^2 \eta_k^3 \eta_l^4 \; W_{\text{NMHV}}^{(ijkl)} + \eta_i^1 \eta_j^2 \eta_k^3 \eta_l^4 \eta_m^1 \eta_n^2 \eta_o^3 \eta_p^4 \; W_{\text{N}^2\text{MHV}}^{(ijkl)(mnop)} + \dots \quad (3.4)$$

where $W_{\text{N}^k\text{MHV}}$ is the N^kMHV amplitude divided by the Parke-Taylor MHV factor. Here, the η's are the dual Grassmann variables [17, 31]. They transform in the fundamental of the $SU(4)$ R-symmetry, as indicated by their upper index $A = 1, 2, 3, 4$, and are associated to the edges of the polygon, indicated by the lower index $i = -1, 0, 1, \dots, n - 2$.

Throughout this chapter we shall be using a rather unorthodox labelling of the edges of the polygon, which is represented in figure 3.1. Namely, we number the edges from bottom to top, with even numbers on one side and odd numbers on the other, like door numbers within a street. Given that we think of the Wilson loop as a sequence of flux-tube states propagating down this *street*, this is the most natural labelling from the OPE viewpoint. It makes it particularly simple to locate the j-th pentagon in the tessellation: it is the pentagon whose middle edge ends on edge j. The map between this labelling and the conventional cyclic ordering is explained in the caption of figure 3.1.

The super loop (3.4) has UV suppression factors associated to its cusps.[3] One can find in the literature several different ways of renormalizing the loop, such as to remove these factors. The one most commonly used is the *ratio function* $\mathcal{R} \equiv W_{\text{super}}/W_{\text{MHV}}$, first introduced in [17]. For our discussion, however, the OPE renormalization is better suited: it is obtained by dividing the super loop (3.4) by all the pentagons in its decomposition and by multiplying it by all the middle squares [22]

$$\mathcal{W} \equiv W_{\text{super}}/\text{w} \qquad \text{with} \qquad \text{w} \equiv \left(\prod_{i=1}^{n-4} \langle W_{i'\text{th pentagon}} \rangle \right) / \left(\prod_{i=1}^{n-5} \langle W_{i'\text{th middle square}} \rangle \right), \quad (3.5)$$

as shown in figure 3.2. The ratio function $\mathcal{R}$ and the loop $\mathcal{W}$ are then easily found to be related to each other by $\mathcal{R} = \mathcal{W}/\mathcal{W}_{\text{MHV}}$. They are essentially equivalent, being both finite and conformally invariant functions of the η's and shape of the loop, but only $\mathcal{R}$ is cyclic invariant.

3.3.1 The Direct Map

Our goal in this section is to find the map between the different ways of gluing the charged transitions together, as in (3.2), and the components of the super loop (3.5). Put differently, we would like to find a map between the η's and the χ's such that $\mathcal{W}$ in (3.5) also admits the expansion

$$\mathcal{W} = \mathcal{P} \circ \mathcal{P} \circ \cdots \circ \mathcal{P} + \chi_1^1 \chi_1^2 \chi_1^3 \chi_1^4 \, \mathcal{P}_{1234} \circ \mathcal{P} \circ \cdots \circ \mathcal{P} + \chi_1^1 \chi_1^2 \chi_1^3 \chi_2^4 \, \mathcal{P}_{123} \circ \mathcal{P}_4 \circ \cdots \circ \mathcal{P} + \dots \quad (3.6)$$

in terms of the χ's.

There are two important properties of the super loop that will be relevant to our discussion.

First, recall that an η is associated to an edge of the polygon while a χ is associated to a pentagon. As such, there are many more terms in the η-expansion (3.4) or (3.5) of the super loop than there are in the χ-expansion (4.14). This is no contradiction, however. The reason is that the η-components are not all linearly independent, since, as mentioned before, they are subject to SUSY Ward identities. On the contrary, the χ-components *all* have different OPE interpretation and, in line with our previous discussion, should be viewed as defining a basis of independent components for the amplitudes. In other words, the map between χ- and η-components is not bijective if not modded out by the SUSY

---

[3]These UV divergences are T-dual to the IR divergences of the on-shell amplitudes.
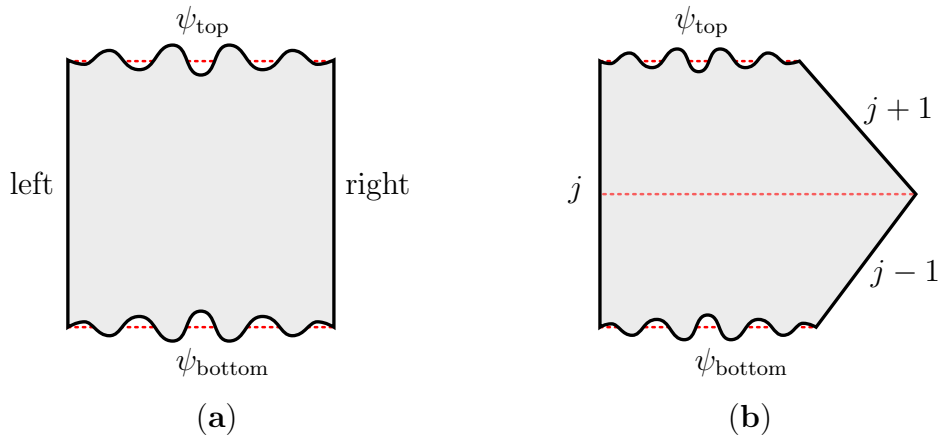
Figure 3.3: **a**) Any square in the OPE decomposition stands for a transition from the state at its bottom (ψ_{bottom}) to the state at its top (ψ_{top}). This transition is generated by a conformal symmetry of the right and left edges of that square (conjugate to the flux time τ). **b**) Similarly, the super pentagon $\mathbb{P}$ represents a transition from the state at its bottom to the state at its top. In the fermionic χ-directions, this transition is generated by a super-conformal symmetry of the $(j-1)$-th, j-th and $(j+1)$-th edges in this figure.

Ward identities. We can then think of the χ-decomposition as a natural way of getting rid of SUSY redundancy.

Second, the η-components of $\mathcal{W}$ are not 'pure numbers', since they carry weights under the little group; e.g., upon rescaling of the twistor $Z_1 \to \alpha Z_1$ the component $\mathcal{W}^{1123}_{\text{NMHV}}$ transforms as $\mathcal{W}^{1123}_{\text{NMHV}} \to \mathcal{W}^{1123}_{\text{NMHV}}/\alpha^2$. These helicity weights cancel against those of the η's, so that $\mathcal{W}$ is weight free in the end. In contrast, the components in (4.14), as well as the corresponding χ's, are taken to be weightless. With this choice, the χ-components coincide with the ones predicted from integrability with no additional weight factors.

We now turn to the construction of the map. The question we should ask ourselves is: *What does it mean to charge a pentagon transition?* Said differently, how do we move from one pentagon-component to another in the χ decomposition of $\mathbb{P}$ in (3.1)? To find out, it helps thinking of the χ's as fermionic coordinates of sort and recall how usual (meaning bosonic) variables are dealt within the OPE set up.

The bosonic cross ratios are naturally associated with the symmetries of the middle squares. Namely, we can think of any middle square as describing a transition between two flux-tube states, one at its bottom and the other one at its top, as depicted in 3.3.**a**. Attached to this square are three conformal symmetries that preserve its two sides (left and right). To move in the space of corresponding cross ratios (τ, σ, ϕ) we act on the bottom

state with these symmetries

$$\psi_{\text{bottom}} \quad \longrightarrow \quad e^{-H\tau + iP\sigma + iJ\phi}\, \psi_{\text{bottom}}\,. \tag{3.7}$$

Equivalently, we could act with the inverse transformations on the state at the top (ψ_{top}), since these are symmetries of the left and right sides sourcing the flux. In other words, the OPE family of Wilson loops is obtained by acting on all the twistors below each middle square with the conformal symmetries of that square.

Similarly, to move in the space of 'fermionic coordinates' we should act with a supercharge. In contrast to the previous case, these are now associated to the pentagons in the OPE decomposition. A pentagon transition represents the transition between two flux-tube states, one on the bottom square and the other on the top square – the transition being induced from the shape of the pentagon. So what we should do is to find the supercharge that preserves the three sides of the pentagon sourcing the two fluxes, i.e., the sides $j-1$, j and $j+1$ in figure 3.3.b, and act with it on the state at its bottom (ψ_{bottom}) or, equivalently, with the inverse symmetry on the state at its top (ψ_{top}). There is precisely one chiral supercharge that does the job, as we now describe.

Recall that we have 16 chiral supercharges at our disposal, that is, $\mathcal{Q}_A^a$ where A is an R-charge index and a is an $SL(4)$ twistor index. By construction they annihilate the super loop $\mathcal{W}$ on which they act as [32]

$$\mathcal{Q}_A^a = \sum_{i=-1}^{n-2} Z_i^a \frac{\partial}{\partial \eta_i^A} \qquad \text{with} \qquad \mathcal{Q}_A^a\, \mathcal{W} = 0\,. \tag{3.8}$$

By definition, for a given supercharge not to act on, say, the i-th side of the super loop, we need the coefficient of $/\partial \eta_i^A$ to vanish. This can be achieved by contracting the $SL(4)$ index a with a co-twistor Y such that $Y \cdot Z_i = 0$. In our case, since we want $\mathcal{Q}$ to be a symmetry of the three sides of a pentagon, the co-twistor should be orthogonal to Z_{j-1}, Z_j and Z_{j+1}. There is exactly one such co-twistor:

$$Y_j \equiv Z_{j-1} \wedge Z_j \wedge Z_{j+1}\,. \tag{3.9}$$

It is then straightforward to define the operator $/\partial \chi_j^A$ that charges the j-th pentagon. It acts as $Y_j \cdot \mathcal{Q}^A$ on the state ψ_{bottom} entering the j-th pentagon from the bottom or, equivalently, on what have created this state. In other words, $/\partial \chi_j^A$ is defined as $Y_j \cdot \mathcal{Q}^A$ in (3.8) but with the summation restricted to edges lying below the j-th pentagon:

$$\boxed{\frac{\partial}{\partial \chi_j^A} \equiv \frac{1}{(\mathbf{j}-\mathbf{1})_j\, (\mathbf{j})_j\, (\mathbf{j}+\mathbf{1})_j} \sum_{i=-1}^{j-2} Y_j \cdot Z_i \frac{\partial}{\partial \eta_i^A}\,.} \tag{3.10}$$

19

Alternatively we could act on the state ψ_{top} at the top of the pentagon by restricting the summation to edges lying above the j-th pentagon and flipping the overall sign. These two prescriptions yield the same result since the two actions differ by $Y_j \cdot \mathcal{Q}^A$ where $\mathcal{Q}^A$ is the full supercharge annihilating the super loop.

The normalization factor multiplying the sum in (3.10) needs some explanation. It is introduced to make $/\partial \chi_j^A$ weight free. In other words, it is defined such as to remove the weight of the co-twistor Y_j used to define our supercharge. In our notation, $(\mathbf{i})_j$ extracts the weight of the twistor Z_i in the j-th pentagon. This operation is unambiguous once we require it to be *local* with respect to the j-th pentagon, meaning that it should only make use of the five twistors of this pentagon. Indeed, given a pentagon p with five twistors $Z_a, \ldots, Z_e$, the unique conformally invariant combination carrying weight with respect to a is given by

$$(\mathbf{a})_p{}^4 = \frac{\langle abcd \rangle \langle cdea \rangle \langle deab \rangle \langle eabc \rangle}{\langle bcde \rangle^3} \,. \tag{3.11}$$

Uniqueness is very simple to understand. If another such expression existed, its ratio with (3.11) would be a conformal cross-ratio, which of course does not exist for a pentagon. A nice equivalent way of thinking of the weight (3.11) is as the NMHV tree level amplitude for the corresponding pentagon, that is

$$(\mathbf{i})_j^{-4} = W_{j\text{-th} \, \diamond}^{(iiii) \, \text{tree}} \,. \tag{3.12}$$

(Stated like this, the idea of dividing out by such weights is not new, see discussion around (132) in [22].) Multiplying three such weights to make the normalization factor in (3.10), we would get

$$((\mathbf{j} - \mathbf{1})_j \, (\mathbf{j})_j \, (\mathbf{j} + \mathbf{1})_j)^4 = \frac{\langle Z_{j-1}, Z_{j+1}, Z_{t|j}, Z_j \rangle^3 \, \langle Z_j, Z_{b|j}, Z_{j-1}, Z_{j+1} \rangle^3}{\langle Z_{j+1}, Z_{t|j}, Z_j, Z_{b|j} \rangle \, \langle Z_{b|j}, Z_{j-1}, Z_{j+1}, Z_{t|j} \rangle \, \langle Z_{t|j}, Z_j, Z_{b|j}, Z_{j-1} \rangle} \,, \tag{3.13}$$

where $Z_{t|j}/Z_{b|j}$ refer to the top/bottom twistors of the j-th pentagon respectively. Equivalently, $Z_{t|j}/Z_{b|j}$ are the middle twistors of the $(j+1)$-th/$(j-1)$-th pentagons, see figure 3.1. For further discussion of these weights and their rewriting see appendix A.2.

Finally, there are two minor ambiguities in the above construction on which we should comment. One is the overall normalization of (3.11) or (3.12) which is not fixed by the symmetry argument above. The convention chosen here is equivalent to setting

$$\langle \mathcal{P}_{1234} \rangle = \left[\frac{\langle Z_0, Z_1, Z_2, Z_{-1} \rangle}{(\mathbf{0})_1 (\mathbf{1})_1 (\mathbf{2})_1} \right]^4 \mathcal{W}_{\text{pentagon NMHV}}^{(-1,-1,-1,-1)} = 1 \,. \tag{3.14}$$

20
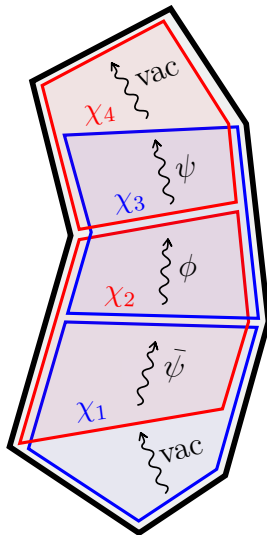
Figure 3.4: Leading OPE contribution to the NMHV octagon component $\mathcal{P}_1 \circ \mathcal{P}_2 \circ \mathcal{P}_3 \circ \mathcal{P}_4 = \frac{\partial}{\partial\chi_1^1}\frac{\partial}{\partial\chi_2^2}\frac{\partial}{\partial\chi_3^3}\frac{\partial}{\partial\chi_4^4}\mathcal{W}$. For this component, each of the four pentagons in the octagon decomposition carries one unit of R-charge and fermion number. From the flux tube point of view, this corresponds to the sequence of transitions in equation (3.16).

A second minor ambiguity comes from the fourth power in (3.11) or (3.12). Due to its presence, to extract any weight we need to compute a fourth root, giving rise to a $\mathbb{Z}_4$ ambiguity. In practice we start from a point where the right hand side of (3.13) is real and positive for any j and pick the positive fourth root when extracting the weight on the left. Then everything is real and can be nicely matched against the integrability predictions. This seems reminiscent of the sort of positivity regions of [33–35]. It would be interesting to study the $\mathbb{Z}_4$ ambiguity further, and possibly establish a connection to the positivity constraints of [33–35].

3.3.2   Interlude : Sanity Check

As a check of our map (3.10) we consider an eight-leg scattering amplitude, i.e., an octagon or, equivalently, a sequence of four pentagons. For concreteness, we focus on the example of $\mathcal{P}_1 \circ \mathcal{P}_2 \circ \mathcal{P}_3 \circ \mathcal{P}_4 = \frac{\partial}{\partial\chi_1^1}\frac{\partial}{\partial\chi_2^2}\frac{\partial}{\partial\chi_3^3}\frac{\partial}{\partial\chi_4^4}\mathcal{W}$ at tree level and evaluate it in terms of the nine OPE variables $\{\tau_i, \sigma_i, \phi_i\}$. At this order, the OPE ratio $\mathcal{W}$ coincides with the ratio function $\mathcal{R}$ and we can easily extract components of the latter from the package [36]. For large OPE

times we find that

$$\mathcal{P}_1 \circ \mathcal{P}_2 \circ \mathcal{P}_3 \circ \mathcal{P}_4 = e^{-\tau_1 - i\phi_1/2} \times e^{-\tau_2} \times e^{-\tau_3 + i\phi_3/2} \times f(\sigma_i) + \ldots \tag{3.15}$$

which is actually already a non-trivial check of our construction. Indeed, we have four charged pentagons each of which injects one unit of R-charge and one unit of fermion number. As such, the lightest states that will flow in the three middle squares are a fermion $\bar{\psi}_1$ (with helicity $-1/2$) in the first square, a scalar ϕ_{12} (with no helicity) in the second square and the conjugate fermion $\psi_{123} = \psi^4$ (with helicity $+1/2$) in the last middle square. In short, the leading process contributing to this amplitude should correspond to the sequence of transitions

$$\text{vacuum} \xrightarrow{\mathcal{P}_1} \bar{\psi}_1 \xrightarrow{\mathcal{P}_2} \phi_{12} \xrightarrow{\mathcal{P}_3} \psi_{123} \xrightarrow{\mathcal{P}_4} \text{vacuum} , \tag{3.16}$$

as represented in figure 3.4. The three exponential factors in (3.15) are in perfect agreement with this expectation.

Most importantly, the function $f(\sigma_i)$ should be given by the multiple Fourier transform of the sequence of pentagon transitions. It beautifully is. This and other similar checks – at tree level and at loop level – will be the subject of a separate longer publication [3] whose main goal will be to precisely confront the program advocated here against the available perturbative data for non-MHV amplitudes.

3.3.3 The Inverse Map

It is rather straightforward to invert the map (3.10) such as to obtain the $/\partial\eta$'s in terms of the $/\partial\chi$'s. For that aim, it is convenient to put back the weights in (3.10) and define

$$\mathcal{D}_A^{(j)} \equiv (\mathbf{j-1})_j \, (\mathbf{j})_j \, (\mathbf{j+1})_j \, \frac{\partial}{\partial \chi_j^A} = Y_j \cdot \sum_{i=-1}^{j-2} Z_i \, \frac{\partial}{\partial \eta_i^A} . \tag{3.17}$$

Given the triangular nature of this map, charging the first few edges at the bottom is as easy as writting the first few $\mathcal{D}$'s explicitly. For the bottom edge, for instance, we immediately find that

$$\mathcal{D}_A^{(1)} = Y_1 \cdot Z_{-1} \frac{\partial}{\partial \eta_{-1}^A} \qquad \Rightarrow \qquad \frac{\partial}{\partial \eta_{-1}^A} = \frac{\mathcal{D}_A^{(1)}}{Y_1 \cdot Z_{-1}} , \tag{3.18}$$

while taking this into account and moving to the following edge yields

$$\frac{\partial}{\partial \eta_0^A} = \frac{(Y_1 \cdot Z_{-1})\mathcal{D}_A^{(2)} - (Y_2 \cdot Z_{-1})\mathcal{D}_A^{(1)}}{(Y_1 \cdot Z_{-1})(Y_2 \cdot Z_0)} \,, \tag{3.19}$$

and so on.

By following this recursive procedure we will eventually find that $\slashed{\partial}\eta_j$ is given as a linear combination of $\mathcal{D}^{(j+2)}$, $\mathcal{D}^{(j+1)}$, ..., $\mathcal{D}^{(1)}$. In plain words, it means that charging the edge j entails charging the entire sequence of pentagons lying all the way from that specific edge to the bottom of the polygon. The drawback is that it has be so even for an edge standing arbitrarily far away from the bottom of the polygon. This, however, is at odds with the locality of the OPE construction, in which a random pentagon in the decomposition only talks to its neighbours (through the flux-tube state that they share) and has little knowledge of how far it stands from the bottom. Besides, it introduces an artificial discrimination between bottom and top, despite the fact that our analysis could, at no cost, be run from the top. The way out is easy to find: the bottom tail of the inverse map is pure mathematical illusion, or, put differently, the inverse map beautifully truncates such as to become manifestly top/bottom symmetric.

In sum, instead of a sum over $j + 2$ $\mathcal{D}$'s, what we find is that (for $3 \le j \le n - 2$) $\slashed{\partial}\eta_j$ is given by the linear combination of the five neighboring pentagons only (see figure 3.5)

$$\boxed{\frac{\partial}{\partial \eta_j^A} = \frac{\langle Y_{j-2}, Y_{j-1}, Y_j, Y_{j+1} \rangle \mathcal{D}_A^{(j+2)} + \quad \cdots \quad + \langle Y_{j-1}, Y_j, Y_{j+1}, Y_{j+2} \rangle \mathcal{D}_A^{(j-2)}}{(Y_{j-1} \cdot Z_{j+1})(Y_{j+1} \cdot Z_{j-1})(Y_{j-2} \cdot Z_j)(Y_{j+2} \cdot Z_j)}} \,. \tag{3.20}$$

Mathematically, this relation originates from the five-term identity

$$\langle Y_{j-2}, Y_{j-1}, Y_j, Y_{j+1} \rangle Y_{j+2} + \quad \cdots \quad + \langle Y_{j-1}, Y_j, Y_{j+1}, Y_{j+2} \rangle Y_{j-2} = 0 \,, \tag{3.21}$$

which holds for any choice of five (co-)twistors and which simply follows from them having four components. Once we plug the definition (3.17) into the right hand side of (3.20), most terms cancel out because of this identity. Those that survive are boundary terms and it is straightforward to work them out in detail. They precisely lead to the single term in the left hand side of (3.20).[4]

---

[4] To see that only the term proportional to $\partial/\partial \eta_j$ survives it is useful to note that the orthogonality relations $Y_{j-2} \cdot Z_{j-1} = Y_{j-1} \cdot Z_{j-1} = Y_j \cdot Z_{j-1} = 0$ allow us to freely extend slightly the summation range of some of the five terms in (3.20). In turn, these relations follow trivially from the definition (3.9) of the co-twistors. Finally, to check the overall normalization of both sides in (3.20), it is convenient to use the identity $\langle Y_{j-2}, Y_{j-1}, Y_j, Y_{j+1} \rangle = (Y_{j-1} \cdot Z_{j+1})(Y_{j+1} \cdot Z_{j-1})(Y_{j-2} \cdot Z_j)$.
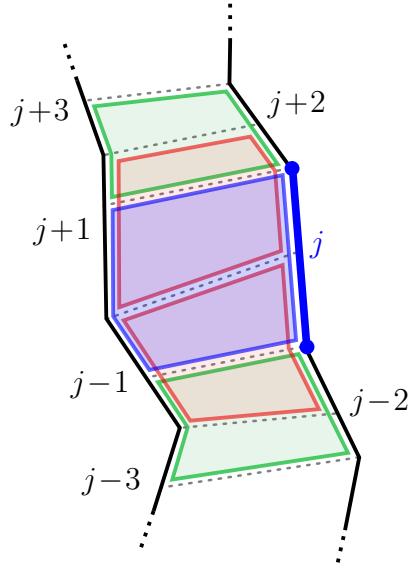
Figure 3.5: A remarkable feature of our construction is that the inverse map turns out to be local. Namely, charging edge j is done by charging the five pentagons touching this edge and these five pentagons alone. We notice in particular that the two outermost pentagons in this neighbourhood, which are shown in green above, are touching the endpoints of edge j only.

Actually, it is possible to interpret the inverse map (3.20) such that it also applies to the very first edges of the polygon, like in (3.18) and (3.19), provided that we properly understand what we mean by Y_0, Y_{-1}, Y_{-2} and Y_{-3}. (These co-twistors will show up when using (3.20) for $/\partial\eta_2$, $/\partial\eta_1$, $/\partial\eta_0$ and $/\partial\eta_{-1}$.) For this we can pretend that there are extra edges at the bottom of the polygon and the previous derivation would still go through.[5] Of course, for these bottom (or top) cases, it is easier to proceed recursively as in (3.18) and (3.19).

This concludes our general discussion of the map. The proposals (3.20) and (3.10) are the main results of this chapter.

---

[5]We can simply define $(Y_0, Y_{-1}, Y_{-2}, Y_{-3}) \equiv (Y_{\{0,-1,1\}}, Y_{\{*,0,-1\}}, Y_{\{-1,*,*\}}, Y_{\{*,*,*\}})$, with $Y_{\{i,j,k\}} \equiv Z_i \wedge Z_j \wedge Z_k$ and Z_* being arbitrary twistors, which drop out of the final result. At the same time, we also set $(\mathcal{D}_0\mathcal{W}, \mathcal{D}_{-1}\mathcal{W}, \mathcal{D}_{-2}\mathcal{W}, \mathcal{D}_{-3}\mathcal{W}) = (0, 0, 0, 0)$.

3.3.4 Easy Components and the Hexagon

A polygon with n edges has a top pentagon and a bottom pentagon, plus $n-6$ pentagons which are neither top nor bottom and referred to as middle ones. Charging the bottom or the top pentagons is considerably simpler than charging any middle one. Let us focus on the bottom since the top is treated analogously. According to our general map (3.10), we see that the differential operator that charges the bottom pentagon, $/\partial\chi_1$, is simply proportional to $\partial/\partial\eta_{-1}$,

$$\frac{\partial}{\partial\chi_1} = \frac{Y_1 \cdot Z_{-1}}{(\mathbf{0})_1(\mathbf{1})_1(\mathbf{2})_1} \times \frac{\partial}{\partial\eta_{-1}} \tag{3.22}$$

which we can further simplify to (see e.g. (A.17) in the appendix for a thorough explanation)

$$\frac{\partial}{\partial\chi_1} = (-\mathbf{1})_1 \times \frac{\partial}{\partial\eta_{-1}}. \tag{3.23}$$

In other words, up to a trivial factor which absorbs the weight in $/\partial\eta_{-1}$, charging a bottom pentagon is the same as extracting components with η's at the very bottom of our polygon. Similarly, charging the top-most pentagon is equivalent to putting η's on the topmost edge. It could hardly be simpler. Explicitly, for any polygon, there are five NMHV components which are easy to construct:

$$\begin{aligned}
\mathcal{P}_{1234} \circ \mathcal{P} \circ \cdots \circ \mathcal{P} \circ \mathcal{P} &= w[4]\, \mathcal{W}^{(-1,-1,-1,-1)}, \\
\mathcal{P}_{123} \circ \mathcal{P} \circ \cdots \circ \mathcal{P} \circ \mathcal{P}_4 &= w[3]\, \mathcal{W}^{(-1,-1,-1,n-2)}, \\
\mathcal{P}_{12} \circ \mathcal{P} \circ \cdots \circ \mathcal{P} \circ \mathcal{P}_{34} &= w[2]\, \mathcal{W}^{(-1,-1,n-2,n-2)}, \\
\mathcal{P}_1 \circ \mathcal{P} \circ \cdots \circ \mathcal{P} \circ \mathcal{P}_{234} &= w[1]\, \mathcal{W}^{(-1,n-2,n-2,n-2)}, \\
\mathcal{P} \circ \mathcal{P} \circ \cdots \circ \mathcal{P} \circ \mathcal{P}_{1234} &= w[0]\, \mathcal{W}^{(n-2,n-2,n-2,n-2)}.
\end{aligned} \tag{3.24}$$

where $w[m] \equiv ((-\mathbf{1})_1)^m\, ((\mathbf{n}-\mathbf{2})_{n-4})^{4-m}$.

These are what we call the *easy components*. Morally speaking, from the first to the last line, we can think of the easy components as inserting an F, ψ, ϕ, $\bar\psi$, $\bar F$ excitation and their conjugate at the very bottom and top of our polygon.

For an hexagon we have only two pentagons and thus the easy components in (3.24) with $n = 6$ suffice to describe the NMHV hexagon, see figure 4.43. All other components can be trivially obtained by Ward identities. For example, we can use invariance under

$$Y_2 \cdot \mathcal{Q} = \sum_k Y_2 \cdot Z_k \frac{\partial}{\partial\eta_k} = Y_2 \cdot Z_{-1}\frac{\partial}{\partial\eta_{-1}} + Y_2 \cdot Z_0\frac{\partial}{\partial\eta_0} + Y_2 \cdot Z_4\frac{\partial}{\partial\eta_4} \tag{3.25}$$

25
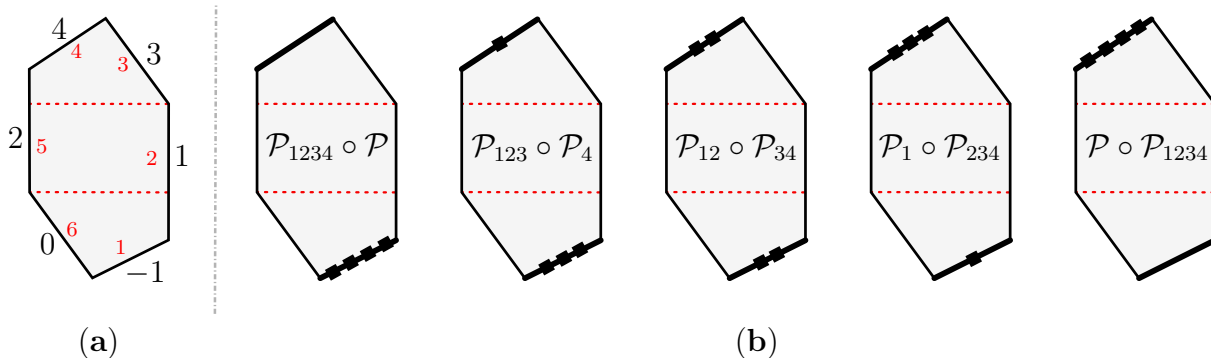
Figure 3.6: **(a)** OPE friendly edge labelling used in this chapter (big black outer numbers) versus the more conventional cyclic labelling (small red inner numbers) for the hexagon. **(b)** The five *easy components* of the NMHV hexagon. Each black square represents a dual Grassmann variable η. For the hexagon these five components provide a complete base for all NMHV amplitudes.

to replace any component with an index associated to the edge 0 to a linear combination of components with η's associated to the top and bottom edges -1 and 4. Those, in turn, are the components which we can neatly compute from the OPE construction. For example, it immediately follows that

$$\mathcal{W}^{(-1,-1,-1,0)} = \alpha \, \mathcal{P}_{1234} \circ \mathcal{P} + \beta \, \mathcal{P}_{123} \circ \mathcal{P}_4 \,, \tag{3.26}$$

with

$$\alpha = -\frac{Y_2 \cdot Z_{-1}}{Y_2 \cdot Z_0 \left((-\mathbf{1})_1\right)^4} \,, \qquad \beta = -\frac{Y_2 \cdot Z_4}{Y_2 \cdot Z_0 \left((-\mathbf{1})_1\right)^3 \left(\mathbf{4}_2\right)^1} \,. \tag{3.27}$$

Similarly, we can easily write down any other hexagon NMHV component in terms of the OPE basis. Of course, this is equivalent to using the general inverse map (3.20), worked out in the previous section.

There are other components whose OPE expansions closely resemble those of the *nice* components (3.24). A notable example is the so-called *cusp-to-cusp* hexagon scalar component $\mathcal{R}^{\text{hex}}_{-1,0,3,4}$ and its heptagon counterpart $\mathcal{R}^{\text{hep}}_{-1,0,4,5}$. Such components were extensively analyzed in the past using the OPE [22, 27, 37, 38].[6] What is nicest about them is their utter simplicity at tree level, being described by a simple scalar propagator from the bottom cusp $(-1,0)$ to the top cusp $(n-3,n-2)$. Based on the OPE intuition, one would

---

[6]Recall once again that we are using here a slightly unconventional labelling of the edges as indicated in figure 3.1.b; These same cusp-to-cusp component were denoted $\mathcal{R}_{6134}$ and $\mathcal{R}_{7145}$ in [22] and $\mathcal{R}_{2356}$ in [37].

therefore imagine that this component should not behave that differently from the one in the middle line in (3.24). Indeed one observes that the expansion of this component and of the cusp-to-cusp components are exactly the same to leading order at large τ and to any loop order. Both are described by a single scalar flux tube excitation. However, as soon as two-particle contributions kick in – in the sub-leading collinear terms – these components start differing. A similar story is present for all other components in the family (3.24). For example, gluonic components were intensively studied in [24].[7] The hexagon fermionic component $\mathcal{W}^{(-1,-1,-1,4)}$ was recently studied in [39].[8]

Finally let us note that the weight factors showing up in (3.24) are not a novelty. Already in [22] it was explained that to properly deal with weight free quantities we better remove the weight of each pentagon by dividing out by the corresponding charged counterpart, see (132) and surrounding discussion in [22]. Nevertheless, in practice, in all previous OPE studies of super amplitudes, the weights $(-\mathbf{1})_1$ and $(\mathbf{n}-\mathbf{2})_{n-5}$ of the bottom and top twistors with respect to the corresponding pentagons were, for the most part, ignored. Sometimes this is fine. For instance, if we are interested in amplitudes at loop level we can always divide the ratio function by its tree level expression obtaining a weight free function of cross-ratios which we can unambiguously match with the OPE. Said differently, we can always normalize the tree level result by hand such that it agrees with the leading terms in the OPE. In particular, for the purpose of comparing with the hexagon function program [40–43] and using the OPE to generate high loop order predictions, it is overkilling to carry these weights around. Moreover, with the choice of twistors in [22], such weights actually evaluate to 1 which is one further reason why we never needed to take them into account.

Having said all that, of course, to be mathematically rigorous, weight free quantities (3.24) are what we should always manipulate. In particular, for higher n-gons, and as soon as we also charge middle pentagons, it is important to keep track of these weights to properly make contact with the OPE predictions [3].

3.3.5 Parity

The charged pentagon construction provides us with a novel intuition about how to understand parity at the Wilson loop level.

---

[7]A simple tree-level gluonic example of this universality for the leading terms in the OPE was considered in detail in the "Tree Heptagon exercise" on the first day of the 6th edition of the Mathematica School http://msstp.org/?q=node/289.

[8]This component was denoted $\mathcal{W}^{(1114)}$ in the cyclic labelling in [39].

Recall that the action of parity on a scattering amplitude is very simple. It is a symmetry of the amplitude under which a positive helicity gluon transforms into a negative helicity one, a positive helicity fermion transforms into its negative helicity conjugate counterpart and finally a scalar excitation is trivially conjugated. All in all, this can be summarized in the following nice relation [44]

$$\int \prod_{i=-1}^{n-2} d^4\tilde{\eta}_i \ e^{\sum_{i=-1}^{n-2} \bar{\tilde{\eta}}_i \tilde{\eta}_i} A[\tilde{\eta}, \lambda, \tilde{\lambda}] = A[\bar{\tilde{\eta}}, \tilde{\lambda}, \lambda] \,. \tag{3.28}$$

However, the relation between amplitudes and super Wilson loops involves stripping out the MHV tree-level factor along with going from the original amplitude $\tilde{\eta}$'s to the Wilson loop dual Grassman variables η's.[9] Together, these operations obscure the action of parity for this stripped object. How is parity symmetry realized on the super Wilson loop? Put differently, how does parity relate different ratio function components? To our knowledge this question has not been answered before. Here we propose that – once decomposed using the OPE χ-components – parity at the Wilson loop level is no more complicated than in the original amplitude language. Precisely, we claim that our variables allow for a straightforward analogue of (3.28) in the Wilson loop picture as

$$\int \prod_{i=1}^{n-4} d^4\chi_i \ e^{\sum_{i=1}^{n-4} \bar{\chi}_i \chi_i} \mathcal{R}[\chi, Z] = \mathcal{R}[\bar{\chi}, W] \,, \tag{3.29}$$

where W_j are Hodge's *dual* momentum twistors [45]. The latter can be thought of as parity conjugate of the Z's and, up to an overall factor which drops out in (3.29), are given by[10]

$$W_j \equiv Z_{j-2} \wedge Z_j \wedge Z_{j+2} \,. \tag{3.30}$$

Note that this is nothing but the conventional definition of the dual twistor involving three consecutive edges; the shifts of 2 in the index are just an outcome or our labelling, see figure 3.1.

The general relation (3.29) is a generating function for all parity relations between N^kMHV components and N^{n-4-k}MHV components, such as the relation

$$\mathcal{P}_{1234} \circ \mathcal{P} = \mathcal{P} \circ \mathcal{P}_{1234}|_{Z \to W} \tag{3.31}$$

---

[9]The convention for the labelling of the η's and $\tilde{\eta}$'s varies quite a lot in the literature. Our notation here is in line with [16] and [33–35] for example (modulo the non-cyclic labelling of the edges of course).

[10]Dual momentum twistors (as well as usual momentum twistors) are reviewed in some detail in appendix A.1, see formula (A.4) for an explicit expression relating them to the original momentum twistors, including all factors. Here we are dealing with weight free quantities and as a result, we can always safely drop any normalization from either Z's or W's on the left or right hand sides in (3.29).

between two NMHV hexagon components, for instance, or the relation

$$\mathcal{P}_{123} \circ \mathcal{P}_{14} \circ \mathcal{P}_{234} = \mathcal{P}_4 \circ \mathcal{P}_{23} \circ \mathcal{P}_1|_{Z \to W} \tag{3.32}$$

relating NMHV and N^{2}MHV seven-point amplitudes. More precisely, to convert such identity into a relation for ratio function components, it is suffices to divide both sides by $\mathcal{W} = \mathcal{P} \circ \mathcal{P} \circ \mathcal{P}$.[11] After doing so, the same relation in (3.32) reads

$$\frac{\partial}{\partial \chi_1^1} \frac{\partial}{\partial \chi_1^2} \frac{\partial}{\partial \chi_1^3} \frac{\partial}{\partial \chi_2^1} \frac{\partial}{\partial \chi_2^4} \frac{\partial}{\partial \chi_3^2} \frac{\partial}{\partial \chi_3^3} \frac{\partial}{\partial \chi_3^4} \mathcal{R}^{\text{heptagon N}^2\text{MHV}} = \frac{\partial}{\partial \chi_1^4} \frac{\partial}{\partial \chi_2^2} \frac{\partial}{\partial \chi_2^3} \frac{\partial}{\partial \chi_3^1} \mathcal{R}^{\text{heptagon NMHV}} \Bigg|_{Z \to W} \tag{3.33}$$

where the χ derivatives are given in terms of conventional η derivatives in (3.10). Another more extreme example following from (3.29) is the relation

$$\mathcal{P}_{1234} \circ \mathcal{P}_{1234} \circ \mathcal{P}_{1234} = \mathcal{P} \circ \mathcal{P} \circ \mathcal{P}|_{Z \to W} \tag{3.34}$$

which encodes the fact that for seven points N^{3}MHV is the same as $\overline{\text{MHV}}$. It is straightforward to generate more such relations by picking different components in (3.29).

Note that relations such (3.33) are quite unconventional. We are not entitled to compare different η-components of the ratio function simply because they do not carry the same helicity weights. Equating different η-components would be tantamount to comparing apples and oranges. In contrast, when extracting the χ-components as in (3.33) we generate weight free quantities since the χ's – contrary to the η's – carry no weight. This is what allows us to write parity relations at the level of the Wilson loop in terms of simple relations such as (3.32)–(3.33) or, simply, in terms of the master relation (3.29), without the need of dressing the components by additional weight factors.

Having decoded in detail the notation behind our main claim (3.29), let us now explain how the relations (3.32)–(3.33) are nicely suggested by the pentagon approach. Then, we will explain what sort of checks/derivations we have performed.

Parity, first and foremost, is a symmetry that swaps the helicity of the external particles in the $\mathcal{N} = 4$ supermultiplet that are being scattered, see (3.28). Similarly, parity also flips the helicity of the flux-tube excitations. Flipping the helicity of a flux-tube excitation is trivial: it can be accomplished by simply flipping the signs of all angles ϕ_j's, while keeping the times τ_j and distances σ_j invariant [1, 21, 22, 46]. This is precisely what the

---

[11]The latter is symmetric under $Z \to W$ so we can evaluate it with either twistors Z or dual twistors W.

transformation $Z \leftrightarrow W$ accomplishes![12]

This explains the substitution rule in the right hand side of (3.31)–(3.34). To complete the picture we also have to act with parity on the pentagon transitions. Naturally, it is expected to swap the several super pentagon components in (3.1) in exactly the same way that it acts on the usual super-field multiplet expansion (replacing the positive helicity gluon with no $\tilde{\eta}$'s with the negative helicity gluon with 4 $\tilde{\eta}$'s and so on.). This translates into

$$\mathcal{P}_{1234} \leftrightarrow \mathcal{P} \ , \qquad \mathcal{P}_{123} \leftrightarrow \mathcal{P}_4 \ \text{etc,} \tag{3.35}$$

which is precisely what is encoded in (3.32)–(3.33) or, more generally, in (3.29). In particular, these prescriptions neatly relate N^kMHV and N^{n-k-4}MHV amplitudes, as expected for parity.

While (3.29) is what the OPE naturally suggests, the previous paragraph is obviously not a proof. In any case, (3.29) is a concrete conjecture for the realization of parity at the Wilson loop level that we should be able to establish (or disprove) rather straightforwardly starting from (3.28), without any reference whatsoever to the OPE. It would be interesting if a simple and elegant derivation of (3.29) existed, perhaps following the same sort of manipulations as in [47]. This would elucidate further the origin of the (weight free) super OPE Grassmann variables χ.

What we did was less thorough. To convince ourselves of the validity of (3.29) we did two simpler exercises: On the one hand, using the very convenient package by Bourjaily, Caron-Huot and Trnka [36] we extensively tested (3.29) for a very large number of ratio functions from NMHV hexagons to N^3MHV decagons, both at tree and at one loop level.[13] On the other hand, we also looked for an analytic derivation of (3.29) from (3.28). We did not find a particularly illuminating proof that establishes this in full generality but we did manage to prove several sub-examples. In appendix A.3, for instance, we illustrate how one can rigorously establish the relation

$$\underbrace{\mathcal{P}_{1234} \circ \cdots \circ \mathcal{P}_{1234}}_{j} \circ \underbrace{\mathcal{P} \circ \mathcal{P}}_{n-4-j} = \underbrace{\mathcal{P} \circ \cdots \circ \mathcal{P}}_{j} \circ \underbrace{\mathcal{P}_{1234} \circ \mathcal{P}_{1234}}_{n-4-j}\Big|_{Z \to W} \ . \tag{3.36}$$

---

[12]More precisely, it is a very instructive exercise to observe that under $Z_j \to W_j$ the cross-ratios in formula (160) in [22] precisely transform as $(\tau_j, \sigma_j, \phi_j) \to (\tau_j, \sigma_j, -\phi_j)$. When preforming such check it is important to take into account the conversion between the edge labelling used here and there, see caption of figure 3.1.

[13]When checking such identities for a very large number of edges, the package becomes unpractically slow. The trick is to open the package and do a "find/replace operation" to eliminate several `Simplify` and `FullSimplify` throughout. For analytical checks of relations such as (3.32)–(3.33), these simplifications are superfluous.

3.4 Discussion

In this chapter we have constructed a simple map between N^kMHV amplitudes and so-called *charged pentagon transitions*. This map allows one to OPE expand amplitudes with arbitrary helicity configurations at any value of the coupling.

In the dual super-loop description of the amplitude, the charged transitions are operators that act on the color flux tube. They can be realized as combinations of a properly chosen supercharge $\mathcal{Q}$ and the more standard bosonic pentagon operator $\mathcal{P}$, and collected into a super pentagon

$$\mathbb{P} = \mathcal{P} \prod_{A=1}^{4} \left(\mathbb{1} + \chi^A Q_A \right) , \qquad (3.37)$$

where the χ's are new (weight-free) Grassmann variables associated to the pentagons in the tessellation of the n-gon. The full super loop is then obtained by merging these pentagons together,

$$\mathcal{W}_n = \langle \mathbb{P}_1 \circ \mathbb{P}_2 \circ \cdots \circ \mathbb{P}_{n-4} \rangle , \qquad (3.38)$$

as previously done in (3.2). The χ-components of the super transition $\mathbb{P}$ can be bootstrapped using the underlying flux-tube integrability, in pretty much the same way as their bosonic counterparts [22, 24, 27, 28]. In this chapter we proposed a map between these χ-components of the super Wilson loop $\mathcal{W}_n$ and its more conventional η-components [16, 29]. This map, given in (3.10) and (3.20), therefore provides the key missing ingredient in the finite coupling OPE expansion of any helicity amplitude.

The map (3.10) can also be regarded as a definition of the charged transitions. In this construction, we charge a pentagon by acting with the corresponding super-symmetry generators on all the edges at its bottom (top). This is the same as acting on the flux-tube state entering the pentagon from the bottom (top) – via the flux operator-state correspondence – and is therefore equivalent to (3.37).[14]

This point of view is useful in providing a nice connection between the charged transitions and their non-charged counterparts. To illustrate this, consider a standard pentagon transition between a fermion and some other state, $P(\bar{\psi}_A(p) | \dots) = \langle \dots | \mathcal{P} | \bar{\psi}_A(p) \rangle$. As the momentum of this excitation, p, goes to zero, the fermion effectively becomes a super-symmetry generator Q_A [26, 48]. Therefore, we expect that in this limit this bosonic transition can be related to the charged transition $P_A(0 | \dots) = \langle \dots | \mathcal{P} \cdot Q_A | 0 \rangle$. Indeed,

---

[14]This is pretty much the way the super loop was generated in [16, 29].

while bootstrapping these transitions we have recently observed curious relations of the sort,

$$P_A(0|\dots) \propto \oint\limits_{p=0} \frac{dp}{2\pi} \hat{\mu}_\psi(p) P(\bar{\psi}_A(p)|\dots) \tag{3.39}$$

which seems to embody this idea in a rather sharp way.

We are currently exploring such directions and their generalizations and will present our findings elsewhere. Here we would like to briefly mention two interesting implications:

First, in the same way that we considered fermions $\bar{\psi}$ with zero momentum, we could also consider adding their conjugate ψ, which effectively becomes the conjugate supersymmetry generator $\bar{\mathcal{Q}}$. This would naively define a non-chiral super pentagon admitting an expansion both in χ's and in $\bar{\chi}$'s. It is tempting to muse that it should be related to the non-chiral super loop proposed in [49] and further studied in [50].

Second, the relation (3.39) between $\mathcal{Q}$ and $\bar{\psi}$ can be regarded as a local OPE definition of a charged edge or, equivalently, of the action of $/\!\!\partial\eta$ on the super loop. Under such definition, our map (3.10) translates into a set of relations that includes the SUSY Ward identities, notably, and that begs to be interpreted directly from the flux tube. Naively, we expect them to encode certain discontinuities of the OPE series upon edge-crossing of the fermions. It would be fascinating to clarify this point and instructive to see if some simple OPE contour manipulation could provide a *derivation* of supersymmetry from the flux tube theory.

Let us end with further outlook. There is by now a very large reservoir of knowledge on perturbative scattering amplitudes in planar $\mathcal{N} = 4$ SYM theory, tightly related to the large amount of symmetries they are subject to (originating from both the original and dual Wilson loop descriptions). On the other hand, we have the pentagon approach, fully non-perturbative and valid all the way from weak to strong coupling. This approach sacrifices some of the most basic symmetries of the amplitudes, such as supersymmetry, parity and cyclicity. In return, it renders the most non-trivial symmetry of all – *integrability* – both manifest and practical. We think this is a worthy trade off, especially if the more conventional symmetries can be recovered in the end. Our map (3.10) is one realization of this philosophy, where different amplitudes that are related by supersymmetry are being assigned to the *same* OPE series. Moreover, as discussed above, we now start to understand that supersymmetry and parity also have, after all, a rather natural OPE incarnation. In our quest for the ultimate solution to the scattering amplitude problem, the next symmetry to attack is probably cyclicity. Hopefully it will also turn out to be easier than we now think!

Chapter 4

POPE for all helicities II

4.1   Introduction

The main goal of the pentagon operator product expansion (POPE) program [1] is to provide an explicit representation of *any* gluon scattering amplitude in planar $\mathcal{N} = 4$ Super Yang-Mills (SYM) theory at *finite* coupling. With our current understanding of the POPE approach, such an answer will come in the form of an infinite sum, akin to a sort of partition function, over all possible excitations of the chromodynamic flux tube of the planar theory. More precisely, a scattering amplitude involving n gluons is dual to a polygonal Wilson loop with n edges which we decompose into $n-3$ successive fluxes/squares. In this picture, the transition from one flux to the next is induced by a pentagon operator. Hence, the amplitude can be identified with a form factor representation of a correlation function of the $n-4$ pentagon operators. The matrix elements of these operators are computed following a somehow standard integrable bootstrap [1]. We shall refer to the summand arising in this form factor representation, as the *POPE integrand*. This integrand depends, amongst other things, on the $n-5$ flux tube states which propagate in each of the $n-5$

middle squares
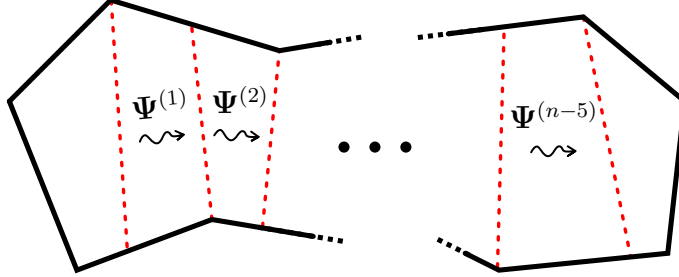
$$\texttt{integrand} = \texttt{integrand}(\mathbf{\Psi}^{(1)}, \ldots, \mathbf{\Psi}^{(n-5)}) \tag{4.1}$$

Such states are generically multi-particle states parametrized by a rapidity for each of the excitations. For instance, we could have, in the i-th square, a state with two gluons of positive helicity, a bound state of two gluons of negative helicity, one scalar and a pair of fermions:[1]

$$\mathbf{\Psi}^{(i)} = \left\{ F_1(u_1), F_1(u_2), F_{-2}(u_3), \phi^{AB}(u_4), \psi^C(u_5), \psi^D(u_6) \right\} . \tag{4.2}$$

A finite coupling solution for scattering amplitudes in this gauge theory hinges on finding explicit expressions for the OPE integrand (4.1) for any possible multi-particle flux tube state such as (4.2).

As described in detail below, what renders this seemingly gargantuan task feasible is a fortunate factorization of the OPE integrand into considerably simpler building blocks which we can analyse separately. It is perhaps worth mentioning from the get-go that this factorization is by no means obvious. It stands as another wonderful (but mysterious) $\mathcal{N} = 4$ SYM gift. Were it not for it, one would hardly imagine bootstrapping the multi-particle contributions with ease. Indeed, except for the first few particles contributions, almost no explicit form factor summands for correlation functions in integrable theories are explicitly worked out. A notable exception is the $2d$ Ising model. The unexpected simplicity we are encountering in $\mathcal{N} = 4$ SYM theory motivates its portrait as the *Ising model of Gauge Theories*.

The three building blocks into which the OPE integrand factorizes are dubbed the *dynamical part*, the *matrix part* and the *form factor part*,

$$\texttt{integrand} = (\texttt{dynamical part}) \times (\texttt{matrix part}) \times (\texttt{form factors part}), \tag{4.3}$$

---

[1]Here A, B, C and D are $SU(4)$ R-charge indices and the indices on F indicate the helicity of the gluonic excitation.

with the latter form factors being non-trivial for non-MHV processes only. Here is what we know about these building blocks :

Dynamical part - This is the part of the OPE integrand that is universally present, which applies to all cases, MHV or non-MHV, and which treats all flux tube excitations on a same footing, regardless of their quantum numbers / R-charges. It is the most dynamical component of the integrand, hence its name, and not surprisingly it exhibits the most complicated coupling dependence. Its overall form is however extremely simple since it is factorized into a product over elementary pentagon transitions linking the various flux tube excitations and a product over square measures and Boltzmann weights of each excitation. The geometry of the scattering amplitude, in particular, only enters through these Boltzmann weights. All the transitions, measures, energies and momentum appearing here are also rather universal. Most of them have already been spelled out, see e.g. [22–24, 28, 39, 51], and all of them will be summarized in this chapter.

Matrix part - The matrix part takes care of the $SU(4)$ group theoretical factor of the integrand. It can only show up when flux tube excitations with R-indices are present, and is otherwise totally absent. (It is also trivial whenever there is only one way to distribute the R-indices.) This component of the integrand has the distinguished feature of being a *coupling independent* rational function of the particles' rapidities, with no obvious factorization. Taming this group theoretical factor is an interesting algebraic problem on its own but is beyond the scope of this chapter.

Form factors part - Lastly, we have the non-MHV form factors. They are only needed for non-MHV amplitudes, which are composed of so-called *charged* pentagon transitions [2, 22, 39]. Luckily, these form factors are not independent objects. Instead, we can construct them from their relation to the bosonic (or MHV) transitions with fermionic excitations frozen to zero momentum. Applying this logic, we will obtain their expressions for all excitations and transitions. The final result can then be tested against perturbative results as well as using self-consistency checks such as parity symmetry.

The main result of this chapter is a complete recipe for writing the two coupling dependent factors in (4.3), that is the complete flux tube integrand up to the matrix part. This can be seen as 2/3 of the full POPE program set above and is spelled out in section 4.2. In section 4.3 we perform several perturbative checks of our POPE elements. The comparisons that we have performed test both the form factors and the dictionary proposed in [2] between N^{k}MHV amplitudes and charged pentagon sequences in a rather non-trivial way.

4.2 The abelian part

In this section we present the expression for the abelian part of the POPE integrand. It captures by definition what remains of the full integrand after stripping out the matrix part. (In some cases, when there is just no matrix part, the abelian part is of course everything. This is the case for instance for states made out of gluons or their bound states, which are intrinsically abelian.) As explained in the introduction, the abelian part is composed of the dynamical and form factors parts,

$$\texttt{abelian} = (\texttt{dynamical part}) \times (\texttt{non-MHV form factors part}). \qquad (4.4)$$

Conventionally, for MHV, only the dynamical part remains. For non-MHV, the latter remains the same, but form factors should be added to the story. These ones are not really independent and can be directly derived from suitable MHV processes, as we shall explain in this section.

4.2.1 The dynamical part

We start with the main component. This one captures, in particular, the information about the geometry, i.e. the cross ratios σ_i, τ_i, ϕ_i of the polygon, and can be written as [1]

$$\begin{aligned}
\texttt{dynamical part} = {} & P(\ 0\ |\boldsymbol{\Psi}^{(1)})\,\mu(\boldsymbol{\Psi}^{(1)})\,e^{-E(\boldsymbol{\Psi}^{(1)})\tau_1 + ip(\boldsymbol{\Psi}^{(1)})\sigma_1 + im(\boldsymbol{\Psi}^{(1)})\phi_1} \\
& \times P(\overline{\boldsymbol{\Psi}}^{(2)}|\overline{\boldsymbol{\Psi}}^{(1)})\,\mu(\boldsymbol{\Psi}^{(2)})\,e^{-E(\boldsymbol{\Psi}^{(2)})\tau_2 - ip(\boldsymbol{\Psi}^{(2)})\sigma_2 + im(\boldsymbol{\Psi}^{(2)})\phi_2} \\
& \times P(\boldsymbol{\Psi}^{(2)}|\boldsymbol{\Psi}^{(3)})\,\mu(\boldsymbol{\Psi}^{(3)})\,e^{-E(\boldsymbol{\Psi}^{(3)})\tau_3 + ip(\boldsymbol{\Psi}^{(3)})\sigma_3 + im(\boldsymbol{\Psi}^{(3)})\phi_3} \\
& \times P(\overline{\boldsymbol{\Psi}}^{(4)}|\overline{\boldsymbol{\Psi}}^{(3)})\dots,
\end{aligned} \qquad (4.5)$$

where $E(\boldsymbol{\Psi})$, $p(\boldsymbol{\Psi})$ and $m(\boldsymbol{\Psi})$ are the energy, momentum and angular momentum of the multi-particle state $\boldsymbol{\Psi}$. We have $n-5$ such states in total, in accordance with the number of middle squares in the tessellation, and for each of them we have a corresponding square measure $\mu(\boldsymbol{\Psi})$, see [1]. Finally, two consecutive squares with multi-particle states $\boldsymbol{\Phi}$ and $\boldsymbol{\Psi}$ are connected by means of a pentagon transition $P(\boldsymbol{\Phi}|\boldsymbol{\Psi})$ or $P(\overline{\boldsymbol{\Psi}}|\overline{\boldsymbol{\Phi}})$, where the bar stands for the state where all excitations are replaced by their conjugate and their order reversed. The fact that each other pentagon appears with such reversed states is a direct consequence of the alternating nature of the pentagon tessellation as illustrated in figures 4.1 and 4.2. The alternating signs multiplying the momenta of the states in consecutive middle squares have the same origin.
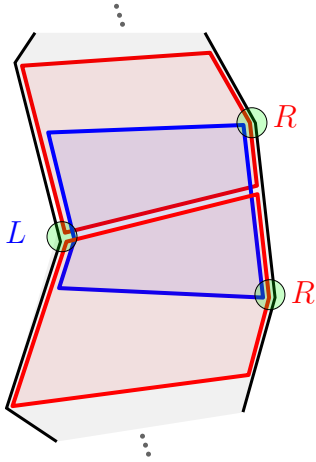
Figure 4.1: Every two successive pentagons in the POPE decomposition are flipped with respect to each other. Namely, if the cusp of one pentagon is pointing to the right then the next one is pointing to the left and so on, $\cdots \to \mathcal{P}^R \to \mathcal{P}^L \to \mathcal{P}^R \to \mathcal{P}^L \to \cdots$.

The factorization observed above is not a surprise and follows from symmetry considerations of the OPE. In contrast, the simplicity of $\mathcal{N} = 4$ SYM theory starts to manifest itself as soon as we start exploring the multi-particle nature of the various pieces. What happens here is that all the above mentioned blocks factorize further into one- and two-particle blocks! To describe this factorization we introduce the notation Ψ_n with $n = 1, \ldots, N$ to indicate the n-th excitation of the multi-particle state $\boldsymbol{\Psi}$. Then, the energy, momentum, angular momentum and measure all factorize into their single particle counterparts as[2]

$$\mu(\boldsymbol{\Psi}) \, e^{-E(\boldsymbol{\Psi})\tau \pm ip(\boldsymbol{\Psi})\sigma + im(\boldsymbol{\Psi})\phi} = \prod_{n=1}^{N} \mu(\Psi_n) \, \exp\left[-E(\Psi_n)\tau \pm ip(\Psi_n)\sigma + im(\Psi_n)\phi\right] , \quad (4.6)$$

where the sign $\pm = (-1)^{j+1}$ multiplying the momenta for states in the j-th middle square is a simple outcome of the conventions mentioned above, see figure 4.2. It is convenient to use a hatted measure $\hat{\mu}$ to denote collectively the measure and the accompanying Boltzmann factor, since these ones always come together. With this notation, the factorization we just described would simply read $\hat{\mu}(\boldsymbol{\Psi}) = \prod_n \hat{\mu}(\Psi_n)$. Most importantly, we observe a similarly neat factorization for the pentagon transitions into fundamental 2-particle transitions [1,

---

[2]In [1] the measure part also included combinatorial factors for identical excitations. These factors can instead be associated to the summation over the flux excitation that should be done in a way that avoids double counting.
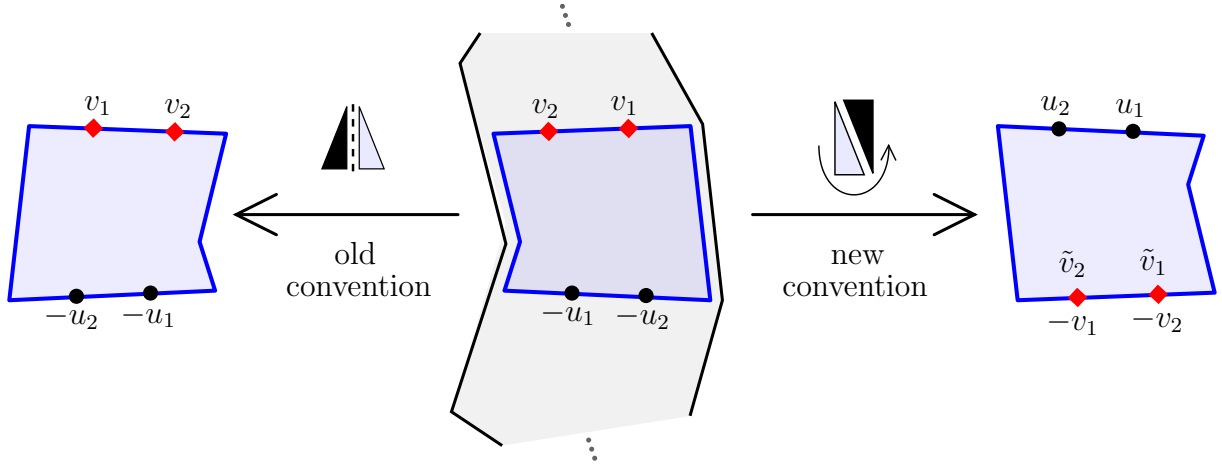
Figure 4.2: When inserting the resolution of the identity between each pentagon it is desirable to relate one sort of pentagon in figure 4.1 (say the ones with the cusp to the left) to the other kind to render things more uniform. To do so, in previous POPE works, a pentagon with a cusp to the left was related to a pentagon with its cusp to the right by a "reflection", which maps the bottom to the bottom and the top to the top. In this chapter, instead, we relate a pentagon with its cusp to the left to a pentagon with its cusp to the right by a "rotation", which maps the bottom to the top and the top to the bottom. In principle both ought be equivalent. In practice, because of annoying minus signs inside some square roots in several pentagon transitions, the second convention is considerably more convenient as it avoids several ambiguities that would be present otherwise. In this new convention, after rotating the pentagon we relabel the associated rapidities as illustrated in this figure. This leads to an alternating sign $(-1)^j$ multiplying the flux tube space variables as written in (4.5).

$22, 24, 51, 52]^3$

$$P(\mathbf{\Phi}|\mathbf{\Psi}) = \frac{\prod\limits_{n,m} P(\Phi_n|\Psi_m)}{\prod\limits_{n>n'} P(\Phi_n|\Phi_{n'}) \prod\limits_{m<m'} P(\Psi_m|\Psi_{m'})} \ . \tag{4.7}$$

The measures themselves are not independent from the pentagon transitions. On the contrary, they can be extracted from the decoupling pole present in 2-particle transitions

---

[3]Let us stress again that formula (4.7) only captures the dynamical part of the transition. In the case where $\mathbf{\Phi} = 0$ and $\mathbf{\Psi} = \phi\phi$, for example, we get from (4.7) that $P_{\phi\phi}(0|u,v) = 1/P_{\phi|\phi}(u|v)$ while in [23] we had $P_{\phi\phi}(0|u,v) = 1/(g^2(u - v + 2i)(u - v + i)) \times 1/P_{\phi|\phi}(u|v)$ which differs by a rational prefactor and by the factor $1/g^2$. The former rational factor is interpreted here as being part of the matrix part and thus discarded, while the power of $1/g^2$ is just absent because of our new normalization of $P_{\phi|\phi}$ (see appendix B).

involving identical in- and out- going particles,

$$\operatorname*{Res}_{v=u} P_{\Psi|\Psi}(u|v) = \frac{i}{\mu_\Psi(u)} \,. \tag{4.8}$$

We see that to fully describe the dynamical part all we need are the two-particle pentagon transitions between any pair of single particle excitations. Most of them were already written down in the literature, see e.g. [22–24, 28, 39, 51]. It was found that, for any pair of excitations $\{\Psi, \Phi\}$, the pentagon transition takes the rather universal form

$$P_{\Psi|\Phi}(u|v)^2 = \mathcal{F}_{\Psi\Phi}(u,v) \frac{S_{\Psi\Phi}(u,v)}{S_{\star\Psi\Phi}(u,v)} \,, \tag{4.9}$$

where $S_{\Psi\Phi}(u,v)$ is the scattering phase (in the symmetric channel) for the excitations Ψ and Φ and $S_{\star\Psi\Phi}(u,v)$ is its mirror counterpart.[4] The functions $\mathcal{F}_{\Psi\Phi}(u,v)$ are simple functions of the rapidities, involving eventually the Zhukowski variables. In table 4.1 we present our ansatz for these functions for all pairs of excitations.

In the end, to evaluate the transition we still need to take the square-root of (4.9) which poses some ambiguity on the branch choice. This ambiguity can be partially fixed through comparison with data or with help of some reasonable normalization conditions as done in appendix B. Explicit expressions for all the transitions and measures are also given in this appendix (altogether with the transitions involving bound states of gluons and small fermions [23]).

In concluding, we recall that there are two main dynamical inputs behind these ansätze. The most important (and still mysterious) one is the *fundamental relation*

$$P_{X|Y}(u|v) = \pm S_{XY}(u,v) P_{Y|X}(v|u) \,, \tag{4.11}$$

which comes with a minus sign whenever both X and Y are fermionic. Combined with the factorization property (4.7) it guarantees that general transitions fulfill proper Watson and decoupling equations. The other essential constraint is dubbed the *mirror axiom* which states that

$$P_{X|Y}(u^{-\gamma}|v) = P_{\bar{Y}|X}(v|u) \,, \quad \text{or more generally} \quad P_{X|\boldsymbol{\Psi}}(u^{-\gamma}|\mathbf{v}) = P_{\bar{\boldsymbol{\Psi}}|X}(\mathbf{v}|u) \,, \tag{4.12}$$

---

[4]When Ψ is a gluon or scalar excitation, the mirror S-matrix is given by analytically continuing the physical one in the standard way, $S_{\star\Psi\Phi}(u,v) = S_{\bar{\Psi}\Phi}(u^\gamma, v)$. For fermions, the lack of a mirror transformation u^γ renders the relation between the mirror S-matrix and the physical one less straightforward. It involves a so-called anomalous mirror transformation as detailed in [23], see e.g. appendix A.4 therein.

$$\mathcal{F}_{\phi F}(u|v) = 1 \,,$$

$$\mathcal{F}_{\phi\psi}(u|v) = -\frac{1}{(u-v+\frac{i}{2})} \,,$$

$$\mathcal{F}_{\phi\phi}(u|v) = \frac{1}{(u-v)(u-v+i)} \,,$$

$$\mathcal{F}_{FF}(u|v) = \frac{(x^+y^+-g^2)(x^+y^--g^2)(x^-y^+-g^2)(x^-y^--g^2)}{g^2x^+x^-y^+y^-(u-v)(u-v+i)} \,,$$

$$\mathcal{F}_{F\psi}(u|v) = -\frac{(x^+y-g^2)(x^-y-g^2)}{g\sqrt{x^+x^-}y(u-v+\frac{i}{2})} \,,$$

$$\mathcal{F}_{F\bar\psi}(u|v) = -\frac{g\sqrt{x^+x^-}y(u-v+\frac{i}{2})}{(x^+y-g^2)(x^-y-g^2)} \,,$$

$$\mathcal{F}_{F\bar F}(u|v) = \frac{g^2x^+x^-y^+y^-(u-v)(u-v+i)}{(x^+y^+-g^2)(x^+y^--g^2)(x^-y^+-g^2)(x^-y^--g^2)} \,,$$

$$\mathcal{F}_{\psi\psi}(u|v) = -\frac{(xy-g^2)}{\sqrt{gxy}(u-v)(u-v+i)} \,,$$

$$\mathcal{F}_{\psi\bar\psi}(u|v) = -\frac{\sqrt{gxy}}{(xy-g^2)} \,,$$

(4.10)

Table 4.1: Summary of prefactors for all twist-one squared transitions, with $x = x(u), y = x(v)$ and $x = \frac{1}{2}(u+\sqrt{u^2-4g^2})$ the Zhukowski variable. They agree with those found in the literature up to minor redefinitions (see appendix A for details).

where $-\gamma$ denotes the inverse mirror rotation and with $\mathbf{v}$ a set of spectator rapidities.[5] Combined with (4.11) the mirror axiom can be used to argue for the ansatz (4.9) as well as to solve for the prefactor $\mathcal{F}$. Finally, it is worth stressing that the solution to such bootstrap axioms is by no means unique and comparison with perturbative data is therefore crucial in backing up our proposals. This shall be discussed at length below.

---

[5]Technically, X in this equation is restricted to be a gluonic or a scalar excitation. This is because, as explained in [23], the mirror rotation for the fermions is of a more exotic type, mapping the fermions into higher-twist excitations.

4.2.2 Charged transitions and form factors

In the OPE framework, one can cover all helicity amplitudes at once by introducing a super pentagon transition [2]

$$\mathbb{P} = \mathcal{P} + \chi^A \mathcal{P}_A + \chi^A \chi^B \mathcal{P}_{AB} + \chi^A \chi^B \chi^C \mathcal{P}_{ABC} + \chi^A \chi^B \chi^C \chi^D \mathcal{P}_{ABCD} , \qquad (4.13)$$

where χ^A is a Grassmann parameter in the fundamental representation of the $SU(4)$ R-symmetry group, and where $\mathcal{P}_{A_1 \ldots A_k}$, or $P^{[k]}$ for short, is the so-called charged transition transforming in the k-th antisymmetric product. In the same way that arbitrary MHV amplitudes can be described by sequences of bosonic pentagons $\mathcal{P}$, one can generate all non-MHV amplitudes by gluing super pentagon transitions together, e.g.

$$\mathcal{W} = \underbrace{\mathcal{P} \circ \mathcal{P} \circ \cdots \circ \mathcal{P}}_{\text{MHV}} + \chi_1^1 \chi_1^2 \chi_1^3 \chi_1^4 \underbrace{\mathcal{P}_{1234} \circ \mathcal{P} \circ \cdots \circ \mathcal{P}}_{\text{NMHV}} + \chi_1^1 \chi_1^2 \chi_1^3 \chi_2^4 \underbrace{\mathcal{P}_{123} \circ \mathcal{P}_4 \circ \cdots \circ \mathcal{P}}_{\text{NMHV}} + \ldots$$

$$(4.14)$$

That this is enough information for recovering the many components of the super Wilson loop is not a priori obvious, since the χ parameters here are attached to the pentagons in the sequence, and not to all possible edges of the loop. However, the missing 'degrees of freedom' are somewhat superfluous since controlled by supersymmetry, and, as explained in [2], the χ components are as many supersymmetry independent components as necessary to fix a general super amplitude.

The physics that takes place on the flux tube is essentially the same regardless of whether some of the pentagons are charged or not. What can possibly differ is the R-charge flow throughout the pentagon evolution. Since the R-charge dependence was factored out into the matrix part at the very beginning, one can ask if the abelian part proposed in (4.7) can also be applied as it stands to these charged processes. The answer turns out to be positive up to a minor modification: the inclusion of the so-called non-MHV form factors, as sketched in (4.4). The need for these form factors is not a novelty and was previously stressed in [22, 51] from the study of certain components of the NMHV hexagon. To pave the way to our general discussion, let us start by reviewing briefly, on a simple example, why these form factors are needed at all, or equivalently why is the dynamical part not enough for describing the abelian part of non-MHV amplitudes.

Consider the χ-component $\mathcal{P}_{1234} \circ \mathcal{P}$, or equivalently $\mathcal{P} \circ \mathcal{P}_{1234}$, of an NMHV hexagon. From R-charge conservation the excitations allowed on these transitions are the same as in the bosonic MHV case $\mathcal{P} \circ \mathcal{P}$. As such, at twist zero we have the vacuum, at twist one the positive and negative helicity gluons, F and $\bar{F}$, etc. Despite this similarity, one does not expect the transitions, integrands, and full amplitude to be the same for the two

processes, since e.g. the MHV process treats symmetrically positive and negative helicity gluons while the non-MHV one does not. (This is also immediately confirmed at weak coupling by looking at the corresponding amplitudes.) At the level of the POPE integrand for a single gluon,

$$
\begin{aligned}
\mathcal{P} \circ \mathcal{P} &= 1 + \int \frac{du}{2\pi} \hat{\mu}_F(u) \qquad + \int \frac{du}{2\pi} \hat{\mu}_{\bar{F}}(u) \qquad + \ldots, \\
\mathcal{P}_{1234} \circ \mathcal{P} &= 1 + \int \frac{du}{2\pi} \hat{\mu}_F(u)\, f(u) + \int \frac{du}{2\pi} \hat{\mu}_{\bar{F}}(u)\, \bar{f}(u) + \ldots, \\
\mathcal{P} \circ \mathcal{P}_{1234} &= 1 + \int \frac{du}{2\pi} \hat{\mu}_F(u)\, \bar{f}(u) + \int \frac{du}{2\pi} \hat{\mu}_{\bar{F}}(u)\, f(u) + \ldots,
\end{aligned}
\tag{4.15}
$$

this difference follows from the fact that the gluons are either produced or annihilated in the presence of a charged transition $P^{[4]}$ in the NMHV cases and it results in the gluonic form factors f and $\bar{f}$. In other words, the dynamical part described before must be completed with the knowledge of these form factors, which in the present cases simply read [22]

$$
f(u) = \frac{x^+ x^-}{g^2} = 1/\bar{f}(u),
\tag{4.16}
$$

where $x^{\pm} = x(u \pm \frac{i}{2})$ with $x(u) = (u + \sqrt{u^2 - 4g^2})/2$ the Zhukowski map of the rapidity u. Note that such factor cannot be absorbed in the matrix part both because the matrix part is, by definition, independent of the coupling and because in this abelian case there is no matrix part.

Our main proposal is that the same structure persists for generic transitions. Namely, the effect of charging a pentagon, ignoring the matrix part, is to dress the abelian part by elementary form factors associated to each excitation present on the pentagons. More specifically, we propose that the charged version of (4.7) reads

$$
P^{[r]}(\boldsymbol{\Phi}|\boldsymbol{\Psi}) = g^{\frac{r(r-4)}{8}} \times \left[\prod_i \left(h_{\Phi_i} \right)^r \times \prod_i \left(h_{\bar{\Psi}_i} \right)^r \right] \times P(\boldsymbol{\Phi}|\boldsymbol{\Psi}),
\tag{4.17}
$$

where $\boldsymbol{\Phi} = \{\Phi_i\}$ is the incoming set of excitations at the bottom square of the pentagon, $\boldsymbol{\Psi} = \{\Psi_i\}$ the outgoing set of excitations at the top, and $r = 0, 1, \ldots, 4$ the amount of R-charge carried by the pentagon. The rules of the game are extremely simple. The result is factorized and for each excitation, or more precisely for each field creating the excitation at the bottom or conjugate field annihilating it at the top, we associate a form factor. The form factor can thus be thought of as being attached to the field and represents the net effect of charging the transition, as illustrated in figure 4.3.

$$P^{[r]}(\Psi|\Phi) = \begin{array}{c} \bar{\bar{\Phi}} \\ \mathcal{Q}^r \\ \Psi \end{array} = \begin{array}{c} (h_{\bar{\Phi}})^r \\ \bar{\bar{\Phi}} \\ \Psi \\ (h_{\Psi})^r \end{array} = (h_{\Psi})^r \times P(\Psi|\Phi) \times (h_{\bar{\Phi}})^r$$

Figure 4.3: The net effect of charging a pentagon is to dress each excitation on its edges by a corresponding form factor. This one is attached to the field that creates or annihilates the corresponding excitation in the bottom to top evolution picture. The picture above illustrates our conventions, with a state Ψ at the bottom being created by a field Ψ and a state Φ at the top being annihilated by the field $\bar{\bar{\Phi}}$. The form factors associated to these fields are then $(h_{\Psi})^r$ and $(h_{\bar{\Phi}})^r$, with r the R-charge of the charged pentagon, or equivalently, the number of times we act with a supercharge $\mathcal{Q}$.

We immediately verify that the general rule (4.17) properly reduces to (4.15) in the case of a single gluon. Indeed, as mentioned earlier, the form factor f above accounts for the difference between a gluon F produced on top of a charged and an uncharged pentagon, i.e.

$$f(u) = P^{[4]}_{0|F}(0|u)/P_{0|F}(0|u). \tag{4.18}$$

By convention, or equivalently by applying (4.7) blindly, $P(0|u) = 1$, while (4.17) gives us

$$P^{[4]}_{0|F}(0|u) = g^0 \times (h_{\bar{F}}(u))^4 \times 1, \tag{4.19}$$

that is

$$f(u) = (h_{\bar{F}}(u))^4 \qquad \Leftrightarrow \qquad h_{\bar{F}}(u) = \left(\frac{x^+ x^-}{g^2}\right)^{\frac{1}{4}}. \tag{4.20}$$
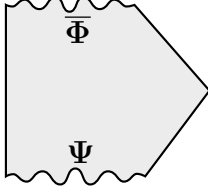
Similarly, we would read that

$$h_F(u) = \left(\frac{g^2}{x^+ x^-}\right)^{\frac{1}{4}}. \tag{4.21}$$
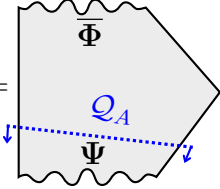
The remaining questions are what are the form factors for the other excitations, why is the form factor for a composite state a product of elementary ones, and why is (4.17) valid at all? The quick answers are that, due to their expected simple dependence (see (4.16)), form factors are easily extracted from data analysis, as done in [22], and that their factorized form is consistent with all the constraints the charged transitions must fulfill, as shall be discussed in section 4.2.3 below. However, one can do much better than that and actually *derive* the rule (4.17) *directly* from the uncharged transitions (4.7). The important

observation [2] is that charging a pentagon is the same as acting with a supersymmetry generator on one of its edges, as we will now explain.

To start with, we recall that one can view the pentagon transitions as form factors for a pentagon operator acting on the flux tube Hilbert space of states

$$P(\mathbf{\Psi}|\mathbf{\Phi}) = \langle\mathbf{\Phi}|\mathcal{P}|\mathbf{\Psi}\rangle = \qquad\qquad\qquad\qquad (4.22)$$

As explained in [2], all we need to do in order to add a unit of R-charge to a pentagon $\mathcal{P}$ is to act with a supersymmetry generator $\mathcal{Q}$ on the bottom state or, equivalently, with $-\mathcal{Q}$ on the top state. Here $\mathcal{Q}$ is the unique supercharge that commutes with $\mathcal{P}$ and is represented by ∂_χ on the super loop (4.14), see [2]. This leads to the relation :

$$P_A(\mathbf{\Psi}|\mathbf{\Phi}) = \langle\mathbf{\Phi}|\mathcal{P}_A|\mathbf{\Psi}\rangle = \langle\mathbf{\Phi}|\mathcal{P}\mathcal{Q}_A|\mathbf{\Psi}\rangle = \qquad\qquad (4.23)$$

Importantly, supersymmetry generators are realized on the flux as zero momentum fermions [48]. That is, to act on the state $|\mathbf{\Psi}\rangle$ with a supercharge $\mathcal{Q}_A$, we add to it a fermion and then send the momentum of that fermion to zero. This directly links the charged transitions to their un-charged counterparts, allowing us to extract all information about the former from the latter.

Let us show more precisely how this works. Consider for example the transition from the vacuum at the bottom to a single fermion $\bar{\psi}(u)$ at the top. Such transition is only possible if we equip the transition with R-charge as in the charged transition $P_A(0|u) = \langle\bar{\psi}(u)|\mathcal{P}_A|0\rangle$. To obtain the latter transition from an uncharged one we can start with a similar fermion $\bar{\psi}(v)$ at the bottom, i.e. from $P_{\bar{\psi}\bar{\psi}}(v|u)$. We now wish to take the limit in which the momentum of the fermion $\bar{\psi}(v)$ goes to zero, so that it becomes a supersymmetry generator acting at the bottom. In appendix C we show carefully how the zero momentum limit should be taken and in particular what is the proportionality factor. We find that

$$\mathcal{Q}|0\rangle = \sqrt{\frac{\Gamma_{\text{cusp}}}{2g}}\lim_{p\to 0}|p\rangle = \lim_{v\to\infty}\sqrt{\frac{\Gamma_{\text{cusp}}}{2ig}\frac{d\check{v}}{dp_{\bar{\psi}}}\mu_{\bar{\psi}}(\check{v})}\,|\bar{\psi}(\check{v})\rangle\,, \qquad (4.24)$$

44

where, following the notations of [23], the 'check mark' on top of the rapidity v, i.e. $\check{v}$, indicates that the analytical continuation to the rapidity plane neighbouring the zero momentum point (reached at $v = \infty$) has been done (see [23] for further details). Using this prescription, as well as the large v behaviours given in appendix B.4, we conclude that

$$P^{[1]}_{0|\bar{\psi}}(0|u) = \lim_{v \to \infty} \sqrt{\frac{\Gamma_{\text{cusp}}}{2ig} \frac{d\check{v}}{dp_{\bar{\psi}}} \mu_{\bar{\psi}}(\check{v})} \times P_{\bar{\psi}|\bar{\psi}}(\check{v}|u) = g^{-\frac{3}{8}} \left(\frac{g}{x(u)} \right)^{\frac{1}{4}}, \qquad (4.25)$$

where the upper label in $P^{[1]}$ indicates the amount of R-charge or equivalently the number of χ's carried by the pentagon. The fermionic creation transition (4.25) is obviously of the type (4.17)[6]

$$P^{[1]}_{0|\bar{\psi}}(0|u) \equiv g^{-\frac{3}{8}} \times h_{\psi}(u) \times P_{0|\bar{\psi}}(0|u) = g^{-\frac{3}{8}} \times h_{\psi}(u), \qquad (4.26)$$

with

$$h_{\psi}(u) = (g/x)^{1/4} \qquad (4.27)$$

the form factor for a single antifermion. As expected it shows a simple dependence on the rapidity u of the excitation, once expressed in terms of the Zhukowski variable $x = x(u)$, as found earlier for the gluons.

It is not so much difficult to include more excitations in the top and check the factorization of the form factors. Suppose, for instance, that we start with a multi-particle transition involving fermions and send the momentum of one of them to zero as prescribed by (4.24). As a result of the multi-particle factorization (4.7), the multi-particle form factors must factorize as well.

We can see this at work on simple examples, using the same $P^{[1]}$ procedure as before. For instance, we can at no cost consider the same fermion creation transition with a gluonic excitation $F_a(w)$ added on the top. This yields

$$P^{[1]}_{0|\bar{\psi}F_a}(0|u, w) = \lim_{v \to \infty} \sqrt{\frac{\Gamma_{\text{cusp}}}{2ig} \frac{d\check{v}}{dp_{\bar{\psi}}} \mu_{\bar{\psi}}(\check{v})} \times P_{\bar{\psi}|\bar{\psi}F_a}(\check{v}|u, w), \qquad (4.28)$$

where, again, the upper index indicates that this new transition is taking place on top of a pentagon carrying one unit of R-charge. It exactly differs from the chargeless transition defined through (4.7) by the form factors. Indeed, using the factorization of the dynamical part (4.7) together with (4.25), (4.27) and (B.4), we verify that

$$P^{[1]}_{0|\bar{\psi}F_a}(0|u, w) = g^{-\frac{3}{8}} h_{\psi}(u) h_{F_{-a}}(w) P_{0|\bar{\psi}F_a}(0|u, w), \qquad (4.29)$$

---

[6]Recall that following (4.7) we are working in a convention where the un-charged creation transition of any excitation X is trivial. With the χ-labelling this reads $P^{[0]}_{0|X}(0|u) = 1$.

with

$$h_{F_a}(u) = \left[\frac{g^2}{x\left(u + \frac{ia}{2}\right) x\left(u - \frac{ia}{2}\right)} \right]^{(\mathrm{sign}\,a)/4}, \qquad (4.30)$$

in agreement with (4.20) and (4.21) for $a = -1$ and $a = +1$, respectively.

Instead of adding matter to the fermion $\bar{\psi}$ at the top, one can imagine replacing it by a pair $\phi\psi$ or a triplet $\psi\psi\psi$ (always with the small fermion $\bar{\psi}(\check{v})$ at the bottom) and hence access to the as-yet-unknown ϕ and $\bar{\psi}$ form factors. A proper analysis would require introducing a matrix part, whose main role is to project the pair/triplet to the $SU(4)$ channel with one unit of R-charge. However, in both cases, the matrix part plays no role as far as the form factors are concerned.[7] One can thus proceed without knowing its explicit form and directly relate the ϕ and $\bar{\psi}$ form factors to the large v behaviours of the $P_{\bar{\psi}|\phi}(\check{v}|u)$ and $P_{\bar{\psi}|\psi}(\check{v}|u)$ transitions. Using expressions in appendix B.4 one gets the system of equations

$$h_\phi(u) h_{\bar{\psi}}(w) = g^{3/8} \lim_{v \to \infty} \sqrt{\frac{\Gamma_{\mathrm{cusp}}}{2ig} \frac{d\check{v}}{dp_{\bar{\psi}}} \mu_{\bar{\psi}}(\check{v})} \times P_{\bar{\psi}|\phi}(\check{v}|u) P_{\bar{\psi}|\psi}(\check{v}|w) = \left(\frac{x(w)}{g} \right)^{1/4},$$

$$\prod_{i=1}^{3} h_{\bar{\psi}}(u_i) = g^{3/8} \lim_{v \to \infty} \sqrt{\frac{\Gamma_{\mathrm{cusp}}}{2ig} \frac{d\check{v}}{dp_{\bar{\psi}}} \mu_{\bar{\psi}}(\check{v})} \times \prod_{i=1}^{3} P_{\bar{\psi}|\psi}(\check{v}|u_i) = \left(\frac{x(u_1) x(u_2) x(u_3)}{g^3} \right)^{1/4},$$

$$(4.31)$$

whose only reasonable solution is

$$h_\phi(u) = 1, \qquad h_{\bar{\psi}}(u) = (x/g)^{1/4}. \qquad (4.32)$$

Equations (4.27), (4.30), and (4.32) finalize our proposal for the charged transitions (4.17). A couple of consistency checks for it will be given in the next sub-section. One easy test can actually be run immediately. It comes from the physical requirement that a pair of conjugate excitations should decouple on a charged transition exactly as they do in the uncharged case. That is, the *square limit* (4.8) must remain the same on a charged transition.[8] Including the form factors, this condition translates into

$$\operatorname*{Res}_{v=u} P_{\Phi|\Phi}(u|v)\, h_\Phi(u) h_{\bar{\Phi}}(v) = \frac{i}{\mu_\Phi(u)}, \qquad (4.33)$$

---

[7]For completeness, we have indeed that the matrix part is $\propto 1/(u - w + 3i/2)$ and $\propto 1/\prod_{i<j}(u_i - u_j + i)$ for the two cases at hand, i.e. for a state $\phi(u)\psi(w)$ and $\psi(u_1)\psi(u_2)\psi(u_3)$ at the top, respectively. Because it shows no dependence at all on the rapidity v of the fermion $\bar{\psi}(\check{v})$ at the bottom, it cannot contribute to the form factors.

[8]Put differently, the propagation on the square is diagonal, so it cannot be charged.

$$g^{\frac{3(3-4)}{8}}\left(h_{\bar{\psi}}(u)\right)^3$$

$$\bar{\psi}$$

$$\chi_1^1\chi_1^2\chi_1^3$$

$$\chi_2^4$$

$$\psi$$

$$g^{\frac{1(1-4)}{8}}\left(h_{\psi}(u)\right)^1$$
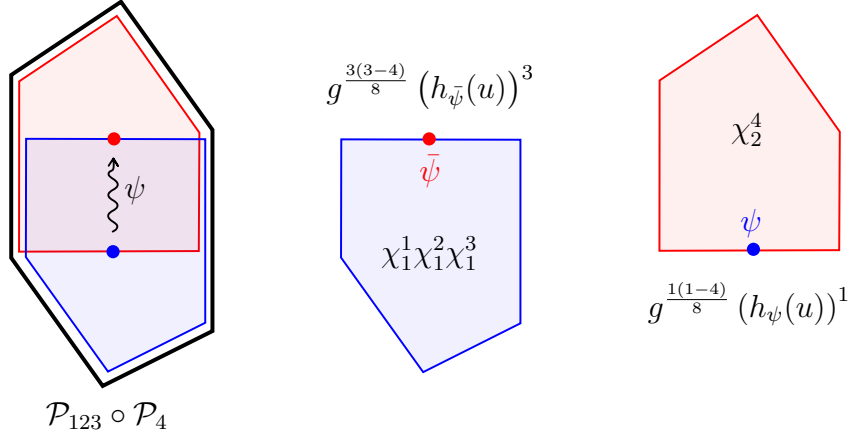
$$\mathcal{P}_{123}\circ\mathcal{P}_4$$

Figure 4.4: Leading twist transition for the hexagon component $\mathcal{P}_{123}\circ\mathcal{P}_4$. In this example, we assign the form factor $\left(h_{\bar{\psi}}(u)\right)^3$ to the bottom (blue) pentagon and $(h_\psi(u))^1$ to the top (red) pentagon.

which enforces

$$h_\Phi(u)h_{\bar{\Phi}}(u) = 1\,. \tag{4.34}$$

This relation is easily seen to be satisfied.

In the end our form factors are all simply given in terms of Zhukowski variables. Putting them together, for a polygon with n edges, gives us the full form factors part in (4.3) as

$$\texttt{form factors part} = \prod_{i=0}^{n-5} g^{\frac{r_i(r_i-4)}{8}}\left(h_{\boldsymbol{\Psi}^{(i)}}\right)^{r_i}\left(h_{\bar{\boldsymbol{\Psi}}^{(i+1)}}\right)^{r_i}\,, \tag{4.35}$$

where the index i on top of the matter fields refers to the i'th square, with $i=0$ being the first one at the very bottom and $i=n-4$ the last one at the very top,[9] while the *same* index i in r_i refers to the i'th pentagon transition between states $\boldsymbol{\Psi}^{(i)}$ and $\boldsymbol{\Psi}^{(i+1)}$, with r_i units of R-charge. Note in particular that each excitation in a given square is assigned two form factors – one for each of the pentagons that overlap on this particular square. A simple example is depicted in figure 4.4.

As a summary, we can now write the OPE decomposition for a polygon with n edges

---

[9]We recall that the states in the very bottom ($i=0$) and very top ($i=n-4$) squares are both vacuum with measure and form factors equal to one.

in a rather compact form. Up to the matrix part of course, we have

$$\mathbb{P} \circ \mathbb{P} \circ \ldots \circ \mathbb{P}|_X = \sum \prod_{i=0}^{n-5} \hat{\mu}_{\boldsymbol{\Psi}^{(i)}} \, g^{\frac{r_i(r_i-4)}{8}} \, \left(h_{\boldsymbol{\Psi}^{(i)}}\right)^{r_i-r_{i-1}} \, P^{R/L}\big(\boldsymbol{\Psi}^{(i)}|\boldsymbol{\Psi}^{(i+1)}\big), \qquad (4.36)$$

with X a choice of χ component, with r_i Grassmann variables χ's in pentagon i, and with $P^{R/L}(\boldsymbol{\Psi}^{(i)}|\boldsymbol{\Psi}^{(i+1)}) = P(\boldsymbol{\Psi}^{(i)}|\boldsymbol{\Psi}^{(i+1)})$ or $P(\overline{\boldsymbol{\Psi}}^{(i+1)}|\overline{\boldsymbol{\Psi}}^{(i)})$ for i even or odd.

In what follows we shall perform two sort of checks of our proposal. The first kind of checks – with which we will conclude this section – are internal self-consistency checks of the POPE proposal. The second sort of checks concern explicit comparison against perturbative data and are the main focus of section 4.3.

4.2.3   Consistency checks

In this section we shall present two consistency checks of the non-MHV form factors presented above. Namely, we will first see that they are consistent with parity and finally observe that they are compatible with the general axioms for multiparticle transitions.

Parity

We have proposed in [2] a simple realization of parity within the POPE approach. In a given pentagon with r units of $R-$charge, the action of parity conjugates its $R-$charge, i.e. $r \to 4 - r$, which means flipping the chirality of the external particles that are being scattered, but also the chirality of the flux tube excitations, namely $\psi \leftrightarrow \bar{\psi}$ and $F \leftrightarrow \bar{F}$. This can be achieved by simply flipping the signs of the angles ϕ appearing in the square propagation factor of the OPE integrand.

In more concrete terms, parity symmetry establishes the following relation between the OPE components

$$\mathbb{P} \circ \mathbb{P} \circ \ldots \circ \mathbb{P}|_X = (\mathbb{P} \circ \mathbb{P} \circ \ldots \circ \mathbb{P}|_{\bar{X}})|_{\phi \to -\phi} \, . \qquad (4.37)$$

where $\bar{X}$ is the complement of the component X, namely

$$\bar{X} = \int \prod_{i=1}^{n-4} d^4\chi_i \, e^{\sum_{i=1}^{n-4} \bar{\chi}_i \chi_i} X \bigg|_{\bar{\chi} \to \chi} \, . \qquad (4.38)$$

For example, we can relate an NMHV component with $X = \chi_1^1 \chi_1^2 \chi_1^3 \chi_2^4$ to an N^{n-5}MHV with its complement $\bar{X} = \chi_1^4 \chi_2^1 \chi_2^2 \chi_2^3 \cdots \chi_{n-4}^1 \chi_{n-4}^2 \chi_{n-4}^3 \chi_{n-4}^4$. For parity to be a symmetry

48

of the super Wilson loop, the POPE decomposition should be invariant under $r \to 4 - r$ together with a flip of the chirality of all the flux tube excitations, namely

$$\sum \prod_{i=0}^{n-5} \hat{\mu}_{\mathbf{\Psi}^{(i)}} \, g^{\frac{r_i(r_i-4)}{8}} \left(h_{\mathbf{\Psi}^{(i)}}\right)^{r_i - r_{i+1}} \, P^{R/L}\big(\mathbf{\Psi}^{(i)}|\mathbf{\Psi}^{(i+1)}\big) \tag{4.39}$$

$$= \sum \prod_{i=0}^{n-5} \hat{\mu}_{\bar{\mathbf{\Psi}}^{(i)}} \, g^{\frac{(r_i-4)r_i}{8}} \left(h_{\bar{\mathbf{\Psi}}^{(i)}}\right)^{(4-r_i)-(4-r_{i+1})} \, P^{R/L}\big(\overline{\mathbf{\Psi}}^{(i)}|\overline{\mathbf{\Psi}}^{(i+1)}\big)\Bigg|_{\phi_i \to -\phi_i},$$

up to an unphysical relative normalization. Note that the overall power of g is parity invariant by itself. Now, the pentagon transitions and measures change at most by a sign under this transformation (namely when fermions are involved) but they do not distinguish the chirality of the flux tube excitations otherwise. Finally, using the relation (4.34) we see that the form factor part is also invariant and thus parity is nicely satisfied.

Bootstrap axioms

Given the set of elementary transitions (4.9), the multiparticle ansatz (4.7) solves minimally for the Watson, mirror and decoupling axioms that the multiparticle transitions are conjectured to satisfy [1, 22–24]. Any other solution to the same bootstrap equations would differ from (4.7) by a so-called Castillejo-Dalitz-Dyson (CDD) factor. The charged transitions introduced in (4.17) and their associated non-MHV form factors are particular examples of non-minimal solutions featuring totally factorized CDD factors. Indeed, as we shall now explain, the non-MHV form factors are such as to make the charged transitions (4.17) a valid solution to the multiparticle bootstrap equations.

As already mentioned, the main feature of the prefactor in (4.17) is that it is totally factorized. As such it is oblivious to the ordering of the excitations at both the bottom and the top of the pentagon. It then does not affect the Watson equation encoding the transformation property of the transitions upon permutation of excitations in the past or in the future.[10] A factorized prefactor is also automatically regular and non-vanishing when bottom and top rapidities coincide. The decoupling pole and the decoupling condition for

---

[10]Note however that the non-MHV prefactor is *not* invariant under the exchange of a bottom and a top excitation. It cannot therefore be seen as a CDD factor for the elementary transitions (4.9) without spoiling their fundamental relations to the flux tube S-matrix (4.11). Examples of (factorized) CDD factors for the elementary transitions are given at the end of the appendix B. These are redefinitions of the individual pentagon transitions that preserve the fundamental and mirror relations, eq. (4.11) and first eq. in (4.12), respectively. They also preserve the decoupling pole (4.8), when applicable, but renormalize the square measures.

the multiparticle transitions are thus preserved, as already stressed around eq. (4.34). It remains to check the *mirror axiom* (4.12) which was introduced when bootstrapping the pentagon transitions involving gluons or scalars. For this mirror relation to be satisfied by the charged transitions, the form factor should obey the relation

$$h_\Phi(u^{-\gamma}) = h_{\bar{\Phi}}(u) \, . \tag{4.40}$$

This relation is immediately observed for scalars while for gluons it follows from the relation $x^\pm(u^{-\gamma}) = g^2/x^\pm(u).$[11] In fact, the validity of both axioms directly follows from the relation between the charged transition and a zero momentum fermion (4.24) (taken to be one of the $\boldsymbol{\Psi}$ excitations in (4.12) for example).

4.3   Comparison with data

We would like now to test our proposal (4.36) for the POPE integrand against available data at weak coupling. Historically, this comparison was absolutely instrumental in unveiling the general ansatz for the form factors.

The data we use is extracted from the package [36], which generates non-MHV amplitudes at tree level for any number of particles. The same package also yields one loop amplitudes but for the purpose of this chapter we restrict our attention to tree-level checks only.

In the POPE we have essentially five different types of elementary excitations, $F, \psi, \phi, \bar{\psi}, \bar{F}$, and fifteen different pairings of them into transitions. These two numbers are in correspondence with the five independent NMHV hexagons and fifteen independent NMHV heptagons, respectively. At leading twist, the hexagons essentially probe the measures and the form factors. The heptagons on the other hand probe all building blocks of the integrand and, in particular, the pentagon transitions involving mixed types of particles. In this section we will confront our predictions against both hexagons and heptagons thus probing all these ingredients at once.

At the same time, these checks also provide us with a strong test of the map between N^kMHV amplitudes and charged pentagons proposed in [2]. This one maps any N^kMHV amplitude, as specified by choosing an η-component of the super loop, to a very precise linear combination of the OPE friendly χ-components (4.14) and vice-versa. It is the latter χ-components that admit a neat OPE interpretation and thus offer direct access to the various pentagon transitions.

---

[11]Beware that mirror transformation takes different form for scalars and gluons [22, 53].

To illustrate this point, let us consider a random η-component, say the NMHV heptagon component $\mathcal{W}^{(-1,-1,1,2)}$ multiplying the monomial $\eta_{-1}^A \eta_{-1}^B \eta_1^C \eta_2^D \epsilon_{ABCD}$ (see figure 4.8.**a** for the convention of the edge labelling). According to our discussion, we expect it *not* to have an obvious OPE expansion and indeed this is precisely what we find. To see it we extract this tree-level component[12] from the package [36] as

```
evaluate@superComponent[{1,2},{3},{},{},{},{4},{}]@treeAmp[7,1]
```

and, to make it into a weight free quantity, multiply it by the weights $((-\mathbf{1})_1)^2 (\mathbf{1})_1 (\mathbf{2})_2$ with $(\mathbf{i})_j$ the weight of the twistor Z_i in the jth pentagon (see [2] for more details), which we can express in terms of OPE variables using the twistors in [22].[13] We denote this properly normalized heptagon component as $\mathbb{W}^{(-1,-1,1,2)}$. In terms of OPE variables we have

$$\mathbb{W}^{(-1,-1,1,2)} = \frac{e^{-\sigma_1 - \frac{i\phi_1}{2}}}{1 + e^{-2\tau_1}} = e^{-\sigma_1 - \frac{i\phi_1}{2}} - e^{-\sigma_1 - 2\tau_1 - \frac{i\phi_1}{2}} + \mathcal{O}(e^{-4\tau_1}), \qquad (4.41)$$

which clearly defies any reasonable OPE interpretation![14]

Of course, this does *not* mean that we cannot describe this component within the POPE approach. On the contrary, as explained in [2], once using the inverse map we can express any component as a linear component of the nice χ-components which in turn we can describe at any loop order within the POPE. In this case, using the expression (21) of [2]

---

[12]Actually, the package extracts the ratio function component $\mathcal{R}^{(i,j,k,l)} = \mathcal{W}^{(i,j,k,l)}/\mathcal{W}_{\text{MHV}}$, but at tree level they are the same.

[13]As is often the case, while this is the correct mathematical procedure, the naive evaluation of $\mathcal{W}^{(-1,-1,1,2)}$ with the twistors in [22] would yield the very same result since, in this case, the weights simply evaluate to 1.

[14]To start with, it simply does not depend on the OPE variables τ_2, σ_2, ϕ_2 at all, as if only the vacuum were propagating in the second square of this heptagon. Even if we were to accept that, other puzzles would immediately appear when interpreting the large τ_1 expansion: the first term looks like a twist zero contribution – like the vacuum does – but with a non-trivial σ_1 and ϕ_1 dependence – contrary to the vacuum. There is no natural candidate for what anything like this would be. Also suspicious is the fact that only even twists show up once we expand the result out at large τ_1. Moreover terms in the near collinear expansion shout trouble: their dependence in σ_1 is so simple that they would not have any sensible Fourier transform into momentum space. In short: this component is as weird as it could be from an OPE perspective.

we would find

$$
\begin{aligned}
\mathbb{W}^{(-1,-1,1,2)} = {} & \mathcal{P}_{12} \circ \mathcal{P} \circ \mathcal{P}_{34}\, e^{-\sigma_1-\sigma_2-\tau_2+\frac{i\phi_1}{2}} + \\
& \mathcal{P}_{12} \circ \mathcal{P}_3 \circ \mathcal{P}_4 \left(e^{-2\sigma_1-\tau_1-\tau_2-\frac{i\phi_1}{2}-\frac{i\phi_2}{2}} + e^{-\sigma_1-\tau_2+\frac{i\phi_1}{2}-\frac{i\phi_2}{2}} + e^{-\sigma_1-\sigma_2-2\tau_2+\frac{i\phi_1}{2}+\frac{i\phi_2}{2}} - \right. \\
& \left. e^{-\sigma_1-\sigma_2+\frac{i\phi_1}{2}+\frac{i\phi_2}{2}} \right) + \\
& \mathcal{P}_{12} \circ \mathcal{P}_{34} \circ \mathcal{P} \left(-e^{-2\sigma_1-\tau_1-\frac{i\phi_1}{2}} - e^{-\sigma_1-\sigma_2-\tau_2+\frac{i\phi_1}{2}+i\phi_2} - e^{-\sigma_1+\frac{i\phi_1}{2}} \right) + \\
& \mathcal{P}_{123} \circ \mathcal{P} \circ \mathcal{P}_4 \left(e^{-2\sigma_1-\tau_2-\frac{i\phi_2}{2}} + e^{-\sigma_1-\sigma_2-\tau_1+i\phi_1+\frac{i\phi_2}{2}} + e^{-\sigma_2+\frac{i\phi_2}{2}} \right) + \\
& \mathcal{P}_{123} \circ \mathcal{P}_4 \circ \mathcal{P} \left(e^{-\sigma_1-\tau_1-i\phi_1} + e^{-\sigma_1-\tau_1+i\phi_1} + e^{-\sigma_2-\tau_2+i\phi_2} + e^{-\sigma_1-\sigma_2-\tau_1-\tau_2+i\phi_1+i\phi_2} + \right. \\
& \left. e^{-2\sigma_1-2\tau_1} - e^{-2\sigma_1} + 1 \right) + \\
& \mathcal{P}_{1234} \circ \mathcal{P} \circ \mathcal{P} \left(e^{-2\sigma_1-\tau_1+\frac{i\phi_1}{2}} + e^{-\sigma_1-\frac{i\phi_1}{2}} \right).
\end{aligned}
$$

$$(4.42)$$

It is amusing to see how this precise linear combination of χ-components, each with a nice OPE expansion, combines into the component (4.41) without any obvious OPE picture. Conversely, and perhaps less trivially, according to [2], a generic χ-component is a precise linear combination of several η- components. These are the components that we shall directly confront against the integrability inspired predictions in the following subsections.

4.3.1 NMHV Hexagon

Due to R-charge conservation, different NMHV components will support different flux tube transitions. The hexagon – made out of two pentagons – is the simplest case where we can clearly see this at work. For the components $\mathcal{P}_{1234} \circ \mathcal{P}$ and $\mathcal{P} \circ \mathcal{P}_{1234}$, encountered before, the excitations flowing in the middle square should form an R-charge singlet (for example we could have the vacuum, any bound state of gluons, a pair $\psi_1 \bar{\psi}_{234}$, etc.). For $\mathcal{P}_{123} \circ \mathcal{P}_4$ ($\mathcal{P}_1 \circ \mathcal{P}_{234}$) we should have excitations with the same total R-charge as for a fermion (anti-fermion), that is the state should be in the fundamental (antifundamental) representation of $SU(4)$. Finally for $\mathcal{P}_{12} \circ \mathcal{P}_{34}$ we need the same R-charge as for a scalar, i.e. a state in the vector representation of the R-symmetry group. These five components form a basis over which we can expand any other component [2].

We can write explicitly the OPE integrand for these nice components. At leading twist,
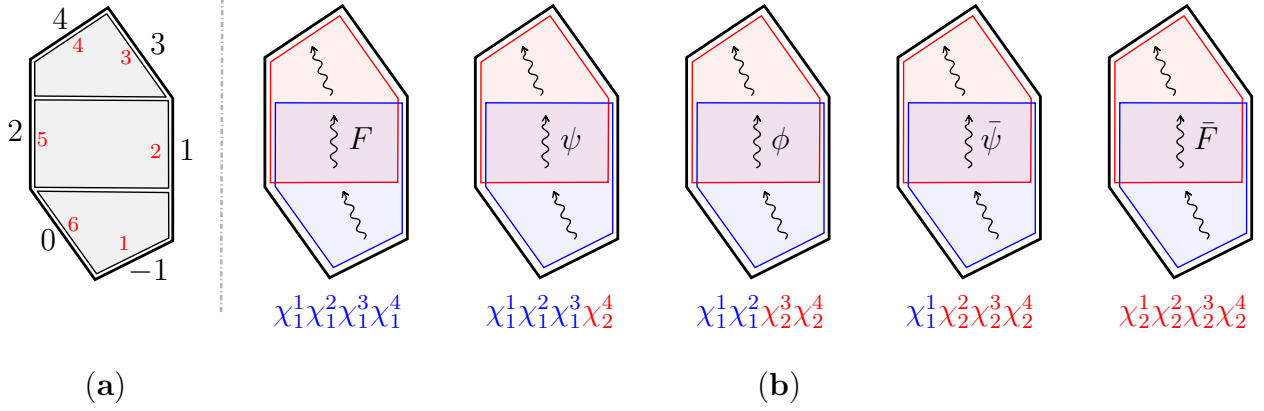
Figure 4.5: (**a**) OPE friendly edge labelling used in this chapter (big black outer numbers) versus the more conventional cyclic labelling (small red inner numbers) for the hexagon. (**b**) The five components of the NMHV hexagon and the corresponding excitations at twist one. In the first and last component we have written the particle appearing first in perturbation theory.

they are (see figures 4.4 and 4.5)

$$\mathcal{P}_{1234} \circ \mathcal{P} = 1 + \int_{\mathbb{R}} \frac{du}{2\pi} \hat{\mu}_{F_1}(u) (h_{F_{-1}}(u))^4 (h_{F_1}(u))^0 + \int_{\mathbb{R}} \frac{du}{2\pi} \hat{\mu}_{F_{-1}}(u) (h_{F_1}(u))^4 (h_{F_{-1}}(u))^0 + \dots ,$$

$$\mathcal{P}_{123} \circ \mathcal{P}_4 = g^{-\frac{3}{4}} \int_{\mathcal{C}} \frac{du}{2\pi} \hat{\mu}_{\psi}(u) (h_{\bar{\psi}}(u))^3 h_{\psi}(u) + \dots ,$$

$$\mathcal{P}_{12} \circ \mathcal{P}_{34} = g^{-1} \int_{\mathbb{R}} \frac{du}{2\pi} \hat{\mu}_{\phi}(u) (h_{\phi}(u))^2 (h_{\phi}(u))^2 + \dots ,$$

$$\mathcal{P}_1 \circ \mathcal{P}_{234} = g^{-\frac{3}{4}} \int_{\mathcal{C}} \frac{du}{2\pi} \hat{\mu}_{\bar{\psi}}(u) h_{\psi}(u) (h_{\bar{\psi}}(u))^3 + \dots ,$$

$$\mathcal{P} \circ \mathcal{P}_{1234} = 1 + \int_{\mathbb{R}} \frac{du}{2\pi} \hat{\mu}_{F_{-1}}(u) (h_{F_1}(u))^0 (h_{F_{-1}}(u))^4 + \int_{\mathbb{R}} \frac{du}{2\pi} \hat{\mu}_{F_1}(u) (h_{F_{-1}}(u))^0 (h_{F_1}(u))^4 + \dots .$$

(4.43)

Although in the first and last line we have the same allowed excitations, the form factors break the symmetry between the positive and negative helicity gluons. In particular, the first terms in $\mathcal{P}_{1234} \circ \mathcal{P}$ and $\mathcal{P} \circ \mathcal{P}_{1234}$ appear at tree level and the last terms are delayed to two loops, as confirmed from data.

As thoroughly described in [23], the contour of the integration $\mathcal{C}$ for the fermions is over a two-sheeted Riemann surface and can be conveniently splitted into two contributions: the large and small sheet contours. The large sheet contour is performed over the real axis with a small positive imaginary part whereas the small sheet contour is a counter-clockwise half-moon on the lower complex plane. It is then natural to treat these contributions independently as coming from a large fermion ψ_L and a small fermion ψ_S. In appendix B.2 we provide the explicit formulae for the analytic continuation of the pentagon transitions from the large to the small sheet.

Let us now study in detail the component $\mathcal{P}_{123} \circ \mathcal{P}_4$ at leading twist as an illustration of a check against data (see figure 4.4). The OPE integral splits into two terms corresponding to the large and small fermion contributions

$$\mathcal{P}_{123} \circ \mathcal{P}_4 = g^{-\frac{3}{4}} \int_{\mathcal{C}_{\text{large}}} \frac{du}{2\pi} \, \hat{\mu}_{\psi_L}(u) \, (h_{\bar{\psi}_L}(u))^3 \, h_{\psi_L}(u) + g^{-\frac{3}{4}} \int_{\mathcal{C}_{\text{small}}} \frac{du}{2\pi} \, \hat{\mu}_{\psi_S}(u) \, (h_{\bar{\psi}_S}(u))^3 \, h_{\psi_S}(u) \, .$$

(4.44)

In this case the contour of integration $\mathcal{C}_{\text{small}}$ does not enclose any singularity, resulting in a vanishing contribution of the second term at any value of the coupling [23]. We are only left with the first term that should be integrated slightly above the real axis. Using the explicit expressions for the measure and form factor at leading order in the coupling, we obtain

$$\mathcal{P}_{123} \circ \mathcal{P}_4 = e^{-\tau + i\phi/2} \int_{\mathbb{R}+i0} \frac{du}{2\pi} \frac{-i\pi}{\sinh(\pi u)} e^{2iu\sigma} + \mathcal{O}(g^2) \, .$$

(4.45)

According to the map worked out in [2], this component should relate to a component of the super amplitude as follows

$$\mathcal{P}_{123} \circ \mathcal{P}_4 = ((-\mathbf{1})_1)^3 \, (\mathbf{4})_2 \, \mathcal{W}^{(-1,-1,-1,4)} \, ,$$

(4.46)

where, as before, the pre-factor $(\mathbf{i})_j$ stands for the weight of the twistor Z_i in the jth pentagon. In order to extract this component we use the aforementioned package by running the following line in Mathematica

```
evaluate@superComponent[{1,2,3},{},{},{4},{},{}]@treeAmp[6,1]
```

still using the twistors given in [22].[15] Upon expanding the outcome at leading order in the twist and taking into account the weights, we obtain a perfect match validating our conjecture for this particular transition.

---

[15]Note that one should convert between the OPE friendly and the cyclic labelling of the edges. Figure 4.5.**a** shows both labellings for the hexagon.

The same type of checks are straightforward to generalize to the rest of the components or to one loop level using the same package [36]. These probe the expressions for the form factors presented in (4.35) at weak coupling. We have also verified the correctness of our conjectures beyond leading twist when also the pentagon transitions start to play a role. In the next section, we probe them more directly using the NMHV heptagon.

4.3.2   NMHV Heptagon

The NMHV heptagon is the appropriate laboratory to test the pentagon transitions involving all possible pairings of the fundamental excitations. In particular, it is the first polygon where the transitions between excitations in different squares arise. All the POPE building blocks take now part in and consequently they are all scrutinised.

The heptagon has fifteen independent components [2] represented in figure 4.6. Five of them, in the top line of that figure, can be constructed in a similar manner to the hexagon by charging the outermost pentagons. To generate the remaining ten independent components, it is unavoidable charging the middle pentagon. According to [2], charging the middle pentagon typically involves rather nontrivial linear combinations of the super amplitude η- components. Since we are also interested in testing this map, in what follows we will focus mostly on such examples in which the middle pentagon is charged.

To leading twist each of the fifteen heptagon components probes a different pentagon transition, see figure 4.6. We verified that their near collinear expansions are indeed in perfect agreement with the proposals of the previous section once expanded out to leading order in perturbation theory. Interesting as they are, the analysis of these cases follow [22] almost verbatim and is therefore not particularly illuminating to present it in detail. Instead, in this section we will consider a richer example involving multi-particle states in both middle squares. A second example can be found in Appendix D. These examples allow one to get a good picture of how generic transitions show up at weak coupling. They also probe considerably more structures in a very non-trivial way and allow us to stress the important role of the so-called *small fermions*. The matrix part in the first one is trivially equal to 1 and in the second case it is simple and has been determined before in [23].

The examples where more complicated matrices appear were also tested but we leave them for a future publication, where the general construction of the matrix part will be presented. All in all, we have tested *all* possible transitions at tree level up to twists three in one square and two in the second one and several twist three (in both squares) transitions with simple matrix part (in a total of 429 processes).
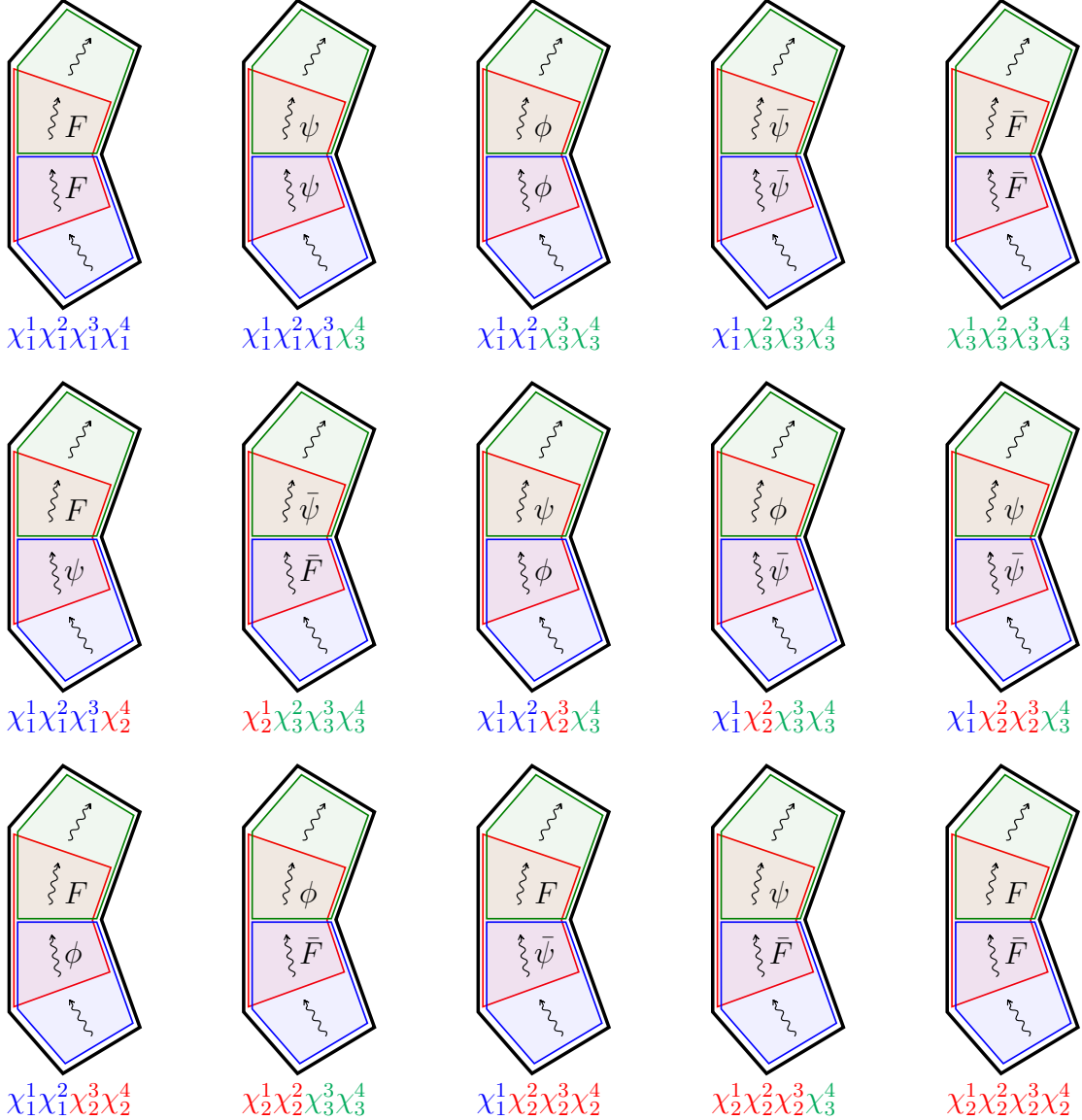
Figure 4.6: Fifteen independent components for the NMHV heptagon with the corresponding excitations at twist one. The components in the first line involve charging the bottom and top pentagons only while the second and third line correspond to the remaining ten components where the middle pentagon is also charged. As illustrated here, each such component can be used as a direct probe of a pentagon transition.
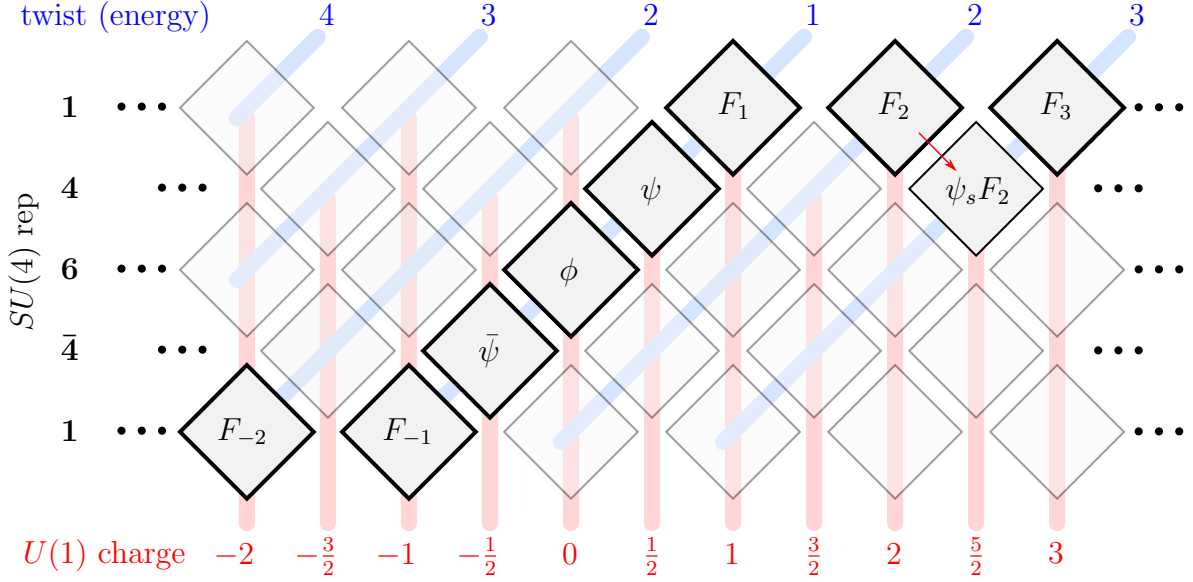
Figure 4.7: Fundamental excitations together with the effective excitation $\psi_s F_2$ (a.k.a. $\mathcal{D}^2_{1\dot{2}}\psi$) used in the example.

It is instructive to present one such example in detail. We will analyse the $\mathcal{P} \circ \mathcal{P}_{123} \circ \mathcal{P}_4$ component through the POPE lens. As mentioned above, to make things more interesting and nontrivial we will look at some high twist contribution involving several particles and/or bound-states. To be precise we shall consider the term proportional to

$$e^{-3\tau_1 - 3i\phi_1} \times e^{-3\tau_2 + 5/2i\phi_2} \tag{4.47}$$

as illustration. What flux tube physical processes govern this contribution? To answer this question it suffices to list everything that has the right quantum numbers to be allowed to flow. In the case at hand we are looking at states with twist 3 both in the first middle square and the second square. We are searching for states with helicity -3 in the first square and $+5/2$ in the second square. Finally, we have R-charge considerations. For the sequence $\mathcal{P} \circ \mathcal{P}_{123} \circ \mathcal{P}_4$ we necessarily have an R-charge singlet in the first middle square and a state in the fundamental ($\mathbf{4}$) representation of $SU(4)$ in the second middle square. All in all, this information restricts the matter content enormously.

In the first square, for example, the absolute value of the helicity is maximal, equal to the twist of the state. This saturation is achieved for purely gluonic states only, see figure 4.7. There are therefore only three possible states in the first middle square,

$$\left| F_{-1}(u) F_{-1}(v) F_{-1}(w) \right\rangle, \qquad \left| F_{-2}(u) F_{-1}(v) \right\rangle, \qquad \left| F_{-3}(u) \right\rangle. \tag{4.48}$$

57

The first two are multi-particle states and kick in at higher loop orders. The last one, corresponding to a bound-state of three negative helicity gluons, is the only one showing up at leading order at weak coupling.

In the second square things are more interesting. With helicity 5/2 there are only two possible states we could envisage:

$$|F_1(u)F_1(v)\psi(w)\rangle\,, \qquad |\psi(w)F_2(u)\rangle\,. \tag{4.49}$$

At first we could imagine discarding both since they are both multi-particle states; however, when fermions are involved the coupling analysis is more subtle. The point is that fermions can be either small or large and in the former case they act as sort of symmetry generators [23]. As such each of the states in (4.49) can be split into two cases depending on whether the fermion is small or large. In particular, the second state $|F_2(u)\psi(v)\rangle$ with the fermion evaluated in the small fermion domain can be seen as a supersymmetry generator acting on the excitation $F_2(u)$ thus generating a *single* effective weak coupling excitation – see figure 4.7 – and as such might show up already at leading order at weak coupling. (At the same time the first state $|F_1(u)F_1(v)\psi(w)\rangle$ with ψ being a small fermion would behave as a two particle state and thus show up only at higher orders in perturbation theory.)

In sum, to match against tree level data it suffices to focus on the process

$$\mathtt{vacuum} \to F_{-3}(u) \to \psi(w)F_2(v) \to \mathtt{vacuum}\,, \tag{4.50}$$

which is what we turn to now. In this case the matrix part is trivial. Indeed, the R-charge index of the fermion is unambiguously fixed once we pick an R-charge configuration for the various χ's. In other words, the matrix part in (4.3) is equal to one and the full integrand is just a product of the dynamical part and the form factor contribution. According to (4.5) and (4.35) these read

$$\mathtt{dynamical\ part}\ =\ \hat{\mu}_{F_{-3}}(u)\,\hat{\mu}_{\psi}(w)\,\hat{\mu}_{F_2}(v)\,\frac{P_{\bar{\psi}|F_3}(w|u)P_{F_{-2}|F_3}(v|u)}{P_{\bar{\psi}|F_{-2}}(w|v)P_{F_2|\psi}(v|w)}\,, \tag{4.51}$$

$$\mathtt{form\ factors\ part}\ =\ \frac{1}{g^{\frac{3}{4}}}\,(h_{F_3}(u))^0\,(h_{F_{-3}}(u))^3\,(h_{\bar{\psi}}(w))^3\,(h_{F_{-2}}(v))^3\,h_{\psi}(w)\,h_{F_2}(v) \tag{4.52}$$

which we simply multiply together to obtain the POPE prediction

$$\mathcal{W}_{F_{-3}\to\psi\,F_2} = \int_{\mathbb{R}}\frac{du}{2\pi}\int_{\mathbb{R}}\frac{dv}{2\pi}\int_{\bar{\mathcal{C}}_{\mathrm{small}}}\frac{dw}{2\pi}\,(\mathtt{dynamical\ part})\times(\mathtt{form\ factors\ part})\,, \tag{4.53}$$

where $\bar{\mathcal{C}}_{\text{small}}$ is the *complex conjugate* version of the half-moon contour mentioned below (4.43), hence running in the upper half u plane, in agreement with the alternating conventions in (4.5). (Equivalently, depending on the $\pm$ sign in front of $ip\sigma$ in (4.5) we use an $\pm i\epsilon$ prescription for integration around zero momentum fermions in the corresponding square.) Plugging all the building blocks together, we therefore arrive at

$$\mathcal{W}_{F_{-3} \to \psi\, F_2} \;=\; e^{-3\tau_1 - 3i\phi_1} \times e^{-3\tau_2 + 5/2i\phi_2} \times \tag{4.54}$$

$$\times \int_{\mathbb{R}} \frac{du}{2\pi} \int_{\mathbb{R}} \frac{dv}{2\pi} \int_{\bar{\mathcal{C}}_{\text{small}}} \frac{dw}{2\pi} \frac{w\, \Gamma\left(\frac{5}{2}+iu\right) \Gamma(2-iv)\Gamma\left(\frac{7}{2}-iu+iv\right)}{2i\left(u^2+\frac{9}{4}\right)\left(v^2+1\right)\left((v-w)^2+1\right)} e^{2iu\sigma_1 - 2i(v+w)\sigma_2} + \mathcal{O}\left(g^2\right),$$

and verify that, despite the funny fractional powers of the coupling appearing in the individual ingredients, the resulting integrand has a regular expansion in g^2 and starts at tree level, as expected. (This phenomenon is not accidental and is discussed further in the conclusions of the chapter.)

One of the three integrals involves a small fermion $\psi(w)$ integrated over its corresponding small fermion contour $\bar{\mathcal{C}}_{\text{small}}$. An important universal property of small fermions is that they can always be straightforwardly integrated out (at any value of the coupling in fact). In this tree level example we see that the only singularity inside the half moon encircling the upper half plane is the single pole at $w = v + i$. The fermion integral thus collapses into the corresponding residue contribution which freezes w to be attached to the rapidity v in a Bethe string like pattern. The interpretation of such strings is that the fermion is acting as a symmetry generator on the other excitation in this square, the bound-state of gluons $F_2(v)$. The result of this action is an effective twist 3 weak coupling excitation, see figure 4.7, which is described by the Bethe string.

In sum, after integrating out the small fermion we end up with the integrations in u and v for a single effective particle in each square. The resulting integral can then be straightforwardly performed leading to the prediction

$$\mathcal{W}_{F_{-3} \to \psi\, F_2} = \frac{e^{-3\tau_1 - 3\tau_2 - 3i\phi_1 + 5i\phi_2/2}}{\left(e^{2\sigma_1}+1\right)^3 \left(e^{2\sigma_2}+1\right)^3 \left(e^{2\sigma_2+2\sigma_1} + e^{2\sigma_2} + e^{2\sigma_1}\right)^5} \times \left(e^{13\sigma_1 + 2\sigma_2} + 5\, e^{11\sigma_1 + 4\sigma_2} + 8\, e^{13\sigma_1 + 4\sigma_2}\right.$$

$$+ 10\, e^{9\sigma_1 + 6\sigma_2} + 35\, e^{11\sigma_1 + 6\sigma_2} + 28\, e^{13\sigma_1 + 6\sigma_2} + 10\, e^{7\sigma_1 + 8\sigma_2} + 60\, e^{9\sigma_1 + 8\sigma_2} + 105\, e^{11\sigma_1 + 8\sigma_2}$$

$$+ 56\, e^{13\sigma_1 + 8\sigma_2} + 5\, e^{5\sigma_1 + 10\sigma_2} + 35\, e^{7\sigma_1 + 10\sigma_2} + 105\, e^{9\sigma_1 + 10\sigma_2} + 130\, e^{11\sigma_1 + 10\sigma_2} + 55\, e^{13\sigma_1 + 10\sigma_2}$$

$$\left.+ e^{3\sigma_1 + 12\sigma_2} + 8\, e^{5\sigma_1 + 12\sigma_2} + 28\, e^{7\sigma_1 + 12\sigma_2} + 56\, e^{9\sigma_1 + 12\sigma_2} + 55\, e^{11\sigma_1 + 12\sigma_2} + 20\, e^{13\sigma_1 + 12\sigma_2}\right).$$
$$\tag{4.55}$$

This example clearly illustrates the importance of checking the integrability against perturbative data. After all, it is clearly a tall order to reproduce any result of the complexity of (4.55). According to the proposal in [2], the amplitude $\mathcal{P} \circ \mathcal{P}_{123} \circ \mathcal{P}_4$ can be
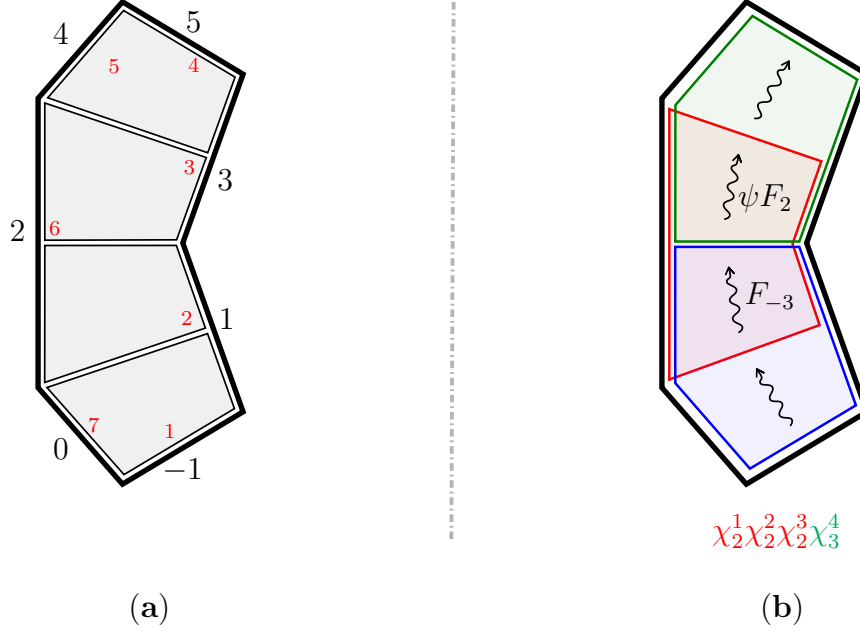
Figure 4.8: (a) The POPE friendly edge labelling used in this chapter (big black outer numbers) versus the more conventional cyclic labelling (small red inner numbers) for the heptagon. (b) The NMHV heptagon process analysed in this section.

extracted from standard η-components as

$$
\left(\frac{\partial}{\partial\chi_2}\right)^3 \frac{\partial}{\partial\chi_3} \mathcal{W} = \frac{(\mathbf{5})_3}{((\mathbf{1})_2(\mathbf{2})_2(\mathbf{3})_2)^3} \left(\langle 1,2,3,-1\rangle \frac{\partial}{\partial\eta_{-1}} + \langle 1,2,3,0\rangle \frac{\partial}{\partial\eta_0}\right)^3 \frac{\partial}{\partial\eta_5} \mathcal{W} \tag{4.56}
$$

$$
= \frac{(\mathbf{5})_3}{((\mathbf{1})_2(\mathbf{2})_2(\mathbf{3})_2)^3} \left(\langle 1,2,3,-1\rangle^3 \, \mathcal{W}^{(-1,-1,-1,5)} + \langle 1,2,3,-1\rangle^2\langle 1,2,3,0\rangle \, \mathcal{W}^{(-1,-1,0,5)} \right.
$$

$$
\left. + \langle 1,2,3,-1\rangle\langle 1,2,3,0\rangle^2 \, \mathcal{W}^{(-1,0,0,5)} + \langle 1,2,3,0\rangle^3 \, \mathcal{W}^{(0,0,0,5)}\right) . \tag{4.57}
$$

Each of these components can be obtained by running similar code lines in Mathematica as in the previous example of the hexagon, using the heptagon twistors in the Appendix A of [22]. Once we evaluate the brackets and the weights, we expand the result at large τ_1 and τ_2 and pick the term proportional to (4.47). In this way we obtain a perfect match with the expression (4.55)!

These are formidable checks of the full POPE construction as they are probing, at the same time, the map between charging pentagons and charging edges of [2] as well as the (weak coupling expansion of) the various elements of the POPE integrand. We performed several other checks of this sort (more than a hundred of them) always obtaining

60

a perfect match. For completeness, we present another example in appendix D. We also explored some higher loop data but our analysis there was much less thorough. It would be interesting to push it much further both in higher twists and higher loops. In particular, it would be nice to make contact with the very interesting recently uncovered heptagon bootstrap [54].

4.4 Discussion

In this chapter we put forward the full coupling dependent part of the POPE integrand. This is an important step towards the completion of the OPE program stated in the beginning.

One of the most amusing features of the POPE which renders it so efficient at weak coupling is that the number of particles contributing at a given loop order grows very slowly with the loop order.

To be precise we should recall the notion of weak coupling *effective particles* and *small fermions*. What happens at weak coupling is that on top of any number of fundamental excitations – that is gluons and their bound-states, scalars and fermions – we can add arbitrarily many so-called small fermions ψ or $\bar{\psi}$ which behave roughly as supersymmetry generators acting on the fundamental excitations and morphing them into what one calls *effective particles*, see figure 4.9. Technically the way this works is that the POPE integrals over the small fermions can always be integrated out explicitly leading to string-like structures attached to the rapidities of the fundamental excitations. These strings are the mathematical depiction of the effective particles.

To estimate the coupling dependence of each POPE process we simply take the POPE integrand (4.2) for a given matter content and look for the leading power of g of each of the factors in the dynamical and form factor part (the matrix part being coupling independent). When doing this we should pay special attention to the fermions as small and large fermion measures, transitions and form factors scale quite differently at weak coupling. At the end of the day, the results we find are remarkably simple. Take the hexagon for instance. We readily find that each OPE process scales as

$$g^{M^2+\left(K-\frac{r_b-r_t}{4}\right)^2-\frac{1}{16}(r_t+r_b)(8-r_t-r_b)}, \tag{4.58}$$

where r_b are the number of χ's in the bottom pentagon and r_t is the number of χ's of the top pentagon. (The fact that $r_t = r_b = 0$ is equivalent to $r_t = r_b = 4$ is the statement that
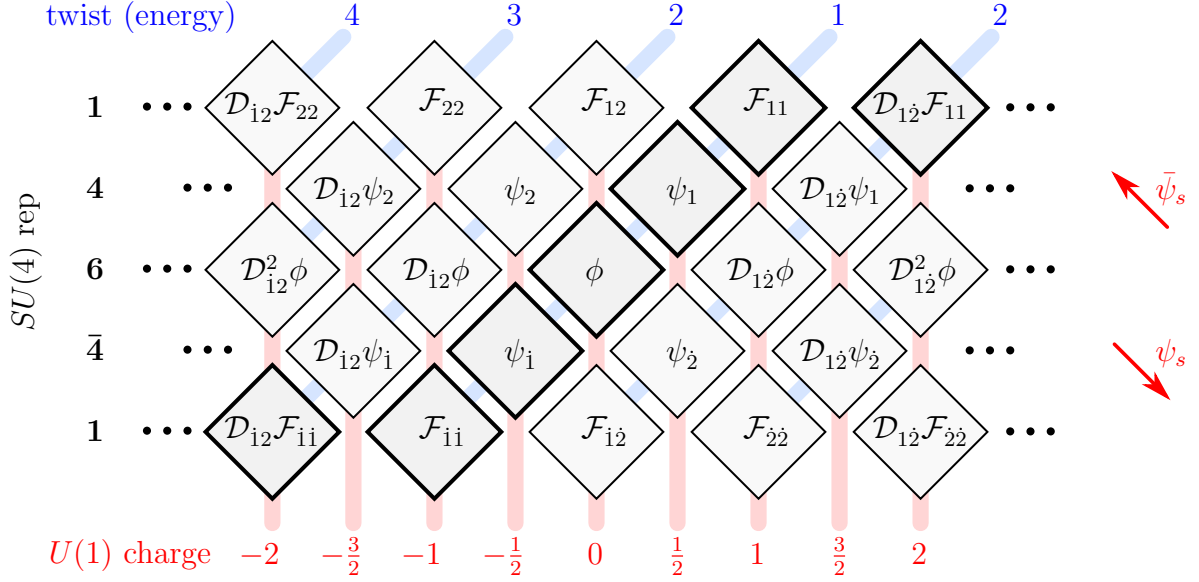
Figure 4.9: Table of weak coupling excitations of the flux tube. The fundamental excitations are sitting on the boldfaced squares with the twist-one excitations on the diagonal and the gluon bound states on the two semi-infinite lines at the top and bottom of the table. Additionally one can generate a plethora of effective particles, by attaching small fermions ψ_s or $\bar{\psi}_s$ to these fundamental excitations, as they act as supersymmetry generators. Besides the excitations represented in this table, one could generate other excitations by attaching both ψ_s and $\bar{\psi}_s$ to a fundamental excitation. This gives rise to a third dimension not represented here, where excitations involving $\mathcal{D}_{2\dot{2}}$ are sitting.

for 6 points MHV and N^{2}MHV are trivially related by parity to one another. For NMHV we have $r_t = 4 - r_b$.) Finally K and M contain the information about the matter content. We have

$$M = N_F + N_\psi + N_\phi + N_{\bar{\psi}} + N_{\bar{F}} \qquad \text{and} \qquad K = N_F + \frac{1}{2}N_\psi - \frac{1}{2}N_{\bar{\psi}} - N_{\bar{F}} - \frac{1}{2}N_{\psi_S} + \frac{1}{2}N_{\bar{\psi}_S}. \tag{4.59}$$

Here N_F ($N_{\bar{F}}$) indicate the total number of gluons of positive (negative) helicity or their bound-states and N_ψ denotes the number of usual (i.e. large) fermions while N_{ψ_S} is the number of small fermions. The exponent in (4.58) is always an even number (which is nothing but twice the number of loops). Let us expand a bit on the physics of (4.58) and (4.59).

We see that M is the total number of excitations except for small fermions. In other words, since the small fermions can always be integrated out to simply change the flavour

of the other excitations, M is nothing but the total number of effective excitations,

$$M = \texttt{number of effective excitations}. \tag{4.60}$$

Take for example a process with 6 effective excitations for the MHV hexagon. From (4.58) we see that it will first show up at eighteen loops (if $K = 0$) or even later (if $K \neq 0$). Up to seven loops, for instance, we shall never need more than 3 effective particles to describe the six point MHV scattering amplitude!

Next we have K which contrary to M can be positive or negative. Consider first a configuration containing only fundamental excitations and no small fermions. Then K is the average of ratios of the $U(1)$ charge to bare twist of each excitation. It is a sort of measure of helicity violation. Equivalently, if we associate a weight of $1 - j/2$ to an excitation in the j-th row in figure 4.9 then K is the average of these weights which we can therefore depict as a vertical centre of mass position of sorts in this figure. This second description is the most convenient one to generalize to the case where we add small fermions to the mix. As indicated by the red arrows in figure 4.9, such small fermions transform the various excitations moving them up or down in this table. With the precise signs in (4.59) we see that the interpretation as the average of rows is perfectly kept when we move to a description purely in terms of effective excitations. In short,

$$K = \texttt{vertical centre of mass of figure 4.9}. \tag{4.61}$$

In sum, OPE processes are coupling suppressed by two effects: large number of particles and large helicity violations.

We see that for a given number of effective particles M the processes that minimize the loop order are those for which $K = \frac{r_b - r_t}{4}$. For the NMHV hexagon this means $K = \frac{r_b - 2}{2}$ which translates into the intuitive statement that the centre of mass position K should coincide with that of the leading order excitation flowing in that hexagon as identified in figure 4.5b. Conversely, for a given number of effective particles M the processes that maximize the loop order are those for which K is as large as possible (positive or negative depending on weather r_b is less or greater than r_t). For MHV, for instance, the processes that maximize $|K|$ are the states containing nothing but gluons. In that case (4.58) reduces to

$$g^{2N_F^2 + 2N_{\bar{F}}^2} \tag{4.62}$$

reproducing the counting in [24], see equation (44) there. As explained in [24], because these states maximize $U(1)$ charge they are very easily identified in perturbation theory by taking a so-called double scaling limit. This sector also appears to be instrumental in

making contact with the hexagon bootstrap program [40–43, 55] as thoroughly explored recently in [56], using technology from [57]. In this regard, it would be interesting to see if the OPE loop thresholds (4.62) parallel some sort of complexity jumps or qualitative changes in the hexagon function representations.

A similar loop counting can be straightforwardly performed for higher n-gons where we find that a given OPE sequence first shows up at g^{2l} with the number of loops l given by

$$
2l = \sum_{i=1}^{n-5} \left[M_i^2 - M_i M_{i+1} + \left(K_i - \frac{r_i - r_{i+1}}{4} \right)^2 - K_i K_{i+1} \right] - \sum_{i=1}^{n-4} \frac{1}{16} r_i \left(8 - r_{i-1} - r_{i+1} \right).
$$

(4.63)

Here M_i and K_i are associated to the i-th middle square and are defined, for a given matter content flowing in that square, exactly as above (4.59).[16] Obviously, the interpretation as (4.60) and (4.61) continues to hold. Similarly, the r_i are the number of χ's in the i-th pentagon with $r_0 \equiv r_1$ for $i = 1$ and $r_{n-3} \equiv r_{n-4}$ for the boundary cases. Note in particular that for heptagons and highers the loop counting is not simply a sum of squares. Now some terms contribute with a minus sign. An interesting outcome of this fact is that with higher n-gons we can often engineer processes with large number of particles at relatively low loop order by considering polygons with many edges and slowly injecting more and more particles and χ's as we move along the tessellation, in the same way as one efficiently starts a car by gently pushing it down a road. The longer the road, and the more help one gets along the way, the easiest it is to start the car. This is often quite useful if one wishes to test higher particle contributions at weak coupling without going to prohibitively high loop orders. Some examples of this enhancement were already discussed in a purely gluonic context in [24]. For instance, we can set all r's to two, start with a scalar in the first square and add one scalar in each square until a maximum halfway through the tessellation where we start decreasing one by one the number of scalars. A simple counting exercise shows that this configuration will first appear at tree-level for any polygon. To give an example, we could check a process involving 4998 scalars in a myriagon already at tree-level!

In [58] the matrix part, the last missing piece in the POPE integrand, is analysed and in [59] the outcome of this analysis is unveiled for the hexagon case. Together with the result herein presented these works flash out the initial proposal in [1] to completion. Nonetheless, in our view, they are not simply the end. Having a fully non-perturbative proposal for scattering amplitudes in a four dimensional gauge theory is very exciting but more exciting still is the perspective of using it to extract sharp physics out of it at weak, strong and finite coupling, thus substantially enlarging our understanding of non-perturbative quantum field theory.

---

[16]The values for M_{n-4} and K_{n-4} should be set to zero.

Chapter 5

Hexagon Resummation

5.1 Introduction

$\mathcal{N} = 4$ Super Yang Mills is a special theory in which the integrability of the planar regime allows us to compute observables at any value of the coupling. Two such observables are the expectation value of null polygonal Wilson loops and scattering amplitudes, which are dual to each other [11–15, 60].

These observables are what the Pentagon Operator Product Expansion (POPE) [1] program studies. This is an expansion around the collinear limit in which the Wilson loop expectation value is given as an infinite sum over flux tube excitations created at the bottom and absorbed at the top of the polygon. The building blocks have been bootstrapped at any value of the coupling and matched against data [2, 3, 22–24, 28, 39, 51] and in [59], the complete POPE series for the hexagon was unveiled.

A natural question to ask is if this expansion can be resummed to reproduce the full kinematical dependence of the amplitude. In general this is not a simple problem since already at tree level we need to sum over an infinite set of excitations. The resummation of the POPE was considered before both at weak and strong coupling. At weak coupling, in [56, 57] a procedure for the resummation of the single particle gluon bound states or double scaling limit was presented whereas at strong coupling in [61, 62] the contribution of gluons and mesons were studied.

However, the POPE weak coupling resummation where the full set of flux tube excitations is taken into account is still pending. This might seem a rather difficult task since we need to sum over the contributions of all possible combinations of gluons, scalars and

fermions. The way out is that we can reorganize the excitations into effective particles. As was put forward in [3] the number of effective particles needed to reproduce an amplitude grows very slowly with loop order. In fact, to compute the six point amplitude at tree level and one loop only states with one effective particle are needed.

The one effective particle states are formed by one fundamental excitation –could be a gluon bound state, a scalar or a large fermion– and an arbitrary number of small fermions (antifermions) which are then integrated out. As we shall see, the fundamental excitation and the small fermions are organized in Bethe strings which allows us to perform the integrations straightforwardly. Since the string patterns are derived from the matrix part of the POPE integrand which is coupling independent, we use these results to compute the one effective particle measures at finite coupling. We later evaluate these measures at tree level and sum over all one effective particle states to get a rational function which reproduces the 6 point tree level amplitude for *general kinematics*. In the end, the tree level resummation turns out to be very simple.

The chapter is organized as follows. In section 5.2 we first review the hexagon POPE building blocks and consider the one effective particle states, presenting their measures at finite coupling. In section 5.3 we evaluate these measures at tree level and perform the resummation. In the same section we explain how this result reproduces the NMHV 6 point amplitude at tree level. We conclude with some final remarks.

5.2 Hexagon POPE and one effective particle states

Let us first recall the results spelled out in [59] that provide the building blocks for our derivation. The hexagon Wilson loop we want to compute is given as a sum over all possible flux tube excitations parametrized by rapidities u_i

$$\mathcal{W}_6 = \raisebox{-1em}{} = \sum_m \frac{1}{S_m} \int \frac{du_1 \dots du_m}{(2\pi)^m} \, \Pi_{\text{dyn}} \times \Pi_{\text{FF}} \times \Pi_{\text{mat}} \,, \tag{5.1}$$

where S_m is a symmetry factor. The integrand is nicely factored out into a *dynamical* and *form factor* parts which carry the coupling dependence and a *matrix* factor which takes

66
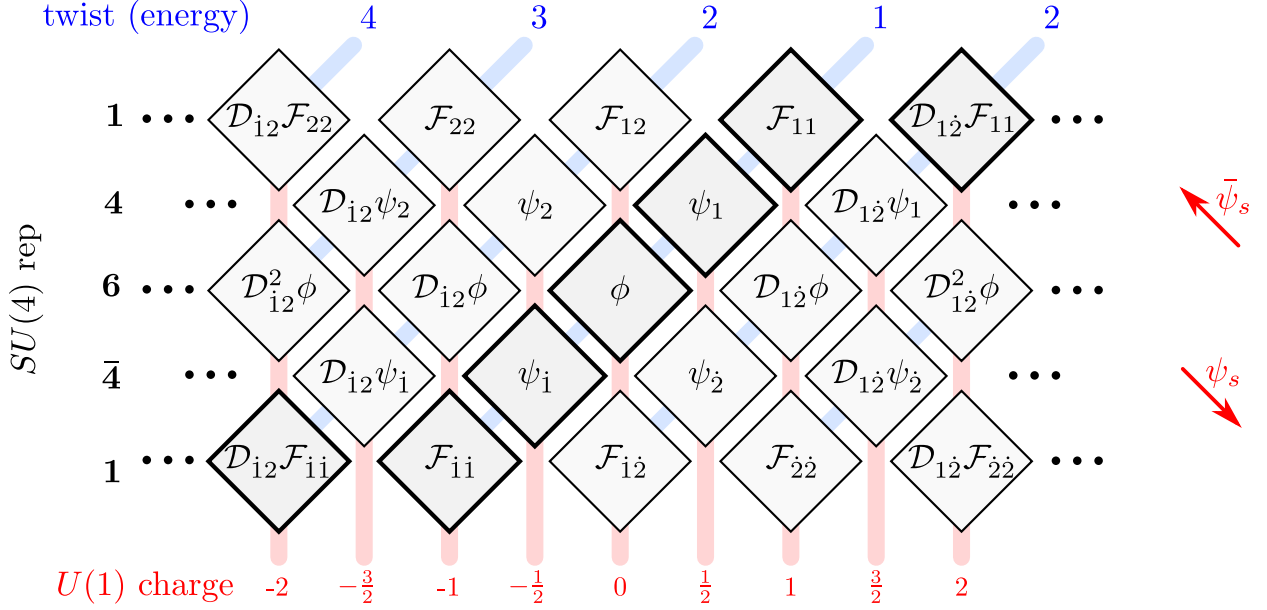
Figure 5.1: Table of effective weak coupling excitations presented in [3, 23]. The fundamental excitations are in the bold squares. The effective particles can be formed by adding small fermions or antifermions.

care of the R-symmetry structure of the theory. The first factor is universal and reads

$$\Pi_{\text{dyn}} = \prod_i \mu(u_i) e^{-E(u_i)\tau + ip(u_i)\sigma + im_i\phi} \times \prod_{i<j} \frac{1}{|P(u_i|u_j)|^2} \, , \tag{5.2}$$

where $\{\tau, \sigma, \phi\}$ are respectively the flux tube time, space and angle (related to the three conformal cross ratios of the hexagon); $E(u_i)$, $p(u_i)$ and m_i are the energy, momentum and angular momentum of the excitation; $P(u_i|u_j)$ are the pentagon transitions between different excitations and $\mu(u_i)$ the corresponding measures. We will often use the notation $\hat{\mu}(u) = \mu(u) e^{-E(u)\tau + ip(u)\sigma + im\phi}$. The fundamental flux tube excitations are gluon bound states, fermion, antifermion and scalar: $\{F_b, \psi, \bar{\psi}, \phi\}$. They are represented in the bold squares of figure 5.1.

The next factor in the POPE integrand is non trivial only for Next to Maximally Helicity Violating (NMHV) hexagons (i.e. charged pentagons) and is given by

$$\Pi_{\text{FF}} = g^{\frac{1}{8}r_1(r_1-4)+\frac{1}{8}r_2(r_2-4)} \times \prod_i h(u_i)^{r_2-r_1} \, , \tag{5.3}$$

67

where r_i is the R-charge in the i-th pentagon and $h(u_i)$ are the so called *form factors* derived in [3]. The last factor is the matrix part which takes into account the contraction of the SU(4) R-symmetry indices of each pentagon. It has the following form

$$
\begin{aligned}
\Pi_{\text{mat}} \;=\;& \frac{1}{K_1! K_2! K_3!} \int \prod_{i=1}^{K_1} \frac{dw_i^1}{2\pi} \prod_{i=1}^{K_2} \frac{dw_i^2}{2\pi} \prod_{i=1}^{K_3} \frac{dw_i^3}{2\pi} \times \\
& \times \frac{g(\mathbf{w}^1) g(\mathbf{w}^2) g(\mathbf{w}^3)}{f(\mathbf{w}^1, \mathbf{w}^2) f(\mathbf{w}^2, \mathbf{w}^3) f(\mathbf{w}^1, \mathbf{v}) f(\mathbf{w}^2, \mathbf{s}) f(\mathbf{w}^3, \bar{\mathbf{v}})} \ ,
\end{aligned}
\tag{5.4}
$$

where w_i are auxiliary roots of three different types and $\{v_i, s_i, \bar{v}_i\}$ are rapidities for fermions, scalars and antifermions, respectively; the functions $g(\mathbf{w}) = \prod_{i<j}(w_i - w_j)^2[(w_i - w_j)^2 + 1]$, $f(\mathbf{w}, \mathbf{v}) = \prod_{i,j}[(w_i - v_j)^2 + \frac{1}{4}]$ and the number of auxiliary rapidities K_j are the solution to the equations

$$
\begin{aligned}
N_\psi - 2K_1 + K_2 &= \delta_{r_1,3} \ , \\
N_\phi + K_1 - 2K_2 + K_3 &= \delta_{r_1,2} \ , \\
N_{\bar\psi} + K_2 - 2K_3 &= \delta_{r_1,1} \ ,
\end{aligned}
\tag{5.5}
$$

where N_ψ, N_ϕ and $N_{\bar\psi}$ are respectively the number of fermions, scalars and antifermions.

Together with the pentagon transitions, form factors and energies presented in [3, 22], these expressions are all the necessary ingredients to compute the hexagon Wilson loop as a series in the collinear limit. From them we shall derive the one effective particle measures that we later resum at tree level.

As we shall be working mostly with NHMV amplitudes, let us review some useful notation. The hexagon super Wilson loop can be decomposed into POPE components $P^{[r_1]} P^{[r_2]}$, where r_i is the total R-charge in the i-th pentagon and it takes values $0 \leq r_i \leq 4$. For N^kMHV components we have that $\sum_i r_i = 4k$. Therefore the hexagon NMHV $(r_1 + r_2 = 4)$ has five different POPE components. Depending on which POPE component we are considering, there is a subset of allowed excitations determined by the representation of the SU(4) R-symmetry in which the state transforms. For instance, for the NMHV component $P^{[2]} P^{[2]}$ we could have the excitations: ϕ, $\bar\psi\bar\psi$, $\psi\psi F_a$, etc.

The fermionic excitations have the important feature that they can be separated into *large* and *small fermions*. This is because in terms of the Bethe rapidity the fermion integration contour involves two different Riemann sheets, one in which the fermions have large momenta and another one in which their momenta is small [23]. The integration contour can be split into two so that each new contour lives only in one of the two Riemann sheets, as figure 5.2 shows.
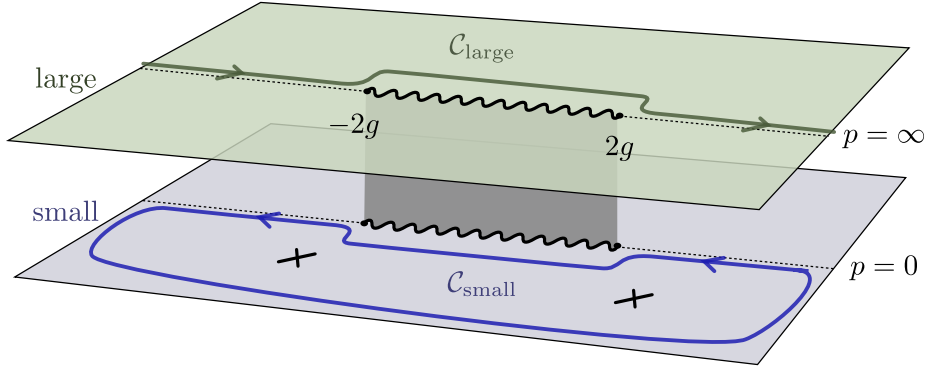
68

Figure 5.2: The fermion contour of integration in terms of the rapidity u involves a Riemann surface with two sheets –one in which the momenta is large and another one in which it is small– connected by a branch cut between $u = -2g$ and $u = 2g$. The original contour in [23] can be split into two different contours $\mathcal{C}_{\text{large}}$ and $\mathcal{C}_{\text{small}}$, each one on a different sheet. The small fermion contour $\mathcal{C}_{\text{small}}$ might enclose poles coming from interactions with other excitations.

In the small sheet there are potential poles enclosed by the contour $\mathcal{C}_{\text{small}}$. These would come from the interaction of the small fermions with other excitations. When attached to another particle, the small fermions ψ_s act as supersymmetry generators [48] and create a sea of effective excitations, some of which are shown in figure 5.1. We can also add an arbitrary number of pairs of small fermion-antifermion $\psi_s \bar{\psi}_s$ (or derivatives D_+), creating the so called *descendants* depicted in figure 5.3. The name is because, as explained in [26,63,64], at weak coupling there is an enhancement of symmetry from SU(4) to SL(2|4) and the flux tube excitations can be packed in SL(2) conformal blocks. The primaries correspond to the excitations in the plane presented in figure 5.1, obtained by the action of small fermions or antifermions. On the other hand, the descendants correspond to the excitations in the vertical direction in figure 5.3 obtained by the action of pairs of small fermion-antifermion $\psi_s \bar{\psi}_s$. Although this symmetry is exact only up to one loop, we will keep the terminology for the finite coupling discussion.

In sum, we can distinguish an effective excitation by its position on the three dimensional space shown in figure 5.3. The three parameters are: the helicity of the excitation a, its number of descendants n and the SU(4) R-symmetry representation in which it transforms $\hat{r}$ (distinguishing between the two sets of singlet excitations shown in the first and last row of figure 5.1). As we explain in the following sections, to perform the tree level resummation we fix the SU(4) representation and sum the measures of the effective particles over a (from $-\infty$ to ∞) and over n (from 0 to ∞).
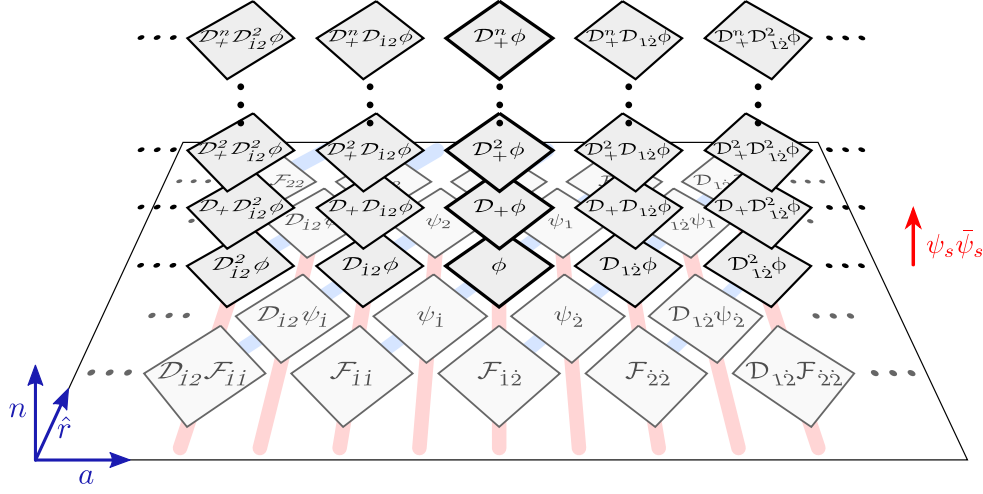
Figure 5.3: Table of effective weak coupling excitations including the first n descendants of the particles transforming in the vector representation of SU(4). The plane in the bottom contains the primary excitations depicted in figure 5.1. A descendant is formed by acting with a pair $\psi_s \bar{\psi}_s$ (or derivative D_+) on one of these excitations. Moving away from this plane in the vertical direction corresponds to adding more descendants. An effective excitation is characterized by its helicity a, the SU(4) R-symmetry representation labelled by $\hat{r}$ and its number of descendants n.

One effective particle states

A one effective particle Φ is formed by one fundamental excitation –referred to in the following as Φ_0– and an arbitrary number N_{ψ_s} ($N_{\bar{\psi}_s}$) of small fermions (antifermions) that are integrated out. Higher number of effective particles include more than one fundamental excitation. In terms of effective excitations, a POPE hexagon component reads

$$P^{[r_1]} P^{[r_2]} = \sum_{\Phi} \int \frac{du}{2\pi} e^{-E_\Phi(u)\tau + ip_\Phi(u)\sigma + im_\Phi \phi} \mu_\Phi^{[r_1,r_2]}(u) + \dots \,, \qquad (5.6)$$

where the dots account for higher effective particles and we have adopted the notation $\mu_\Phi^{[r_1,r_2]}(u) \equiv \left[g^{\frac{1}{8}r_1(r_1-4)+\frac{1}{8}r_2(r_2-4)} h_\Phi(u)^{r_2-r_1} \right] \mu_\Phi(u)$. The effective measures μ_Φ will be given by an expression of the sort

$$\mu_\Phi = \int_{\mathcal{C}_{\text{small}}} \frac{dv_1 d\bar{v}_1 \dots}{(2\pi)^{N_{\psi_s}+N_{\bar{\psi}_s}}} \Pi_{\text{dyn}}(\Phi_0 \psi_s^{N_{\psi_s}} \bar{\psi}_s^{N_{\bar{\psi}_s}}) \, \Pi_{\text{FF}}(\Phi_0 \psi_s^{N_{\psi_s}} \bar{\psi}_s^{N_{\bar{\psi}_s}}) \, \Pi_{\text{mat}}(\Phi_0 \psi_s^{N_{\psi_s}} \bar{\psi}_s^{N_{\bar{\psi}_s}}) \,, \quad (5.7)$$

where v_i ($\bar{v}_i$) are the rapidities of the small fermions (antifermions) and $\mathcal{C}_{\text{small}}$ is the small fermion contour shown in figure 5.2.

70

One advantage of this approach is that the amount of effective particles needed to fully reproduce a scattering amplitude at a given perturbative order grows very slowly with the loop order. For instance, one effective particle states are sufficient to reproduce amplitudes at tree level and one loop, states with two effective particles are enough up to five (four) loops for MHV (NMHV) amplitudes, etc [3]. Moreover, having a compact formula for effective particles with arbitrary number N_{ψ_s} $(N_{\bar{\psi}_s})$ of small fermions represents a huge simplification for the starting point of the resummation. In the following we describe the combinatorics involved in the small fermion integrations, the reader might want to skip this discussion and jump to the next section.

The small fermion integrations in (5.7) can be carried out straightforwardly by residues. The relevant poles between different rapidities arise from the matrix part[1]. Since this part of the integrand is coupling independent, the structure of poles will be the same at any value of the coupling. Although taking residues might be trivial, we need to do so for an arbitrary number of integration variables (remember we can add infinite pairs $\psi_s\bar{\psi}_s$). As we explain in the following, instead of taking all the possible residues we can find a pattern in which the small fermions attach to the fundamental excitation forming a Bethe string. Then we would only need to multiply by an appropriate combinatoric factor. Computing the integrals in this way is much more efficient and in practice it is the only way to account for a very large number of small fermions and auxiliary rapidities.

Let us explain how the structure of these strings arises with a simple example. Consider a scalar excitation and its descendants $\phi(\psi_s\bar{\psi}_s)^n$ which contribute to the POPE component $P^{[2]}P^{[2]}$. These are the excitations in the tower at the center of figure 5.3. We want to find the pattern in which the small fermions and antifermions attach to the scalar.

For $n = 0$ the matrix part is trivial so that we have only the scalar measure $\mu_\phi(u)$. For $n = 1$, the effective measure (multiplied by the corresponding square propagation factor) is given by

$$\hat{\mu}_{\phi\psi_s\bar{\psi}_s}(u) = \int\limits_{\mathcal{C}_{\text{small}}} \frac{dv_1\,d\bar{v}_1}{(2\pi)^2} \frac{\hat{\mu}_\phi(u)\hat{\mu}_{\psi_s}(v_1)\hat{\mu}_{\bar{\psi}_s}(\bar{v}_1)}{|P_{\phi|\psi_s}(u|v_1)|^2\,|P_{\phi|\bar{\psi}_s}(u|\bar{v}_1)|^2\,|P_{\psi_s|\bar{\psi}_s}(v_1|\bar{v}_1)|^2} \times \frac{1}{g} \times \Pi_{\text{mat}}(\phi\psi_s\bar{\psi}_s)\,,$$

(5.8)

where $1/g$ is the form factor contribution. Since the matrix part is what determines the poles, let us write it explicitly. According to (5.5), we have one auxiliary root of each type

[1]Here we redefine the pentagon transition between small fermion and gluon bound state in the following way $P_{F_b|\psi_s}(u|v)_{\text{here}} = (u - v + ia/2)^{-1}P_{F_b|\psi_s}(u|v)$ [3] so that the factor $(u - v + ia/2)^{-1}$ is part of the matrix part and the statement is indeed true for all flux tube excitations.

which leads to

$$\Pi_{\text{mat}}(\phi\psi_s\bar{\psi}_s) = \int_{\mathbb{R}} \frac{dw_1^1 dw_1^2 dw_1^3}{(2\pi)^3} \frac{1}{f(w_1^1,w_1^2)f(w_1^2,w_1^3)f(w_1^1,v_1)f(w_1^2,u)f(w_1^3,\bar{v}_1)} \,, \quad (5.9)$$

$$= \frac{6v_1^2 + 4u^2 + 6\bar{v}_1^2 - 4u\bar{v}_1 - 4uv_1 - 8v_1\bar{v}_1 + 45}{\left((u-v_1)^2 + \frac{9}{4}\right)\left((u-\bar{v}_1)^2 + \frac{9}{4}\right)\left((v_1-\bar{v}_1)^2 + 4\right)} \,, \quad (5.10)$$

where $f(u,v) = (u-v)^2 + 1/4$ as before. Next we would replace this factor in (5.8) and integrate over v_1, $\bar{v}_1$. The integration contour $\mathcal{C}_{\text{small}}$ is the half moon in the lower half of the complex plane shown in figure 5.2. This means that the poles that we are going to pick are $v_1 = u - 3/2i$ and $\bar{v}_1 = u - 3/2i$. In other words, we find that the Bethe string is formed by a scalar with rapidity u and a small fermion and antifermion both attached at a distance $3/2i$ below it. As we shall see, it is convenient to think of the small fermions as auxiliary roots and obtain the same string skipping the intermediate step (5.10). In this way we can perform all the integrations in (5.8) (over small fermions and auxiliary roots) by studying the structure of the poles in the matrix part (5.9) and finding a pattern in which we take the residues.

Let us see how we find the same string in this manner. Each function $f(v,u)$ in (5.9) gives two poles: one at $v = u - i/2$ and another one at $v = u + i/2$. Since we know that the small fermion rapidities should be evaluated in the lower half of the complex plane, we shall take the residues at the poles with negative imaginary part. Starting with the auxiliary root w_1^2 we take the residue at $w_1^2 = u - i/2$. After that, the denominator in (5.9) becomes $f(w_1^1, u - i/2)f(u - i/2, w_1^3)f(w_1^1, v_1)f(w_1^3, \bar{v}_1)$ so next we take the residues at $w_1^1 = u - i$ and $w_1^3 = u - i$ (here the order does not matter). That leaves us with the product $f(u-i,v_1)f(u-i,\bar{v}_1)$ and the residues at $v_1 = u - i3/2$, $\bar{v}_1 = u - i3/2$ which give us the same string as before. This pattern in which we take the residues can be represented by the following picture
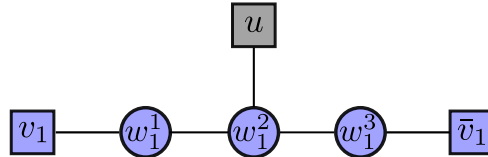
where the top node in gray corresponds to the scalar with rapidity u, the square node in the left (right) represents the small fermion (antifermion) and the circular nodes the auxiliary roots[2]. We start by integrating out the node closer to the fundamental excitation, in this

---

[2]Note that in the previous pattern we can identify the line with the blue nodes with the Dynkin diagram of SL(2|4).

case w_1^2. The residues are taken at positions $u - i\#/2$, where $\#$ is the number of line segments between the fundamental node and the one we are integrating out.

Now we pass to the next descendant $n = 2$. If we compute the matrix part as in (5.10) we would find the problem that simplifying the sum over residues is not trivial and that the result has a numerator with a one page long polynomial which we omit here. We can avoid this intermediate complication by finding a pattern in which we can take the residues as we did for $n = 1$. The integrand of the matrix part is proportional to

$$\Pi_{\text{mat}}^{(\text{int})}[\phi(\psi_s \bar{\psi}_s)^2] \propto \frac{g(\mathbf{w}^1)g(\mathbf{w}^2)g(\mathbf{w}^3)}{f(\mathbf{w}^1, \mathbf{w}^2)f(\mathbf{w}^2, \mathbf{w}^3)f(\mathbf{w}^1, \mathbf{v})f(\mathbf{w}^2, u)f(\mathbf{w}^3, \bar{\mathbf{v}})}, \tag{5.11}$$

where now each set of small fermions and auxiliary rapidities has two elements. Note that (5.11) includes the matrix part integrand for $n = 1$. If we start integrating out the first half of the rapidities $\{w_1^2, w_1^1, w_1^3, v_1, \bar{v}_1\}$ following the pattern derived for $n = 1$ we find that the pattern for $n = 2$ is
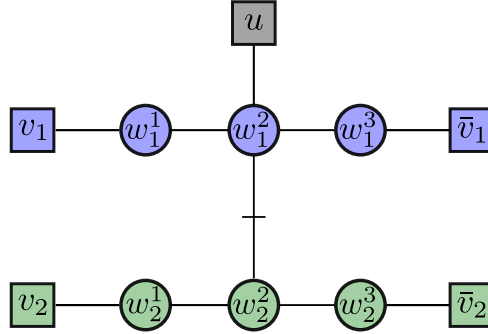
where the rows in blue and green are separated by i. This means that the residues for the second half of the rapidities are evaluated at $\{w_2^2 = u - i3/2, w_2^1 = u - i2, w_2^3 = u - i2, v_2 = u - i5/2, \bar{v}_2 = u - i5/2\}$. The Bethe string is then formed by the scalar with rapidity u, one small fermion and antifermion at $u - i3/2$ and another pair of small fermion and antifermion at $u - i5/2$. This string is depicted in the third column of figure 5.4.

However, this time we could have used different rapidities provided that they belong to the same set (e.g. take first the residue in w_2^2 instead of w_1^2). In other words, we can make a permutation of nodes in a given set without altering the outcome. Therefore we need to multiply the result by a combinatoric factor, which in this case is $(2!)^5$ (we have five sets with two rapidities each).

The generalization of these patterns to higher descendants is straightforward. From (5.5) we see that for each new pair of $(\psi_s \bar{\psi}_s)$ we have one more auxiliary root of each type.

73
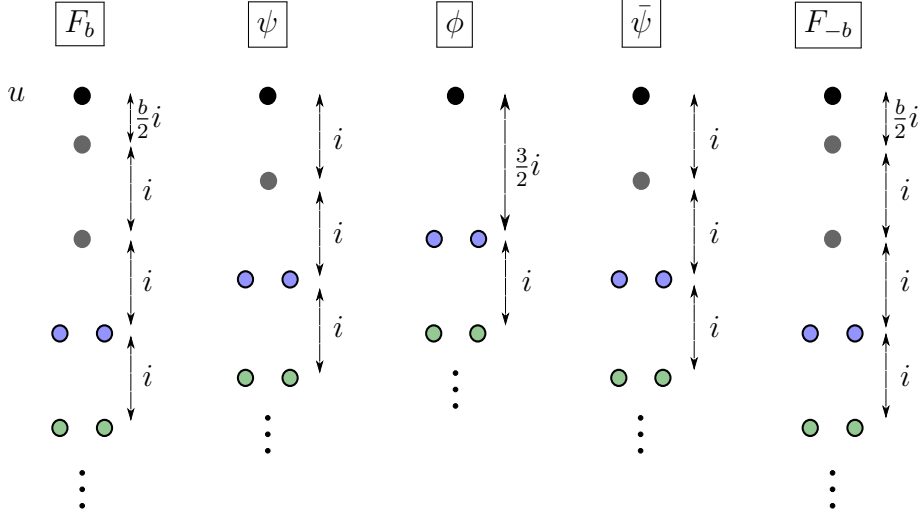
Figure 5.4: String patterns in which the small fermions attach for excitations in the vector representation of SU(4). These are the excitations appearing in the POPE component $P^{[2]}P^{[2]}$. The box at the top of each column labels the fundamental excitation to which the small fermions attach. In black, the fundamental excitation with rapidity u; in gray, the small fermions (antifermions) needed to have an excitation transforming in this representation. In blue (green) the first (second) pair of n descendants $(\psi_s \bar{\psi}_s)$. The arrows show the separation between the different excitations in the rapidity plane. As we can see, the patterns are symmetric between positive and negative helicity states.

Then all we need to do is to add another row of nodes separated by i to the previous one. From this pattern we can easily see the structure of the Bethe string: the first pair ($n = 1$) of small fermion-antifermion attaches to the scalar $3/2i$ below it, for the next pair the separation is $5/2i$ and for the following pairs we keep adding i.

For other fundamental excitations we can derive similar patterns. In appendix E we explore other examples and give more details on the general structure of these patterns. A general feature is that the separation between small fermions is always i, so to know the Bethe strings the only piece of information we need is the separation between the fundamental excitation and the first small fermion and antifermion. That is, if the fundamental excitation has a rapidity u, the first small fermion (antifermion) that is attached will be evaluated at a rapidity $u - i\xi_{1(2)}$, where $\xi_{1(2)}$ varies depending on the fundamental

fundamental/antifundamental

F_b/F_{-b} $\psi/\bar\psi$ ϕ $\bar\psi/\psi$ F_{-b}/F_b
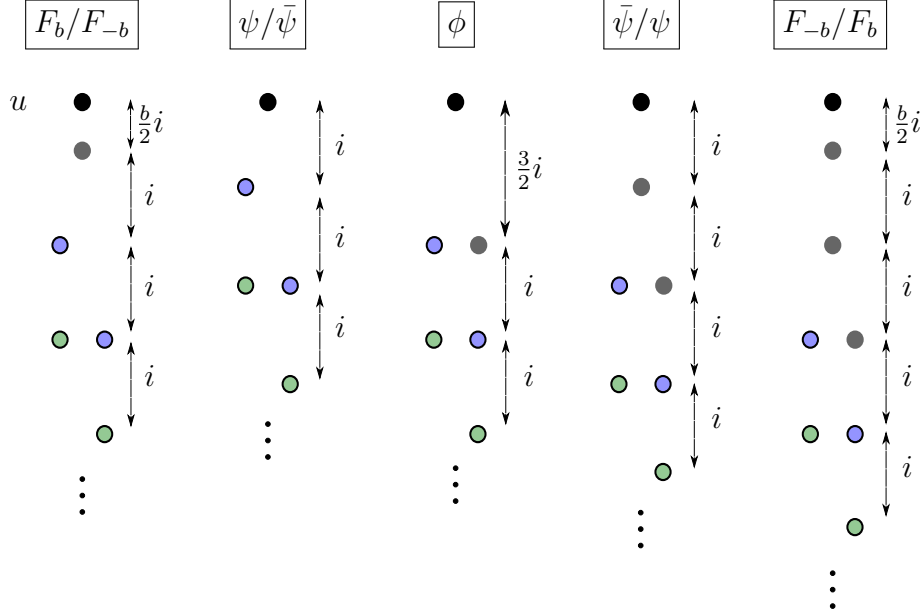
Figure 5.5: String patterns in which the small fermions attach to form an effective excitation transforming in the fundamental representation of SU(4). These are the patterns needed for the POPE component $P^{[3]}P^{[1]}/P^{[1]}P^{[3]}$. The notation is the same as in Figure 5.4. In this case the fermion and antifermion forming a descendant do not attach at the same distance from the fundamental excitation, but are shifted by i.

excitation. For instance, for a scalar we have $\xi_1 = \xi_2 = 3/2$, for a fermion we would find $\xi_1 = 1$, $\xi_2 = 2$, for a positive helicity b gluon bound state $\xi_1 = |b|/2$, $\xi_2 = |b|/2 + 2$ and similarly for the conjugate excitations. The strings for excitations in a given representation of the R-symmetry group are presented in figures 5.4-5.6. Notice that the only difference between the different representations is that the small fermions (or antifermions) close to the top can be either part of the primary excitation (gray) or a descendant (blue/green).

Now that we know how the strings of small fermions form we can compute the energy, momentum and angular momentum of the effective excitation. They are simply given by the sum of the individual pieces evaluated at the corresponding rapidities in the Bethe string. For instance, for the state $\phi\psi_s\bar\psi_s$ studied above we obtain $E_{\phi\psi_s\bar\psi_s}(u) = E_\phi(u) + E_{\psi_s}(u - 3/2i) + E_{\bar\psi_s}(u - 3/2i)$.

singlet

F_b/F_{-b} $\psi/\bar\psi$ ϕ $\bar\psi/\psi$ F_{-b}/F_b
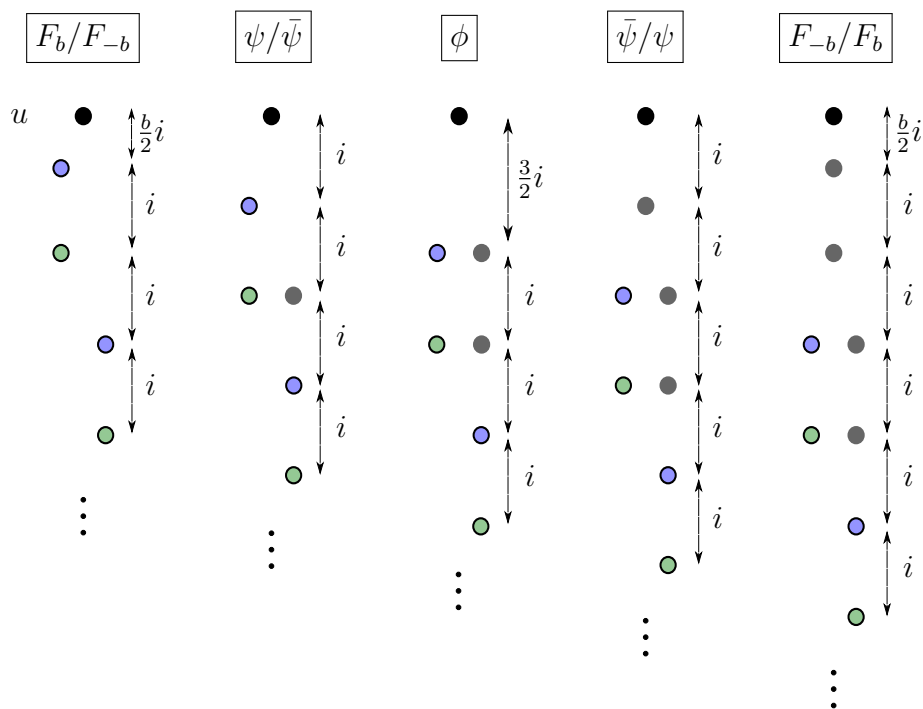
Figure 5.6: String patterns for excitations transforming in the singlet representation of SU(4). The notation is the same as in Figure 5.4. The first (second) excitation in each box refers to the pattern appearing at tree level for the POPE component $P^{[4]}P^{[0]}$ ($P^{[0]}P^{[4]}$). For the MHV ($\overline{\text{MHV}}$) case $P^{[0]}P^{[0]}(P^{[4]}P^{[4]})$ all excitations appear first at one loop.

Similarly (although the calculation is a bit more involved), we can compute the one effective particle measure $\mu_\Phi^{[r_1,r_2]}(u)$. It has the same universal structure as the one for a fundamental particle and reads

$$\mu_\Phi^{[r_1,r_2]}(u) = \left[g^{\frac{1}{8}r_1(r_1-4)+\frac{1}{8}r_2(r_2-4)}\, h_\Phi(u)^{r_2-r_1} \right] \frac{M_\Phi(u)}{f_{\Phi_0}(u)f_{\Phi_0}(-u)}\, \mathsf{exp}_\Phi(u)\,, \tag{5.12}$$

where the functions $f_X(u)$ are given in appendix A of [3] [3]. The exponential part is given by

$$\mathsf{exp}_\Phi(u) \;=\; \exp\left[-2\kappa_\Phi(u)^t \cdot \mathcal{M} \cdot \kappa_\Phi(u) + 2\tilde\kappa_\Phi(u)^t \cdot \mathcal{M} \cdot \tilde\kappa_\Phi(u)\right]\,, \tag{5.13}$$

[3] For small fermions we have $f_{\psi_s(\bar\psi_s)}(u) = 1$, hence only f_{Φ_0} appears in (5.12).

with

$$\kappa_\Phi(u) = \kappa_{\Phi_0}(u) + \sum_{k=1}^{N_{\psi_s}} \kappa_{\psi_s}(u - i(\xi_1 + k - 1)) + \sum_{k=1}^{N_{\bar\psi_s}} \kappa_{\bar\psi_s}(u - i(\xi_2 + k - 1)), \qquad (5.14)$$

and similarly for $\tilde\kappa_\Phi(u)$, where $\xi_{1(2)}$ label the position at which the first small fermion (antifermion) attaches to the fundamental excitation as above. The vectors κ_X and matrix $\mathcal{M}$ are given in appendix C of [23]. The form of this vector is reminiscent of the one for gluons after fusion [24].

The factor in square brackets in (5.12) is present only for NMHV amplitudes. The form factor $h_\Phi(u)$ can be computed straightforwardly and reads

$$h_\Phi(u) = h_{\Phi_0}(u) \left[\prod_{k=1}^{N_{\psi_s}} h_{\psi_s}(u - i(\xi_1 + k - 1)) \right] \left[\prod_{k=1}^{N_{\bar\psi_s}} h_{\bar\psi_s}(u - i(\xi_2 + k - 1)) \right]. \qquad (5.15)$$

Because the form factors satisfy $h_{\bar\Phi}(u) h_\Phi(u) = 1$, in general there will be many cancellations. For instance, for the component $P^{[2]} P^{[2]}$ all the individual form factors exactly cancel. For other components only some of the first and last small fermions/antifermions contribute to the form factor (this can be seen straightforwardly in Figures 5.4-5.6 since there are pairs of fermion-antifermion with the same rapidity).

The prefactor $M_\Phi(u)$ is obtained from the product of different prefactors $F_{X|Y}(u,v)$ contained in the pentagon transitions between the various components of the effective particle. The explicit formulas for $M_\Phi(u)$ are presented in appendix F. These are the relevant functions at weak coupling that we shall use in the next section to resum the full series and reproduce the six point tree level amplitude.

5.3   Tree level resummation

In the previous section we found that the small fermions attach to a fundamental excitation in simple patterns that are easy to generalize for any number of pairs $(\psi_s \bar\psi_s)^n$ (see figures 5.4-5.6). With this information we computed the one effective particle measures and form factors.

As the counting in [3] shows, the effective one particle states are sufficient to reproduce the full amplitude up to one loop. Here we will focus on the tree level NMHV amplitude, so from now on we will assume that the POPE component $P^{[r_1]} P^{[r_2]}$ has $r_1 + r_2 = 4$.

As one might expect, several simplifications occur at tree level. Let us look first at the square propagation factor in (5.6). The total angular momentum is given by the helicity of the effective particle on the plane. The individual energies can be set to one, so that the total tree level energy is the twist of the effective excitation. Finally, since the small fermion momentum starts at one loop, the total momentum is given by the large excitation which has $p = 2u + \mathcal{O}(g^2)$. To be clear, let us write explicitly these factors for the POPE component $P^{[2]}P^{[2]}$. The relevant excitations transform in the vector representation of $SU(4)$ and are shown in figure 5.3. The POPE component reads

$$P^{[2]}P^{[2]} = \sum_{n=0}^{\infty} \int \frac{du}{2\pi} e^{i2u\sigma} \left[e^{-(1+2n)\tau} \mu^{[2,2]}_{\phi(\psi_s\bar{\psi}_s)^n}(u) + e^{-(2+2n)\tau+i\phi} \mu^{[2,2]}_{\psi\psi_s(\psi_s\bar{\psi}_s)^n}(u) + \ldots \right] + \mathcal{O}(g^2),$$

(5.16)

where the measures are evaluated at tree level and the dots represent the contribution of the remaining one effective particle states in the vector representation.

The effective measures –combined with the corresponding form factors– are also simplified at tree level. In fact we can easily pack all of them into a single formula where, given the R-charge of the pentagons, we vary the helicity and number of descendants. Here we see explicitly that to describe the possible effective excitations we need to move in the three dimensional space shown in figure 5.3. The NMHV measures read

$$\mu^{[r_1,r_2]}_{a,n}(u) = \frac{(-1)^{a-\hat{r}/2}\Gamma\left(\frac{|a|}{2} - iu - \frac{\hat{r}}{4}\right)\Gamma\left(\frac{|a|}{2} + iu + \frac{3\hat{r}}{4}\right)}{\Gamma(n+1)\Gamma\left(|a| + \frac{\hat{r}}{2} + n\right)}(-1)^n (iu + \alpha_+)_n (iu + \alpha_-)_n + \mathcal{O}(g^2),$$

(5.17)

where $\hat{r} = r_1(r_2)$ if the excitation has negative (positive) helicity (e.g. for $[r_1, r_2] = [3, 1]$ we would have $\hat{r} = 1$ for the excitation ψ and $\hat{r} = 3$ for $\phi\bar{\psi}_s$), $\alpha_\pm = 1 + \frac{|a|}{2} + \frac{\hat{r}}{4} \pm \frac{|r_1-r_2|}{4}$ and $(x)_n$ is the Pochhammer symbol.

Finally, to obtain the tree level NMHV component $P^{[r_1]}P^{[r_2]}$ we simply sum over all possible values of a and n. The result is quite simple and reads

$$P^{[r_1]}P^{[r_2]} = \delta_{|r_1-r_2|,4} + \sum_{a,n} \int \frac{du}{2\pi} e^{-(|a|+\hat{r}/2+2n)\tau+2iu\sigma+ia\phi} \mu^{[r_1,r_2]}_{a,n} + \mathcal{O}(g^2),$$

(5.18)

where $\delta_{|r_1-r_2|,4}$ accounts for the vacuum contribution if the excitations allowed are in the singlet representation of $SU(4)$. The sum in a is over the integers or half integers depending on the component we are considering.

From (5.17) and (5.18) we can see explicitly how parity symmetry works. Given our definition of $\hat{r}$, the transformation $r_j \to 4 - r_j$ is equivalent to the replacement $\phi \to -\phi$

up to an overall sign [4]. This is nothing but the equivalence between NMHV and $\overline{\text{NMHV}}$ for the six point amplitude.

To reproduce the POPE component we now need to perform the sums over a and n and the momentum integral, which is what we turn to next.

Sum over descendants and momentum integral

The sum over descendants in (5.18) can be carried out trivially, giving a hypergeometric function

$$P^{[r_1]}P^{[r_2]} = \delta_{|r_1-r_2|,4} +$$

$$\sum_a \int \frac{du}{2\pi} e^{-(|a|+\hat{r}/2)\tau+2iu\sigma+ia\phi} \frac{(-1)^{a-\hat{r}/2}\Gamma\left(\frac{|a|}{2}-iu-\frac{\hat{r}}{4}\right)\Gamma\left(\frac{|a|}{2}+iu+\frac{3\hat{r}}{4}\right)}{\Gamma(|a|+\frac{\hat{r}}{2})} \times \quad (5.19)$$

$$\times {}_2F_1\left(\frac{|a|}{2}+iu+\frac{\hat{r}}{4}+1-\frac{r_{12}}{4}, \frac{|a|}{2}+iu+\frac{\hat{r}}{4}+1+\frac{r_{12}}{4}; |a|+\frac{\hat{r}}{2}; -e^{-2\tau}\right) + \mathcal{O}(g^2)\,.$$

This is indeed to be expected since at this perturbative order the $SL(2)$ conformal symmetry is unbroken[5]. The trick to perform the momentum integral is to trade the sum over descendants n for an integral in a parameter t: $\sum_n \to \int_0^1 dt$, or in other words, use an integral representation for the hypergeometric function. With this replacement all other operations (remaining integrations and sum over helicity) become trivial. The integral representation we shall use is

$$ {}_2F_1(\mathsf{a,b;c;z}) = \frac{\Gamma(\mathsf{c})}{\Gamma(\mathsf{b})\Gamma(\mathsf{c-b})} \int_0^1 dt\, t^{\mathsf{b}-1}(1-t)^{\mathsf{c-b}-1}(1-t\mathsf{z})^{-\mathsf{a}}\,. \quad (5.20)$$

Let us explain how the full procedure works for the component $P^{[2]}P^{[2]}$. After making the replacement (5.20), we find that the integrand of (5.19) (with $\hat{r} = 2$ and $r_{12} = 0$) takes the simple form

$$\int_0^1 dt\, e^{if(t)u}\, g^{[2,2]}(t)\left[e^{-\tau-\sigma}(t-1)\right]^{|a|} e^{ia\phi}\,, \quad (5.21)$$

---

[4]The cases where there is a minus sign can be understood from the exchange on the Grassmann variables χ^A in the expansion of the superpentagon $\mathbb{P}$ (see [2]). For instance, comparing $P^{[3]}P^{[1]} = \mathcal{P}_{123} \circ \mathcal{P}_4$ with the parity conjugate of $P^{[1]}P^{[3]} = \mathcal{P}_1 \circ \mathcal{P}_{234}$ given by $\mathcal{P}_{234} \circ \mathcal{P}_1$ we get a minus sign.

[5]In fact, in [64] similar expressions were obtained when computing the hexagon remainder function.

where $f(t) = 2\sigma - \ln[(1-t)(1+e^{-2\tau} t)/t]$ and $g^{[2,2]}(t) = -t^{1/2} e^{-\tau} (1-t)^{-3/2} (1+te^{-2\tau})^{-3/2}$.
Note that u appears only in the exponent. When the integrand is written in this form, it is
apparent that the integration over u trivially gives a delta function $\delta(f(t))$ which in turn
localizes t to the value –between zero and one– where $f(t) = 0$. We call this value $t^\star$ and
it is given by

$$t^\star = \frac{1}{2} e^{2\tau} \left(\sqrt{(e^{2\sigma} - e^{-2\tau} + 1)^2 + 4e^{-2\tau}} - e^{2\sigma} + e^{-2\tau} - 1 \right). \tag{5.22}$$

That leaves us with the simple expression

$$\int_0^1 dt \int_{-\infty}^{\infty} \frac{du}{2\pi} e^{if(t)u} g^{[2,2]}(t) \left[e^{-\tau-\sigma} (t-1) \right]^{|a|} e^{ia\phi} = \frac{g^{[r_1,r_2]}(t^\star)}{|f'(t^\star)|} \left[e^{-\tau-\sigma} (t^\star - 1) \right]^{|a|} e^{ia\phi}, \tag{5.23}$$

where the prime denotes the derivative of the function with respect to t. We might be
tempted to sum (5.23) over a and equate the result to $P^{[2]}P^{[2]}$, however we need to be a
bit more careful. This is because the replacement (5.20) is valid when $\Re(\mathsf{c}) > \Re(\mathsf{b}) > 0$,
which implies that for some values of the helicity a this replacement is not correct. For the
component $P^{[2]}P^{[2]}$ the replacement is strictly valid for $|a| > 1$, so we need to perform an
analytic continuation.

If we analytically continue the result (5.23) (i.e. integral in u) as in figure 5.7 we see
that in deforming the contour of integration we pick an extra term coming from the pole at
$u = i/2$ for $a = 0$. However, what we want is the analytic continuation of the integrand in
$P^{[2]}P^{[2]}$ and then integrate over the real axis. The difference between the two is precisely
the residue at $u = i/2$ for $a = 0$. Since in the analytic continuation of the integral the
contour has clockwise direction the residue comes with a minus sign. That means that in
order to get the final result we need to cancel the pole contribution by adding the residue

$$r^{[2,2]} = \operatorname*{Res}_{u=\frac{i}{2}} \left[e^{-\tau+2iu\sigma} \Gamma\left(-iu - \tfrac{1}{2}\right) \Gamma\left(iu + \tfrac{3}{2}\right) {}_2F_1\left(iu + \tfrac{3}{2}, iu + \tfrac{3}{2}; 1; -e^{-2\tau}\right) \right] = -\frac{e^{-\sigma}}{2\cosh\tau}.$$

Although the terms with $|a| = 1$ corresponding to $\psi\psi_s$ ($\bar\psi\bar\psi_s$) and their descendants have a
pole at $u = 0$ we can simply integrate slightly over the real axis $\mathbb{R} + i\epsilon$. This is precisely
the correct prescription for the integration of the large fermion (see $\mathcal{C}_{\text{large}}$ in figure 5.2).

In the end, the POPE component $P^{[2]}P^{[2]}$ reads

$$P^{[2]}P^{[2]} = \frac{g^{[2,2]}(t^\star)}{|f'(t^\star)|} \sum_{a=-\infty}^{\infty} \left[e^{-\tau-\sigma} (t^\star - 1) \right]^{|a|} e^{ia\phi} + r^{[2,2]} + \mathcal{O}(g^2). \tag{5.24}$$

80
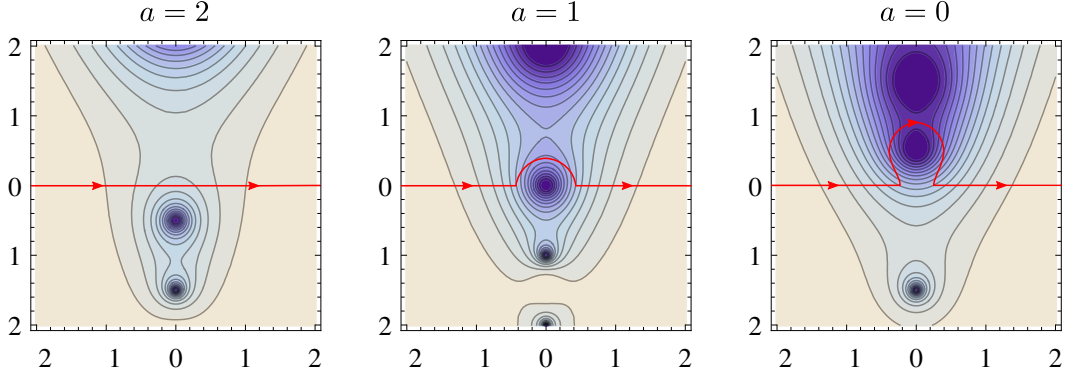
Figure 5.7: Integrand of component $P^{[2]}P^{[2]}$ in the u complex plane for different values of the helicity a (the parameters τ, σ and ϕ are set to zero); larger values of the integrand are shown in darker colours. In red the contour of integration that gets deformed in performing the analytic continuation of (5.23). To the left, the integrand with $a = 2$ for which the integral representation is still valid so that the integration contour is over the real line. The first problematic case occurs at $a = 1$ (center), where we have a pole at $u = 0$; however, we can integrate slightly over the real axis at that point so that effectively the integration contour is unchanged. For $a = 0$ (right) we can deform the contour such that we end with the original contour over the real axis minus (clockwise orientation) the residue at $u = i/2$. To get the final result we need to cancel this residue.

For the remaining components the same procedure applies. In general, we have

$$P^{[r_1]}P^{[r_2]} = \delta_{|r_1-r_2|,4} + \frac{g^{[r_1,r_2]}(t^\star)}{|f'(t^\star)|} \sum_a \left[e^{-\tau-\sigma}(t^\star - 1) \right]^{|a|} e^{ia\phi} + r^{[r_1,r_2]} + \mathcal{O}(g^2), \qquad (5.25)$$

where the relevant functions $g^{[r_1,r_2]}(t)$ and $r^{[r_1,r_2]}$ are shown in appendix G.

Let us emphasize that the key step in this simplification came from the replacement of the sum over descendants to an integral, which at tree level is straightforward, since it amounts to use one of the integral representations for the hypergeometric function. It remains a question if the same procedure can be easily applied at higher loops[6]. In this way all we are left to do is the last sum over the helicity a which is what we present in the next section.

---

[6]In [65] the one loop MHV case has been worked out.

Sum over helicity

Finally we can perform the sum over the helicity of the effective excitations. As we see in (5.25), the dependence in a is the same for all components and is given by $e^{ia\phi}[e^{-\tau-\sigma}(t^{\star} - 1)]^{|a|}$, so the sum over a is a geometric series. We can perform this sum in the regime where it converges and then analytically continue the result. In particular, the sum converges in the collinear limit (large τ)[7], so we can do the sum close to this region and then analytically continue the result for any value of τ. For example, for $P^{[2]}P^{[2]}$ we do not need to separate the sum and a runs over the integers, so that we find

$$
\begin{aligned}
P^{[2]}P^{[2]} &= \frac{g^{[2,2]}(t^{\star})}{|f'(t^{*})|} \sum_{a \in \mathbb{Z}} e^{ia\phi} \left[e^{-\tau-\sigma}(t^{\star} - 1) \right]^{|a|} + r^{[2,2]} \\
&= \frac{e^{-\tau}\left(e^{\sigma} + 2e^{-\tau}\cos(\phi)\right)}{\left(e^{-2\tau} + 1\right)\left(2e^{\sigma-\tau}\cos(\phi) + e^{2\sigma} + e^{-2\tau} + 1\right)} + \mathcal{O}(g^2),
\end{aligned}
\tag{5.26}
$$

which nicely matches the data as explained in the next section. Notice that for $P^{[2]}P^{[2]}$ there is a symmetry between positive and negative helicity. In general this is not the case, so when $r_1 \neq r_2$ we need to separate the sum for negative and positive values of a. Following the same procedure with the other components we complete the resummation of the hexagon POPE series at tree level.

Comparison with tree NMHV amplitude

To compare against data we use the map between amplitude and POPE components that was put forward in [2]. Recall that from supersymmetry [30] we need only five NMHV components to express any other hexagon NMHV component. The map between the linear independent components and the POPE basis we have been using is very simple for the hexagon. It is given by

$$
\begin{aligned}
P^{[4]}P^{[0]} &= ((\mathbf{1})_1)^4 & \mathcal{W}^{(1111)}, \\
P^{[3]}P^{[1]} &= ((\mathbf{1})_1)^3 \, (\mathbf{4})_2 & \mathcal{W}^{(1114)}, \\
P^{[2]}P^{[2]} &= ((\mathbf{1})_1)^2 ((\mathbf{4})_2)^2 \, \mathcal{W}^{(1144)}, \\
P^{[1]}P^{[3]} &= (\mathbf{1})_1 \, ((\mathbf{4})_2)^3 \, \mathcal{W}^{(1444)}, \\
P^{[0]}P^{[4]} &= ((\mathbf{4})_2)^4 \, \mathcal{W}^{(4444)},
\end{aligned}
\tag{5.27}
$$

---

[7]We can see in the definition of $t^{\star}$ that when taking this limit the dangerous terms outside and inside the square root cancel.

where $\mathcal{W}$ is the renormalized Wilson loop introduced in [1], $(\mathbf{i})_j$ denotes the weight of the i-th twistor in pentagon j as in [2] and we have used cyclic labelling for the edges. The hexagon twistors are given in Appendix H. In this case the weights evaluate to -1 for the first, third and last line and $+1$ for the other two.

At tree level we can compare directly the renormalized Wilson loop $\mathcal{W}^{\mathrm{NMHV}}$ with the NMHV ratio function of colour-ordered amplitudes $\mathcal{R}^{\mathrm{NMHV}} = \mathcal{A}^{\mathrm{NMHV}}/\mathcal{A}^{\mathrm{MHV}}$ [8]. As can be derived from the recursion relations [44, 66], the six point NMHV ratio function $\mathcal{R}_6^{\mathrm{NMHV}}$ at tree level is given by the sum of R-invariants [17, 67]

$$\mathcal{R}_{6,\,\mathrm{tree}}^{\mathrm{NMHV}} = R_{135} + R_{136} + R_{146}\,, \text{ where} \tag{5.28}$$

$$R_{ijk} = \frac{\delta^{(4)}\left(\langle j-1, j, k-1, k\rangle \eta_i + \mathrm{cyclic}\right)}{\langle i, j-1, j, k-1\rangle\langle j-1, j, k-1, k\rangle\langle j, k-1, k, i\rangle\langle k-1, k, i, j-1\rangle\langle k, i, j-1, j\rangle}\,,$$

and we have expressed the R-invariants in terms of momentum twistors reviewed in Appendix H. The delta function ensures that we have a polynomial of degree four in the dual Grassmann variables η_i. In practice we work with the specific set of η's which correspond to a specific component of (5.28)[9]. For example, the component $\mathcal{R}^{(1144)}$ reads

$$P^{[2]}P^{[2]} = -\mathcal{R}_{6,\,\mathrm{tree}}^{(1144)} = -\frac{\langle 2345\rangle\langle 5123\rangle}{\langle 1234\rangle\langle 3451\rangle\langle 4512\rangle} - \frac{\langle 3456\rangle\langle 5613\rangle}{\langle 1345\rangle\langle 4561\rangle\langle 6134\rangle}\,. \tag{5.29}$$

Finally, in order to compare against the POPE resummed expressions we only need to plug in the twistors in the relevant tree level ratio functions. Doing so for the ratio function component (5.29) we find precisely the tree level term for $P^{[2]}P^{[2]}$ shown in (5.26). Proceeding in a similar fashion for the rest of the components we find perfect agreement for all of them.

5.4 Discussion

In this chapter we presented the tree level resummation of the hexagon POPE reproducing the six point NMHV amplitude. We did so by summing over all possible one effective particle states.

---

[8]We can also write this ratio as $\mathcal{R}^{\mathrm{NMHV}} = \mathcal{W}^{\mathrm{NMHV}}/\mathcal{W}^{\mathrm{MHV}}$. At loop level one would also need to consider the contribution from $\mathcal{W}^{\mathrm{MHV}}$ in the denominator.

[9]Alternatively, we could extract these ratio function components from the package [36] which computes also one loop ratio functions.

First, we found a way to perform all the small fermion integrals by examining the matrix part of the POPE integrand. We discovered that the small fermions attach to a fundamental excitation following simple patterns creating the strings shown in figures 5.4-5.6. This allowed us to compute the one effective particle measures and form factors at finite coupling.

The one effective particle states are characterized by their helicity a, number of descendants n and $SU(4)$ R-symmetry representation. We found that the NMHV tree level measures $\mu_{a,n}^{[r_1,r_2]}(u)$ can be written in the compact formula (5.17) in terms of these parameters. Given a POPE component, we converted the sum over all possible one effective particle states into a sum over the helicity a and number of descendants n, so that a general POPE component has the form

$$P^{[r_1]}P^{[r_2]} = \delta_{|r_1-r_2|,4} + \sum_{a,n} \int \frac{du}{2\pi}\, \hat{\mu}_{a,n}^{[r_1,r_2]}(u) + \mathcal{O}(g^2)\,.$$

The tree level resummation turned out to be very simple. Once we performed the sums and rapidity integral in the following order

$$\sum_n \to \int \frac{du}{2\pi} \to \sum_a$$

and used some identities for special functions, we recovered the simple rational functions of the tree level six point NMHV amplitudes.

Of course, the ideal case would be to perform the finite coupling resummation. This would make manifest some of the symmetries of the amplitudes –like cyclicity– obscured in the POPE series. A natural step in that direction is to repeat the procedure described here at higher loops or with larger polygons. In fact, in [65] it is shown that the one loop MHV hexagon can be resummed using the techniques discussed here. Starting from the heptagon Wilson loop, the pentagon transitions between effective excitations are necessary and were worked out in [68, 69]. Finding methods like [56, 57] to systematically resum all contributions at a given perturbative order would prove most useful. It would also be interesting to find connections between the different looking weak and strong coupling resummations.

The simple patterns found at finite coupling and the almost straightforward resummation of the hexagon at tree level shed an optimistic light on the POPE program as an efficient method for computing the full kinematical regime of scattering amplitudes for larger number of particles and higher loop orders where less is known about them.

Part II

S-matrix Bootstrap

Chapter 6

Appetizer

In the second part of this thesis we take a different approach and, instead of studying a specific theory, consider the space of Quantum Field Theories (QFTs).

As we discuss in the following, by asking the right questions it is possible to constrain the space of QFTs compatible with some given physical principles. This approach is known as the Bootstrap philosophy and has proven very fruitful, specially for Conformal Field Theories. By imposing consistency conditions on physical observables like correlation functions, one is able to establish bounds that effectively rule out regions on the space of CFTs. It is often the case that at the boundary of these bounds we can identify interesting physical models.[1]

For massive QFTs, a natural object to study is the S-matrix encoding the interactions of the theory. In an effort to determine the strong interactions, the S-matrix program pursued during the 60's made a lot of progress in understanding the analytic properties of S-matrix elements. However, with the formulation of QCD and development of perturbative tools this program fell out of fashion. Nevertheless, applying the bootstrap philosophy to integrable theories produced notable results such as the exact S-matrices of [72].

Inspired by the remarkable success of the conformal bootstrap, the S-matrix program for general QFTs was rebooted in [5,6]. The main assumptions used there to derive bounds are: Lorentz symmetry, unitarity, crossing symmetry and analyticity of the S-matrix. In the rest of the chapter we consider the simplest scenario in two spacetime dimensions discussed in [6] as an appetizer for the following chapters.

---

[1]Perhaps the most famous example is the bootstrap associated to the three-dimensional Ising model, which provides the best approximation to its critical exponents [70,71].
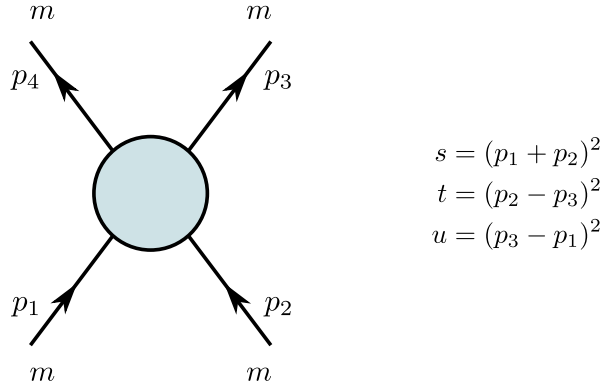
$$s = (p_1 + p_2)^2$$
$$t = (p_2 - p_3)^2$$
$$u = (p_3 - p_1)^2$$

Figure 6.1: The $2 \to 2$ particle scattering matrix element of scalar particles with the same mass m studied in this section along with the Mandelstam invariants s, t, u.

Let us focus on the two-to-two particle scattering matrix element of scalar particles with the same mass m depicted in figure 6.1. From Lorentz invariance, this scattering matrix element depends only on the three Mandelstam invariants s, t, u constructed out of the four momenta and satisfying the usual relation $s + t + u = 4m^2$ (see figure 6.1 for momentum conventions). Furthermore, because of the two-dimensional kinematics, the set of two incoming momenta is the same as the outgoing one, so we can set one of the Mandelstam invariants to be zero, e.g. $u = 0$. This leaves us with a scattering element depending on a single independent Mandelstam invariant $S(s)$. For identical external particles crossing symmetry flips s and t giving the constraint $S(s) = S(t = 4m^2 - s)$. The unitarity of the S-matrix implies that, for physical values of the center of mass energy $(\sqrt{s} > 2m)$, the absolute value of the two-to-two element satisfies $|S(s)|^2 \leq 1$. In summary, we have the following properties for the two-to-two scattering matrix element:

$$S(p_1, p_2, p_3, p_4) = S(s) \qquad \text{(Lorentz+2D)} \qquad (6.1)$$
$$S(s) = S(4m^2 - s) \qquad \text{(crossing)} \qquad (6.2)$$
$$|S(s)|^2 \leq 1, \quad s > 4m^2 \qquad \text{(unitarity)} \qquad (6.3)$$

Let us now turn to the analytic properties of $S(s)$ in the complex s-plane. These properties are summarized in figure 6.2. At $s = 4m^2$ we have a branch point indicating the two particle threshold, that is when we can start having intermediate states with two particles. From crossing (6.2), there is another branch point at $s = 0$. Bound states appear as poles in the segment $s \in [0, 4m^2]$ and for each s-channel bound state with squared mass m_B^2 there is a corrsponding t-channel bound state $4m^2 - m_B^2$. Other possible thresholds appear as further branch points at higher values of the center of mass energy (for instance
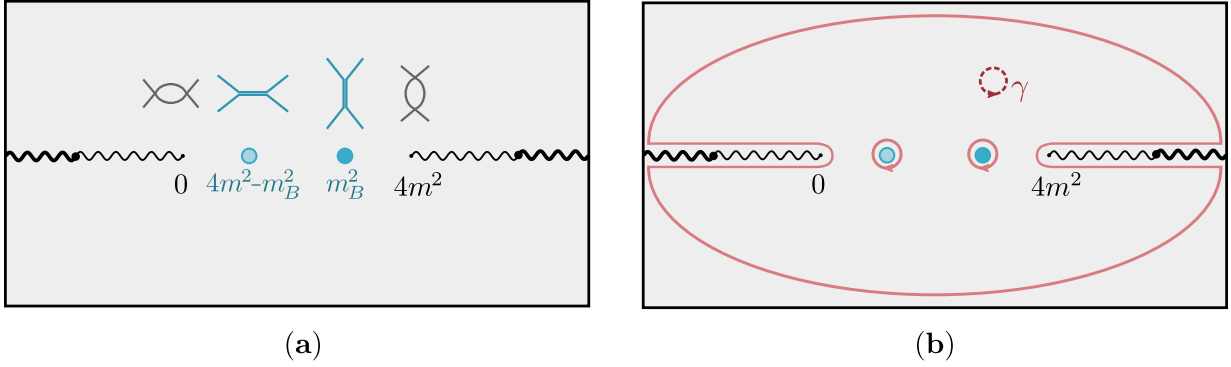
(a)   (b)

Figure 6.2: **(a)**Physical sheet of the two-to-two scattering matrix element $S(s)$. Bound states appear as poles in the segment $s \in \left[0, 4m^2\right]$ where the S-matrix is real. There are branch cuts starting at $s = 4m^2$ and $s = 0$ associated to the two-particle threshold in the s- and t-channel, respectively. The bold wavy lines represent other possible branch cuts for higher particle thresholds. Unitarity is evaluated right above the right hand cut. **(b)** The contour γ used in the derivation of the dispersion relation. As we deform it we pick the contribution from the poles and branch cuts.

$s = (3m)^2, (m + m_B)^2$, etc.) giving rise to a complicated Riemann surface. The Riemann sheet depicted in figure 6.2, where we have the physical values of s is referred to as the *physical sheet*. We also assume the property $S(s^*) = [S(s)]^*$ known as *real analyticity*.

With the knowledge of the analytic properties we can write an ansatz known as dispersion relation for the S-matrix element. The idea is to use Cauchy's integral theorem to write an ansatz where the poles and discontinuities across the branch cuts appear explicitly. Starting from a contour γ enclosing no singularities (see figure 6.2 **(b)**) we can deform it and pick the singularities resulting in[2]

$$S(s) = \frac{1}{2\pi i} \oint_\gamma \frac{S(x)}{x - s} = S_\infty - \frac{g^2}{s - m_B^2} - \frac{g^2}{4m^2 - s - m_B^2} + \int\limits_{4m^2}^{\infty} \rho(x)dx \left(\frac{1}{x - s} + \frac{1}{x - 4m^2 + s} \right) ,$$

(6.4)

where S_∞ is a constant satisfying $|S_\infty| \leq 1$, the discontinuity is parametrized by $\rho(x) = (2\pi i)^{-1} \left[S(s + i\epsilon) - S(s - i\epsilon) \right]$ and we have used crossing symmetry (6.2) to write everything in terms of g and $\rho(x)$. We have also assumed that the S-matrix decays fast enough at infinity, so that the contribution of the arches in figure 6.2 **(b)** is neglected. The residue at the bound state pole g^2 provides the non-perturbative definition of the coupling. The

---

[2]For simplicity we are writing the dispersion relation for a single bound state (i.e. the analytic structure in figure 6.2) but the generalization to more bound states is straightforward.
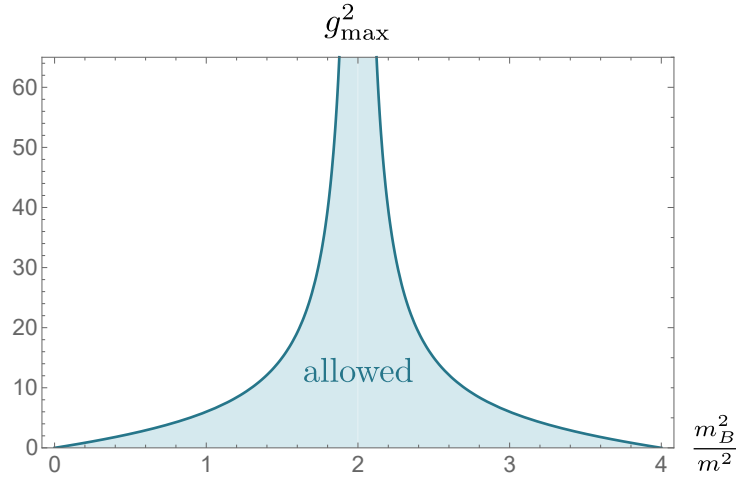
Figure 6.3: Maximum coupling g^2_{max} as a function of the bound state mass. Putative QFTs compatible with the spectrum assumptions should have couplings inside the allowed region in blue. The plot is obtained from the residue at $s = m^2_B$ of solution (6.6).

dispersion relation (6.4) is a powerful representation since it already trivializes crossing symmetry and analytic properties. Generalizations of it will appear in the following chapters.

Now that we know the properties of the two-to-two scattering element, let us ask a Bootstrap question. As put forward in [6], a meaningful question is:

Q: Given the spectrum $\{m, m_B, ...\}$, what is the maximum cubic coupling g? (6.5)

Physically the existence of an upper bound on the coupling g makes sense since by increasing it the binding energy grows and we would be able to create more bound states or the mass of the bound state would be smaller, which in either case contradicts the initial assumption for the spectrum. Mathematically, we are considering a dispersion relation (6.4) where the number and position of poles is fixed and maximizing one of the parameters in the ansatz, subject to the unitarity constraint (6.3). In general, this is a tough problem to solve and numerical tools are needed. However, for this particular case with a single crossing symmetric function the problem is simple enough to be solved analytically.

Let us first see how this works for a theory without bound states. In this case, there are no poles in the physical sheet and we could maximize $S(s^*)$ at some point inside this plane[3]. From unitarity (and crossing) we know that the function $S(s)$ is bounded by one

---

[3]For instance the middle of the strip $s_* = 2m^2$ where the function is real and which would measure an effective quartic coupling.

at the right and left hand cut. Since we have an analytic function, we can use the power of complex analysis and invoke the maximum modulus principle to state that the value inside the physical sheet cannot be bigger than the value at its boundary (i.e. the left and right cuts). That is, the biggest the function can be inside the physical sheet is $S(s^*) = 1$ which leads us to free theory.

To answer the bootstrap question (6.5) involving bound states, we can apply the same logic provided we divide by a crossing symmetric function with the correct poles and whose absolute value is one at the cuts. This function, which also gives the solution to the maximization problem is[4]:

$$S(s) = \pm \frac{\sqrt{s}\sqrt{4m^2 - s} + m_B\sqrt{4m^2 - m_B^2}}{\sqrt{s}\sqrt{4m^2 - s} - m_B\sqrt{4m^2 - m_B^2}}. \tag{6.6}$$

Its residue at $s = m_B^2$ provides the upper bound on the cubic coupling plotted in figure 6.3. That is, if someone gives us the non-perturbative coupling of a putative theory with the same spectra, we can immediately check if it is allowed or excluded; in other words, if it is compatible with the postulated principles.

Let us comment on few properties of the bound in figure 6.3. First, the divergence at $m_B^2 = 2m^2$ is a consequence of the screening of s- and t-channel poles in (6.4) at this value of the bound state mass. Note also the symmetry under the exchange $m_B^2 \leftrightarrow 4m^2 - m_B^2$. This is because every solution for a squared bound state mass m_B^2 is also a solution for $4m^2 - m_B^2$ provided we multiply by an overall minus sign which exchanges the role of s- and t-channel poles in (6.4).

The solution (6.6) saturates the unitarity constraint (6.3), which means the rest of the $2 \to n$ processes are zero. This hints to an integrable theory which has no particle production and indeed for the positive sign in (6.6) (or the right half in figure 6.3) the S-matrix corresponds to the sine Gordon theory[5]. This is in accordance with the expectation mentioned in the introduction that often at the boundary of these bounds we can find interesting theories. As for the left hand side of the bound in figure 6.3, there is no known physical model corresponding to the negative sign in (6.6).

This concludes the review of the simplest S-matrix bootstrap scenario. In the next chapter we consider a more complicated problem where the particles transform under a

---

[4]In case the initial spectrum has more than one bound state, the optimal solution is simply a product of factors like (6.6). As described in [6], an example of a theory saturating this multi-bound state bound is the Scaling Ising model field theory with magnetic field which has the spectrum $\{m, 2\cos(\pi/5)m, 2\cos(\pi/3)m\}$.

[5]In the rapidity parametrization of the energy $s = 4m^2\cosh^2(\theta)$, (6.6) is nothing but the Castillejo-Dalitz-Dyson (CDD) factor $S_{\text{CDD}}(\theta) = -\frac{\sinh\theta + i\sin\lambda}{\sinh\theta - i\sin\lambda}$.

global symmetry group. As we shall see, this simple generalization will unveil a very rich structure in the space of S-matrices.

Chapter 7

O(N) Bootstrap

7.1 Introduction

In this chapter we continue the exploration of the space of gapped quantum field theories following [5, 6, 73] by focusing on two dimensional theories with a global symmetry under which particles transform. We will consider the two-to-two scattering processes of particles transforming in the vector representation of $O(N)$. As we will see, such processes turn out to be way richer than their analogous counterparts without global symmetry.

As described in much more detail in the next section, kinematically, such two-to-two scattering amplitudes live in the Mandelstam physical sheet or equivalently in the physical strip $0 < \text{Im}(\theta) < \pi$ in terms of the hyperbolic rapidity θ. Direct s-channel processes take place at the lower boundary of this strip, for real rapidity. There, the various amplitudes are bounded by unitarity as $|S_{\text{rep}}(\theta)|^2 \leq 1$ where rep are the various possible representations formed by the two incoming particles. At the upper boundary of the physical sheet we have the crossed t-channel processes. Here is where global symmetry manifests itself rather strikingly as a tension between unitarity and crossing symmetry. Indeed, under crossing transformations, the various individual components are trivially swapped but when we translate that back to the representation basis – for which s-channel unitarity was so conveniently simple – we obtain a very non-trivial mixing of the various representations. In this upper boundary we then have $|\sum_{\text{rep}'} \mathbb{d}_{\text{rep,rep}'} S_{\text{rep}'}(i\pi - \theta)|^2 \leq 1$ where $\mathbb{d}$ is a constant N-dependent matrix of purely group theoretical origin. Exploring the space of S-matrices with global symmetry thus amounts to studying the space of functions living in this strip and bounded at its boundary in such coupled way. It is this fascinating problem which we

will consider here.[1]

By looking for theories which maximize particular couplings, we will rediscover in this way the two most famous integrable models with $O(N)$ symmetry – the $O(N)$ non-linear sigma model and the $O(N)$ Gross-Neveu model – whose S-matrices were found by Zamolodchikov and Zamolodchikov in their seminal 1979 paper [72]. For $N = 2$, we rediscovered the S-matrix for the kinks of the Sine-Gordon model. Furthermore, we make contact with a much less known integrable solution [75]. We also found some other analytic solutions whose physical (ir)relevance is discussed below. Some other times, these maximization problems require numerics. Both in the analytic and numerical examples, we will often unveil a very rich structure of infinitely many resonances in the various Riemann sheets for the putative S-matrices with the largest possible physical couplings.

In section 7.2 we introduce the $O(N)$ S-matrix setup and we review Zamolodchikovs' S-matrices mentioned above. We also explain the general numerical setup in this section. We then discuss in section 7.3 how the integrable S-matrices can be rediscovered from these numerics when we impose very specific spectra of bound states (or absence thereof). As we move away from these special points, the S-matrices develop very interesting new features. We present in the same section some numerical results for some non-integrable cases. In section 7.4 we describe an analytic large N analysis which yields some intuition for the rich mathematical structures found numerically. We then present the analytic solution of various cases along with some general analytic properties for the S-matrices. Finally in section 7.5 we give some concluding remarks.

7.2 Setup, key examples and numerics

7.2.1 S-matrices

We consider relativistic particles of mass m transforming in the $O(N)$ vector representation. Our particles have an $O(N)$ index $i = 1, \ldots, N$ and an hyperbolic rapidity θ parametrizing its energy and momentum as the usual: $E \pm P = m \exp(\pm\theta)$. Lorentz boosts act as translations in hyperbolic rapidity hence Lorentz invariant quantities depend on difference of rapidities only. An example which will be the focus of this chapter is the two-to-two

---

[1]The higher dimensional counterpart is currently being investigated in [74]
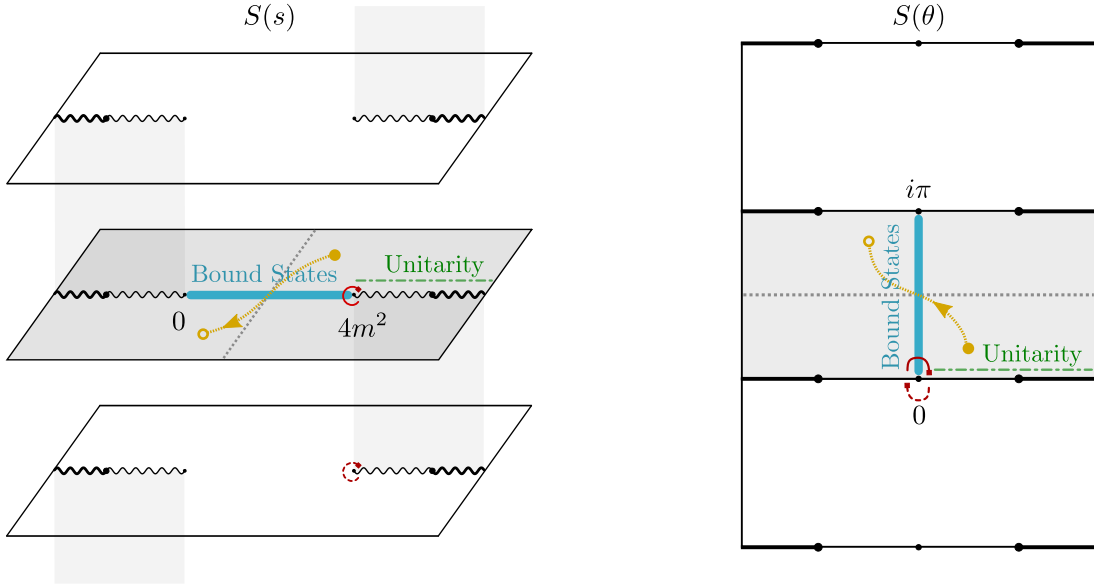
Figure 7.1: Mapping between s and θ variables. The cuts corresponding to the two particle thresholds with branch points at $s = 0$ and $s = 4m^2$ get opened in the θ plane. These cuts are square roots, so that going twice around one of the branch points leaves you back where you began. This is exemplified in the red path for the branch point $s = 4m^2$ (or the regular point $\theta = 0$). The thick lines in black represent possible inelastic thresholds. Unitarity is imposed for physical values of the center of mass energy $s \geq 4m^2$ ($\theta > 0$) represented by the green dashed line. The physical sheet(strip) in $s(\theta)$ is highlighted in grey. The bound state poles are located in the window $s \in [0, 4m^2]$ ($\theta \in [0, i\pi]$) (blue line). Finally, the points in yellow are related by crossing which acts as a reflection around $s = 2m^2$ ($\theta = i\pi/2$). Notice that in general there are infinitely many sheets.

particle S-matrix $S_{ij}^{kl}(\theta)$ defined in the standard way[2]

$$|\theta_1, i_1; \theta_2, i_2\rangle_{\text{out}} = \mathbb{S}_{i_1 i_2}^{j_1 j_2}(\theta = \theta_1 - \theta_2)|\theta_1, j_1; \theta_2, j_2\rangle_{\text{in}}. \tag{7.1}$$

In terms of Mandelstam invariants, we have $s/m^2 = 4 - t/m^2 = 2 + 2\cosh(\theta)$ and $u = 0$ in two dimensions. The very useful map between s and θ opens up the two particle cut and is depicted in figure 7.1.

The S-matrix can be coded into three functions corresponding to the three possible

---

[2]In two dimensions the initial and final rapidities are the same because of energy-momentum conservation.

$$S_{ij}^{kl}(\theta) = \sigma_1(\theta)\delta_{ij}\delta^{kl} + \sigma_2(\theta)\delta_i^l\delta_j^k + \sigma_3(\theta)\delta_i^k\delta_j^l$$

Crossing	$\sigma_1(i\pi - \theta) = \sigma_3(\theta)$		
	$\sigma_2(i\pi - \theta) = \sigma_2(\theta)$		
Unitarity	$\|\sigma_2(\theta) + \sigma_3(\theta)\|^2 \leq 1,$		
	$\|\sigma_2(\theta) - \sigma_3(\theta)\|^2 \leq 1,$	for	$\theta > 0$
	$\|N\sigma_1(\theta) + \sigma_2(\theta) + \sigma_3(\theta)\|^2 \leq 1$		

Table 7.1: Crossing and unitarity for the S-matrix in the component decomposition (7.2). Crossing simply re-shuffles the functions in this language but unitarity is more complicated.

$O(N)$ invariant tensors with four indices

$$\mathbb{K}_{ij}^{kl} = \delta_{ij}\delta^{kl} = \quad , \qquad \mathbb{I}_{ij}^{kl} = \delta_i^l\delta_j^k = \quad , \qquad \mathbb{P}_{ij}^{kl} = \delta_i^k\delta_j^l = \quad$$

or, equivalently, to the three irreducible representations arising in the product of two fundamental incoming representations. Explicitly, we have

$$\mathbb{S}(\theta) \quad = \quad \sigma_1(\theta)\mathbb{K} + \sigma_2(\theta)\mathbb{I} + \sigma_3(\theta)\mathbb{P} \tag{7.2}$$
$$= \quad S_{\text{sing}}(\theta)\mathbb{P}_{\text{sing}} + S_{\text{anti}}(\theta)\mathbb{P}_{\text{anti}} + S_{\text{sym}}(\theta)\mathbb{P}_{\text{sym}}. \tag{7.3}$$

with a trivial translation between these two equivalent descriptions

$$\sigma_{\text{sym}} = \sigma_2 + \sigma_3, \qquad \sigma_{\text{anti}} = \sigma_2 - \sigma_3, \qquad \sigma_{\text{sing}} = N\sigma_1 + \sigma_2 + \sigma_3. \tag{7.4}$$

In the component description crossing symmetry is trivial to impose since under crossing transformations we swap incoming and outgoing particles so that the $O(N)$ invariant tensors are simply re-shuffled. In the irreducible representation description unitarity is straightforward since by preparing a two-particle state in a definite $O(N)$ representation we diagonalize (7.1). Crossing symmetry and unitarity in both descriptions are summarized in tables 7.1 and 7.2. Alternatively, one could also work in a basis where crossing is diagonalized as in [76].

We assume here that the particles being scattered are the lightest particles in the theory. There could also be bound states showing up in the S-matrix of two fundamental

$$\mathbb{S}(\theta) = S_{\text{sing}}(\theta)\mathbb{P}_{\text{sing}} + S_{\text{anti}}(\theta)\mathbb{P}_{\text{anti}} + S_{\text{sym}}(\theta)\mathbb{P}_{\text{sym}}$$

	$S_{\text{sing}}(i\pi - \theta) = \frac{1}{N}S_{\text{sing}}(\theta) + \left(\frac{1}{2} - \frac{N}{2}\right)S_{\text{anti}}(\theta) + \left(\frac{N}{2} + \frac{1}{2} - \frac{1}{N}\right)S_{\text{sym}}(\theta)$
Crossing	$S_{\text{anti}}(i\pi - \theta) = -\frac{1}{N}S_{\text{sing}}(\theta) + \frac{1}{2}S_{\text{anti}}(\theta) + \left(\frac{1}{2} + \frac{1}{N}\right)S_{\text{sym}}(\theta)$
	$S_{\text{sym}}(i\pi - \theta) = \frac{1}{N}S_{\text{sing}}(\theta) + \frac{1}{2}S_{\text{anti}}(\theta) + \left(\frac{1}{2} - \frac{1}{N}\right)S_{\text{sym}}(\theta)$
Unitarity	$|S_{\text{rep}}(\theta)|^2 \leq 1, \quad \theta > 0$

Table 7.2: Crossing and unitarity for the S-matrix in the representation decomposition (7.3). Unitarity is simple since the various representations diagonalize the scattering evolution while crossing is complicated as it mixes the various representations.

particles. They would transform in the singlet, anti-symmetric or symmetric traceless representation of $O(N)$ and show up as a pole in the corresponding channel. For instance, if there is a single bound state transforming in the anti-symmetric representation with mass $m_{\text{BS}} = 2\cos(\lambda/2)$ there is a pole in the corresponding channel as[3]

$$S_{\text{anti}} \simeq \frac{g_{\text{anti}}^2}{s - m_{\text{BS}}^2} \qquad \Leftrightarrow \qquad S_{\text{anti}} \sim \frac{\mathcal{J}g_{\text{anti}}^2}{\theta - i\lambda} \tag{7.5}$$

which then, according to crossing, would lead to poles in the t-channel for all components as can be read from table 7.2,

$$S_{\text{sing}} \sim \left(\tfrac{1}{2} - \tfrac{N}{2}\right) \times \frac{\mathcal{J}g_{\text{anti}}^2}{i\pi - \theta - i\lambda}, \qquad S_{\text{anti}} \sim \tfrac{1}{2} \times \frac{\mathcal{J}g_{\text{anti}}^2}{i\pi - \theta - i\lambda}, \qquad S_{\text{sym}} \sim \tfrac{1}{2} \times \frac{\mathcal{J}g_{\text{anti}}^2}{i\pi - \theta - i\lambda}. \tag{7.6}$$

It is because of the interplay between these various channels, also illustrated in the tension between simplifying unitarity and crossing at the same time as summarized in tables 7.1 and 7.2, that the $O(N)$ bootstrap problem is so much richer than the single component case.

7.2.2 Integrable $O(N)$ S-matrices

In this section we review the integrable S-matrices with $O(N)$ symmetry obtained by Zamolodchikov and Zamolodchikov in [72]. In this seminal work, starting from the de-

---

[3]$\mathcal{J} = 2\sin(\lambda)$ is a trivial Jacobian. Notice that here we define the coupling g_{rep}^2 to be the residue of the S-matrix $S_{\text{rep}}(s)$ and not of $T_{\text{rep}}(s)$ so we would need one further simple Jacobian if we were to compare the results in this chapter with the conventions in [6].

composition (7.2), factorized scattering, saturation of unitarity and crossing symmetry are imposed. It was found that under these conditions the S-matrix can be almost completely determined and for N>2 takes the form[4]

$$\mathbf{S}^{\text{int}}(\theta) \equiv \begin{pmatrix} S_{\text{sing}}(\theta) \\ S_{\text{anti}}(\theta) \\ S_{\text{sym}}(\theta) \end{pmatrix} = \prod_{j=1}^{M} \frac{\sinh\theta - i\sin\alpha_j}{\sinh\theta + i\sin\alpha_j} \, \mathbf{S}^{\text{NLSM}}(\theta) \,. \tag{7.7}$$

where M is a non-negative integer, α_j are free parameters, and

$$\mathbf{S}^{\text{NLSM}}(\theta) = \begin{pmatrix} -1 \\ -\frac{\theta - i\pi}{\theta + i\pi} \\ -\frac{\theta - i\pi}{\theta + i\pi}\frac{\theta - i\lambda_{\text{GN}}}{\theta + i\lambda_{\text{GN}}} \end{pmatrix} F_{\pi + \lambda_{\text{GN}}}(\theta) F_{2\pi}(\theta) \,, \qquad F_a(\theta) \equiv \frac{\Gamma\left(\frac{a + i\theta}{2\pi}\right)\Gamma\left(\frac{a - i\theta + \pi}{2\pi}\right)}{\Gamma\left(\frac{a - i\theta}{2\pi}\right)\Gamma\left(\frac{a + i\theta + \pi}{2\pi}\right)} \,. \tag{7.8}$$

where $\lambda_{\text{GN}} \equiv \frac{2\pi}{N-2}$. Here NLSM stands for Non-linear Sigma Model and GN stands for Gross-Neveu for reasons that will become clear shortly. Let us review and highlight a few of the many very interesting features of (7.7) and (7.8)

1. The first thing to note is that this solution has a very rich pattern of poles and zeros in the infinitely many copies of the Mandelstam s plane (equivalently, in the infinitely many strips in the θ plane as illustrated in figure 7.1) as made explicit by the various gamma functions in the functions $F_a(\theta)$. At the same time note that the product $F_{\pi - \lambda_{\text{GN}}}(\theta) F_{2\pi}(\theta)$ does *not* contain any poles (or zeroes) inside the physical strip. The vector in (7.8) multiplying these F's also does not have any poles inside the physical strip (only a zero inside the strip at $\theta = i\lambda_{\text{GN}}$ and a zero at the boundary of the strip at $\theta = i\pi$ for some components.)

2. Therefore, potential bound state poles must come from the Castillejo-Dalitz-Dyson (CDD) pre-factor which is the product in (7.7) for $\alpha_j \in [0, \pi]$. The simplest solution commonly referred to as the 'minimal' solution corresponds to setting $M = 0$, i.e. to introducing no CDD factors and hence no bound states.[5] Beautifully, there is a

---

[4]As explained in [72], the Yang-Baxter equations describing factorized scattering have different solutions for $N = 2$ and $N > 2$.

[5]There are of course infinitely many other solutions which would also have no bound states. We could for example take any $M > 0$ with all $\alpha_j \in [-\pi, 0]$ which would correspond to inserting further zeroes in the physical strip but no poles. The 'minimal' solution is minimal because it is not polluted by these extra zeroes and has therefore the simplest analytical structure inside the physical strip.
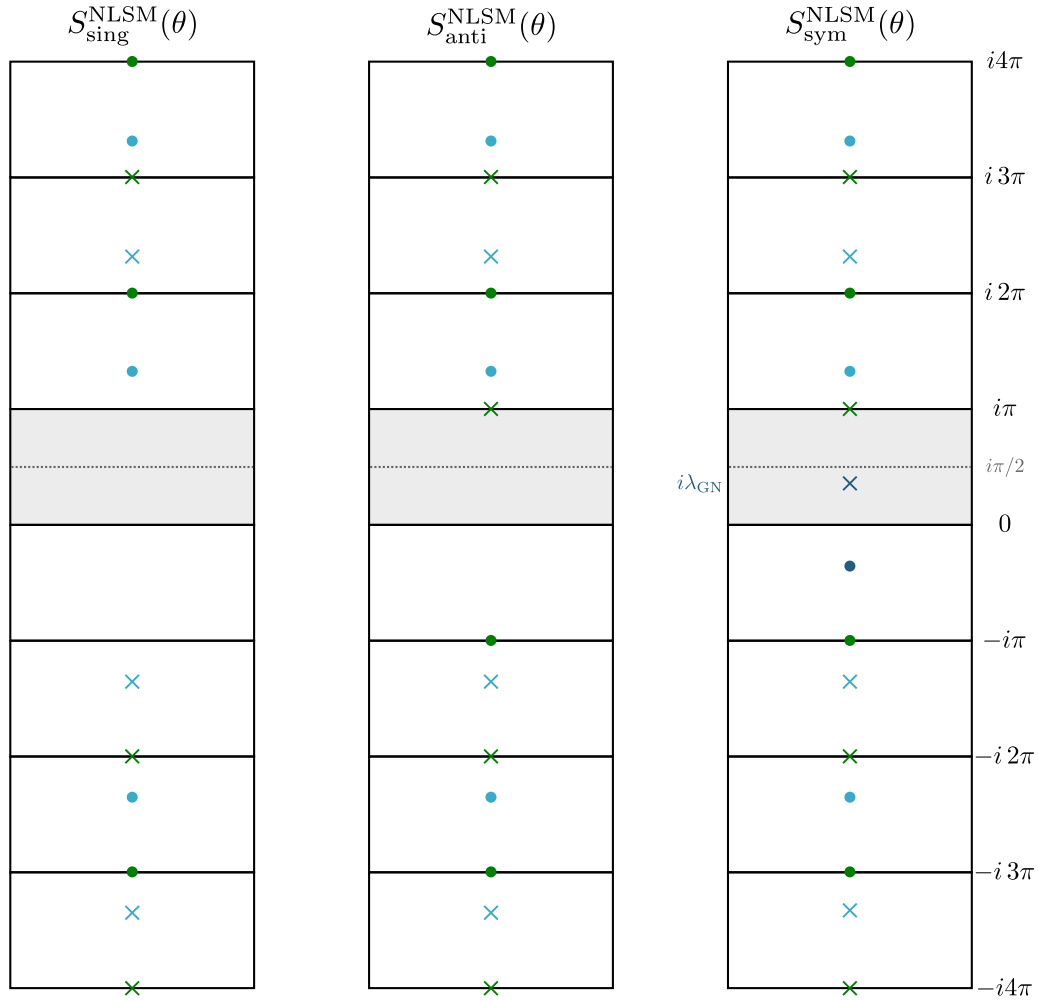
Figure 7.2: Analytic structure of the non-linear sigma model S-matrix in the θ plane corresponding to the 'minimal' integrable solution. The physical strip is highlighted in grey. The bullets • represent simple poles and the crosses × simple zeros. There is a zero × in the physical strip in the symmetric component at the position $\theta = i\lambda_{\mathrm{GN}} = 2\pi/(N-2)$. Integrability implies that unitarity is saturated, i.e. $S_{\mathrm{rep}}(\theta)S_{\mathrm{rep}}(-\theta) = 1$, so that in a given representation a pole at θ has an associated zero at $-\theta$. Crossing mixes the different representations relating points at θ and $i\pi - \theta$ (see discussion around (7.6)).

theory whose S-matrix is precisely given by this choice: it is the $O(N)$ non-linear sigma model [72]. The analytic structure of this solution is presented in figure 7.2.

3. As made explicit in (7.7), when there are bound states at generic positions $\theta = i\alpha_j$ (with $\alpha_j \in [0, \pi]$) they are common to all representations (with an important exception to be discussed in the next point). This means that integrable theories produce very degenerate spectra where bound states in different representations come along at once with the same mass. For example, there is no integrable theory where the particles form a single bound state in the singlet channel. (We can view this as a nice feature: the bootstrap of $O(N)$ symmetric theories with particles in the vector and anti-symmetric representations alone, will necessarily land us outside the integrable world. We will investigate these cases further in section 7.3.2.)

4. A simple exception is when we consider a single CDD factor, i.e. $M = 1$, with $\alpha_1 = \lambda_{GN}$. In this case the CDD factor introduces two poles in the physical strip: one at $\theta = i\lambda_{GN}$ and another one at $\theta = i\pi - i\lambda_{GN}$. However, in the symmetric representation the first one is cancelled by the zero explicitly seen in the vector in (7.8). Therefore we are left with an s-channel pole at $\theta = i\lambda_{GN}$ for the singlet and anti-symmetric representations and a t-channel pole at $\theta = i\pi - i\lambda_{GN}$ for all representations.

   The former are identified as the bound states of the theory[6]. Since both s-channel poles sit at the same position, the bound states have a common mass $m_{\text{sing}} = m_{\text{anti}} = 2\,m\cos(\lambda_{GN}/2)$. There is also a beautiful physical theory corresponding to this S-matrix: it is the $O(N)$ Gross-Neveu model [72]. The structure of poles and zeros of this model is depicted in figure 7.3.

5. There is a subtlety with the last point. For the Gross-Neveu solution the sign of the residues at the s-channel pole $\theta = i\lambda_{GN}$ is appropriate for $N = 7, 8, 9, \ldots$ but opposite of what it should be for $N = 5$ and the pole disappears altogether from the physical sheet as $N = 4$ or $N = 3$.[7]

   (a) For $N = 7, 8, 9, \ldots$ the residues have the proper sign and the bound state interpretation holds perfectly. This case is connected to the $N \to \infty$ limit where things simplify and the theory becomes effectively free.[8]

---

[6]The s- and t-channel poles can be distinguished by the sign of their residue – see (7.12) below for the explicit expected signs.

[7]Recall that we are now discussing $N > 2$ only; we also skip the $N = 6$ case since in this case we have $\lambda_{GN} = i\pi - \lambda_{GN}$ so that s- and t- channel poles collide and it becomes difficult to distinguish them.

[8]Note that the various components of the S-matrix in (7.2) go to 1 or 0 in this limit as expected for

(b) For $N \leq 4$ the potential bound state poles leave the physical strip. Actually, for $N = 3, 4$ the Gross-Neveu and NLSM solutions coincide.[9] This small puzzle is resolved by realizing that the the Gross-Neveu spectrum includes kinks[10] which are the only stable particles below $N = 5$. So for $N = 3, 4$ the S-matrix above cannot describe vector particles of the Gross-Neveu model since they do not exist at all for these values of N.

(c) For $N = 5$ the poles have opposite signs and must be reinterpreted. Actually, the bound states disappear from the spectrum (see equation (6.11) in [72]) so that the poles describe now a pair of kinks instead and correspond to Coleman-Thun poles.

6. Note that at large energy (i.e. $s \to \infty$ or $\theta \to \infty$) we have (for any representation) $S_{\mathrm{rep}}^{\mathrm{int}} \simeq 1 + i a_{\mathrm{rep}} / \log(s)$ so that at very high energy the S-matrices become effectively free but they approach this free limit very slowly, logarithmically so. This logarithm is quite physical, it is a sign of asymptotic freedom of these $O(N)$ integrable theories.

7. Finally, there is another solution to the factorization (Yang-Baxter) equations which appeared in the appendix of [75] and is much less known. To our knowledge, it is has not been understood if there is a physical theory it corresponds to. We make contact with this solution in section 7.4.[11]

This concludes the review of the $N > 2$ solution. For $N = 2$ the solution is even richer, with infinitely many gamma functions and is presented in section 7.3.1 below. The interpretation of the minimal solution in this case is rather different. It describes the scattering of the kinks and anti-kinks of the sine-Gordon model (which is dual to the massive Thirring model where these kinks correspond to the fundamental fermions).

---

a free theory. However, the singlet channel remains finite since it is a sum of N small quantities of order $\mathcal{O}(N^{-1})$. In other words, although each element is very small, the phase space is very large leading to a final net result for the singlet channel. This is a general expected feature of large N theories: because of the large phase space, the singlet component should dominate in this limit. We will re-encounter this clearly in a large N analysis in section 7.4.1 below.

[9]It is simple to see that the CDD factor with $\alpha_1 = \lambda_{\mathrm{GN}} = 2\pi/(N-2)$ equals one for those values of N.

[10]These transform in the spinor representation of $O(N)$ and were studied in [77,78]. The Gross-Neveu spectrum includes as well a tower of anti-symmetric tensors whose S-matrices were obtained in [79].

[11]We became aware of the work [75] after we published version 1 of the present chapter. We thank A.B. Zamolodchikov and S. Komatsu for various inspiring discussions of closely related S-matrices which eventually led us to this reference.
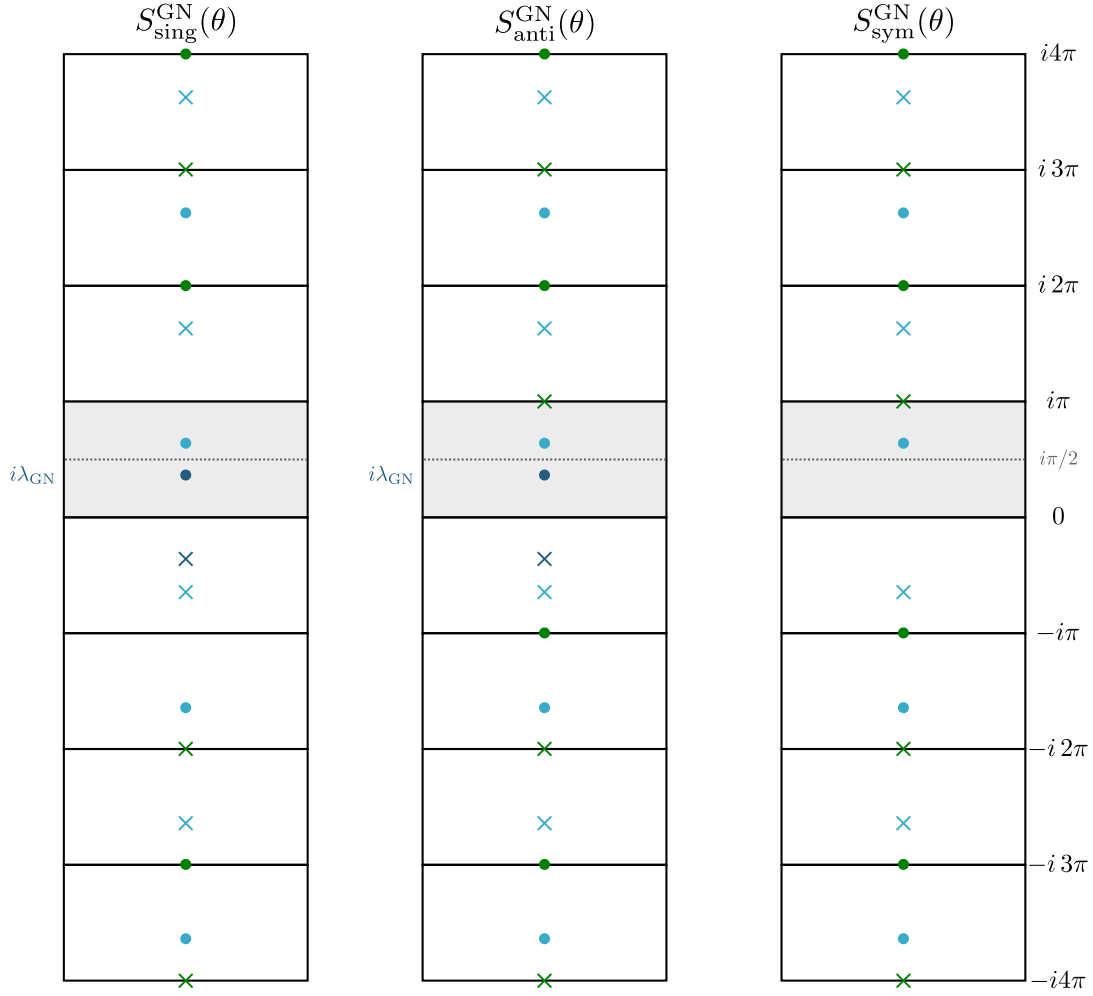
Figure 7.3: Analytic structure of the Gross-Neveu S-matrix in the θ plane. The conventions are the same as in figure 7.2. The dark blue poles ● indicate the bound state poles in the singlet and anti-symmetric representations at $\theta = i\lambda_{\mathrm{GN}} = 2\pi/(N-2)$. The lighter blue poles ● depict the t-channel poles at $\theta = i\pi - i\lambda_{\mathrm{GN}}$. As explained in the main text, the Gross-Neveu and non-linear sigma model S-matrices are related through a CDD factor which introduces the bound state poles in the singlet and anti-symmetric representations and their corresponding t-channel poles in all representations.

7.2.3 Numerical setup

Following the analytic structure of the S-matrix, one can write discretized dispersion relations like the ones used in [3] to get numerical bounds on the couplings. In the present case with global symmetry $O(N)$, there are two main differences: there are three functions $S_{\text{rep}}(s)$ coupled by crossing and the high energy behaviour requires the use of subtractions.

Crossing symmetry tell us that the vector $\mathbf{S} = (S_{\text{sing}}, S_{\text{anti}}, S_{\text{sym}})^\intercal$ satisfies (setting $m = 1$ henceforth) $\mathbf{S}(4 - s) = \mathrm{d} \cdot \mathbf{S}(s)$ where

$$
\mathrm{d} = \begin{pmatrix}
\frac{1}{N} & -\frac{N}{2} + \frac{1}{2} & \frac{N+1}{2} - \frac{1}{N} \\[2mm]
-\frac{1}{N} & \frac{1}{2} & \frac{1}{2} + \frac{1}{N} \\[2mm]
\frac{1}{N} & \frac{1}{2} & \frac{1}{2} - \frac{1}{N}
\end{pmatrix} , \tag{7.9}
$$

as can be read off from table 7.2 in section 7.2.1. Therefore the t-channel poles and the t-channel discontinuities of the vector $\mathbf{S}$ are related to their s-channel counterparts through this same matrix (while in [6] they were simply identical.)

As for the slow decay at infinity this is solved by starting our dispersion relation derivation with the identity[12]

$$
\frac{\mathbf{S}(s) - \mathbf{S}(2)}{s - 2} = \oint \frac{dx}{2\pi i} \frac{1}{x - s} \frac{\mathbf{S}(x) - \mathbf{S}(2)}{x - 2} , \tag{7.10}
$$

where the integral goes over a small circle around a point s inside the physical sheet. Because we divided by $s - 2$ the integrand decays very fast at infinity so we can blow up the contour safely[13] and in this way end up with a contour around the S-matrix poles and the $s-$ and $t-$ channel multi-particle cuts. Using the matrix d in (7.9) to relate t-channel processes to s-channel ones we finally end up with the dispersion relation

$$
\mathbf{S}(s) = \mathbf{S}(2) + \sum_{n=1}^{n_{BS}} \Big(\mathbf{pole}_n(s) + \mathrm{d} \cdot \mathbf{pole}_n(4 - s) \Big) + \int_4^\infty \frac{(s - 2)}{(x - 2)} \left[\frac{\boldsymbol{\rho}(x)}{x - s} - \mathrm{d} \cdot \frac{\boldsymbol{\rho}(x)}{x - 4 + s} \right] dx , \tag{7.11}
$$

---

[12]Note that the *subtraction constants* $\mathbf{S}(2)$ satisfy the crossing condition $\mathbf{S}(2) = \mathrm{d} \cdot \mathbf{S}(2)$ which fixes one of the constants in terms of the other two (e.g. we can eliminate $S_{\text{sing}}(2)$ by writing $S_{\text{sing}}(2) = \frac{1}{2}[(N + 2)S_{\text{sym}}(2) - N S_{\text{anti}}(2)]$).

[13]If the S-matrix approaches a constant at infinity this single subtraction suffices. Note that with this subtraction the integrand vanishes at $1/(x^2 \log(x))$ at infinity for the $O(N)$ symmetric integrable S-matrices of the previous section. Without the subtraction we would have $\mathbf{S}(x)/(x - s) \sim 1/(x \log(x))$ which would not decay fast enough to allow us to blow up the contour.

where the various couplings and bound state masses for the n_{BS} bound states are contained in the vectors

$$\mathbf{pole}_n(s) = \frac{s-2}{m_n^2 - 2}\frac{g_n^2}{s - m_n^2}(\delta_{\text{singlet,rep}_n}, -\delta_{\text{anti,rep}_n}, \delta_{\text{sym,rep}_n})^\intercal \qquad (7.12)$$

where rep_n is the representation under which the n-th bound state transforms. For instance, for the non-linear sigma model we have $n_{BS} = 0$ so we would need no pole vectors. For the Gross-Neveu model we have $n_{BS} = 2$ and these two bound states have the same mass and transform in the singlet and anti-symmetric representation respectively so that in this case we would have two pole vectors $\mathbf{pole}_1^{\text{GN}}(s) = \frac{s-2}{m_{\text{GN}}^2 - 2}\frac{g_{\text{singlet}}^2}{s - m_{\text{GN}}^2}(1,0,0)^\intercal$ and $\mathbf{pole}_2^{\text{GN}}(s) = \frac{s-2}{m_{\text{GN}}^2 - 2}\frac{g_{\text{anti}}^2}{s - m_{\text{GN}}^2}(0,-1,0)^\intercal$.

In the dispersion relations (7.11) we have trivialized crossing taking into account the $O(N)$ symmetry of the problem and possible large energy behaviour. The remaining ingredient is to impose unitarity. In order to do this numerically, we follow [6] and choose a grid of n_{grid} points $s_j > 4$ ($j = 1, \ldots, n_{\text{grid}}$) in which we are to impose unitarity and discretize the densities $\boldsymbol{\rho} \to \boldsymbol{\rho}_j = \boldsymbol{\rho}(s_j)$ with a linear interpolation between these points so that we can explicitly perform the integrals in (7.11) and obtain discretized dispersion relations. The explicit discretization and numerical implementation is explained in appendix I. In this way we impose n_{grid} unitarity constraints $|\mathbf{S}^d(s_j)| \leq 1$, where the superscript d denotes the approximated S-matrix using the discretized dispersion relations.

With this ansatz at hand, we can now choose a bound state spectrum and maximize one of the variables (or combinations of the variables) in the dispersion relation. We could maximize bound state couplings g_n^2 as originally proposed in [6] or the value of the S-matrix at a symmetric point $s = t = 2$ as in the pion toy models in [73] or we could impose a zero at a given value for some component (i.e. add a resonance) and maximize its slope as in [80]. In the next section we will start with a few such maximization questions (some of which are mixed versions of the ones just mentioned) which lead to the integrable S-matrices discussed previously. Then we will move away from these integrable models and find new S-matrices whose physical (ir)relevance we shall speculate about.

7.3 Numerical results

7.3.1 Reproducing integrable models

In this section we show how we can reproduce known integrable theories with $O(N)$ global symmetry. In general, we expect the numerical maximization to reproduce the physical

S-matrices for the appropriate mass spectrum. First, we consider a simple problem which reproduces free theory. Then we focus on the case with bound states and $N > 2$ which gives rise to the Gross-Neveu S-matrix. After that we discuss the maximization procedure leading to the non-linear sigma model. Finally we present the case with $N = 2$ and bound states which reproduces the S-matrix for the kinks of sine-Gordon (or massive Thirring model).

Free theory

Consider a theory with no bound states. Then the various S-matrix components have no poles inside the strip and are therefore bounded by their values at the two boundaries of the strip (i.e. the lower boundary at $\theta \in \mathbb{R}$ and the upper one at $\theta \in i\pi + \mathbb{R}$). At the lower boundary of the physical strip we have unitarity which states that in any of the three representations we have $|S_{\text{rep}}(\theta)| \leq 1$ while in the upper boundary these functions can be as large as allowed by the crossing relations in table 7.2 which relate that upper boundary with the value of the same functions in the lower boundary. For the symmetric component these equations tell us that we can have modulus as large as 1 in the upper boundary which is the same bound as in the lower boundary.[14] Therefore the largest this component can be, anywhere inside the strip is 1 and this is attained for $S_{\text{symmetric}} = 1$ which in turn leads to $S_{\text{rep}} = 1$ for all representations. We see that the theory with no bound states and the largest absolute value for the symmetric component anywhere in the physical strip is the free theory. This is something we can check numerically; it obviously works and is indeed a nice albeit trivial check of our code.

Gross-Neveu

As described in section 7.2.2, there are two bound states appearing in the $2 \to 2$ S-matrix of the fermions of the Gross-Neveu model. These bound states appear in the **singlet and anti-symmetric representations** and have a common mass $m_{\text{GN}} = 2\cos\left(\frac{\pi}{N-2}\right)$. In principle we could maximize any of the two corresponding cubic couplings $g_{\text{sing}}, g_{\text{anti}}$, but it turns out that it is the maximization of g_{anti} which reproduces the Gross-Neveu S-matrix.

---

[14]For the other components the analysis is more complicated and indeed below we will analyze these cases and obtain a myriad of very rich S-matrices. For instance from the first relation in table 7.2 we learn that the singlet component can have magnitude as large as N in the upper boundary with the bound saturated iff the various components saturate unitarity for real θ and are appropriately aligned phases. Similarly, from the second relation we lean that the anti-symmetric component can have absolute value as large as $1 + 2/N$ in the upper boundary.
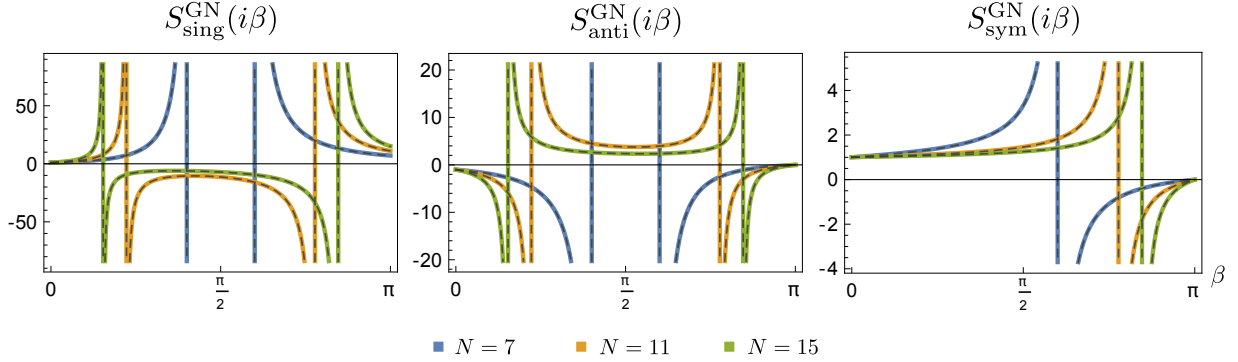
Figure 7.4: Numerical results for the Gross-Neveu spectra $m_{\text{GN}} = 2\cos\left(\frac{\pi}{N-2}\right)$ maximizing the anti-symmetric coupling g_{anti} in the $\theta = i\beta$ line. Notice that the singlet (left) and anti-symmetric (center) S-matrices have two poles: one for each bound state at $\theta = i\lambda_{\text{GN}} = i2\pi/(N-2)$ and another one imposed by the crossing equations at $\theta = i\pi - i\lambda_{\text{GN}}$. The symmetric channel (right) has only the latter pole. The three curves in each representation correspond to different values of N: 7 (blue), 11 (orange) and 15 (green). The bound state pole approaches $\theta = 0$ ($s = 4m^2$) as we increase the parameter N. The numerical results are in perfect agreement with analytic solutions (7.13) plotted in dashed lines. The results were obtained with $n_{\text{grid}} = 70$.

Considering the spectrum above in the dispersion relations (7.11) and implementing the numeric maximization of g_{anti} as explained in section 7.2.3 we find perfect agreement with the integrable solution

$$\mathbf{S}^{\text{GN}}(\theta) = \begin{pmatrix} \frac{\theta+i\pi}{\theta-i\pi}\frac{\theta+i\lambda_{\text{GN}}}{\theta-i\lambda_{\text{GN}}} & & \\ & \frac{\theta+i\lambda_{\text{GN}}}{\theta-i\lambda_{\text{GN}}} & \\ & & 1 \end{pmatrix} F_{\pi-\lambda_{\text{GN}}}(\theta)F_{\pi}(-\theta), \tag{7.13}$$

where $F_a(\theta)$ is defined in (7.8). We performed the numerics for various values of N. In figure 7.4 we show some numerical results against the solution (7.13) for N=7,11,15. The analytic structure of one of the representations is depicted in figure 7.5.

Non-linear sigma model

Another famous integrable model we would like to reproduce is the non-linear sigma model. As discussed in section 7.2.2, this model has no bound states and its S-matrix differs from the Gross-Neveu one by an overall CDD factor. Instead of bound states, the parameter

105
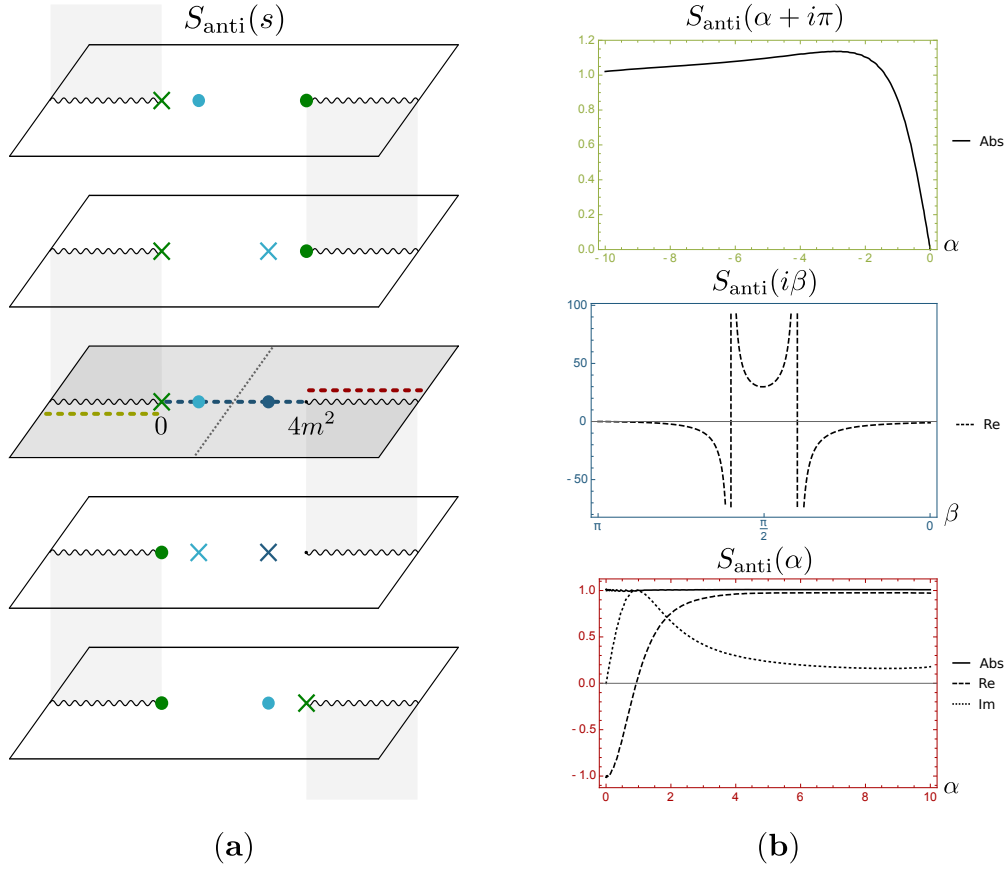
Figure 7.5: (**a**) Analytic structure of the Gross-Neveu anti-symmetric S-matrix in the Mandelstam plane. There is a zero at $s = 0$ (in green), a bound state pole at $s = m_{\mathrm{GN}}^2$ (in dark blue) and a t-channel pole in lighter blue. The green, blue and red dashed lines are respectively the regions below the left cut, between $s \in [0, 4m^2]$ and above the right hand cut where we impose unitarity. (**b**) Numerical results for the corresponding regions in the $\theta = \alpha + i\beta$ plane wit $N = 7$ ($m_{\mathrm{GN}} = 2\cos(\pi/5)$) and $n_{\mathrm{grid}} = 75$. The top panel in green depicts the zero at $\theta = i\pi$ ($s = 0$). The middle panel in blue shows the bound state and t-channel poles. In the red bottom panel we see that unitarity is saturated (solid curve representing the absolute value of the function).

λ_{GN} in (7.8) labels the position of a zero in the symmetric representation. In the numerics, we impose this zero $S_{\mathrm{sym}}(\theta = i\lambda_{\mathrm{GN}}) = 0$ as well as the absence of bound states by setting all cubic couplings to zero. Inspired by the Gross-Neveu case, we maximize the effective quartic anti-symmetric coupling given by $S_{\mathrm{anti}}(i\pi/2)$. With these conditions we are able to reproduce the solution (7.8) as exemplified in figure 7.6 for $N = 6$.

106

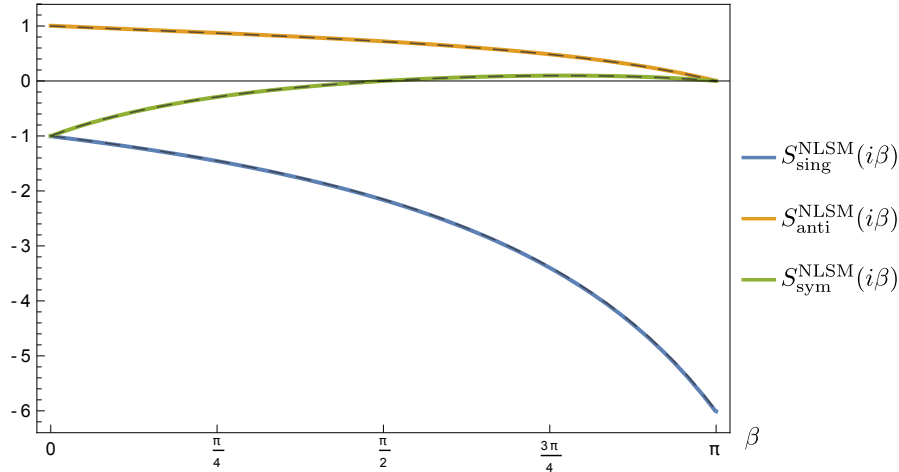Figure 7.6: Numerical results imposing the NLSM zero at $S_{\mathrm{sym}}(i\lambda_{\mathrm{GN}})$ and maximizing $S_{\mathrm{anti}}(i\pi/2)$ for $N = 6$ and $n_{\mathrm{grid}} = 40$. The singlet, anti-symmetric and symmetric S-matrices are plotted respectively in blue, orange and green. These curves perfectly agree with the solution (7.8) in dashed lines. For this value of N the zero sits exactly at the middle of the strip at $\theta = i\pi/2$. Similar plots are obtained for any $N \geq 5$ where only the position of the latter zero changes.

As we decrease N, the zero in the symmetric representation moves towards the upper boundary of the physical strip, reaching it at $N = 4$ and leaving the physical strip for $N < 4$. It would be interesting to understand what is the condition one should impose in order to reproduce the non-linear sigma model for $N < 5$.

In the beautiful work [76] it was pointed out that the space of unitarity, crossing symmetric relativistic S-matrices with $O(N)$ symmetry has a very rich geometric structure with special cusps. Provided we point more or less towards one such cusp, any maximization functional will push us there. They could identify the non-linear sigma model as a cusp in this theory space, without imposing the zero at $S_{\mathrm{sym}}(\theta = i\lambda_{\mathrm{GN}})$. It would be fascinating to explore more throughly the geometry of this S-matrix space, in particular for the various other maximization problems considered in the following sections.

Sine-Gordon kinks

Another important result derived in [72] is given by the case $N = 2$ corresponding to the integrable S-matrix for the sine-Gordon kinks and antikinks.[15] The kink A and antikink

---

[15]Equivalently, one can think about the fundamental fermions of the massive Thirring model.
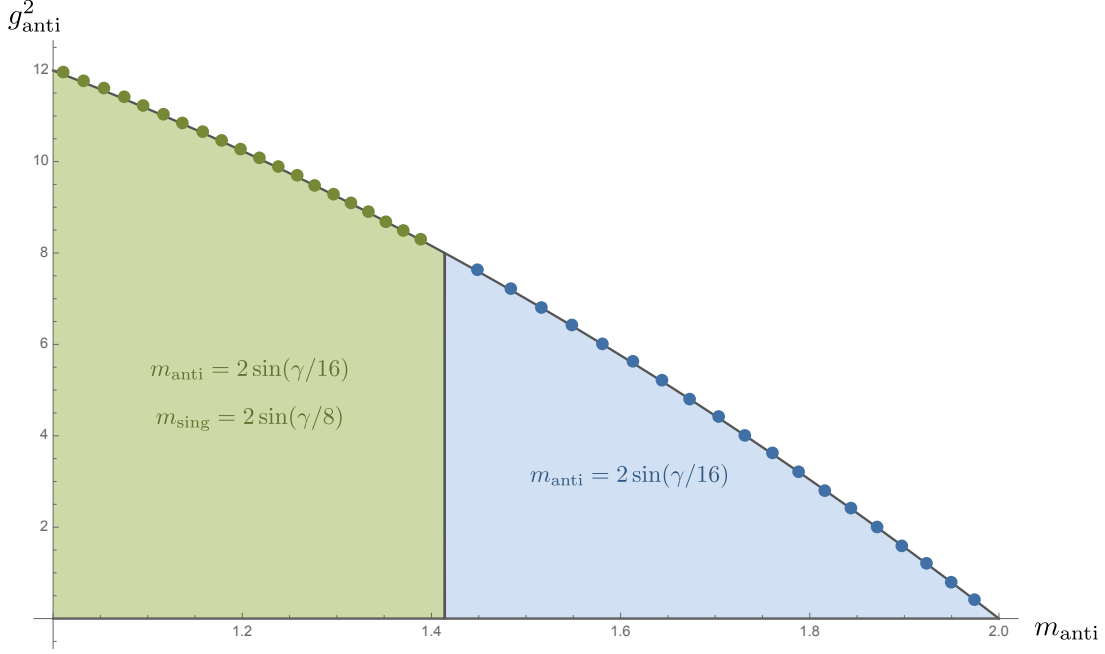
Figure 7.7: Comparison between the $N = 2$ sine-Gordon kinks solution and numerical results. In the blue region corresponding to $4\pi < \gamma < 8\pi$ we impose one bound state in the anti-symmetric representation with mass $m_{\text{anti}} = 2\sin(\gamma/16)$ and a zero $S_{\text{sing}}[i(-\pi + \gamma/8)] = 0$. In the green region where $8\pi/3 < \gamma < 4\pi$ we keep the anti-symmetric bound state and impose a new bound state in the singlet representation with mass $m_{\text{sing}} = 2\sin(\gamma/8)$ as well as a zero $S_{\text{sing}}[i(-\pi + \gamma/2)] = 0$. (We avoid the point $m_{\text{sing}} = \sqrt{2}$ because of our subtraction scheme.) The numerical points obtained with $n_{\text{grid}} = 40$ match perfectly with the analytic solution (truncating the infinite product in (7.15) to 9) depicted in the grey curve.

$\bar{A}$ can be packed into a doublet $A = A_1 + iA_2$ ($\bar{A} = A_1 - iA_2$). The solution has a free parameter γ [16] and reads

$$\mathbf{S}(\theta) = -\frac{1}{\pi} U(\theta) \begin{pmatrix} \sin\left(\frac{8\pi i\theta}{\gamma}\right) - \sin\left(\frac{8\pi^2}{\gamma}\right) \\ \sin\left(\frac{8\pi i\theta}{\gamma}\right) + \sin\left(\frac{8\pi^2}{\gamma}\right) \\ -\sin\left(\frac{8\pi(\pi+i\theta)}{\gamma}\right) \end{pmatrix}, \tag{7.14}$$

---

[16] As explained in [72], this parameter is related to the coupling in the sine-Gordon Lagrangian $\mathcal{L}_{\text{sG}} = \frac{1}{2}(\partial\phi)^2 + m_0^2/\beta^2 \cos(\beta\phi)$ through $\gamma = \beta^2/(1 - \frac{\beta^2}{8\pi})$.

where the prefactor is given by

$$U(\theta) = \Gamma\left(\frac{8\pi}{\gamma}\right)\Gamma\left(1+i\frac{8\theta}{\gamma}\right)\Gamma\left(1-\frac{8\pi}{\gamma}-i\frac{8\theta}{\gamma}\right)\prod_{n=1}^{\infty}\frac{R_n(\theta)R_n(i\pi-\theta)}{R_n(0)R_n(i\pi)}, \quad (7.15)$$

$$R_n(\theta) = \frac{\Gamma\left[2n\frac{8\pi}{\gamma}+i\frac{8\theta}{\gamma}\right]\Gamma\left[1+2n\frac{8\pi}{\gamma}+i\frac{8\theta}{\gamma}\right]}{\Gamma\left[(2n+1)\frac{8\pi}{\gamma}+i\frac{8\theta}{\gamma}\right]\Gamma\left[1+(2n-1)\frac{8\pi}{\gamma}+i\frac{8\theta}{\gamma}\right]}.$$

The S-matrix (7.14) has a very rich structure. As we vary the parameter γ, the bound state spectrum changes. The bound state masses are given by $m_n = 2m\sin(n\gamma/16)$ with $n < 8\pi/\gamma$ and they alternate between the anti-symmetric (n odd) and singlet representations (n even). The bound state with $n = 1$ is the sine-Gordon breather whose S-matrix was rediscovered in [6]. For $\gamma \geq 8\pi$ all bound states disappear from the spectrum (i.e. the corresponding poles leave the physical strip).

We shall focus on two regimes which comprehend $1 < m_1 < 2$:

• For $4\pi \leq \gamma < 8\pi$ there is a single bound state in the **anti-symmetric representation** whose mass takes values $\sqrt{2} < m_{\text{anti}} < 2$ and is given by $m_{\text{anti}} = 2\sin(\gamma/16)$. However, imposing this bound state and maximizing g_{anti} is not enough to reproduce the integrable model. Taking inspiration from the NLSM discussed in the previous section, we shall impose one of the zeros in the solution (7.14). One zero which is always inside the physical strip for this range of γ is $S_{\text{sing}}[i(-\pi + \gamma/8)] = 0$ which can easily be seen in the first component of (7.14).

• For $8\pi/3 < \gamma < 4\pi$ there is another bound state in the **singlet representation** with mass $m_{\text{sing}} = 2\sin(\gamma/8)$, as well as the previous bound state which for this range takes values $1 < m_{\text{anti}} < \sqrt{2}$. For the numerics, we keep maximizing the anti-symmetric coupling and impose one zero inside the physical strip, this time at $S_{\text{sing}}[i(-\pi + \gamma/2)]$.

In figure 7.7 we show the maximum coupling g_{anti} obtained numerically for both regimes which nicely matches the analytic solution (7.14). The S-matrices agree perfectly as well.

In [6] it was shown that the sine-Gordon S-matrix for the lightest breathers is quite special. It has a single bound state flowing (the second lightest breather) and of all theories with a single bound state it is the one with the largest possible coupling. Here we see that the kink S-matrix of sine-Gordon also comes about from a maximization procedure as the theory with $O(2)$ symmetry with the largest possible coupling and appropriate resonances (zeroes). These two are related. As mentioned earlier, breathers are themselves bound states of kinks so we can obtain the breather S-matrix by fusing the kink S-matrix. In

that sense, the kink S-matrix is the most fundamental one and it is nice to see it come up naturally here. There are also intermediate objets such as the scattering of kinks and breathers. It would be very interesting to look for those as well.

7.3.2 Away from integrable points

In this section we present some of the numerical results obtained for non integrable spectra. The simplest possibility is to consider theories with a single bound state transforming in one of the three representations and maximize its associated cubic coupling $g_{\rm rep}$. Figure 7.8 depicts the maximum couplings as we vary the bound state mass $m_{\rm rep}$ and N. In these numerics, we can also read of the corresponding S-matrices. We observe – as in [6] – that they all saturate unitarity (and thus admit no multi-particle production). That is, for $s > 4m^2$ they all satisfy $|S_{\rm rep}| = 1$ within our numerical precision. Also as in [6] we observe that these couplings vanish as the bound state becomes weakly coupled as expected. It should be possible (and interesting) to analyse this perturbative corner analytically.[17] In the next section we will show how these maximal coupling curves (and others) can be reproduced analytically at large N.

What is *not* shown in figure 7.8 is how interesting the corresponding S-matrices are. By plotting them in the complex θ plane we found remarkably rich structures of infinite poles and zeros in the various θ-strips.[18] An example is depicted in figure 7.9.

Interesting as they might be, we will not be able to compare the theories saturating the bounds in figure 7.8 with any known theory. The reason is that since they have no particle production, they should probably be integrable. But since they have a single bound state they cannot satisfy Yang-Baxter. So, if they exist they must be something more exotic. We will speculate further on the physics of such theories in the discussions.

To make contact with known integrable examples we can consider one bound state in the anti-symmetric representation and another one in the anti-symmetric representation with equal mass and maximize the cubic coupling to the anti-symmetric one. When the mass passes by the value $m_{\rm GN} = 2\cos(\frac{\pi}{N-2})$ we do obtain the Gross-Neveu model as seen

---

[17]The interplay with no-particle production could be very interesting to study here since there are no theories with a simple perturbative scalar Lagrangian, $O(N)$ symmetry and no particle production [81]. The known integrable models with $O(N)$ symmetry are strongly coupled isolated points.

[18]Note that we explore the S-matrices across all the Mandelstam cuts while our numerical ansatz is originally designed to parametrize the physical sheet alone. We can do this because unitarity is always saturated from $4m^2$ until the first inelastic threshold which leads to an exact functional relation $S_{\rm rep}(\theta)S_{\rm rep}(-\theta) = 1$ which we can combine with crossing to visit any strip in θ, i.e. any sheet in s. See e.g. [82] for a similar analysis for a theory with a single particle.
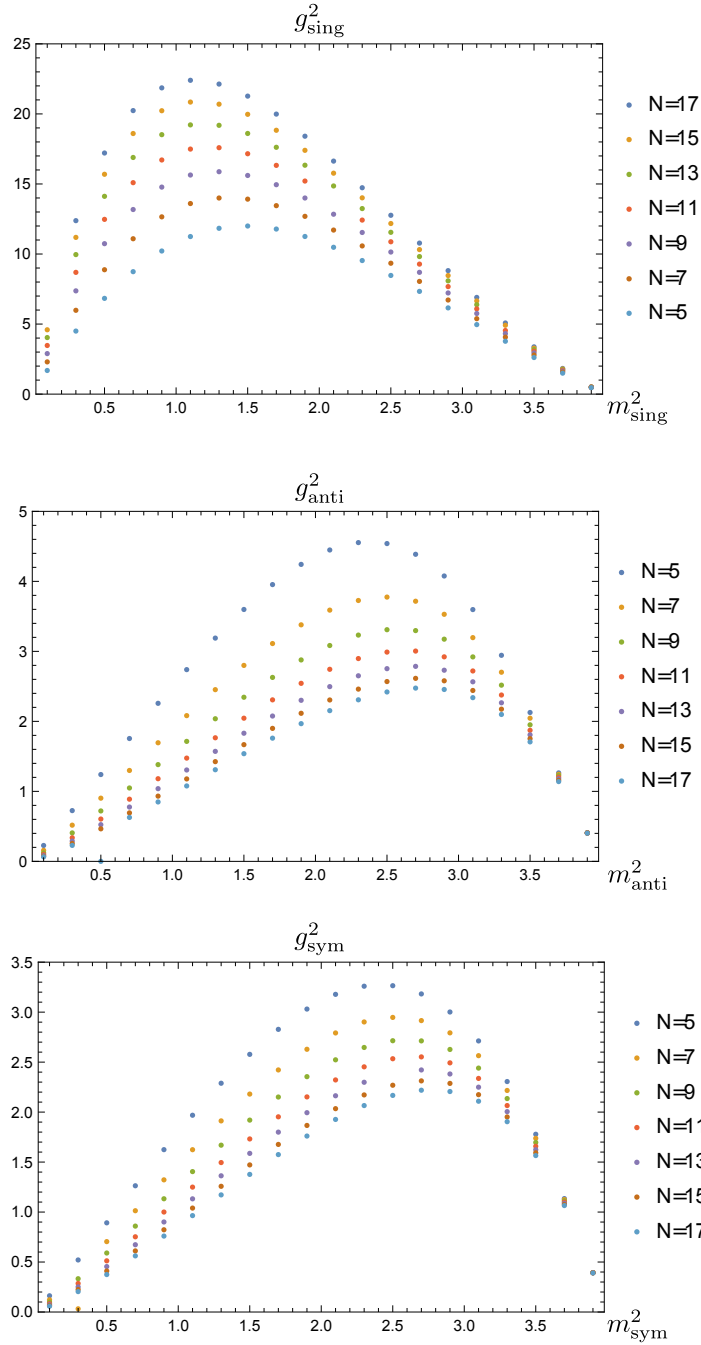
Figure 7.8: Maximum couplings obtained numerically for the case of a single bound state in the singlet (top), anti-symmetric (middle) or symmetric (bottom) representation. The three panels correspond to the three possible representations. (The numerics were done with $n_{\text{grid}} = 70$ and various N's.)
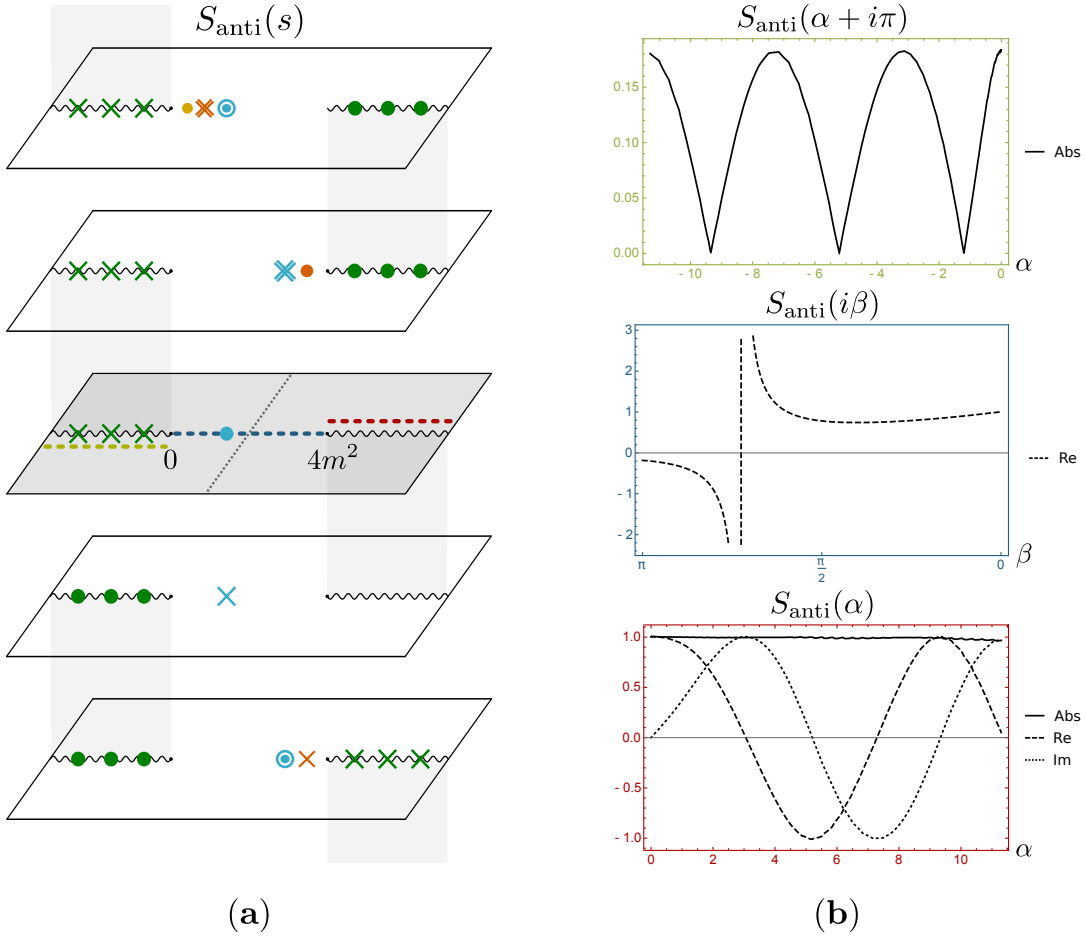
Figure 7.9: **(a)** Analytic structure for $S_{\text{anti}}(s)$ for a theory with a single singlet bound state with maximal cubic coupling. Note the presence of zeroes in the left cut of the physical sheet and the t-channel pole depicted in blue. The red line above the right cut is where we impose unitarity. **(b)** Numerical results for this case in various regions of the $\theta = \alpha + i\beta$ plane with $m_{\text{singlet}} = \sqrt{3}$, $N = 7$ and $n_{\text{grid}} = 70$. In the top panel in green we see that there are infinitely many zeros (resonances) in the $\theta = \alpha + i\pi$ line corresponding to the left cut in the Mandelstam plane. The middle panel in blue shows the t-channel pole. In the red bottom panel, the solid line (absolute value of the function) exhibits the saturation of unitarity, whereas the dashed and pointed lines (real and imaginary parts) show the oscillatory behaviour leading to the zeros of the top green panel. This very rich analytic structure is to be compared with the much simpler figure 7.5 encountered before!
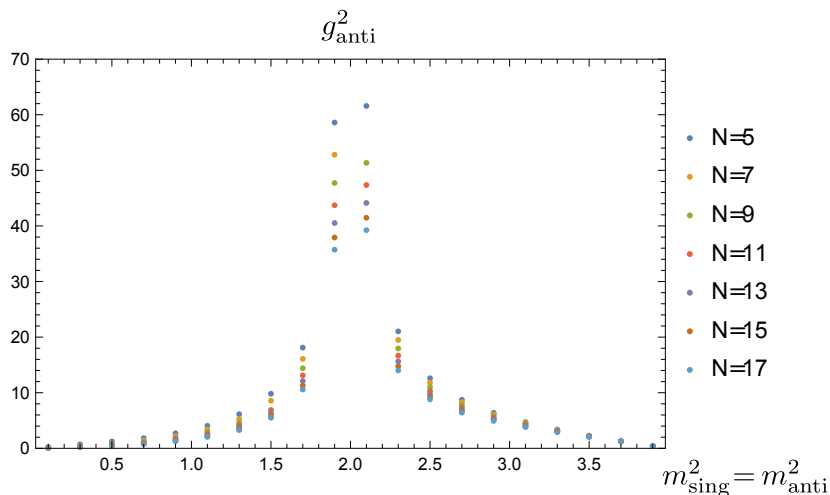
Figure 7.10: Maximum couplings obtained numerically for the case of one bound state in the anti-symmetric representation and another one in the anti-symmetric representation with equal mass. We maximize the anti-symmetric coupling (as in the Gross-Neveu model) and plot for various N. The maximum coupling decreases for larger N. The numerics were done with $n_{\text{grid}} = 70$.

in the previous section. Away from this point, the bound is deformed smoothly but the S-matrices are quite different, with a very exotic analytic structure akin to that illustrated in figure 7.9. The maximum couplings we obtained for various N and bound state masses are shown in figure 7.10. The divergence at $m = \sqrt{2}$ comes from the collision of s and t-channel poles as in [6]. In this case they screen each other by simply setting $g^2_{\text{sing}} = \frac{N}{2} g^2_{\text{anti}}$.

Below, we will revisit some of the cases found numerically here. To do so, first we will get some further insight from a large N analysis in section 7.4.1 before attacking the full finite N case in section 7.4.2.

7.4 Analytic results

7.4.1 Large N

In this section we will consider large N. We will be able in this way to proceed analytically to a much greater extent and get some insights about the general analytic structures to be expected in the finite N optimization numerics.

The key place where N enters and where large N presents some simplifications is in

crossing represented in table 7.2 and quoted here again for convenience:

$$S_{\mathrm{sing}}(i\pi - \theta) \;\; = \;\; \frac{1}{N}S_{\mathrm{sing}}(\theta) + \left(\frac{1}{2} - \frac{N}{2}\right)S_{\mathrm{anti}}(\theta) + \left(\frac{N}{2} + \frac{1}{2} - \frac{1}{N}\right)S_{\mathrm{sym}}(\theta) \quad (7.16)$$

$$S_{\mathrm{anti}}(i\pi - \theta) \;\; = \;\; -\frac{1}{N}S_{\mathrm{sing}}(\theta) + \frac{1}{2}S_{\mathrm{anti}}(\theta) + \left(\frac{1}{2} + \frac{1}{N}\right)S_{\mathrm{sym}}(\theta) \quad (7.17)$$

$$S_{\mathrm{sym}}(i\pi - \theta) \;\; = \;\; \frac{1}{N}S_{\mathrm{sing}}(\theta) + \frac{1}{2}S_{\mathrm{anti}}(\theta) + \left(\frac{1}{2} - \frac{1}{N}\right)S_{\mathrm{sym}}(\theta) \quad (7.18)$$

At real θ all S-matrices saturate unitarity; they are phases so they are all order $\mathcal{O}(N^0)$ functions, even at large N. At the upper boundary of the physical strip, at $\theta \in i\pi + \mathbb{R}$, we can use these crossing equations to see what values the various S-matrices can take. If we can bound the functions in the two boundaries of the physical strip then we can use the maximum modulus principle to bound the functions everywhere inside the strip. That is the main idea which we will explore.

The singlet component can be very large in the upper boundary of the strip. It can be of order $\mathcal{O}(N)$ since it is a linear combination of phases and two of them are weighted by huge coefficients, highlighted in blue in (7.16). The anti-symmetric and symmetric components will be at most of order $\mathcal{O}(N^0)$ at the upper boundary since they are linear combinations of phases but the prefactors in (7.16-7.17) are at most of order $\mathcal{O}(N^0)$. We can imagine the values inside the strip to smoothly interpolate between their two boundaries. Then we would conclude that anti-symmetric and symmetric representations would remain small while singlet would be the much larger dominant contribution. This is of course what we expect in a large N theory since there is a lot of phase space to scatter into when we form a singlet. Technically, in large N vector theories, dimmer-like colour loops dominate. Indeed, in all the examples we will now explore, it is by analyzing the singlet component that we can learn a great deal very easily.

Maximum singlet effective quartic coupling

Suppose we are after the S-matrix with the largest singlet component in the middle of the physical strip, that is at $\theta = i\pi/2$, in a theory with no bound states (i.e. no poles inside the physical strip). The value at the middle of the strip can only be as large as its value at the boundary of the strip by the maximum modulus principle. At the upper boundary, the singlet S-matrix can have at most absolute value $N/2 + N/2 = N$ if the phases S_{sym} and S_{anti} are opposite to each other (at least for real θ) so that the terms in blue in (7.16) add up. So all in all, we have a function without poles which satisfies $|S_{\mathrm{singlet}}(\theta)| \leq 1$ at

114

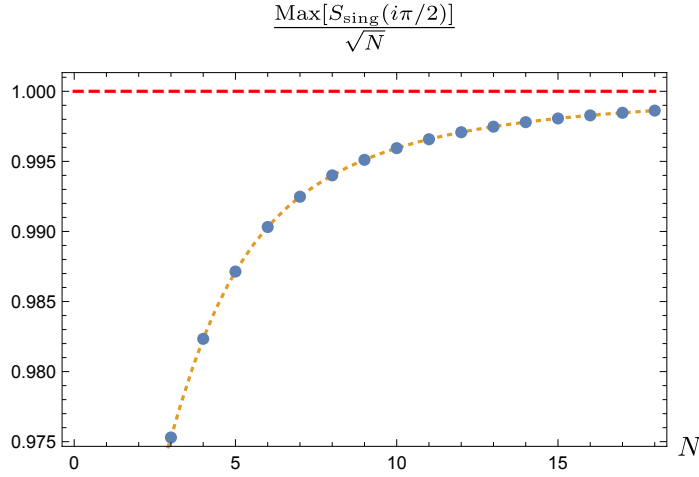$$\frac{\mathrm{Max}[S_{\mathrm{sing}}(i\pi/2)]}{\sqrt{N}}$$

Figure 7.11: Numerical results of the maximization procedure described in section 7.2.3 for the maximal value of the singlet S-matrix at the middle of the physical strip for various values of N. We expect the result to approach $\sqrt{N}$ as $N \to \infty$ as illustrated by the red dashed line. The yellow dotted line which perfectly passes by the numerical blue dots is the result of a more refined finite N analytic analysis which we will consider in section 7.4.2.

real θ and $|S_{\mathrm{singlet}}(i\pi + \theta)| \le N$ at the other boundary of the physical strip. One function which clearly saturates these bounds is

$$S_{\mathrm{singlet}}^{\mathrm{optimal}}(\theta) = e^{\frac{\theta}{i\pi} \log(N)} \tag{7.19}$$

which is indeed a phase for $\theta \in \mathbb{R}$, equal to N times a phase for $\theta \in i\pi + \mathbb{R}$ and real analytic for purely imaginary θ. This is the optimal solution to our problem since the ratio $S_{\mathrm{singlet}}\theta)/S_{\mathrm{singlet}}^{\mathrm{optimal}}(\theta)$ has absolute value smaller or equal to 1 at both boundaries and thus is at most 1 in the middle of the strip. Hence

$$\mathrm{Max}[S_{\mathrm{singlet}}(i\pi/2)] = \sqrt{N} . \tag{7.20}$$

Now we can test this against the numerics described before. Performing them for various values of N leads to results in figure 7.11 which beautifully matches with our prediction (7.20) as we extrapolate to infinite N.

We can also learn about all the S-matrices themselves and their analytic properties. As we saw before, for the singlet component to be as large as possible the symmetric and anti-symmetric components ought to be opposite of each other for real θ so that the two blue terms in (7.16) would add up constructively. In this case, where we impose no poles that force these components to be different, it is natural to assume that $S_{\mathrm{sym}} = -S_{\mathrm{anti}}$

115

everywhere. (This is confirmed by the numerics at any finite N.) Then, (7.16) immediately leads to

$$S_{\text{sym}}(\theta) \simeq \frac{1}{N} S_{\text{sing}}(i\pi - \theta) - \frac{1}{N^2} S_{\text{sing}}(\theta) \,. \tag{7.21}$$

Note that the last term can be dropped inside the physical strip and its boundary *except* at the upper boundary where both terms are small and of order $\mathcal{O}(N^{-1})$. So, summarizing, we have

$$S_{\text{sing}}(\theta) \simeq \exp\left(\frac{\theta}{i\pi}\log(N)\right) \tag{7.22}$$

$$S_{\text{sym}}(\theta) \simeq \exp\left(-\frac{\theta}{i\pi}\log(N)\right) - \frac{1}{N^2}\exp\left(\frac{\theta}{i\pi}\log(N)\right) \tag{7.23}$$

$$S_{\text{anti}}(\theta) = -S_{\text{sym}}(\theta) \tag{7.24}$$

valid anywhere inside *and* on the boundary of the physical strip. (But not elsewhere!) At the upper boundary we get $S_{\text{sym}}(i\pi - \theta) \propto \frac{1}{N}\sin(\frac{\theta}{\pi}\log(N))$ so we see that this solution exhibits an infinite amount of zeros (resonances) right at the upper boundary of the physical strip in the symmetric and anti-symmetric channels. We can again compare this expectation with the finite N numerics to see that these zeros are there indeed, see also figure 7.15 below. These zeroes are a generic feature of the solutions in fact and arose already in another example, see figure 7.9 above. The appearance of infinite resonances and periodicity along the real θ direction were encountered previously in other models like the ones studied in [83] and [84]. In the context of the S-matrix bootstrap resonances were recently discussed in [80].

Finally, note that while (7.22-7.24) are valid only in the physical strip, we can extend the solution to any value of θ since we can combine crossing symmetry with unitarity saturation which reads $S_{\text{rep}}(-\theta) = 1/S_{\text{rep}}(\theta)$. For example, using unitarity we see that these infinitely many zeros at the upper boundary of the physical sheet become poles on the lower boundary of the so called mirror sheet $\text{Im}(\theta) \in [-\pi, 0]$. Then we can use crossing to learn about the analytic structure of this solution in the strip above the physical strip where $\text{Im}(\theta) \in [0, 2\pi]$ and then unitarity again etc. In this way, we can deduce the full analytic structure of this function to be as given as discussed in section 7.4.2 below. We see that at large N the problem simplifies so much that we cannot only solve the maximization problem but also get key insights about the analytical structure of the various S-matrix elements. Indeed, assuming such structure persists at finite N we will be able to guess the full analytic solution for this maximization problem below.

One bound state

Next let us consider the problem of large N theories with a single bound state whose coupling we maximize.

First assume that the bound state is in the **singlet representation**. From the crossing relation (7.16)

$$S_{\text{sing}}(i\pi - \theta) = \frac{1}{N} S_{\text{sing}}(\theta) + \left(\frac{1}{2} - \frac{N}{2}\right) S_{\text{anti}}(\theta) + \left(\frac{N}{2} + \frac{1}{2} - \frac{1}{N}\right) S_{\text{sym}}(\theta), \qquad (7.25)$$

we learn two things. The first one is that the t-channel pole residue is smaller than the s-channel pole by a factor of $1/N$ so that at large N we can effectively drop it and keep a single pole at $\theta = i\lambda$ (the s-channel pole for a bound state of mass $m_{\text{BS}} = 2m \cos(\lambda/2)$). The second thing was discussed in the last section: to make the singlet component as large as possible it is optimal to anti-align the symmetric and anti-symmetric components; in that case the two terms in blue in (7.16) add up so that the singlet component has maximal magnitude N at the upper boundary. The punch-line is that we simply should multiply the solution (7.19) of the previous section by a function which introduces a single pole at $\theta = i\lambda$, is real for purely imaginary θ and is a phase in both boundaries of the physical strip. Such function is

$$f_\lambda(\theta) \equiv \frac{1 - e^{+i\lambda + \theta}}{e^\theta - e^{+i\lambda}} . \qquad (7.26)$$

We thus conclude that the optimal solution is given by

$$S_{\text{sing}}^{\text{optimal}}(\theta) = e^{\frac{\theta}{\pi i} \log(N)} f_\lambda(\theta), \qquad (7.27)$$

and therefore

$$\max\left(g_{\text{sing}}^2\right) = (2 \sin \lambda) \times (2N^{\lambda/\pi} \sin \lambda) \qquad (7.28)$$

where the first factor is a simple Jacobian since we define the coupling as the residue in s. This indeed matches beautifully with the large N extrapolation of our numerics as indicated in figure 7.12. We could also, as in the previous section, further determine the other channel S-matrices. The logic is exactly as before and leads to

$$S_{\text{sym}}^{\text{optimal}}(\theta) = -S_{\text{anti}}^{\text{optimal}}(\theta) = \frac{1}{N} \left[S_{\text{sing}}^{\text{optimal}}(i\pi - \theta) - \frac{1}{N} S_{\text{sing}}^{\text{optimal}}(\theta) \right] . \qquad (7.29)$$

At the boundary of the strip this solution exhibits again a rich pattern of resonances which one can indeed observe in the numerics at finite N.
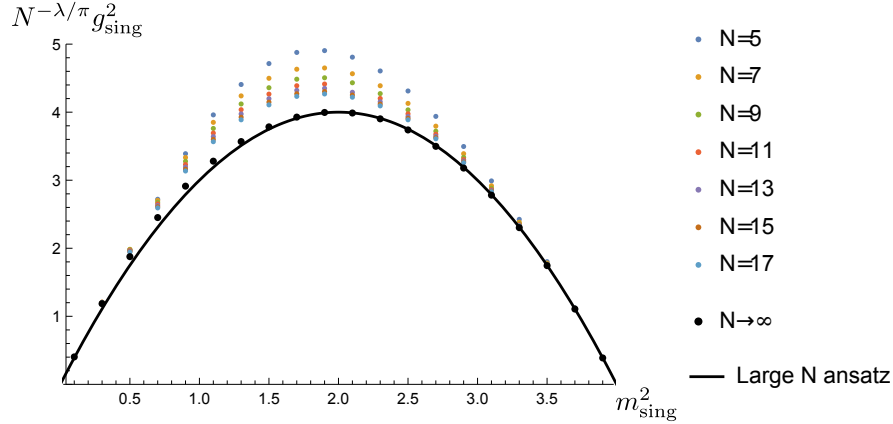
Figure 7.12: Comparison between the numerics discussed in section 7.3.2 and large N analysis for the case with a single pole in the singlet representation. The maximum couplings are rescaled according to the power of N in (7.28). The finite N results in figure 7.8 (coloured points) are extrapolated to infinity (black points) and matched against the large N ansatz (solid line).

As a second example, consider a single pole in the **anti-symmetric representation** *or* in the **symmetric representation**. From (7.25) we see that an s-channel pole in either of these representations induces a t-channel pole in the singlet component whose magnitude is $N/2$ larger. In the right hand side of (7.25) the anti-symmetric and symmetric representations show up with opposite prefactors at large N however the residue in the anti-symmetric case comes with a further minus sign – recall (7.12). Therefore, we see that both problems lead to the very same maximization problem as far as the singlet component is concerned: that of finding a t-channel pole in the singlet channel to be as *large and negative* as possible. Following the same logic as in the previous case we thus conclude that the optimal solution for the singlet representation would read

$$S_{\text{sing}}^{\text{optimal}}(\theta) = -e^{\frac{\theta}{\pi i} \log(N)} f_{\pi-\lambda}(\theta) \,. \tag{7.30}$$

Computing the residue and multiplying by $-2/N$ and the usual Jacobian we then obtain the optimal large N solution which as explained above coincides for these two problems:

$$\max \left(g_{\text{anti}}^2 \right) \big|_{\text{single pole anti}} = \max \left(g_{\text{sym}}^2 \right) \big|_{\text{single pole sym}} = 8 \sin^2(\lambda) N^{-\lambda/\pi} \,. \tag{7.31}$$

In figures 7.13(**a**) and 7.13(**b**) we see that the numerics for these two cases, although different at finite N, beautifully converge towards this universal prediction as we extrapolate them to infinite N.
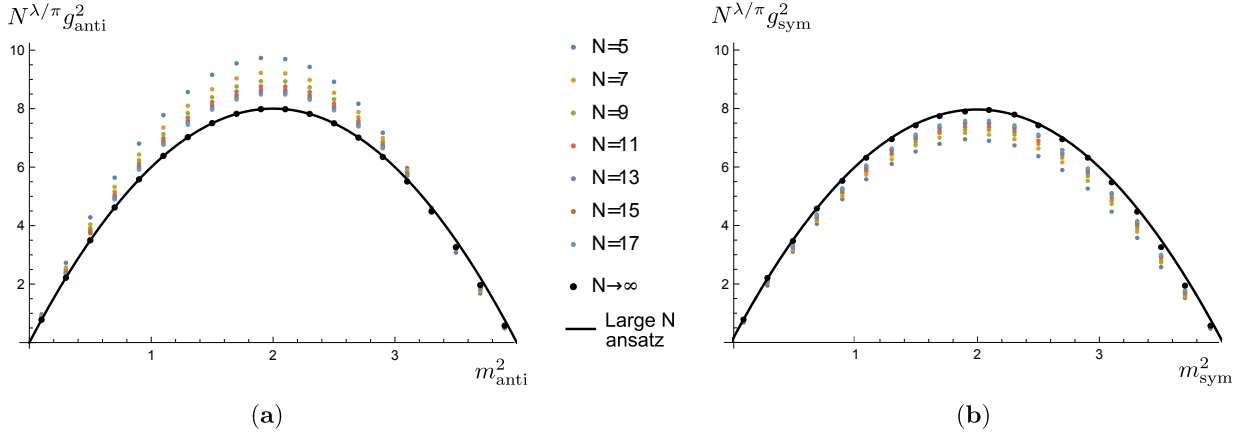
Figure 7.13: Comparison between the finite N numerics and the large N analysis for (**a**) a single bound state in the anti-symmetric representation and (**b**) a single bound state in the symmetric representation. As discussed in the main text, both cases lead to the same maximum coupling at large N given in equation (7.31) and represented here by the solid line.

Note that in all three cases discussed in this section, even when we wanted to maximize couplings in other channels, the key was to study the singlet component at large N. This is in line with the intuition advocated at the beginning of this section.

Two bound states with same mass

Let us consider a final large N example where the theory has two bound states with equal mass, one in the **singlet representation** and another one in the **anti-symmetric representation** and we are maximizing the anti-symmetric coupling. This case is relevant since it contains the Gross-Neveu model for the particular value of the masses $m_{\text{sing}} = m_{\text{anti}} = 2\cos(\pi/(N-2))$. As before, we want to find the large N optimal solution for the singlet representation and use (7.25) to read g_{anti}^2. This solution should be again a phase at the lower boundary of the physical strip and of order $\mathcal{O}(N)$ at the upper boundary. Since there is a bound state in the singlet representation, we should have an s- and a t-channel pole in that component. However, in contrast to (7.27), we cannot omit the t-channel pole because the anti-symmetric representation has also an s-channel pole, i.e. when evaluating (7.25) at $\theta = i\lambda$ we need to keep the first two terms on the right. We thus
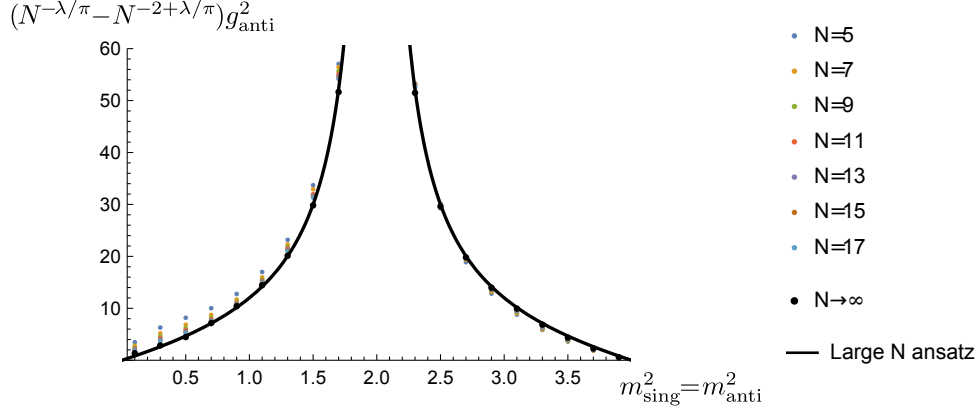
Figure 7.14: Comparison between the finite N numerics and the large N analysis for two equal mass bound states in the singlet and anti-symmetric representations. The maximum couplings are rescaled by the power of N in (7.34). The finite N results in figure 7.10 (coloured points) are extrapolated to $N \to \infty$ (black dots) and compared to the large N result (7.34) (solid black line).

conclude that the optimal solution is given by[19]

$$S_{\text{sing}}^{\text{optimal}}(\theta) = e^{\frac{\theta}{\pi i} \log(N)} \operatorname{sign}(\lambda - \pi/2) f_\lambda(\theta) f_{\pi-\lambda}(\theta) \,. \tag{7.32}$$

From (7.25) we get the following large N equation between the residues

$$\operatorname*{Res}_{\theta=i\lambda} S_{\text{anti}}(\theta) \approx \frac{2}{N} \left[\operatorname*{Res}_{\theta=i\lambda} S_{\text{sing}}(\theta) + \frac{1}{N} \operatorname*{Res}_{\theta=i\pi-i\lambda} S_{\text{sing}}(\theta) \right] \,, \tag{7.33}$$

which after the replacement of the optimal solution (7.32) leads to the maximum coupling

$$\max(g_{\text{anti}}^2) = (2 \sin \lambda) \times \left(N^{-\lambda/\pi} - N^{-2+\lambda/\pi} \right) 4|\tan \lambda| \,. \tag{7.34}$$

The term $N^{-2+\lambda/\pi}$ in the previous equation is subleading for small λ but becomes relevant as we reach $\lambda = \pi$ (e.g. as the mass of the bound states approaches zero). The divergence at $m_{\text{BS}}^2 = 2$ given by the screening of singlet and anti-symmetric poles is nicely reproduced by the factor of $|\tan \lambda|$ in (7.34). In figure 7.14 we confirm that this result nicely matches with the large N extrapolation of the numerics discussed in section 7.2.3.

7.4.2 Finite N

In this section we discuss the analytic solutions at finite N found in two cases: the maximization of $S_{\text{sing}}(i\pi/2)$ without bound states, and a single bound state in the singlet

---

[19]The product $f_\lambda(\theta) f_{\pi-\lambda}(\theta)$ is nothing but the usual CDD factor $f_\lambda(\theta) f_{\pi-\lambda}(\theta) = -\frac{\sinh\theta + i\sin\lambda}{\sinh\theta - i\sin\lambda}$.

representation. As we will see, these solutions preserve some of the features found at large N in the previous section and nicely match the numerical results at finite N.

Maximization/minimization singlet channel without bound states

Consider a theory without bound states where we maximize $S_{\text{sing}}(i\pi/2)$. As discussed in section 7.4.1, at large N the symmetric and anti-symmetric representations antialign so that the singlet channel is as large as possible. Somewhat surprisingly, our numerics show that in the present case the equality $S_{\text{anti}}(\theta) = -S_{\text{sym}}(\theta)$ holds at finite N. We shall impose this condition in our derivation below. Another important feature observed at large N is the presence of a sequence of zeros in $S_{\text{sym}}(\theta)$ at the upper boundary of the physical strip. For each of these zeros, unitarity+crossing implies there is an infinite sequence of zeros and poles in higher sheets. Since this is a general property of $O(N)$ S-matrices, let us carefully explain the logic leading to this structure.

Let us examine the consequences of a zero in the physical strip situated at some value θ^* for a given representation. From unitarity we see that there should be a pole in the $\theta \in [-i\pi, 0]$ strip at $-\theta^*$ for the same representation. Through the crossing equations, this pole implies the presence of more poles at $i\pi + \theta^*$ for all representations in the $\theta \in [i\pi, 2i\pi]$ strip. We can use unitarity again to observe that all representations should have a zero at $-i\pi - \theta^*$. Furthermore, crossing tells us that there are zeros as well at $2i\pi + \theta^*$.[20] Continuing this logic we are naturally lead to the functions $F_a(\theta)$ defined in (7.8) and present in the integrable solutions of section 7.2.2. These functions are explicitly unitary and encode some of the properties the S-matrices should satisfy from crossing.

Going back to the case at hand, we assume (based on numerical observations) that the zeros at $\theta \in i\pi + \mathbb{R}$ are periodically spaced by π^2/ν, where ν is a parameter to determine. Following these zeros through crossing and unitarity as in the argument above we arrive at the following ansatz

$$\mathbf{S}(\theta) = \begin{pmatrix} \frac{\sinh\left[\nu\left(1 - \frac{i\theta}{\pi}\right)\right]}{\sinh\left[\nu\left(1 + \frac{i\theta}{\pi}\right)\right]} \\ -1 \\ 1 \end{pmatrix} \prod_{n=-\infty}^{\infty} F_{\pi + \frac{in\pi^2}{\nu}}(-\theta). \tag{7.35}$$

---

[20]It is easy to see in the crossing equations (7.16-7.18) that a single pole (zero) at θ^* in one of the representations does (not) imply extra poles (zeros) at $i\pi - \theta^*$. If we have more than one pole at θ^*, the functions may conspire in such a way that their residues cancel so that there is no pole at $i\pi - \theta^*$ in a given representation. In contrast, zeros at θ^* in all representations does always imply zeros at $i\pi - \theta^*$ for all representations.

Replacing this ansatz into the crossing equations (7.16-7.18) fixes the remaining parameter ν to be $N = 2\cosh(\nu)$. The analytic structure of this solution is described in figure 7.15.[21]

Another way to write the S-matrices in (7.35) is

$$S_{\text{sing}}(\theta) = e^{-i\theta\nu/\pi} \prod_{l=1}^{\infty} \frac{\sinh\left[\frac{\nu}{\pi}(i\theta - 2l\pi)\right] \sinh\left[\frac{\nu}{\pi}(i\theta + (2l+1)\pi)\right]}{\sinh\left[\frac{\nu}{\pi}(i\theta + 2l\pi)\right] \sinh\left[\frac{\nu}{\pi}(i\theta - (2l+1)\pi)\right]}$$

$$S_{\text{sym}}(\theta) = -S_{\text{anti}}(\theta) = e^{i\theta\nu/\pi} \prod_{l=1}^{\infty} \frac{\sinh\left[\frac{\nu}{\pi}(i\theta + (2l-1)\pi)\right] \sinh\left[\frac{\nu}{\pi}(i\theta - 2l\pi)\right]}{\sinh\left[\frac{\nu}{\pi}(i\theta - (2l-1)\pi)\right] \sinh\left[\frac{\nu}{\pi}(i\theta + 2l\pi)\right]}$$

which allows one to make direct contact with the large N results of section 7.4.1 rather trivially. Indeed, at large N we have $\nu \simeq \log(N)$ so that all arguments in these expressions are very large. As such, inside each θ strip we can simplify all sinh's to one of its exponentials. In this way we see that inside any θ strip any component is given by a simple power of N times $e^{\mp i\theta\nu/\pi}$. For instance, in the physical sheet we recover (7.22) and (7.23) (recall that inside the strip we can drop the last term in (7.23)). The above representation is also more suitable for numerical evaluation, since when truncating the product to some $l_{\max}$ we keep the poles and zeros closer to the physical strip. In fact, it was using this representation with $l_{\max} = 50$ that we generated the yellow curve in figure 7.11.

If instead we want to minimize $S_{\text{sing}}(i\pi/2)$ we would be led to the same solution with an overall minus sign.

Given that the solution (7.35) saturates unitarity, it is natural to ask if it also obeys Yang-Baxter equations. As one can check it does satisfy factorization and in fact was written before in the appendix of [75]![22] To our knowledge, a physical model corresponding to this integrable S-matrix is yet to be identified.[23]

---

[21]For $N = 2$ the solution (7.35) reduces to $\mathbf{S}(\theta) = \left(\frac{\pi - i\theta}{\pi + i\theta}, -1, 1\right)^{\mathsf{T}} F_\pi(-\theta)$.

[22]There, equation A.5 should have an infinite product instead of a sum.

[23]This integrable S-matrix bears strong resemblance with the one in [85] where also $S_{\text{anti}}(\theta) = -S_{\text{sym}}(\theta)$ (or equivalently $\sigma_2(\theta) = 0$ in the decomposition (7.2)). In that case there is also a periodicity related to N, which takes values $|N| < 2$ and for $N = 0$ this solutions beautifully relates to self-avoiding polymers, see also [86, 87]. The relative coefficients of the various S-matrix channels in [75] and [85] differ by a simple analytic continuation $\nu \to i\mu$ while the overall factor is related in a more involved way. It would be interesting to explore further the connections between these two solutions.
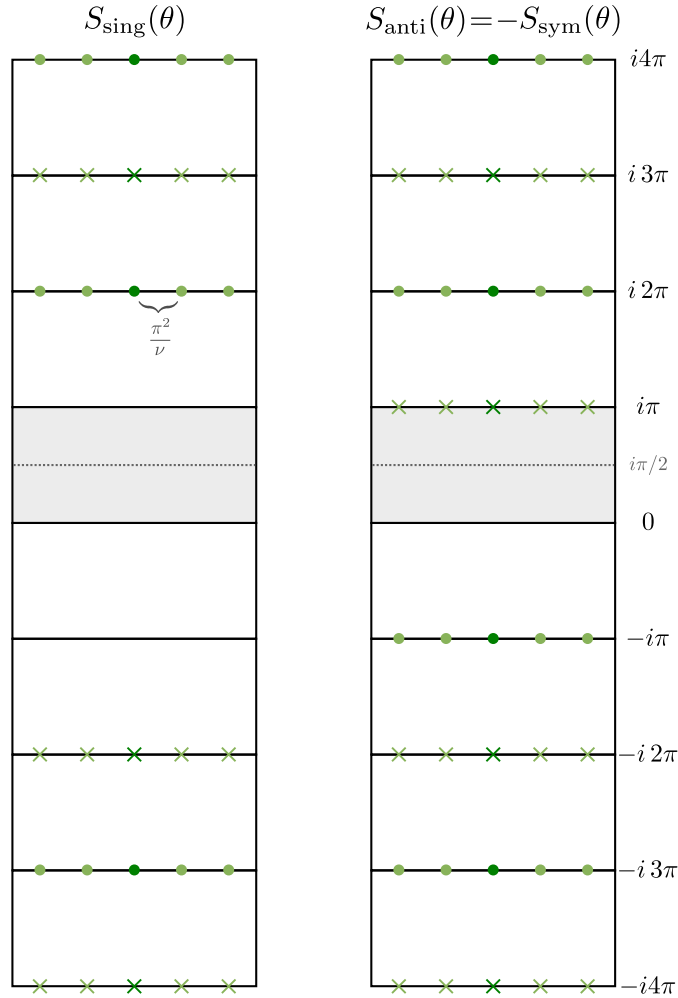
Figure 7.15: Analytic structure of the solution to the maximization of the singlet representation $S_{\mathrm{sing}}(i\pi/2)$ without bound states presented in (7.35). It is also a solution to the Yang-Baxter equations with $\sigma_2 = 0$, first written in [75]. The anti-symmetric and symmetric representations are the same up to a minus sign. The horizontal spacing between zeros and poles is π^2/ν, where ν is given by $N = 2\cosh(\nu)$. The central poles and zeros in dark green form the structure that remains in the $N = 2$ limit. The minimization problem differs by an overall minus sign.

One bound state in singlet representation

Let us now derive the finite N solution for the case of a theory with a single bound state in the **singlet representation**.

The first thing we notice from the numerics is that, as in the previous example, the large N equality $S_{\mathrm{anti}}(\theta) = -S_{\mathrm{sym}}(\theta)$ holds at finite N. Secondly, there are also zeros at the upper boundary of the physical strip. This time however there is no zero at $\theta = i\pi$ and what was a single sequence of zeros in the previous example splits now into two strings starting at $\theta = i\pi \pm \zeta$, where ζ is a parameter to determine. In the following we will assume that $S_{\mathrm{anti}}(\theta) = -S_{\mathrm{sym}}(\theta)$ and that the spacing between zeros in each string is again given by π^2/ν which is consistent with numerical observations (see green structure in figure 7.16).[24]

Let us now consider the implications of a single pole at $\theta = i\lambda$ in the singlet channel corresponding to the bound state. For this we use the crossing relations simplified by the condition $S_{\mathrm{anti}}(\theta) = -S_{\mathrm{sym}}(\theta)$. One of the equations reads

$$S_{\mathrm{sym}}(\theta) = \frac{1}{N} \left[S_{\mathrm{sing}}(i\pi - \theta) - S_{\mathrm{sym}}(i\pi - \theta) \right] . \tag{7.36}$$

If we evaluate this equation at $\theta = i\lambda$, we conclude that the t-channel poles should cancel each other so that $S_{\mathrm{sym}}(i\lambda)$ remains finite (recall that there is only one s-channel pole for the singlet representation). In other words, their residues must be the same. One can check using unitarity that this implies the existence of a double zero (pole) for $S_{\mathrm{sym}}(2i\pi - i\lambda)$ $(S_{\mathrm{sym}}(-2i\pi + i\lambda))$.[25] By the crossing+unitarity logic described before, the double pole will propagate to higher sheets creating the pattern depicted in blue in figure 7.16. Let us stress the general property of the $O(N)$ S-matrices we just derived: whenever a pole appears only in the singlet representation there will be a tower of double poles and zeros in higher sheets for all representations.

The next thing to note is that the value $\mathbf{S}(0)$ fixes $\mathbf{S}(i\pi n)$ for any $n \in \mathbb{Z}$ through crossing. In particular, if we read from the numerics the value $\mathbf{S}(0)$ we can compute the sign of the S-matrices at $\mathbf{S}(i\pi n)$. In the present case we have $\mathbf{S}(0) = (1, 1, -1)^{\intercal}$ which leads to alternating signs every $i\pi$ for all representations. For $S_{\mathrm{sing}}(\theta)$, this means that as we move in the imaginary line segment $\theta \in [0, i\pi]$, we should start with a positive function which then has the s- and t-channel poles and end with a negative value. Since each pole changes the sign of the function, we conclude that there should also be a zero in this line (another pole would imply there are other bound states) at some position $\theta = i\mu_1 - i\pi$. For $S_{\mathrm{anti}}(\theta) = -S_{\mathrm{sym}}(\theta)$ the single t-channel pole is consistent with the change of sign. Following the new zero through crossing and unitarity –keeping in mind the double poles and zeros produced in higher sheets– we arrive at the orange structure in figure 7.16.

---

[24]The fact that the there are two copies of strings of zeros at $\theta = i\pi \pm \zeta \pm n\pi^2/\nu$ follows from real analyticity $S^*(s) = S(s^*)$ or $S^*(\theta) = S(-\theta^*)$.

[25]We have that $S_{\mathrm{sing,sym}}(\theta) \sim \frac{r}{\theta - (i\pi - i\lambda)}$ and $S_{\mathrm{sym}}(i\pi + \theta) = \frac{1}{N} \left[\frac{1}{S_{\mathrm{sing}}(-\theta)]} - \frac{1}{S_{\mathrm{sym}}(-\theta)} \right]$ so that $S_{\mathrm{sym}}(2i\pi - i\lambda) \approx \frac{1}{N} \left[\frac{1}{r}(\theta - i\pi + i\lambda) - \frac{1}{r}(\theta - i\pi + i\lambda) \right]$ which indeed has a double zero.

124
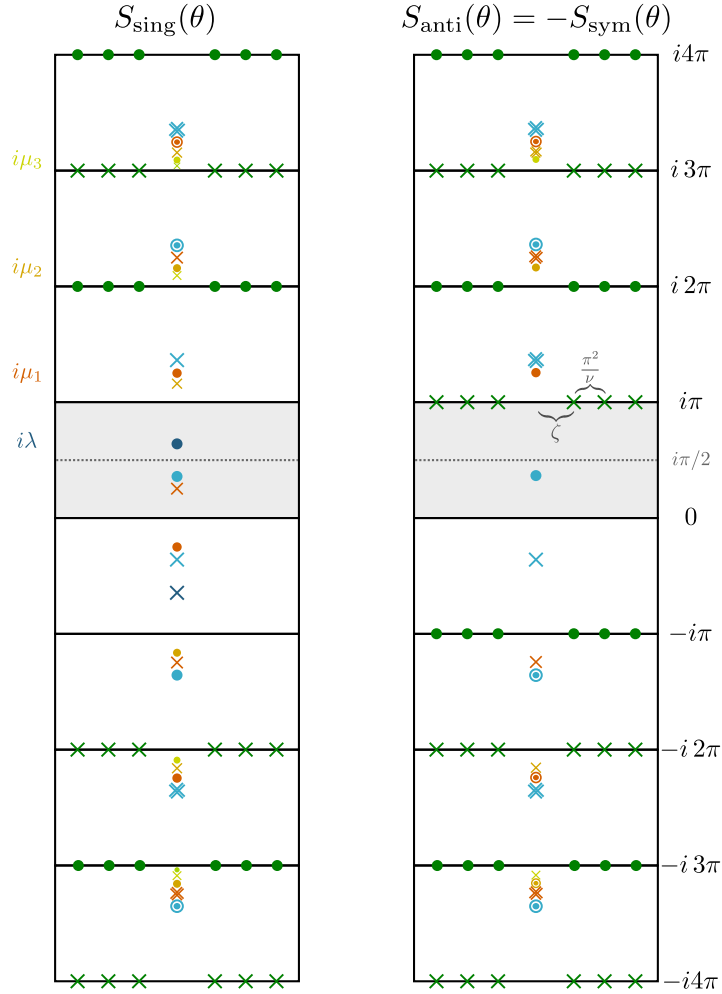
Figure 7.16: Analytic structure of the solution to the maximization of g_{sing} with no other bound states given in (7.37). The anti-symmetric and symmetric representations are the same up to a minus sign. The double crosses ⨳ and circles ⊙ represent double zeros and poles, respectively. The parameters μ_i specify the position of the new zeros and poles appearing in the singlet representation. The first zeroes at the upper boundary of the physical strip depicted in green are located at $\theta = i\pi \pm \zeta$ and the rest are spaced by multiples of π^2/ν.

If we repeat the exercise in the second strip $\theta \in [i\pi, 2i\pi]$ we easily see the need for a new zero in $S_{\mathrm{sing}}(\theta)$ (yellow cross in figure 7.16). This is actually the case in every strip, so that we end up with infinite parameters μ_n which label the position of the first new pole in the $n-$th strip.

ζ	1.804
μ_1	5.401
μ_2	8.548
μ_3	11.68
μ_4	14.86

Table 7.3: Values for the parameters ζ and $\mu_{i\leq 4}$ with $N = 5$ and $m^2_{\rm sing} = 3.1$ ($\lambda = 0.98$), obtained by the method explained in appendix J.

Collecting the analytic structure discussed above and depicted in figure 7.16, we write the ansatz for the S-matrix

$$\mathbf{S}(\theta) = \begin{pmatrix} G(\theta) \\ 1 \\ -1 \end{pmatrix} \frac{\pi - \lambda + i\theta}{\pi - \lambda - i\theta} F^2_{\pi-\lambda}(\theta) \left(\prod_{i=1}^{\infty} \frac{\mu_i + i\theta}{\mu_i - i\theta} F^2_{\mu_i}(\theta) \right) \left(\prod_{n=0}^{\infty} F_{-i\zeta - \frac{in\pi^2}{\nu}}(\theta) F_{i\zeta + \frac{in\pi^2}{\nu}}(\theta) \right),$$

(7.37)

where μ_i and ζ are parameters to determine in function of λ and N and we have defined

$$G(\theta) = \frac{i\theta - \lambda}{i\theta + \lambda} \frac{i\theta + \lambda - 2\pi}{i\theta - \lambda + 2\pi} \left(\prod_{i=1}^{\infty} \frac{i\theta + \mu_i - \pi}{i\theta - \mu_i + \pi} \frac{i\theta - \mu_i - \pi}{i\theta + \mu_i + \pi} \right) \frac{\Gamma\left[\frac{\nu}{\pi^2}(\theta - i\pi + \zeta)\right] \Gamma\left[\frac{\nu}{\pi^2}(-\theta + i\pi + \zeta)\right]}{\Gamma\left[\frac{\nu}{\pi^2}(-\theta - i\pi + \zeta)\right] \Gamma\left[\frac{\nu}{\pi^2}(\theta + i\pi + \zeta)\right]}.$$

(7.38)

The remaining parameters μ_i and ζ can be fixed by using crossing symmetry. As explained in details in appendix J, the system of equations we need to solve has the nice form

$$\left[\prod_{i=1}^{\infty} \frac{\mu_i^2 - \pi^2 n^2}{\mu_i^2 - \pi^2 (n+1)^2} \right] h(n, \zeta) = 1,$$

(7.39)

which can be solved numerically very efficiently and to arbitrary accuracy. An example of the values obtained by solving the above equations is given in table 7.3. We suspect (7.39) should have a nice and simple physical interpretation; it would be very interesting to find it.

The cases discussed above satisfied $S_{\rm anti}(\theta) = -S_{\rm sym}(\theta)$ which greatly simplified our task of finding a solution to unitarity and crossing equations. For all other cases we studied
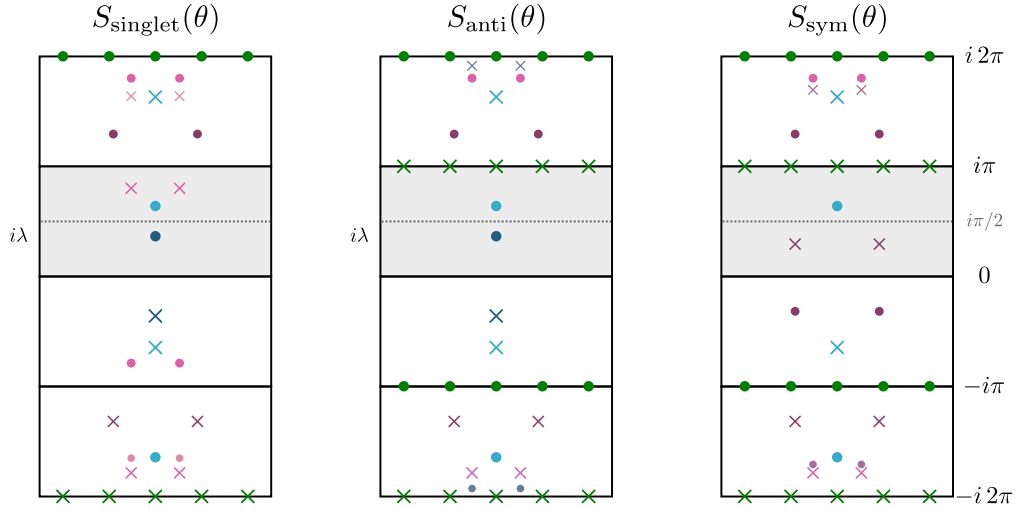
126

Figure 7.17: Sketch of the analytic structure of more exotic S-matrices found by considering bound states in the singlet and anti-symmetric representations with $m_{\text{sing}} = m_{\text{anti}} < m_{\text{GN}}$ and maximizing the anti-symmetric coupling g_{anti}.

this equality no longer holds, so that finding the full analytic solution is more complicated. Although we do not have the analogue of (7.39) for other cases, we were able to obtain (at least some of) the analytic structure of other solutions. For example, considering bound states in the **singlet and anti-symmetric representations** with the same mass, one finds –for the mass range $m_{\text{sing}} = m_{\text{anti}} < m_{\text{GN}}$– the poles and zeros depicted in figure 7.17. This case exhibits an ever richer structure with pairs of zeros inside the physical strip and patterns that repeat each other in a fractal way as we move outside the physical strip. Other maximization problems lead to S-matrices of roughly the same complexity. It would be nice to obtain the full analytic solution in these cases.

7.5   Discussion

We analysed the space of $O(N)$ symmetric two-dimensional relativistic quantum field theories whose lightest particles transform in the fundamental representation. We carved out part of this space by looking for $2 \to 2$ candidate S-matrices which maximize various couplings (be them cubic couplings given by the physical residues of the S-matrix or effective four point couplings given by the S-matrix amplitudes evaluated in some symmetric point in the physical sheet).

In the boundary of this theory space we identified known integrable S-matrices describing the excitation scattering in the $O(N)$ non-linear sigma model (NLSM), the $O(N)$ Gross-Neveu model, the kinks of the Sine-Gordon theory or the yet unknown model for solution (7.35) first discovered by Hortacsu, Schroer and Thun in [75]. The NLSM S-matrix was beautifully identified to lie at a cusp of the space of unitarity and crossing invariant S-matrices in [76]. It would be very interesting to connect our various bounds to their proposed picture for the S-matrix space and its cusps. We studied, for instance, the other cusp found in that work and found that its analytic structure is reminiscent of the general pattern found here, with infinitely many resonances at the boundary and inside the physical sheet.

We can already anticipate that the less known and quite exotic integrable solution (7.35) is also a cusp. This is yet another reason to look for the corresponding physical theory. We expect it should describe some planar processes as the self-avoiding polymers of [85] since the only allowed color structures are

$$
\mathbb{S}_{ij}^{kl}(s) \;=\; \sigma_1(s) \;\;\smile\!\!\frown\;\; + \;\; \sigma_3(s) \;\;)(\;.
$$

It would be very interesting to explore the possible connections with the models described in [86] and [87].

So far, we encountered already at least three cusps in the space of theories where integrability holds: The NLSM found in [76], the free theory of section 7.3.1 and the more exotic solution of [75] in section 7.4.2. It would be fascinating to understand mathematically the emergence of Yang-Baxter equations at the cusps of this space. While natural from a physical point of view, the emergence of these cubic equations remains a completely mathematical mystery in this context. Can we find other solutions to YB (perhaps some never discovered before) for other symmetry groups?

Also at the boundary of this physical space we identified even more exotic S-matrices. These saturate unitarity so that

$$
\mathbb{S}_{2\to2}^{\text{exotic}}(s) = \sum_{\text{rep}} S_{\text{rep}}(s)\mathbb{P}_{\text{rep}} \qquad \text{with} \qquad |S_{\text{rep}}(s)|^2 = 1 \qquad \text{for} \qquad s > 4m^2. \qquad (7.40)
$$

where the sum is over the three possible representations rep $=$ (singlet, anti, sym)$^\mathsf{T}$. These theories have an extremely rich pattern of resonances with infinitely many of them in the various sheets of the Mandelstam plane as explored in the main text (see for example

figures 7.16 and 7.17).[26] Because they saturate unitarity, these optimal solutions admit zero particle production so that $\mathbb{S}_{2\to3}^{\text{exotic}}(s) = \mathbb{S}_{2\to4}^{\text{exotic}}(s) = \cdots = 0$ just like the integrable models. However, contrary to those these exotic S-matrices do *not* obey the Yang-Baxter relations.

Can we have proper physical theories with no particle production and no Yang-Baxter? Probably not. Since Yang-Baxter is not satisfied, the $3 \to 3$ S-matrix cannot consistently factorize into a product of two-to-two S-matrices (like for an integrable theory). If this S-matrix is not factorized (and hence supported on an additional conservation δ function consistent with this factorization), it should have a regular part. This regular part can be analytically continued by crossing into $S_{2\to4}$ which thus should not be strictly zero [89, 90]. These exotic S-matrices, with strictly zero particle production are thus likely unphysical.

Having said that, perhaps we need not completely discard these S-matrices altogether. After all, while we can probably not accept a strictly zero particle production in a theory whose two body S-matrix does not obey the factorization conditions, can this particle production be very small? In other words, could these S-matrices, with their very rich analytic properties and their infinitely many resonances, be close enough to real physical S-matrices which simply have little particle production?

To properly analyze this question we could try to bootstrap not only the two body S-matrix but also multi-particle components, such as $S_{2\to4}$ and $S_{3\to3}$, altogether and figure out the fate of these S-matrices in this more complete setup. This is a fascinating but very involved problem. Further intuition about the exotic S-matrices might be found in the study of the "special form factors" introduced in [91] properly generalized to a setup with $O(N)$ symmetry. What will these tell us about deformations around the NLSM or the Gross-Neveau model for instance? Can this shed light over the exotic S-matrices we found for masses near those of the Gross-Neveu model?

In the meantime, we can preform some phenomenological games and add some particle production by hand. More precisely, we can redo the numerics modifying the unitarity constraints to read $|S_{\text{rep}}(s)|^2 \leq f_{\text{rep}}(s)$ where $f_{\text{rep}}(s) = 1 - \sigma_{\text{rep}}^{(\text{abs})}$ is equal to 1 until we reach inelastic thresholds and decays to zero for larger values of s. Of course we do not know what these functions are so the best we can do we can do in this simple exercise is to set them to some arbitrary simple functions with these properties and see what one gets. If all functions

---

[26]The resonances come about from an emergent periodicity in hyperbolic rapidity reminiscent of [83]. As pointed out in this paper, such periodicity in $\theta \sim \log(s)$ seems to point towards some sort of limit cycle behavior in the UV. The later are ruled out in local two dimensional unitary field theories [88]. It would be very interesting to find an S-matrix theoretical version of the c-theorem which could rule them out more generally. Perhaps such argument could shed light on the physics of the S-matrices encountered here. We thank Sasha Zamolodchikov for interesting discussions on this point and for bringing [83] to our attention.

are taken to be the same (for example, we could set $f_{\text{rep}}(s) = \exp(-\alpha(s - 16m^2)^2\theta(s - 16m^2))$ starting at the 4 particle threshold) then the new optimization problems are actually trivially related to the ones in the main text as $S_{\text{with particle production}}(\theta) = F(\theta)S_{\text{main text}}(\theta)$ where $F(\theta)$ is given by formula (11) in [6]. In particular, because the solutions are simply dressed by this overall function, all the rich pattern of zeros and poles which we found are still present with particle production. More realistically, different channels will produce particles at different rates so things will be less trivial. At large N we can repeat most of the analysis in section 7.4.1 for fixed imposed particle production. We can also easily run numerics with modified unitarity. The conclusion of this simple analysis – using some randomly chosen particle production functions – is that the various resonances are still there but their positions move around slightly; some acquire some imaginary part, some stay on the t-channel cut. For low energy the S-matrices are comparable to the unphysical ones we got without any particle production provided particle production is not large or changes too abruptly. This is perhaps not so surprising since particle production is a high energy effect of sorts while our maximization probes mostly the low energy region of the S-matrices.

If the infinitely many resonances present in the integrable solution (7.35) and more exotic S-matrices are indeed there for some physical theory (albeit in some slightly shifted positions in the second case), it would be fascinating to unveil their physical origin.

Chapter 8

The Monolith

8.1 Introduction

Here we consider the scattering of $O(N)$ vector particles in two dimensions in the absence of any other stable particles/bound-states as recently revisited in [7, 76]. At first sight, this looks like a harmless mathematical problem which can be stated in a line. We want to study the space of the three functions which have no singularities in the physical strip $0 < \text{Im}(\theta) < \pi$, are purely real when θ is purely imaginary, obey crossing and are bounded by unitarity:

$$
\begin{pmatrix} S_{\text{sing}}(i\pi - \theta) \\ S_{\text{sym}}(i\pi - \theta) \\ S_{\text{anti}}(i\pi - \theta) \end{pmatrix} = \begin{pmatrix} \frac{1}{N} & -\frac{N}{2} + \frac{1}{2} & \frac{N+1}{2} - \frac{1}{N} \\ -\frac{1}{N} & \frac{1}{2} & \frac{1}{2} + \frac{1}{N} \\ \frac{1}{N} & \frac{1}{2} & \frac{1}{2} - \frac{1}{N} \end{pmatrix} \cdot \begin{pmatrix} S_{\text{sing}}(\theta) \\ S_{\text{sym}}(\theta) \\ S_{\text{anti}}(\theta) \end{pmatrix}, \quad \begin{pmatrix} 1 & S_{\text{rep}}(\theta) \\ \frac{1}{S_{\text{rep}}(\theta)} & 1 \end{pmatrix} \succeq 0,
$$

(8.1)

where rep = (sing, sym, anti) and θ is real in the last condition[1]. That is it, this is our problem.

Despite its harmless appearance, this problem is amazingly rich and the S-matrices living at the boundary of this S-matrix space exhibit a large number of unexpected features such as Yang-Baxter factorization at some special points, some rather universal but mysterious emergent periodicity (in the logarithm of the physical energy) and infinitely many

---

[1] The unitarity conditions usually written as a constraint on the absolute value of the S-matrix elements $|S_{\text{rep}}(\theta)| \leq 1$ can be recast as the positive semidefinite condition above.
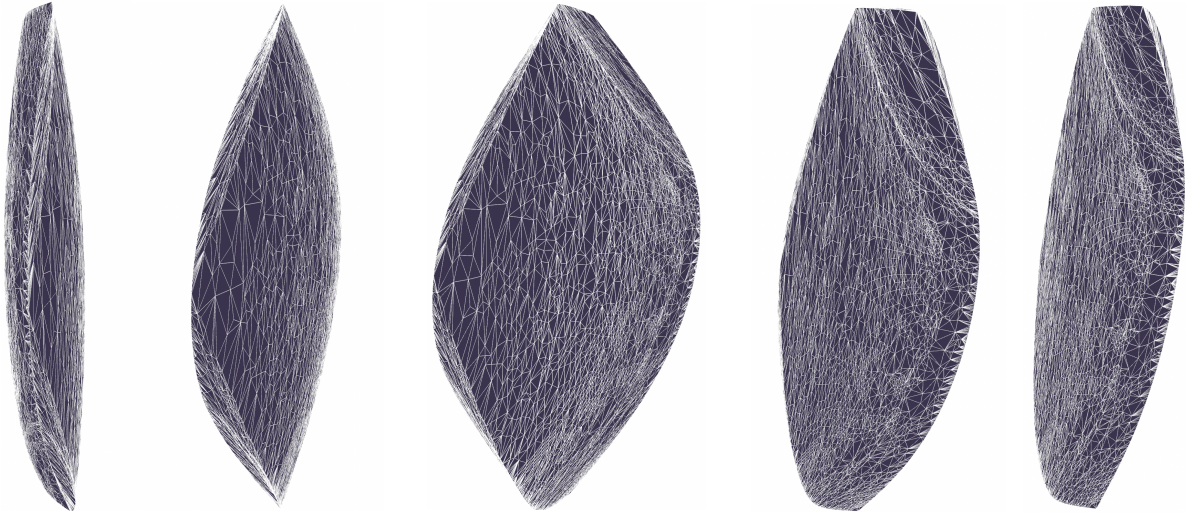
Figure 8.1: Different faces of the S-matrix monolith.

resonances (showing up as poles in higher sheets), sometimes arranged in nice regular patterns, some other times organized in intricate fractal structures. We will also find vertices, edges and faces in the boundary of this space and even some new kind of hybrid structures we dub *pre-vertices*. We find that unitarity is saturated at all points in this boundary except at a single point. For the most part, it is quite a big mystery how all these structures have emerged from such a simple mathematical problem. Figure 8.1 is a snapshot of many of these remarkable features as probed in an interesting three dimensional section of the infinite dimensional S-matrix space which we dub as the *S-matrix monolith*.

8.2 The 3D Monolith

To study the infinite dimensional S-matrix space we need some clever coordinates. One possibility is to parametrize the S-matrix components by dispersion relations; two such dispersions relations were used efficiently in [7] and [76]; the code in [76] is very fast and was the one we used to generate the heaviest plots here while the method used in [76] is more reliable to explore the boundary S-matrices at large rapidities when the numerics are most challenging and was thus the one used to extract the analytic properties of the whence obtained S-matrices at various special points.

To visualize this space, however, we need to pick a lower dimensional section. One natural set of three variables to explore would be to pick a representative value $S_{\text{rep}}(\theta^*)$
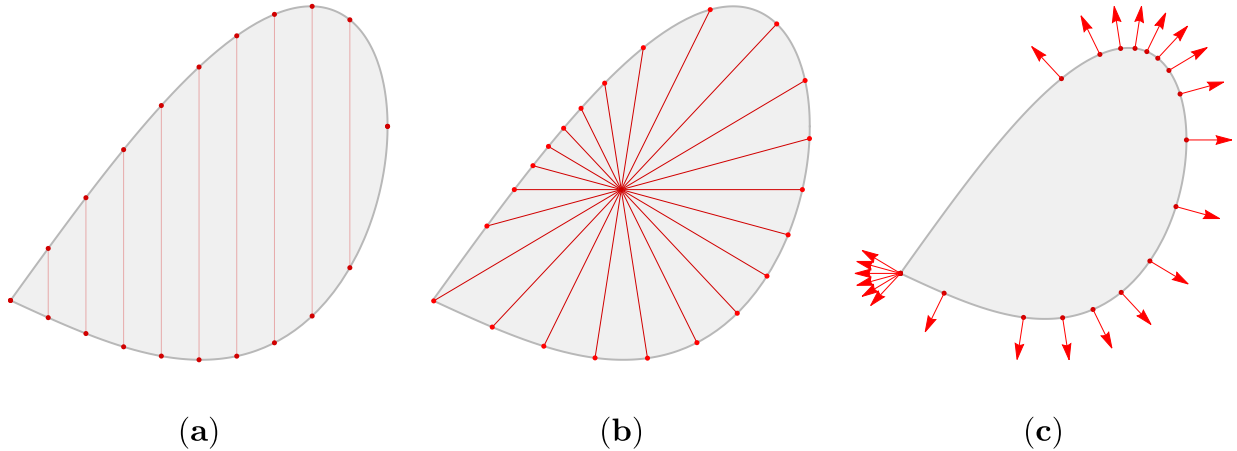
Figure 8.2: Different maximization functionals. In panel (**a**) we fix one of the coordinates and maximize/minimize the other. In the second panel (**b**) we fix a particular direction and perform a radial maximization, which useful for defining the faces of the convex space. Finally in (**c**) we have the normal maximization where we have a uniform distribution of unit vectors and the maximization chooses the points where the normals are aligned with the unit vectors, resulting in a higher concentration of points in high curvature regions.

for each of the three components. It is natural to take θ^* to be a purely imaginary number between 0 and $i\pi$ so that these parameters are real. Recall that $s = 4m^2 \cosh(\theta/2)^2$ so this corresponds to taking $s^* \in [0, 4m^2]$, right between the $t-$ and the $s-$ channel two particle cuts. So these real numbers define an off-shell four point interaction per scattering channel. Two representative points are:

- $s^* = 2m^2$, right in the middle of the physical strip,

- $s^* = 3m^2$, closer to the s–channel cut.

Note that because of crossing, the first relation in (8.1), at $s^* = 2m^2$ (i.e. $\theta^* = i\pi/2$) only two components are independent so with that first choice we do not have a three dimensional space; we only have a plane. For $s^* = 3m^2$ we have three independent components so we do get a volume. We refer to this 3D volume as the *S-matrix monolith*.

The first thing to note is that we are dealing with a compact convex space. Recall that unitarity can be written as the positive semi-definite condition in the right hand side

of (8.1). The space of positive semi-definite matrices is convex, meaning that if we take a linear combination of them we end up with another positive semi-definite matrix. The unitarity conditions apply for real θ ($s > 4m^2$) only, but we can write similar positive semi-definite conditions for $\theta \in i\pi + \mathbb{R}$ using the crossing equations[2]. Finally, since there are no bound states we can invoke the maximum modulus principle and apply the same logic to every point inside the physical strip.

Now let us turn to the type of functionals which can probe this convex space. In this work we use three different types, each one convenient for different purposes. To simplify the discussion, let us think of a two-dimensional toy model with coordinates σ_1, σ_2. One intuitive way to explore this space is to fix one of the coordinates, e.g. σ_2, and maximize/minimize the other coordinate (σ_1) as in figure 8.2 (**a**). Another way would be to point at a particular direction $(\sigma_1, \sigma_2) = R(v_1, v_2)$ and maximize R as in figure 8.2 (**b**). We refer to these maximization functionals as *radial* and they are useful when exploring the faces of the convex space. The third and last type is what we call *normal* functionals. Here, we choose a unit vector (n_1, n_2) and maximize the inner product $(\sigma_1, \sigma_2)(n_1, n_2)^\mathsf{T}$. This inner product is maximized when (σ_1, σ_2) is such that the normal vector at that point coincides with the chosen unit vector (n_1, n_2). The normal functionals are very a nice way to probe the curvature of the convex space, since by choosing a uniform distribution of unit vectors on a circle (or sphere in higher dimensions) we get more points around high curvature places like vertices and less points in almost flat faces as shown in figure 8.2 (**c**). The numerical implementation of these maximization functionals can be carried out using the discretized dispersion relations reviewed in appendix I.

Going back to the three-dimensional object spanned by $S_{\mathrm{rep}}(s^*)$, let us think of what it should be for $s^* = 4m^2$. Since we are exactly at the two-particle threshold we can apply directly the unitarity constraints for each representation $|S_{\mathrm{rep}}(s^* = 4m^2)| \leq 1$ which means the allowed region is a cube (see figure 8.3 top for a nearby point). The vertices of the cube correspond to the eight combinations where the unitarity conditions are saturated $S_{\mathrm{rep}}(s^* = 4m^2) = \pm 1$.

As we change s^* towards the middle of the physical strip, more edges and vertices appear leading to a much more complicated solid as the monolith in figure 8.1 (also shown

---

[2]For example, at the upper boundary of the physical strip (or left hand cut in the s-plane) we have the following condition for the singlet channel:

$$\begin{pmatrix} N & S_{\mathrm{sing}}(\theta) \\ \overline{S_{\mathrm{sing}}(\theta)} & N \end{pmatrix} \succeq 0, \qquad \theta \in i\pi + \mathbb{R}.$$
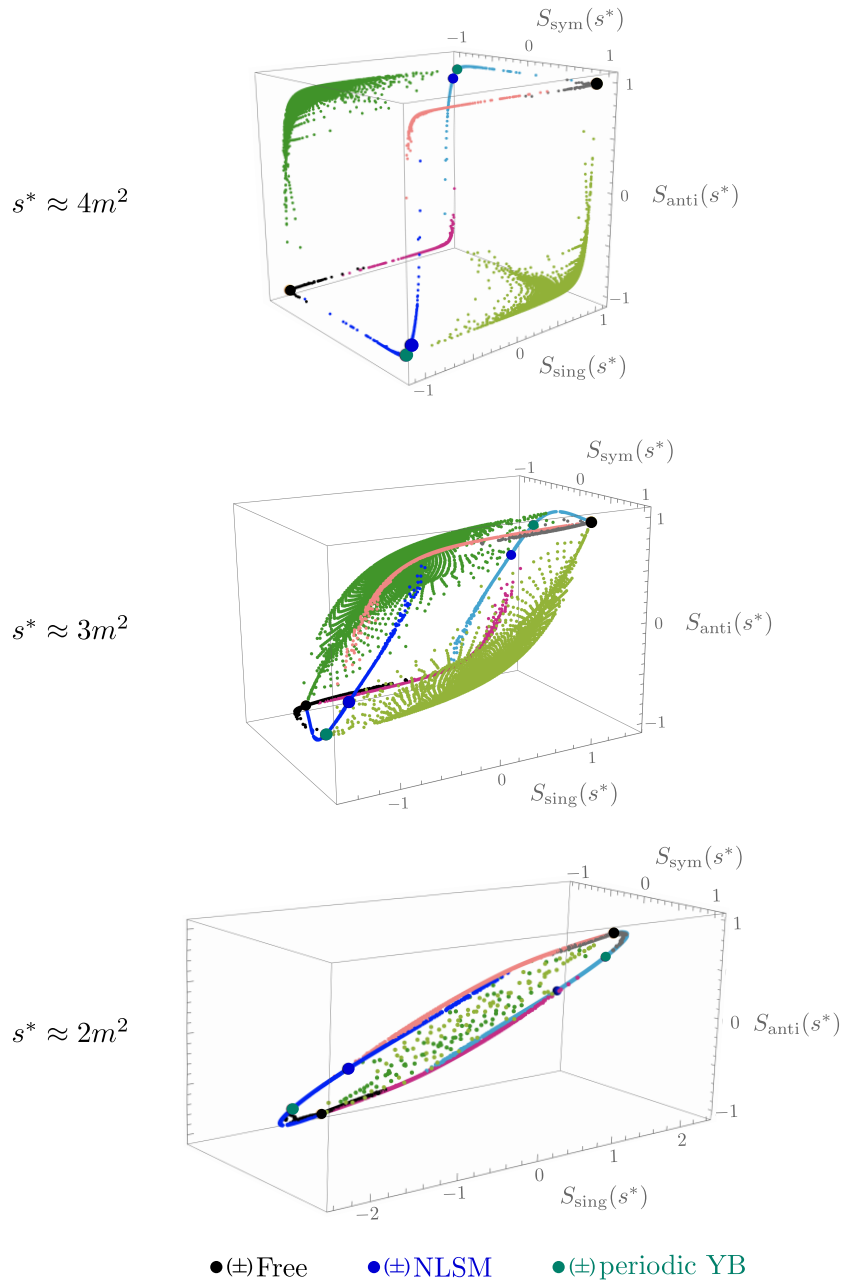
Figure 8.3: Space of allowed S-matrices $S(s^*)$ for $N = 7$ and different values of s^*, obtained using functionals of the normal type. Here we see the morphing of the cube at $s^* = 4m^2$ to the $s^* = 2m^2$ plane. At the boundary of the allowed space we have the 3 (+ 3 flipping all signs) integrable solutions, namely free theory, the NLSM [72] and the periodic Yang-Baxter solution [75]. The coloring corresponds to the associated $S_{\rm rep}(s = 4m^2)$ values as in table 8.1.

135

	$S_{\text{sing}}(\theta = 0)$	$S_{\text{anti}}(\theta = 0)$	$S_{\text{sym}}(\theta = 0)$
■	-1	-1	-1
■	-1	-1	$+1$
■	-1	$+1$	-1
■	-1	$+1$	$+1$
■	$+1$	-1	-1
■	$+1$	-1	$+1$
■	$+1$	$+1$	-1
■	$+1$	$+1$	$+1$

Table 8.1: Colors assigned to the eight different combinations of $S_{\text{rep}}(\theta = 0) = \pm 1$ which help characterize the faces and edges of the monolith.

in the middle figure 8.3).

As mentioned earlier, at the crossing symmetric point $s^* = 2m^2$ the allowed region lives on a plane (see figure 8.3 bottom). This plane is defined by the relation $\sigma_1(2m^2) = \sigma_3(2m^2)$ which follows from crossing in the decomposition (7.2). We call this two-dimensional shape *the slate*.

There are various features shared by the three panels in figure 8.3. The first one is that the allowed region is symmetric under the simultaneous change of signs: $S_{\text{rep}} \to -S_{\text{rep}}$. A second feature is that if we take a generic point on the boundary of the monolith and look at the associated S-matrix element, we see that unitarity is saturated as soon as $s^* < 4m^2$ (in contrast to the cube where by definition unitarity is saturated only at the eight vertices). In figure 8.3 we have assigned colours to each point according to the value of the associated S-matrix element at $s = 4m^2$ ($\theta = 0$) as shown in table 8.1. The colouring is useful to distinguish some of the faces and edges of the convex space.

As a final remark we have that for every value of s^* it is possible to follow six special points lying on the boundary of the allowed region. These correspond to three Yang-Baxter solutions: free theory, the non-linear sigma model (NLSM) and the periodic Yang-Baxter
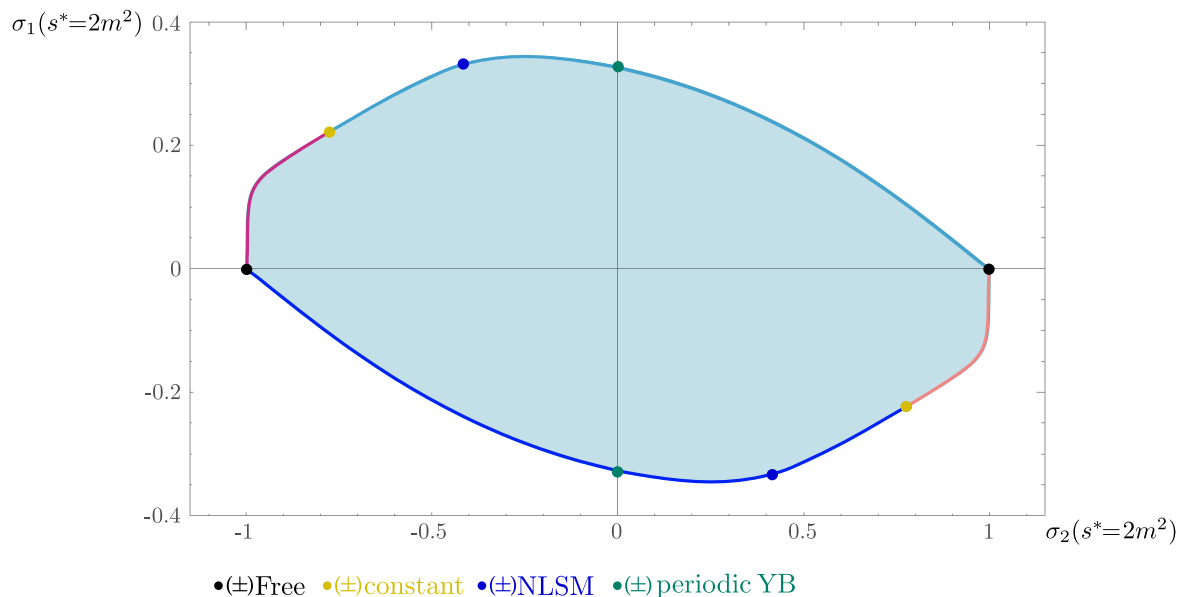
Figure 8.4: The $O(N)$ slate representing the allowed space of S-matrices in the plane $\sigma_1(s^* = 2)$ vs $\sigma_2(s^* = 2)$. The coloring at its boundary matches the convention in table 8.1. We have also marked the points corresponding to known integrable S-matrices and the constant solution in (8.2).

solution of [75] and the same three solutions where we flip all signs in S_{rep} [3].

In the following we explain how these integrable points are special from both the analytic and geometric points of view as well as many other interesting properties of the S-matrices on the surface of the monolith and slate.

8.3 Analytic Properties

8.3.1 The slate

We focus first on the simpler case of the $s^* = 2m^2$ plane where our analytic analysis is more thorough. The allowed region in the σ_i decomposition (7.2) is plotted in figure 8.4

---

[3]Notice that by multiplying any of these solutions by overall CDD factors (with zeros and not poles inside the physical strip to be consistent with the assumption of no bound states) we still get solutions to Yang-Baxter equations but the associated points are not at the boundary of the allowed region, since $S_{\text{rep}}(s^*)$ would be smaller.
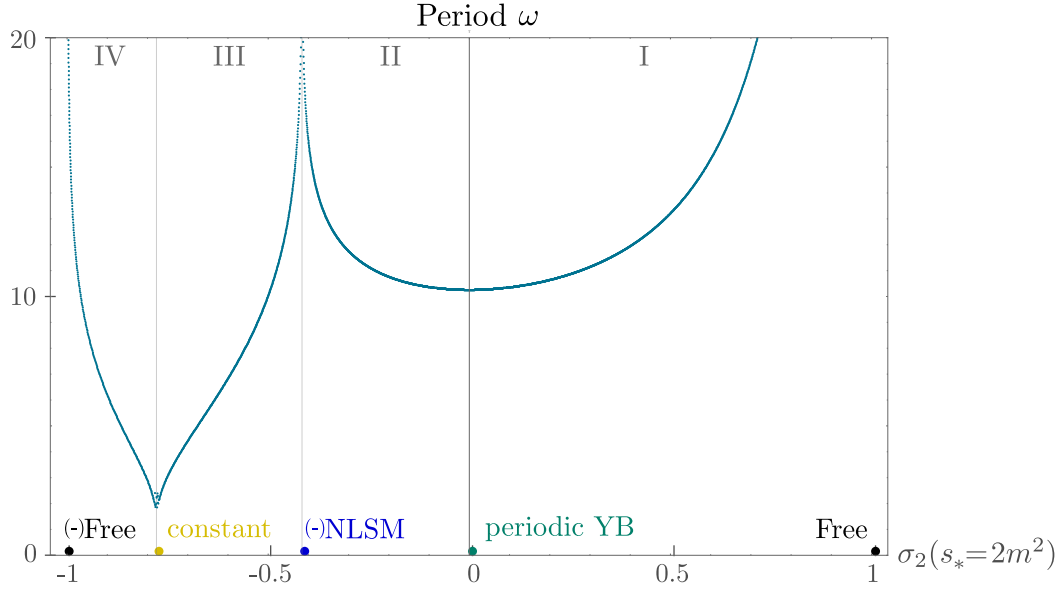
Figure 8.5: Period ω (in the real θ direction) of the S-matrices obtained numerically along the curve defining the boundary of the $s^* = 2m^2$ slate for $N = 7$. The points where the period has a minimum or diverges separate four different regions labeled in roman numerals.

for $N = 7$. The two clear vertices correspond to free theory $S_{\text{rep}} = 1$ (and $S_{\text{rep}} = -1$). The coordinates for the NLSM, periodic YB in the slate are also marked in the figure.

Except for one point along the curve, the associated S-matrices saturate unitarity for all three representations. The special point corresponds to the constant solution:

$$S_{\text{sing}} = -S_{\text{anti}} = \pm 1 \, , \quad S_{\text{sym}} = \mp \frac{N - 2}{N + 2} \, , \tag{8.2}$$

represented by the yellow points in figure 8.4. Amusingly, it is the first instance where the maximization questions asked in the S-matrix bootstrap give rise to a solution that does not completely saturate unitarity ($|S_{\text{sym}}| < 1$). Apart from free theory, (8.2) is the only constant solution on the boundary of the monolith and does not satisfy Yang-Baxter[4].

The most striking and mysterious feature of the S-matrices on the boundary of the slate is that they are periodic in the direction of real rapidity θ. That is, for a given point in the curve where the period is ω, the associated S-matrix element satisfies $S_{\text{rep}}(\theta) = S_{\text{rep}}(\theta + \omega)$. As the periodic Yang-Baxter solution, the S-matrices exhibit a pattern of infinite resonances

---

[4]It is simple to check that the only constant solution compatible with Yang-Baxter and unitarity is free theory.
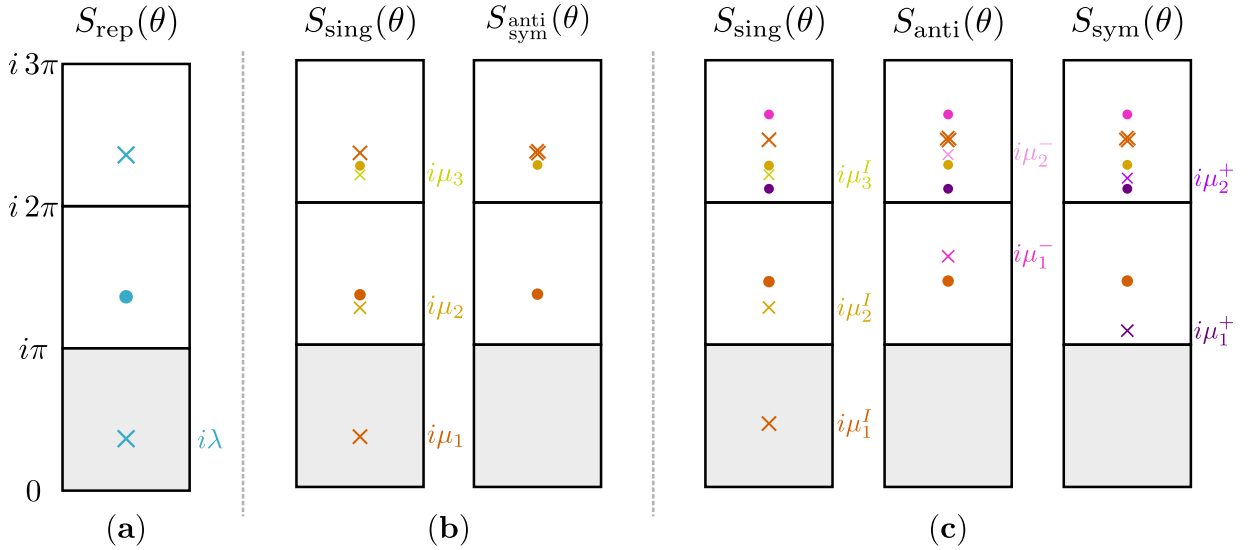
Figure 8.6: Different types of analytic structures appearing in the θ plane, following last chapter's notation. (a) *Simple* structure given by a single ratio of gamma functions $F_{\lambda+\pi}(\theta)$. (b) The simplest *fractal* structure with an infinite set of parameters μ_i labeling the new towers of poles and zeros appearing in higher strips as in (7.37). (c) The general *fractal* structure with three (infinite) sets of parameters $(\mu_i^I, \mu_i^-, \mu_i^+)$ according to the representation (sing, anti, sym) on which the first (i.e. closest to the physical strip) zero/pole appears.

at the boundary of the physical strip (see figure 7.15). They also present more complicated structures of a fractal nature where new towers of poles and zeros arise as we move to higher sheets. The period varies along the upper curve in 8.4 as shown in figure 8.5. Notice that free theory and the NLSM have an infinite period (so that we keep only the central structure shown in figure 7.2 for the latter) and the periodic Yang-Baxter solution is a local minimum of the period. The point where the period goes to zero corresponds to the constant solution (8.2).

By a careful study of the S-matrices obtained numerically, we were able to understand their analytic structure. A generic S-matrix along the curve has two different types of analytic structures which we refer to as *simple* and *fractal*.

The *simple* structures are the building blocks of the $O(N)$ S-matrices studied here. Starting from an initial pole or zero, we can recover all the poles and zeros in higher sheets from crossing and unitarity as explained in the last chapter. This structure is encoded in a particular ratio of gamma functions we called $F_a(\theta)$ shown in figure 8.6 (a) and which

139

we rewrite here for convenience

$$F_a(\theta) \equiv \frac{\Gamma\left(\frac{a+i\theta}{2\pi}\right)\Gamma\left(\frac{a-i\theta+\pi}{2\pi}\right)}{\Gamma\left(\frac{a-i\theta}{2\pi}\right)\Gamma\left(\frac{a+i\theta+\pi}{2\pi}\right)}\ . \tag{8.3}$$

The integrable solutions can be conveniently written in terms of these simple structures. We recall here the expressions for NLSM and the periodic Yang-Baxter (pYB) solutions:

$$\mathbf{S}^{\text{NLSM}}(\theta) = \begin{pmatrix} -1 \\ -\frac{\theta-i\pi}{\theta+i\pi} \\ -\frac{\theta-i\pi}{\theta+i\pi}\frac{\theta-i\lambda_{\text{GN}}}{\theta+i\lambda_{\text{GN}}} \end{pmatrix} F_{\pi+\lambda_{\text{GN}}}(\theta)F_{2\pi}(\theta)\ , \tag{8.4}$$

$$\mathbf{S}^{\text{pYB}}(\theta) = \begin{pmatrix} \frac{\sinh\left[\nu\left(1-\frac{i\theta}{\pi}\right)\right]}{\sinh\left[\nu\left(1+\frac{i\theta}{\pi}\right)\right]} \\ -1 \\ 1 \end{pmatrix} \prod_{n=-\infty}^{\infty} F_{\pi+\frac{in\pi^2}{\nu}}(-\theta)\ , \tag{8.5}$$

where $\lambda_{\text{GN}} = 2\pi/(N-2)$, $\nu = \text{ArcCosh}(N/2)$ and we have used again the notation $\mathbf{S} = (S_{\text{sing}}, S_{\text{anti}}, S_{\text{sym}})^{\intercal}$. Note that each solution has a single parameter (λ_{GN} for NLSM and ν for pYB) and that the infinite product in (8.5) takes care of the periodicity in the real θ direction.

On the other hand, the *fractal* structures require the inclusion of infinite parameters labeling the new structures emerging as we move to higher sheets. The simplest of these structures appeared in the analytic solution (7.37) found in last chapter which depends on an infinite number of parameters μ_i (see figure 8.6 (**b**)). The general *fractal* structure appearing in the S-matrices has new towers in each representation, leading to three infinite sets of parameters (one per representation) as shown in figure 8.6 (**c**).

The S-matrices are then given by a collection of fractal or simple structures appearing either at multiples of the period $\text{Re}(\theta) = n\omega$ or at $\text{Re}(\theta) = (n+\frac{1}{2})\omega$, with $n \in \mathbb{Z}$. It is a beautiful story how these intricate structures move in the complex θ plane interpolating between the different integrable solutions. In the following we explain how the interpolation works in the various regions between the known analytic solutions for the first two strips $0 \le \text{Im}(\theta) \le 2\pi$.

Region I: from Free to periodic YB
We start from free theory where the complex θ plane is devoid of any structure. As soon

as we move towards the periodic YB solution on the boundary curve of 8.4 we get poles and zeros at $\mathrm{Re}(\theta) = n\omega$ in a fractal structure. The pair of zero and pole[5] emerging from $\theta = 0$ allows for the change of sign in the antisymmetric channel: $S_{\mathrm{anti}}(\theta = 0) = +1$ in free theory to $S_{\mathrm{anti}}(\theta = 0) = -1$ in this region (that is from grey to light blue in the coloring of table 8.1). Note that the zeros in the second sheet of S_{sing} (in orange) –giving rise to the fractal structure– are necessary so that there are no poles inside the physical strip. As the period decreases we see as well a simple structure at $\mathrm{Re}(\theta) = (n + \frac{1}{2})\omega$ starting in the symmetric representation (in purple). The simple green structure at multiples of $i\pi$ does not move in the imaginary θ direction and is present in most of the curve.
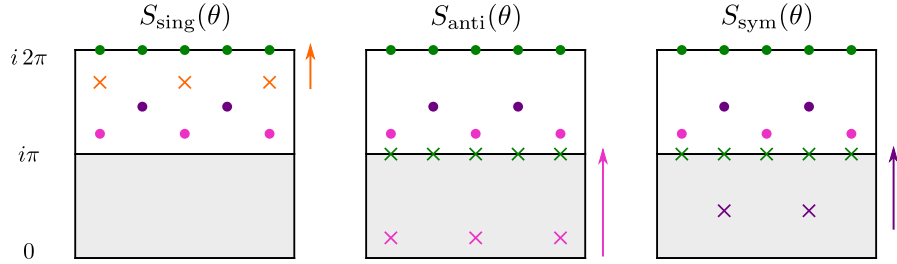
As we keep moving along the curve, both the fractal and simple structures move into higher sheets indefinitely until disappearing. The period keeps decreasing until it reaches the periodic Yang Baxter value: $\omega = 2\pi^2/\nu$. Only the green structure at multiples of $i\pi$ remains, leaving the analytic structure of the periodic Yang Baxter solution.
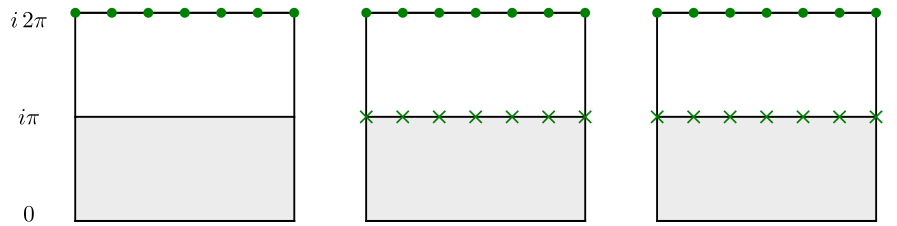
Region II: from periodic YB to (-)NLSM
After passing the periodic YB solution, the period again increases as shown in figure 8.5. New structures of fractal type for $\mathrm{Re}(\theta) = (n + \frac{1}{2})\omega$ and simple for $\mathrm{Re}(\theta) = n\omega$ come from higher sheets and make their way close to the physical strip.

---

[5]Recall that unitarity in the rapidity plane reads: $S_{\mathrm{rep}}(\theta)S_{\mathrm{rep}}(-\theta) = 1$, so that for every zero in θ there is a pole in $-\theta$.
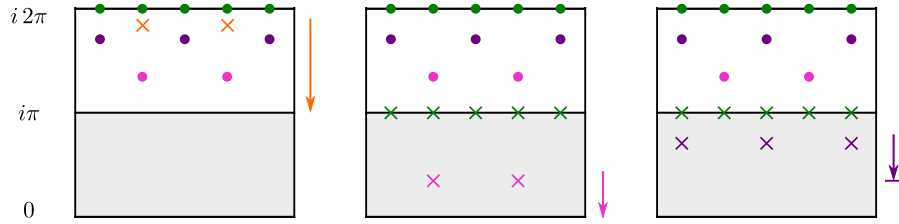
The structures keep lowering until the zeros in the physical strip of S_{anti} (in pink) reach the $\theta \in \mathbb{R}$ line. In the singlet representation, the fractal structure in orange reaches the $\theta \in i\pi + \mathbb{R}$, cancelling the dangerous pole at the upper boundary of the physical strip (similar cancellations follow in higher sheets, proving the necessity of the fractal structures). In the symmetric channel, the simple structure (in purple) keeps lowering until it reaches the $\theta \in i\lambda + \mathbb{R}$ line. In the meantime the period diverges, so that only the central structure remains and we get the NLSM solution.
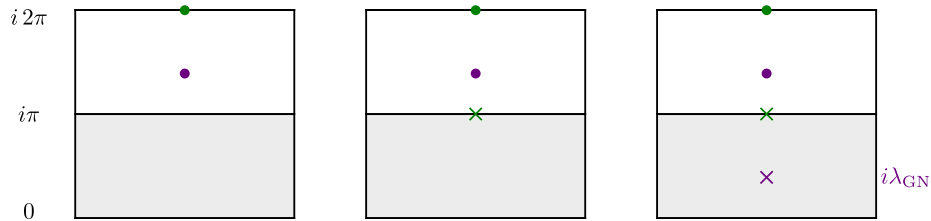
Region III: from (-)NLSM to constant solution
As we pass the NLSM the simple structure in S_{sym} keeps lowering towards the $\theta \in \mathbb{R}$ line and at the same time the period decreases. Meanwhile, a new fractal structure emerges from the $\theta \in \mathbb{R}$ line in the singlet representation, again at $\mathrm{Re}(\theta) = (n + \frac{1}{2})\omega$.
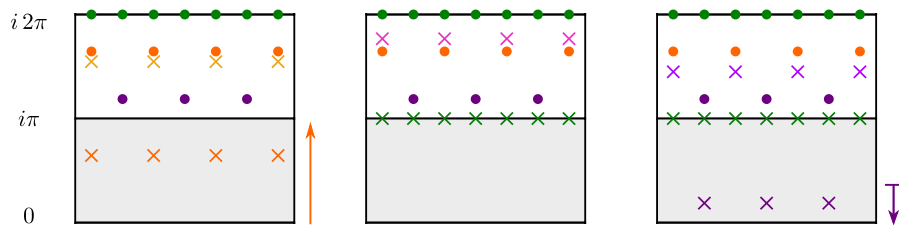
Now a curious phenomenon occurs: as the simple structure reaches and the fractal one heads to the $\theta \in i\pi + \mathbb{R}$ line, the period vanishes. This means there is a collision of infinite poles and zeros at $\mathrm{Im}(\theta) = i\pi, 2i\pi, ...$ and at the real line in the symmetric channel. With this mechanism we reach the constant solution (8.2) where $|S_{\mathrm{sym}}| < 1$!

142

Region IV: from constant solution to (-)Free

Finally, as the period increases in the fourth region we get a new simple structure in the symmetric representation at $\mathrm{Re}(\theta) = (n + \frac{1}{2})\omega$ and the fractal structure moves down towards the real θ line. After the constant solution, the value of S_{sym} inmediatly changes from $-(N-2)/(N+2)$ to -1 so that we have the change of colors from light blue of region III to dark pink in region IV.
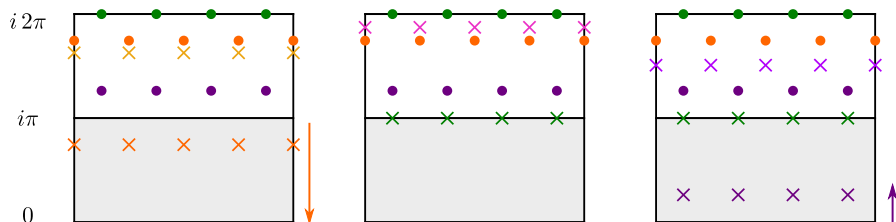
To reach the final point of (-) free theory, all zeros and poles should disappear and a change of sign in $S_{\mathrm{sing}}(\theta = 0)$ should occur (so that we pass from dark pink to black in the notation of table 8.1). Most of the structure disappears as the period again diverges. For the change of sign, the fractal structure in the singlet channel reaches $\theta = 0$ and collides with its unitarity image pole. Thanks to the fractal structure, similar cancellations occur at $\theta = i\pi n$. Up to an overall minus sign, this leaves us back where we started so by following the same logic we can describe the S-matrices on the lower curve of figure 8.4.

As we have seen, there are basically three mechanisms for the appearance/disappearance of structures of poles and zeros in the S-matrices. Namely, collision of zeros and poles, structures moving in the imaginary rapidity direction to higher and higher sheets or moving in the real rapidity direction (e.g. with the period diverging). Although the functions on the 3D monolith are more complicated, the same mechanisms survive.

8.3.2   General analytic properties of the Monolith

Let us now explore the more general S-matrices on the 3D monolith. As one might expect, having a volume with many faces, vertices and edges instead of the $s^* = 2m^2$ slate with a single boundary curve significantly adds complexity to the playground. The biggest difference compared to the problem described in the previous section is that the S-matrices on the monolith are not exactly periodic but have a *generalized periodicity*. This property –as the periodicity in the 2D slate– remains an unsolved mystery.

143

What we mean by the term *generalized periodicity* is that the S-matrices are composed of a central structure with purely imaginary zeros and poles and other structures with equally spaced zeros and poles that appear after some offset in real rapidity. In equations, the S-matrices have the following form:

$$S(\theta) = \mathcal{C}(\theta)\mathcal{G}(\theta + \zeta)\mathcal{G}(-\theta + \zeta), \tag{8.6}$$

where $\mathcal{C}(\theta)$ is the central structure, ζ is the offset and the product $\mathcal{G}(\theta)\mathcal{G}(-\theta)$ is periodic in the real rapidity direction. The first example of such functions was first encountered in chapter 7 when studying the S-matrices maximizing the coupling to a single bound state in the singlet channel. The analytic solution is given in (7.37) and depicted in figure 7.16. Remarkably, a simple modification of this solution describes a line on the boundary of the monolith!

The S-matrices on the boundary of the monolith saturate unitarity except at the constant solution (8.2). This saturation can be understood with the introduction of a dual problem as recently introduced in [8]. There are only six points where the Yang-Baxter equations are satisfied, corresponding to $\pm$(Free, NLSM, pYB) also present in the slate.

At a generic point on the boundary, the fractal structures described in the previous section are still present, but we gain many new parameters from the offset in the real rapidity and the "independent"[6] central structure. We have looked at representative points of some of the faces and edges of the monolith so that we have a rough idea of how the interpolation between different faces takes place. Since we do not have yet the complete picture let us for now restrict to one line on the boundary which we know analytically and where the interpolation between two integrable points is precise.

8.3.3 The $\sigma_2 = 0$ line

There is a special line on the boundary of the monolith parametrized by $\sigma_2(s^*) = 0$. For the two-dimensional slate, this condition selects the periodic YB solution where the S-matrices obey $\sigma_2(s) = 0$ (i.e. for any value of s) and $S_{\mathrm{anti}}(s) = -S_{\mathrm{sym}}(s)$. In the 3D monolith, we have the same situation which greatly simplifies the task of finding an analytic solution. A very similar problem was introduced in chapter 7 when studying the space of S-matrices maximizing the coupling to a single bound state in the singlet representation giving rise to the solution (7.37) with the generalized periodicity described above. It turns out that

---

[6]Of course, this is not exactly true since all parameters are related by crossing.

this S-matrix times a simple CDD factor which cancels the unwanted poles in the physical strip perfectly describes the $\sigma_2(s^*) = 0$ in the monolith. The final expression is[7]

$$
\mathbf{S}(\theta) = \pm \begin{pmatrix} G(\theta) \\ 1 \\ -1 \end{pmatrix} F_\lambda(-\theta) F_{2\pi-\lambda}(-\theta) \left[\prod_{i=1}^{\infty} \frac{\mu_i + i\theta}{\mu_i - i\theta} F_{\mu_i}^2(\theta) \right] \left[\prod_{n=0}^{\infty} F_{-i\zeta - \frac{in\pi^2}{\nu}}(\theta) F_{i\zeta + \frac{in\pi^2}{\nu}}(\theta) \right] ,
$$

(8.7)

where we have defined

$$
G(\theta) \equiv \frac{i\theta - \lambda}{i\theta + \lambda} \frac{i\theta + \lambda - 2\pi}{i\theta - \lambda + 2\pi} \left(\prod_{i=1}^{\infty} \frac{i\theta + \mu_i - \pi}{i\theta - \mu_i + \pi} \frac{i\theta - \mu_i - \pi}{i\theta + \mu_i + \pi} \right) \frac{\Gamma\left[\frac{\nu}{\pi^2}(\theta + \zeta - i\pi)\right] \Gamma\left[\frac{\nu}{\pi^2}(-\theta + \zeta + i\pi)\right]}{\Gamma\left[\frac{\nu}{\pi^2}(\theta + \zeta + i\pi)\right] \Gamma\left[\frac{\nu}{\pi^2}(-\theta + \zeta - i\pi)\right]} .
$$

(8.8)

The infinite set of parameters μ_i can be consistently truncated and determined (along with the offset ζ) using the crossing equations as explained in appendix J. The factors containing λ and μ_i are part of the central structure $\mathcal{C}(\theta)$, whereas the product of gamma functions has precisely the form $\mathcal{G}(\theta + \zeta)\mathcal{G}(-\theta + \zeta)$ of (8.6)[8]. The analytic structure is depicted in figure 8.7 (**a**).

This solution nicely interpolates between the $\pm$ periodic YB solutions, the two signs referring to the two different lines connecting the integrable solutions. The interpolation takes place as follows. The parameter λ –which in (7.37) was related to the mass of the bound state– takes values $\lambda \in [\pi, 2\pi]$ so that the first zero in the antisymmetric and symmetric representations remains inside the physical strip (blue cross in figure 8.7 (**a**)). It can also be used as a parameter for the position along the two lines.

As $\boldsymbol{\lambda \to 2\pi}$ three things happen: first, the anti/sym zero in blue reaches the upper boundary of the physical strip; meanwhile, the orange tower of poles and zeros moves down until the zero in the physical strip of the singlet channel arrives to $\theta = 0$, producing an infinite cancellation of poles and zeros at $S_{\mathrm{rep}}(i\pi n)$; finally the offset reaches the value $\zeta = \pi^2/\nu$ so that we have exactly the analytic structure of pYB shown in figure 7.15.

---

[7]When comparing (7.37) to (8.7), it is useful to note that

$$
F(\lambda, -\theta) F(2\pi - \lambda, -\theta) = \frac{\sinh(\theta) - i\sin(\lambda)}{\sinh(\theta) + i\sin(\lambda)} \frac{+i\theta - \lambda + \pi}{-i\theta - \lambda + \pi} F(\pi - \lambda, \theta)^2 .
$$

[8]Recall that the function $F_a(\theta)$ puts poles and zeros in the vertical (imaginary θ) direction according to unitarity and crossing. It is a simple exercise to rewrite (8.7) in a real periodicity friendly notation as an infinite product of gamma functions akin to the ones in (8.8).
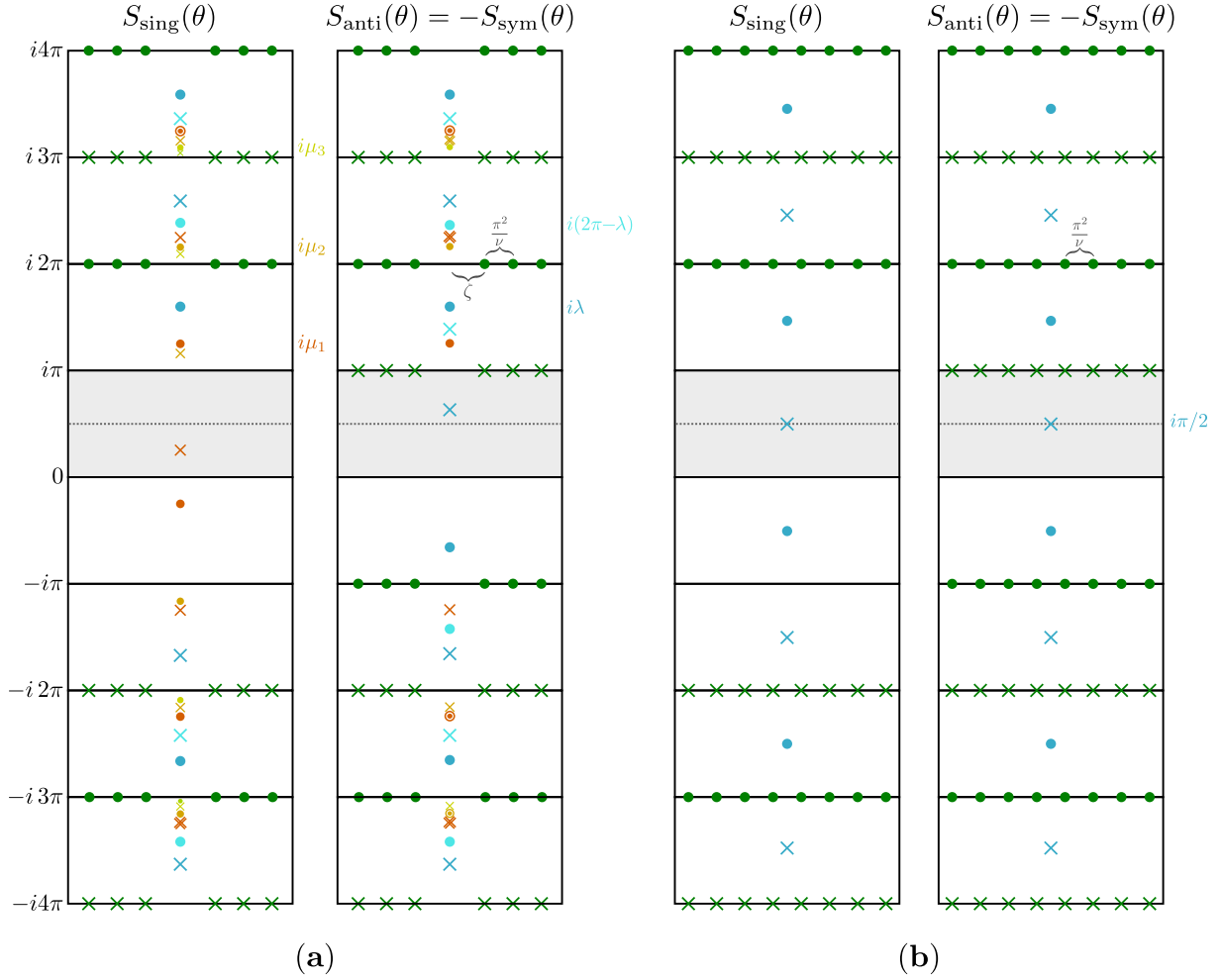
Figure 8.7: (**a**) Analytic structure of solution along the $\sigma_2 = 0$ line given in (8.7). (**b**) The simple analytic structure remaining from (8.7) when $\lambda = 3\pi/2$.

When $\boldsymbol{\lambda \to 3/2\pi}$ something curious happens: the first anti/sym zero (in blue) moves down to the middle of the physical strip and at the same time the first zero in singlet (orange) moves up also to the middle of the physical strip. Again, infinite cancellations occur, leaving behind a single tower of poles and zeros in the imaginary axis and as $\zeta \to \pi^2/(2\nu)$ we have the very symmetric solution:

$$S(\theta) = \tan\left(\frac{i\theta}{2} + \frac{\pi}{4}\right)\left[\prod_{n=0}^{\infty} F_{-\frac{i\pi^2}{\nu}}\left(n+\tfrac{1}{2}\right)(\theta)\, F_{\frac{i\pi^2}{\nu}}\left(n+\tfrac{1}{2}\right)(\theta)\right],$$

whose analytic structure is depicted in figure 8.7 (**b**). On the monolith, this point corresponds to

146

the middle of the green faces in figure 8.3.

Finally, we have the limit $\boldsymbol{\lambda \to \pi}$ which leads us to the other periodic YB solution. Here, we have the blue structure going towards $\theta = 0$ while the orange one keeps moving up until it reaches the upper boundary of the physical strip. In this case, the offset vanishes $\zeta = 0$. Again, the fractal structure of the μ tower permits the perfect cancellation of poles and zeros so that only the periodic resonances of figure 7.15 remain.

As a last remark for this section, let us point out that the fact that we have $S_{\mathrm{anti}}(s) = -S_{\mathrm{sym}}(s)$ for any s on this line clarifies the double change of sign in $S_{\mathrm{rep}}(\theta = 0)$ resulting in the coloring shown in figure 8.3 (from dark (light) green to dark (light) blue edge where pYB lives). In more generic situations, we expect contiguous colors on the monolith to correspond to a change of sign in a single representation.

8.4   Some geometric aspects

So far we have left out of the discussion the geometrical aspects of the monolith. There are straightforward questions like: How many faces and edges does it have? Are all the integrable solutions vertices in this space? Are there more vertices pointing to interesting theories? In this section we will give partial answers to the questions above.

Already from figure 8.4 it is clear that free theory is a vertex. Although not apparent in the same figure, the NLSM is also a vertex. This can be seen in figure 8.8 (see also 8.1 for different angles), since there is a sharp edge ending at this point (it is also possible to see this vertex in the 2D slate by zooming in close to this point). For the periodic YB solution we have a peculiar situation where two edges clearly point at it, but loose their sharpness as they get closer to the integrable point. The loss of curvature is evident when handling a 3D printed version of the monolith and also when looking at the results from maximization with normal functionals (recall that this type of functionals highlight the curvature in the convex space as depicted in figure 8.2), since less points accumulate on the edge as we get closer to the periodic YB solution. We say this point is a *pre-vertex*. The idea is that, once we include constraints imposing some particle production at non-integrable points the bounds would go down everywhere around this point converting the pre-vertex into a genuine vertex.

What about non-integrable points and the constant solution (8.2)? Qualitatively, the latter seems to lie on a flat face, marking the separation between blue and pink regions –i.e. a change of sign in $S_{\mathrm{sym}}(\theta = 0)$– as in the 2D slate. We also observe more edges and smaller faces, in particular close to the free theory vertices, which might indicate more special points on the boundary. A more detailed study of several sections of the monolith is needed to completely answer these questions.
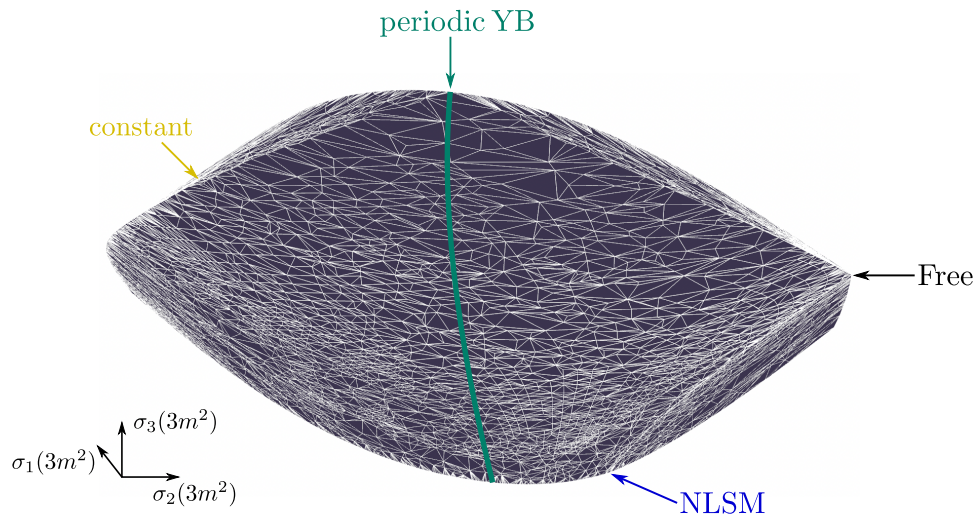
Figure 8.8: A closer look at the monolith, seen at an angle compatible with the plot 8.4. Three arrows point to the integrable solutions corresponding to vertices (Free, NLSM) or pre-vertices (periodic YB) of the monolith.

8.5 Discussion

We have explored the space of massive quantum field theories with no bound states and a global $O(N)$ symmetry in two spacetime dimensions. Focusing on the two-to-two scattering matrix element of particles transforming in the vector representation, we argued that the space of such S-matrices is described by an infinite dimensional convex space. Using various types of maximization functionals, we established bounds on the space of allowed S-matrices. We named a particular three-dimensional section of this space the S-matrix monolith and encountered a rich geometric structure with various edges, vertices, edges that flatten and pre-vertices.

By studying the analytic properties of the S-matrices on the boundary of the monolith, we were able to identify distinctive points and lines on the monolith with known integrable solutions (i.e. free theory, NLSM and periodic YB), a new constant solution which does not saturate unitarity (8.2) and an analytic solution which describes a line connecting two integrable points. The reason why these models appear at geometrically distinguished points on the monolith is however not clear and would be very nice to elucidate.

Except for the constant solution, all S-matrices at the boundary of the monolith saturate unitarity. This property can be understood by the introduction of a convex dual problem as recently explained in [8]. Even though this saturation indicates the absence of particle production, Yang-Baxter equations are only satisfied at the known integrable solutions mentioned above. This puzzle was encountered as well in chapter 7 and it is still an open question how to impose particle

production accurately.

We also uncovered rich structures of poles and zeros arranging themselves into fractal patterns. For the two-dimensional section studied in 8.3.1, we explained how these patterns move on the complex plane interpolating between the different known models. The most striking feature found with this analysis is that the S-matrices are exactly periodic in the rapidity θ parametrizing the center of mass energy or, more generally, obey a "generalized periodicity" described in 8.3.2. It would be very interesting to understand how the periodicity emerges from the maximization problem considered here, as well as its physical implications.

Chapter 9

Final Remarks

In this thesis we have studied scattering amplitudes using two complementary approaches. In the first part we focused on a particular theory whose large number of symmetries makes the computation of observables feasible. Instead, in the second part we explored the space of allowed two-dimensional Quantum Field Theories.

Part I was devoted to the Pentagon Operator Product Expansion (POPE) in $\mathcal{N} = 4$ SYM. In this program scattering amplitudes/ polygonal Wilson loops are computed at finite coupling as a sequence of pentagon transitions between different flux-tube states. In chapter 3 we explained how we can describe different helicity configurations of scattering amplitudes by including charged pentagon transitions and we put forward a map between different combinations of charged pentagons and superamplitude components. In chapter 4 we presented the coupling dependent part of the POPE integrand and understood the role of supersymmetry in defining the charged pentagon transitions. In order to compute the amplitudes for general kinematics, it is necessary to sum over all possible flux-tube excitations. In chapter 5 we saw that the excitations organize themselves into Bethe strings forming effective excitations which can be resummed at weak coupling. We performed this resummation explicitly for the tree-level six-point amplitude.

In part II we adopted the bootstrap philosophy and explored the space of gapped, unitary, Lorentz invariant two-dimensional QFTs with a global $O(N)$ symmetry. In chapter 7 we established various bounds for cubic and quartic couplings and discovered a very rich analytic structure for the $2 \rightarrow 2$ S-matrix elements saturating these bounds. For particular mass spectra, we were able to identify known integrable solutions like the $O(N)$ NLSM and Gross-Neveu model. In chapter 8 we focused on theories without bound states and investigated the associated space of S-matrices. We considered a particular three-dimensional subsection of this convex space that we called the monolith. We found interesting geometric properties and surprising features for the S-matrix elements at its boundary such as periodicity in a parametrization of the center of mass energy.

There are some connections between the two parts of the thesis. In particular, we have seen that integrability played a special role in both cases. In $\mathcal{N} = 4$ SYM, we saw that it was the integrability of the flux-tube dynamics what allowed us to compute the scattering amplitudes at any coupling. In the second part, we were able to reproduce various integrable models using the S-matrix bootstrap approach and moreover, we observed that integrability emerged at special points of the monolith describing the allowed space of two-dimensional QFTs. To give a concrete example of a direct connection, at strong coupling the pentagon transitions involving scalars are directly related to the $O(6)$ NLSM S-matrix appearing at the boundary of the monolith.

$\mathcal{N} = 4$ SYM is still a fertile ground for the development of tools to compute various observables and gain insights into gauge/string dualities. Regarding pentagons and scattering amplitudes/Wilson loops, the first non-planar corrections were put forward in [92] and the study of pentagons in other integrable theories was recently initiated in [93] for ABJM. As for other observables, notable progress has been made in the computation of correlation functions following [94,95] in which the building blocks are hexagon form factors. With the power of integrability, we have reached an exceptional finite coupling description of a four-dimensional gauge theory. The lessons learned in $\mathcal{N} = 4$ SYM along with the techniques created to describe it will certainly prove useful in studying other theories.

Since its revival in [5,6], the S-matrix bootstrap has been applied to a range of two-dimensional [96,97] as well as higher dimensional [73,74] scenarios. Although not explored in this thesis, there is also an analogue *boundary bootstrap* which one can study by considering QFT in AdS with a conformal theory induced at its boundary [5]. It would be very interesting to further explore this direction and feed from the progress achieved in the CFT bootstrap community.

There are several open questions common to the S-matrix bootstrap problems studied so far. One that was understood recently in the two-dimensional case involves saturation of unitarity. We have seen that at the boundary of the bounds we find S-matrix elements (e.g. $S_{2\to2}$) that saturate the unitarity constraints[1]. This saturation can be understood exploiting the convexity of the problem and its dual formulation [8]. However, explaining the origin of this saturation in higher dimensions is still an open problem.

On the other hand, we know that general non-integrable theories should have some particle production but with saturation of unitarity the latter is effectively set to zero. Another open question is how to accurately include particle production constraints. Concerning the analytic structure of the S-matrices, we observed that the optimal solutions exhibit intricate fractal patterns of poles and zeros in the various kinematical sheets as well as a mysterious (generalized) periodicity. It would be fascinating to understand the origin of this periodicity as well as its physical implications.

Finally, we have re-discovered some integrable theories as geometric features in the space of S-matrices. How does integrability emerge at these points? Can we use these type of features

---

[1]A similar saturation occurs within the subspace of multiple amplitudes considered in [96].

to discover and even define other interesting theories in two and higher dimensions? We are optimistic about this direction and believe that accessing physical data of strongly coupled theories such as QCD with these techniques is within reach. It is an exciting time to fully explore the power of the bootstrap philosophy and gain insights into the space of non-perturbative Quantum Field Theories.

References

[1] B. Basso, A. Sever, and P. Vieira, "Spacetime and Flux Tube S-Matrices at Finite Coupling for N=4 Supersymmetric Yang-Mills Theory," Phys. Rev. Lett., vol. 111, no. 9, p. 091602, 2013.

[2] B. Basso, J. Caetano, L. Cordova, A. Sever, and P. Vieira, "OPE for all Helicity Amplitudes," JHEP, vol. 08, p. 018, 2015.

[3] B. Basso, J. Caetano, L. Cordova, A. Sever, and P. Vieira, "OPE for all Helicity Amplitudes II. Form Factors and Data Analysis," JHEP, vol. 12, p. 088, 2015.

[4] L. Córdova, "Hexagon POPE: effective particles and tree level resummation," JHEP, vol. 01, p. 051, 2017.

[5] M. F. Paulos, J. Penedones, J. Toledo, B. C. van Rees, and P. Vieira, "The S-matrix bootstrap. Part I: QFT in AdS," JHEP, vol. 11, p. 133, 2017.

[6] M. F. Paulos, J. Penedones, J. Toledo, B. C. van Rees, and P. Vieira, "The S-matrix bootstrap II: two dimensional amplitudes," JHEP, vol. 11, p. 143, 2017.

[7] L. Córdova and P. Vieira, "Adding flavour to the S-matrix bootstrap," JHEP, vol. 12, p. 063, 2018.

[8] L. Córdova, Y. He, M. Kruczenski, and P. Vieira, "The O(N) S-matrix Monolith," 2019.

[9] L. Brink, J. H. Schwarz, and J. Scherk, "Supersymmetric Yang-Mills Theories," Nucl. Phys., vol. B121, pp. 77–92, 1977.

[10] H. Elvang and Y.-t. Huang, "Scattering Amplitudes," 2013.

[11] L. F. Alday and J. M. Maldacena, "Gluon scattering amplitudes at strong coupling," JHEP, vol. 06, p. 064, 2007.

[12] J. M. Drummond, G. P. Korchemsky, and E. Sokatchev, "Conformal properties of four-gluon planar amplitudes and Wilson loops," Nucl. Phys., vol. B795, pp. 385–408, 2008.

[13] A. Brandhuber, P. Heslop, and G. Travaglini, "MHV amplitudes in N=4 super Yang-Mills and Wilson loops," Nucl. Phys., vol. B794, pp. 231–243, 2008.

[14] Z. Bern, L. J. Dixon, D. A. Kosower, R. Roiban, M. Spradlin, C. Vergu, and A. Volovich, "The Two-Loop Six-Gluon MHV Amplitude in Maximally Supersymmetric Yang-Mills Theory," Phys. Rev., vol. D78, p. 045007, 2008.

[15] J. M. Drummond, J. Henn, G. P. Korchemsky, and E. Sokatchev, "Hexagon Wilson loop = six-gluon MHV amplitude," Nucl. Phys., vol. B815, pp. 142–173, 2009.

[16] S. Caron-Huot, "Notes on the scattering amplitude / Wilson loop duality," JHEP, vol. 07, p. 058, 2011.

[17] J. M. Drummond, J. Henn, G. P. Korchemsky, and E. Sokatchev, "Dual superconformal symmetry of scattering amplitudes in N=4 super-Yang-Mills theory," Nucl. Phys., vol. B828, pp. 317–374, 2010.

[18] S. Caron-Huot and S. He, "Jumpstarting the All-Loop S-Matrix of Planar N=4 Super Yang-Mills," JHEP, vol. 07, p. 174, 2012.

[19] J. M. Drummond, J. M. Henn, and J. Plefka, "Yangian symmetry of scattering amplitudes in N=4 super Yang-Mills theory," JHEP, vol. 05, p. 046, 2009.

[20] J. M. Drummond and L. Ferro, "The Yangian origin of the Grassmannian integral," JHEP, vol. 12, p. 010, 2010.

[21] L. F. Alday, D. Gaiotto, J. Maldacena, A. Sever, and P. Vieira, "An Operator Product Expansion for Polygonal null Wilson Loops," JHEP, vol. 04, p. 088, 2011.

[22] B. Basso, A. Sever, and P. Vieira, "Space-time S-matrix and Flux tube S-matrix II. Extracting and Matching Data," JHEP, vol. 01, p. 008, 2014.

[23] B. Basso, A. Sever, and P. Vieira, "Space-time S-matrix and Flux-tube S-matrix III. The two-particle contributions," JHEP, vol. 08, p. 085, 2014.

[24] B. Basso, A. Sever, and P. Vieira, "Space-time S-matrix and Flux-tube S-matrix IV. Gluons and Fusion," JHEP, vol. 09, p. 149, 2014.

[25] S. S. Gubser, I. R. Klebanov, and A. M. Polyakov, "A Semiclassical limit of the gauge / string correspondence," Nucl. Phys., vol. B636, pp. 99–114, 2002.

[26] B. Basso, "Exciting the GKP string at any coupling," Nucl. Phys., vol. B857, pp. 254–334, 2012.

[27] A. V. Belitsky, "A note on two-loop superloop," Phys. Lett., vol. B718, pp. 205–213, 2012.

[28] A. V. Belitsky, "Nonsinglet pentagons and NMHV amplitudes," Nucl. Phys., vol. B896, pp. 493–554, 2015.

[29] L. J. Mason and D. Skinner, "The Complete Planar S-matrix of N=4 SYM as a Wilson Loop in Twistor Space," JHEP, vol. 12, p. 018, 2010.

[30] H. Elvang, D. Z. Freedman, and M. Kiermaier, "Solution to the Ward Identities for Super-amplitudes," JHEP, vol. 10, p. 103, 2010.

[31] V. P. Nair, "A Current Algebra for Some Gauge Theory Amplitudes," Phys. Lett., vol. B214, pp. 215–218, 1988.

[32] G. P. Korchemsky and E. Sokatchev, "Superconformal invariants for scattering amplitudes in N=4 SYM theory," Nucl. Phys., vol. B839, pp. 377–419, 2010.

[33] N. Arkani-Hamed, J. L. Bourjaily, F. Cachazo, S. Caron-Huot, and J. Trnka, "The All-Loop Integrand For Scattering Amplitudes in Planar N=4 SYM," JHEP, vol. 01, p. 041, 2011.

[34] N. Arkani-Hamed, J. L. Bourjaily, F. Cachazo, A. B. Goncharov, A. Postnikov, and J. Trnka, Grassmannian Geometry of Scattering Amplitudes. Cambridge University Press, 2016.

[35] N. Arkani-Hamed and J. Trnka, "The Amplituhedron," JHEP, vol. 10, p. 030, 2014.

[36] J. L. Bourjaily, S. Caron-Huot, and J. Trnka, "Dual-Conformal Regularization of Infrared Loop Divergences and the Chiral Box Expansion," JHEP, vol. 01, p. 001, 2015.

[37] A. Sever, P. Vieira, and T. Wang, "OPE for Super Loops," JHEP, vol. 11, p. 051, 2011.

[38] A. Sever, P. Vieira, and T. Wang, "From Polygon Wilson Loops to Spin Chains and Back," JHEP, vol. 12, p. 065, 2012.

[39] A. V. Belitsky, "Fermionic pentagons and NMHV hexagon," Nucl. Phys., vol. B894, pp. 108–135, 2015.

[40] L. J. Dixon, J. M. Drummond, and J. M. Henn, "Bootstrapping the three-loop hexagon," JHEP, vol. 11, p. 023, 2011.

[41] L. J. Dixon, J. M. Drummond, C. Duhr, and J. Pennington, "The four-loop remainder function and multi-Regge behavior at NNLLA in planar N = 4 super-Yang-Mills theory," JHEP, vol. 06, p. 116, 2014.

[42] L. J. Dixon, J. M. Drummond, C. Duhr, M. von Hippel, and J. Pennington, "Bootstrapping six-gluon scattering in planar N=4 super-Yang-Mills theory," PoS, vol. LL2014, p. 077, 2014.

[43] L. J. Dixon and M. von Hippel, "Bootstrapping an NMHV amplitude through three loops," JHEP, vol. 10, p. 065, 2014.

[44] N. Arkani-Hamed, F. Cachazo, and J. Kaplan, "What is the Simplest Quantum Field Theory?," JHEP, vol. 09, p. 016, 2010.

[45] A. Hodges, "Eliminating spurious poles from gauge-theoretic amplitudes," JHEP, vol. 05, p. 135, 2013.

[46] A. Sever and P. Vieira, "Multichannel Conformal Blocks for Polygon Wilson Loops," JHEP, vol. 01, p. 070, 2012.

[47] L. J. Mason and D. Skinner, "Dual Superconformal Invariance, Momentum Twistors and Grassmannians," JHEP, vol. 11, p. 045, 2009.

[48] L. F. Alday and J. M. Maldacena, "Comments on operators with large spin," JHEP, vol. 11, p. 019, 2007.

[49] S. Caron-Huot, "Superconformal symmetry and two-loop amplitudes in planar N=4 super Yang-Mills," JHEP, vol. 12, p. 066, 2011.

[50] N. Beisert, S. He, B. U. W. Schwab, and C. Vergu, "Null Polygonal Wilson Loops in Full N=4 Superspace," J. Phys., vol. A45, p. 265402, 2012.

[51] A. V. Belitsky, "On factorization of multiparticle pentagons," Nucl. Phys., vol. B897, pp. 346–373, 2015.

[52] A. V. Belitsky, S. E. Derkachov, and A. N. Manashov, "Quantum mechanics of null polygonal Wilson loops," Nucl. Phys., vol. B882, pp. 303–351, 2014.

[53] B. Basso and A. V. Belitsky, "Luescher formula for GKP string," Nucl. Phys., vol. B860, pp. 1–86, 2012.

[54] J. M. Drummond, G. Papathanasiou, and M. Spradlin, "A Symbol of Uniqueness: The Cluster Bootstrap for the 3-Loop MHV Heptagon," JHEP, vol. 03, p. 072, 2015.

[55] L. J. Dixon, J. M. Drummond, M. von Hippel, and J. Pennington, "Hexagon functions and the three-loop remainder function," JHEP, vol. 12, p. 049, 2013.

[56] J. M. Drummond and G. Papathanasiou, "Hexagon OPE Resummation and Multi-Regge Kinematics," JHEP, vol. 02, p. 185, 2016.

[57] G. Papathanasiou, "Hexagon Wilson Loop OPE and Harmonic Polylogarithms," JHEP, vol. 11, p. 150, 2013.

[58] A. V. Belitsky, "Matrix pentagons," Nucl. Phys., vol. B923, pp. 588–607, 2017.

[59] B. Basso, A. Sever, and P. Vieira, "Hexagonal Wilson loops in planar $\mathcal{N} = 4$ SYM theory at finite coupling," J. Phys., vol. A49, no. 41, p. 41LT01, 2016.

[60] N. Berkovits and J. Maldacena, "Fermionic T-Duality, Dual Superconformal Symmetry, and the Amplitude/Wilson Loop Connection," JHEP, vol. 09, p. 062, 2008.

[61] D. Fioravanti, S. Piscaglia, and M. Rossi, "Asymptotic Bethe Ansatz on the GKP vacuum as a defect spin chain: scattering, particles and minimal area Wilson loops," Nucl. Phys., vol. B898, pp. 301–400, 2015.

[62] A. Bonini, D. Fioravanti, S. Piscaglia, and M. Rossi, "Strong Wilson polygons from the lodge of free and bound mesons," JHEP, vol. 04, p. 029, 2016.

[63] D. Gaiotto, J. Maldacena, A. Sever, and P. Vieira, "Bootstrapping Null Polygon Wilson Loops," JHEP, vol. 03, p. 092, 2011.

[64] D. Gaiotto, J. Maldacena, A. Sever, and P. Vieira, "Pulling the straps of polygons," JHEP, vol. 12, p. 011, 2011.

[65] H. T. Lam and M. von Hippel, "Resumming the POPE at One Loop," JHEP, vol. 12, p. 011, 2016.

[66] A. Brandhuber, P. Heslop, and G. Travaglini, "A Note on dual superconformal symmetry of the N=4 super Yang-Mills S-matrix," Phys. Rev., vol. D78, p. 125005, 2008.

[67] J. M. Drummond and J. M. Henn, "All tree-level amplitudes in N=4 SYM," JHEP, vol. 04, p. 018, 2009.

[68] A. V. Belitsky, "Resummed tree heptagon," Nucl. Phys., vol. B929, pp. 113–136, 2018.

[69] A. V. Belitsky, "Multichannel conformal blocks for scattering amplitudes," Phys. Lett., vol. B780, pp. 66–73, 2018.

[70] F. Kos, D. Poland, and D. Simmons-Duffin, "Bootstrapping Mixed Correlators in the 3D Ising Model," JHEP, vol. 11, p. 109, 2014.

[71] D. Simmons-Duffin, "A Semidefinite Program Solver for the Conformal Bootstrap," JHEP, vol. 06, p. 174, 2015.

[72] A. B. Zamolodchikov and A. B. Zamolodchikov, "Factorized s Matrices in Two-Dimensions as the Exact Solutions of Certain Relativistic Quantum Field Models," Annals Phys., vol. 120, pp. 253–291, 1979. [,559(1978)].

[73] M. F. Paulos, J. Penedones, J. Toledo, B. C. van Rees, and P. Vieira, "The S-matrix Bootstrap III: Higher Dimensional Amplitudes," 2017.

[74] A. L. Guerrieri, J. Penedones, and P. Vieira, "Bootstrapping QCD: the Lake, the Peninsula and the Kink," 2018.

157

[75] M. Hortacsu, B. Schroer, and H. J. Thun, "A Two-dimensional σ Model With Particle Production," Nucl. Phys., vol. B154, pp. 120–124, 1979.

[76] Y. He, A. Irrgang, and M. Kruczenski, "A note on the S-matrix bootstrap for the 2d O(N) bosonic model," JHEP, vol. 11, p. 093, 2018.

[77] E. Witten, "Some Properties of the (psi-Bar psi)**2 Model in Two-Dimensions," Nucl. Phys., vol. B142, pp. 285–300, 1978.

[78] R. Shankar and E. Witten, "The S Matrix of the Kinks of the $(\psi^-\text{bar } \psi)$**2 Model," Nucl. Phys., vol. B141, p. 349, 1978. [Erratum: Nucl. Phys.B148,538(1979)].

[79] M. Karowski and H. J. Thun, "Complete S Matrix of the O($2N$) Gross-Neveu Model," Nucl. Phys., vol. B190, pp. 61–92, 1981.

[80] N. Doroud and J. Elias Miro, "S-matrix bootstrap for resonances," JHEP, vol. 09, p. 052, 2018.

[81] B. Gabai, D. Mazac, A. Shieber, P. Vieira, and Y. Zhou, "No Particle Production in Two Dimensions: Recursion Relations and Multi-Regge Limit," JHEP, vol. 02, p. 094, 2019.

[82] A. Zamolodchikov and I. Ziyatdinov, "Inelastic scattering and elastic amplitude in Ising field theory in a weak magnetic field at $T > T_c$: Perturbative analysis," Nucl. Phys., vol. B849, pp. 654–674, 2011.

[83] A. B. Zamolodchikov, "Z(4) SYMMETRIC FACTORIZED S MATRIX IN TWO SPACE-TIME DIMENSIONS," Commun. Math. Phys., vol. 69, pp. 165–178, 1979.

[84] G. Mussardo and S. Penati, "A Quantum field theory with infinite resonance states," Nucl. Phys., vol. B567, pp. 454–492, 2000.

[85] A. B. Zamolodchikov, "Exact S matrix associated with selfavoiding polymer problem in two-dimensions," Mod. Phys. Lett., vol. A6, pp. 1807–1814, 1991.

[86] F. A. Smirnov, "A Comment on A. Zamolodchikov's paper concerning selfavoiding polymers," Phys. Lett., vol. B275, pp. 109–111, 1992.

[87] P. Fendley, "Taking N —> zero with S matrices," in NATO Advanced Research Workshop on Statistical Field Theories Villa Olmo, Como, Italy, June 18-23, 2001, 2001.

[88] A. B. Zamolodchikov, "Irreversibility of the Flux of the Renormalization Group in a 2D Field Theory," JETP Lett., vol. 43, pp. 730–732, 1986. [Pisma Zh. Eksp. Teor. Fiz.43,565(1986)].

[89] D. Iagolnitzer, "Factorization of the Multiparticle s Matrix in Two-Dimensional Space-Time Models," Phys. Rev., vol. D18, p. 1275, 1978.

[90] D. Iagolnitzer, <u>Scattering in quantum field theories: The Axiomatic and constructive approaches</u>. 1994.

[91] F. A. Smirnov and A. B. Zamolodchikov, "On space of integrable quantum field theories," <u>Nucl. Phys.</u>, vol. B915, pp. 363–383, 2017.

[92] R. Ben-Israel, A. G. Tumanov, and A. Sever, "Scattering amplitudes - Wilson loops duality for the first non-planar correction," <u>JHEP</u>, vol. 08, p. 122, 2018.

[93] B. Basso and A. V. Belitsky, "ABJM flux-tube and scattering amplitudes," 2018.

[94] B. Basso, S. Komatsu, and P. Vieira, "Structure Constants and Integrable Bootstrap in Planar N=4 SYM Theory," 2015.

[95] T. Fleury and S. Komatsu, "Hexagonalization of Correlation Functions," <u>JHEP</u>, vol. 01, p. 130, 2017.

[96] A. Homrich, J. a. Penedones, J. Toledo, B. C. van Rees, and P. Vieira, "The S-matrix Bootstrap IV: Multiple Amplitudes," 2019.

[97] J. Elias Miro, A. L. Guerrieri, A. Hebbar, J. Penedones, and P. Vieira, "Flux Tube S-matrix Bootstrap," 2019.

[98] J. L. Bourjaily, "Efficient Tree-Amplitudes in N=4: Automatic BCFW Recursion in Mathematica," 2010.

[99] G. P. Korchemsky and E. Sokatchev, "Symmetries and analytic properties of scattering amplitudes in N=4 SYM theory," <u>Nucl. Phys.</u>, vol. B832, pp. 1–51, 2010.

APPENDICES PART I

Appendix A

More on Geometry, Pentagons and Parity

In this appendix we review some known facts about the geometry of amplitudes and in particular, pentagons. These facts are then used in section A.3 to prove the parity relation (3.36).

A.1 Variables

Scattering Amplitudes and null polygonal Wilson loops are conventionally parametrized by a plethora of very useful variables. Amongst them, we have momentum twistors Z, spinor helicity variables λ and their parity conjugate $\tilde{\lambda}$, and dual momentum twistors W. Let us introduce them in our notation following [45] closely. We shall start by the momentum twistors Z and construct all other variables from them.

A momentum twistor is a four dimensional projective vector $Z_j \sim \lambda Z_j$. It is associated to each edge of the null polygon, see figure 3.1. Momentum twistors allow us to parametrize the shape of the polygon in an unconstrained way, this being one of their main virtues. Moreover, they transform linearly under conformal transformations and are therefore very useful when dealing with a conformal theory such as $\mathcal{N} = 4$ SYM.

Note the labelling of edges we are using in this paper is tailored from an OPE analysis and is *not* the conventional cyclic labelling commonly used to describing color ordered partial amplitudes. In particular, in our convention, Z_j and Z_{j+1} (or Z_{j-1}) are *not* neighbours; instead they nicely face each other in the polygon tessellation, see figure 3.1. The trivial conversion between our labelling and a more conventional numbering of the edges is presented in the caption of figure 3.1.

Out of four momentum twistors we can build conformal invariant angle brackets

$$\langle ijkl \rangle \equiv \epsilon_{abcd} Z_i^a Z_j^b Z_k^c Z_l^d \qquad \text{or} \qquad \langle ijkl \rangle \equiv Z_i \wedge Z_j \wedge Z_k \wedge Z_l \,. \tag{A.1}$$

We construct spinor helicity variables λ by extracting the first two components of each four dimensional momentum twistors[1]

$$\lambda_i \equiv \begin{pmatrix} 1 & 0 & 0 & 0 \\ 0 & 1 & 0 & 0 \end{pmatrix} \cdot Z_i \,. \tag{A.2}$$

With these spinor helicity variables we can construct Lorentz invariant two dimensional angle brackets

$$\langle i, j \rangle \equiv \epsilon^{\alpha\beta} \lambda_{i,\alpha} \lambda_{j,\beta} \qquad \text{or} \qquad \langle i, j \rangle \equiv Z_i \cdot \mathbb{I} \cdot Z_j \tag{A.3}$$

where $\mathbb{I}_{ab}$ is the usual infinite twistor which one can read off from the first definition. Next we introduce the dual momentum twistors W which can be thought of as the parity conjugate of the Z's. The dual momentum twistors are defined by using three neighbouring standard momentum twistors as

$$W_{j,a} \equiv \epsilon_{abcd} \frac{Z_{j-2}^b Z_j^c Z_{j+2}^d}{\langle j-2, j \rangle \langle j, j+2 \rangle} \qquad \text{or} \qquad W_j \equiv \frac{Z_{j-2} \wedge Z_j \wedge Z_{j+2}}{\langle j-2, j \rangle \langle j, j+2 \rangle} \,. \tag{A.4}$$

Note that with this convenient normalization the dual momentum twistor W_j has the opposite helicity weight as the momentum twistor Z_j. For the very bottom and top we need to tweak the definition (A.4) due to the non-cyclic labelling we are using.[2]

With the dual momentum twistors we can now construct four brackets once more, now denoted with square brackets

$$[ijkl] \equiv \epsilon^{abcd} W_{i,a} W_{j,b} W_{k,c} W_{l,d} \qquad \text{or} \qquad [ijkl] \equiv W_i \wedge W_j \wedge W_k \wedge W_l \,. \tag{A.5}$$

---

[1]More precisely, we can always apply a global $GL(4)$ rotation U to all the twistors (before extracting the first two components) plus a residual $GL(2)$ transformation V to all the spinors (after extracting them from the first two components) such that in total $\lambda_i \equiv V \cdot \begin{pmatrix} 1 & 0 & 0 & 0 \\ 0 & 1 & 0 & 0 \end{pmatrix} \cdot U \cdot Z_i$. Henceforth we set U and V to be the identity matrices. Nevertherless, it is worth keeping in mind that sometimes such transformations can be quite convenient. For instance, the twistors in previous OPE studies – see e.g. appendix of [22] – contain several zero components and will lead to singular λ's if extracted blindly. In those cases, it is quite convenient to preform such generic conformal transformations when constructing the spinor helicity variables.

[2]Explicitly, the only tricky definitions are $W_0 \equiv \frac{Z_2 \wedge Z_0 \wedge Z_{-1}}{\langle 2,0 \rangle \langle 0,-1 \rangle}$, $W_{-1} \equiv \frac{Z_0 \wedge Z_{-1} \wedge Z_1}{\langle 0,-1 \rangle \langle -1,1 \rangle}$ at the bottom and $W_{n-2} \equiv \frac{Z_{n-4} \wedge Z_{n-2} \wedge Z_{n-3}}{\langle n-4, n-2 \rangle \langle n-2, n-3 \rangle}$ and $W_{n-3} \equiv \frac{Z_{n-2} \wedge Z_{n-3} \wedge Z_{n-5}}{\langle n-2, n-3 \rangle \langle n-3, n-5 \rangle}$ at the top, see figure 3.1.

Finally, we come to the parity conjugate spinor helicity variables $\tilde{\lambda}$.[3] They can be now defined as the *last* two components of the dual twistors,

$$\tilde{\lambda}_i = \left(\begin{array}{cccc} 0 & 0 & 1 & 0 \\ 0 & 0 & 0 & 1 \end{array} \right) \cdot W_i \,. \tag{A.6}$$

Out of two such twistors we can construct the Lorentz invariant square brackets

$$[ij] \equiv \epsilon^{\dot\alpha\dot\beta} \tilde{\lambda}_{i,\dot\alpha} \tilde{\lambda}_{j,\dot\beta} \qquad \text{or} \qquad [ij] = W_i \cdot \tilde{\mathbb{I}} \cdot W_j \tag{A.7}$$

where the dual infinity twistor $\tilde{\mathbb{I}}^{ab}$ can once gain be read off from the first definition.

A beautiful outcome of the construction above is that momentum conservation

$$0 = \sum_i \lambda_{i,\alpha} \tilde{\lambda}_{i,\dot\alpha} \qquad \text{for } \alpha = 1,2 \text{ and } \dot\alpha = \dot{1}, \dot{2} \tag{A.8}$$

automatically follows from the definitions above. In other words, as is well known, the use of twistors trivializes momentum conservation.

To summarize: At this point, each edge of our polygon is endowed with a momentum twistor Z_j, a dual momentum twistor W_j and a pair of spinors λ_j and $\tilde{\lambda}_j$. There are also other null segments which play a critical role in our construction: the middle edges that define our tessellation which are represented by the red dashed lines in figure 3.1 and whose corresponding momentum twistors are given in the caption of that same figure. We quote here for convenience:

$$Z_{\text{middle}} = \langle j-2, j, j+2, j-1 \rangle Z_{j+1} - \langle j-2, j, j+2, j+1 \rangle Z_{j-1} \,. \tag{A.9}$$

Let us briefly explain how this equation can be established. This simple exercise beautifully illustrates the power of Hodges' momentum twistors when dealing with the geometry of null lines. First, since $Z_{\text{middle}} \wedge Z_{j-1}$, $Z_{\text{middle}} \wedge Z_{j+1}$ and $Z_{j-1} \wedge Z_{j+1}$ all correspond to the same right cusp in figure 3.1a, we immediately have that $Z_{\text{middle}} = \alpha Z_{j+1} + \beta Z_{j-1}$. At the same time the point $Z_{\text{middle}} \wedge Z_j$ – where the middle line intercepts the left edge in figure 3.1a – lies on the line $Z_{j+2} \wedge Z_j + t Z_{j-2} \wedge Z_j$ between the two left cusps. As such, the middle twistor is also a linear combination of the twistors Z_j, Z_{j-2} and Z_{j+2} and thus $\langle j, j-2, j+2, Z_{\text{middle}} \rangle = 0$. This condition immediately fixes the ratio β/α to be as in (A.9). The normalization of the projective twistor can be fixed arbitrarily with (A.9) being one such choice. Following the logic above, we

---

[3]Literally, the transformation $(\lambda, \bar\lambda) \to (\bar\lambda, \lambda)$ acts on the momentum $p_\mu \sigma^\mu_{\alpha\dot\alpha} = \lambda_\alpha \tilde{\lambda}_{\dot\alpha}$ as a reflection of p_2 since the corresponding Pauli matrix is antisymmetric while all others are symmetric. Once combined with an 180° rotation in the 1-3 plane, we get what is conventionally denoted by parity. In sum, since rotation symmetries are an obvious symmetry, one often slightly abuses notation to denote as parity any transformation whose determinant is -1.

can now also associate to each middle edge a dual twistor W_{middle} and a pair of spinors $\lambda_{\mathrm{middle}}$ and $\tilde{\lambda}_{\mathrm{middle}}$. They will indeed show up below.

We close this section with two useful identities which we shall use latter. The first is

$$\frac{\langle i\hat{i}j\hat{j}\rangle}{[i\hat{i}j\hat{j}]} = \frac{\langle i\hat{i}\rangle\langle j\hat{j}\rangle}{[i\hat{i}][j\hat{j}]} \tag{A.10}$$

where $\hat{i}$ and i are neighbouring edges and so are $\hat{j}$ and j. The second is

$$\langle abcd\rangle = \langle ab\rangle\langle bc\rangle\langle cd\rangle[bc] \qquad \text{and} \qquad [abcd] = [ab][bc][cd]\langle bc\rangle \tag{A.11}$$

which holds for any four consecutive twistors (starting with a followed by b, then c and then d at the end). Note that the second equality in (A.11) follows from the first equality there together with (A.10). It also follows trivially from the first equality in (A.11) under parity which simply interchanges square and angle brackets.

A.2   Pentagons and Weights

In a tessellation of an n-sided polygon, each two consecutive null squares form a pentagon. As depicted in figure 3.1, each such pentagon shares some edges with the larger polygon while some (either one or two) edges are middle edges defined by the tessellation, see also (A.9).

These pentagons play a prominent role in our construction. In particular, here we want to describe their importance in defining the *weight* of a given edge *with respect to a given pentagon*. To simplify our discussion we label the edges of a generic pentagon as a, b, c, d, e.[4]

Pentagons have no cross-ratios. Nevertheless, they are not totally trivial. For instance, they allow us to read of the weight of an edge of the pentagon (with respect to that pentagon) through the pentagon NMHV ratio function components as

$$\mathcal{R}^{(abcd)} = \frac{1}{\mathbf{abcd}} \ , \qquad \mathcal{R}^{(aabc)} = \frac{1}{\mathbf{a}^2\mathbf{bc}} \ , \qquad \mathcal{R}^{(aaaa)} = \frac{1}{\mathbf{a}^4} \ , \tag{A.12}$$

and so on. All such components can be extracted from a single R-invariant beautifully written using momentum twistors in [45, 47],

$$\mathcal{R}^{\mathrm{NMHV\ pentagon}} = \frac{\prod\limits_{A=1}^{4}\left(\langle abcd\rangle\eta_e^A + \langle bcde\rangle\eta_a^A + \langle cdea\rangle\eta_b^A + \langle deab\rangle\eta_c^A + \langle eabc\rangle\eta_d^A\right)}{\langle abcd\rangle\langle bcde\rangle\langle cdea\rangle\langle deab\rangle\langle eabc\rangle} \ . \tag{A.13}$$

---

[4]For example, this pentagon could be the first pentagon in the tessellation in figure 3.1b. In this case we would set $a = Z_2$, $b = Z_0$, $c = Z_{-1}$, $d = Z_1$ and $e = Z_{\mathrm{middle\ line\ ending\ on\ edge\ 2}}$.
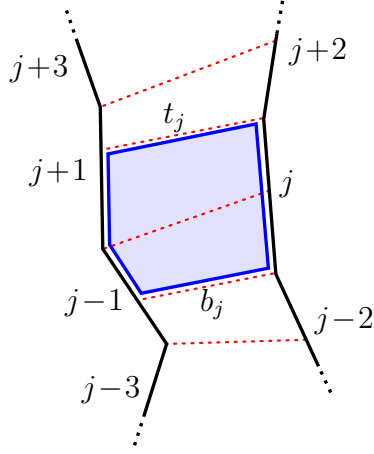
Figure A.1: The weight factor $(\mathbf{j-1})_j(\mathbf{j})_j(\mathbf{j+1})_j$ associated to the j-th pentagon can be expressed in terms of the twistors of the larger polygon. It involves the seven closest edges to that pentagon, as illustrated in the figure. It is clear from this example the advantage of using this edge labelling as opposed to the cyclic one.

From the relations (A.12) we read

$$\mathbf{a}^4 = \frac{\langle abcd \rangle \langle cdea \rangle \langle deab \rangle \langle eabc \rangle}{\langle bcde \rangle^3} \, . \tag{A.14}$$

We can also re-write this relation using (A.11) as

$$\mathbf{a}^4 = \frac{\langle ab \rangle^4 \langle ea \rangle^4}{\langle ab \rangle \langle bc \rangle \langle de \rangle \langle ea \rangle \langle cd \rangle} \Big/ \frac{[cd]^4}{[ab][bc][cd][de][ea]} \tag{A.15}$$

where the familiar Parke-Taylor chains nicely show up.

Furthermore, note that a product of three weights with respect to the same pentagon can be traded by the weight of any of the other two twistors of the pentagon using the first relation in (A.12) with $\mathcal{R}^{(abcd)} = 1/\langle abcd \rangle$. In particular, it follows that

$$\frac{1}{\mathbf{bce}} = \frac{\mathbf{a}}{\langle abce \rangle} = \frac{\mathbf{d}}{\langle dbce \rangle} \, . \tag{A.16}$$

This allows us to massage slightly some of the formulae in the main text. For example, (3.10) can be written a bit more economically using

$$\frac{1}{(\mathbf{j-1})_j \, (\mathbf{j})_j \, (\mathbf{j+1})_j} = \frac{(\mathbf{t_j})_j}{W_j \cdot Z_{t_j}} \qquad \text{or} \qquad \frac{1}{(\mathbf{j-1})_j \, (\mathbf{j})_j \, (\mathbf{j+1})_j} = \frac{(\mathbf{b_j})_j}{W_j \cdot Z_{b_j}} \tag{A.17}$$

165

where t_j and b_j indicate the top or bottom twistors of pentagon j respectively, see figure A.1. Note that it is irrelevant that we do not fix the normalizations of these top and bottom twistors: they drop out in the ratios here constructed.

We can also explicitly evaluate (A.17) by plugging in (A.14) the expressions for the middle momentum twistors (A.9), see figure A.1. When doing so, one finds[5]

$$\left(\frac{1}{(\mathbf{j-1})_j(\mathbf{j})_j(\mathbf{j+1})_j}\right)^4 = \tag{A.18}$$

$$= \frac{\langle j-3,j-1,j+1,j+3\rangle\langle j-2,j-1,j,j+2\rangle\langle j-2,j,j+1,j+2\rangle}{\langle j-2,j-1,j,j+1\rangle^2\langle j-1,j,j+1,j+2\rangle^2\langle j-1,j,j+1,j+3\rangle\langle j-3,j-1,j,j+1\rangle}.$$

A.3 Parity Map

In this section we establish the parity relation (3.36) which we can equivalently cast as

$$\left(\frac{\partial}{\partial\chi_1}\right)^4\ldots\left(\frac{\partial}{\partial\chi_j}\right)^4\mathcal{R} = \left(\frac{\partial}{\partial\chi_{j+1}}\right)^4\ldots\left(\frac{\partial}{\partial\chi_{n-4}}\right)^4\mathcal{R}\bigg|_{Z\to W}. \tag{A.19}$$

To evaluate the left hand side we note that

$$\frac{\partial}{\partial\chi_k} = \frac{\langle k-1,k,k+1,k-2\rangle}{(\mathbf{k-1})_k(\mathbf{k})_j(\mathbf{k+1})_k}\frac{\partial}{\partial\eta_{k-2}} + \ldots \tag{A.20}$$

where the ... contain a linear combination of derivatives from $\partial/\partial\eta_{-1}$ until $\partial/\partial\eta_{k-3}$. Since we are taking the maximum number of each derivative $\partial/\partial\chi_k$, only the term written in (A.20) contributes, while all other terms are already saturated by the previous derivatives. Therefore, at the end we are left with a single ratio function component

$$\mathcal{R}_{(-1)^4\ldots(j-2)^4} \equiv \mathcal{R}^{(-1,-1,-1,-1),\ldots,(j-2,j-2,j-2,j-2)}.$$

We can proceed in a similar fashion for the right hand side of (A.19), restricting the sum in (3.10) to the edges above that pentagon. Keeping track of the multiplicative weight factors, we can now rewrite (A.19) as

$$\frac{\mathcal{R}_{(-1)^4\ldots(j-2)^4}}{\mathcal{R}_{(n-2)^4\ldots(j+3)^4}\big|_{Z\to W}} = \left(\prod_{k=j+1}^{n}\frac{\langle k-1,k,k+1,k+2\rangle}{(\mathbf{k-1})_k(\mathbf{k})_k(\mathbf{k+1})_k}\right)^4_{Z\to W}\bigg/\left(\prod_{k=1}^{j}\frac{\langle k-1,k,k+1,k-2\rangle}{(\mathbf{k-1})_k(\mathbf{k})_k(\mathbf{k+1})_k}\right)^4.$$
$$\tag{A.21}$$

---

[5]As usual, for the bottom and top pentagons we need to adjust this formula slightly. For instance, for $j=1$ we find Z_{-2} in the right hand side which is not defined, see figure 3.1. The fix is very simple: we should simply replace Z_{-2} by the very bottom twistor, that is Z_{-1}. Similarly for the top pentagon, where we should replace Z_{n-1} by the very top twistor Z_{n-2}.

At this point, it is convenient to revert back to a more conventional cyclic notation. We shall revert to cyclic variables using the map in caption of figure 3.1 followed by a simple overall cyclic rotation of all the indices (by a convenient n and j dependent amount). Altogether, we map each edge index k in (A.21) as

$$k \to n - \frac{j}{2} - \frac{1}{2} \delta_{j\,\text{odd}} - \frac{k}{2} \delta_{k\,\text{even}} + \frac{k+3}{2} \delta_{k\,\text{odd}} . \tag{A.22}$$

This change of labelling is illustrated in figure A.2 for $n = 8$ and $j = 3$. To avoid any confusions, we will add a $\mathcal{C}$ to the label of all equations written in this cyclic labelling. Next, it is useful to convert the ratio in (A.21) to two-brackets using (A.15), (A.10) and (A.11). In two-bracket notation, the parity transformation $Z \to W$ simply amounts to interchanging square and angle brackets. At the end of the day, we arrive at the nice expression [6]

$$\frac{\mathcal{R}_{(n)^4...(n-j+1)^4}}{\mathcal{R}_{(n-j-2)^4...(3)^4}|_{Z \to W}} = \frac{\langle 1,2 \rangle ... \langle n,1 \rangle}{\langle n,1 \rangle^4 ... \langle n-j, n-j+1 \rangle^4} \frac{[n-j-2, n-j-1]^4 ... [2,3]^4}{[1,2]...[n,1]} . \tag{A.23}$$

To summarize: The main goal of this appendix is to establish this relation thus proving (3.36).

To do so, we start with the amplitude picture where parity is very well understood – it amounts to the exchange of $\lambda \leftrightarrow \tilde{\lambda}$ and the usual Grassmann variables $\tilde{\eta} \leftrightarrow \bar{\tilde{\eta}}$, see (3.28). We shall show that (A.23) is a simple consequence of the more transparent relation

$$\mathcal{A}_n[1^-, 2^+, ..., (n-j-1)^+, (n-j)^-, ..., n^-] = \mathcal{A}_n[1^+, 2^-, ..., (n-j-1)^-, (n-j)^+, ..., n^+]^* \tag{A.24}$$

for the scattering of $j+2$ negative helicity and $n-j-2$ positive helicity gluons. In a more super-symmetric notation, the quantity on the left hand side is the component $(\tilde{\eta}_1)^4 (\tilde{\eta}_{n-j})^4 ... (\tilde{\eta}_n)^4$ of the super amplitude

$$\mathcal{A}_n = \frac{\delta^8(\sum_{i=1}^n \lambda_i \tilde{\eta}_i)}{\langle 1,2 \rangle ... \langle n,1 \rangle} M_n^{\text{MHV loop}}(\lambda, \tilde{\lambda}) \mathcal{R}(\eta, Z) , \tag{A.25}$$

where $\mathcal{R} = 1 + \mathcal{R}_{\text{NMHV}} + ...$ is the ratio function and $M_n^{\text{MHV loop}}(\lambda, \tilde{\lambda})$ is the MHV amplitude divided by its tree level part. To extract this component we need to recall the relation between the Grassmann variables $\tilde{\eta}$ and η showing up in this expression. In one direction, it reads [47]

$$\tilde{\eta}_i = \frac{\langle i, i+1 \rangle \eta_{i-1} + \langle i+1, i-1 \rangle \eta_i + \langle i-1, i \rangle \eta_{i+1}}{\langle i-1, i \rangle \langle i, i+1 \rangle} , \tag{A.26}$$

---

[6]When simplifying the ratio of weights it is convenient to explore momentum conservation for the various middle squares to see that the dependence on the middle spinors neatly drops out. Recall that for any square momentum conservation $\sum_{j=1}^4 \lambda_j \tilde{\lambda}_j = 0$ readily leads to $\langle 1,2 \rangle [2,3] = -\langle 1,4 \rangle [4,3]$ and $\langle 1,2 \rangle [2,1] = \langle 3,4 \rangle [3,4]$.
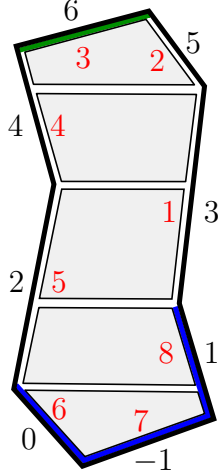
Figure A.2: Example for N^3MHV octagon, $(n = 8, j = 3)$. In blue, the edges charged for $\mathcal{P}_{1234} \circ \mathcal{P}_{1234} \circ \mathcal{P}_{1234} \circ \mathcal{P}$ and in green the edge charged for the parity conjugate $\mathcal{P} \circ \mathcal{P} \circ \mathcal{P} \circ \mathcal{P}_{1234}$. The OPE labelling for the edges is presented in black and in red the cyclic labelling used in this derivation.

while the inverse map is more subtle. It is not unique since we are working on the support of the supersymmetric delta function. In other terms, there is a gauge freedom which we can fix freely. One map that does the job gives $\eta_1 = \eta_2 = 0$ and [98, 99]

$$
\begin{aligned}
\eta_3 &= \langle 2, 3 \rangle \tilde{\eta}_2 \,, \\
\eta_4 &= \langle 2, 4 \rangle \tilde{\eta}_2 + \langle 3, 4 \rangle \tilde{\eta}_3 \,, \\
&\vdots \\
\eta_n &= \langle 2, n \rangle \tilde{\eta}_2 + \ldots + \langle n-1, n \rangle \tilde{\eta}_{n-1} \,.
\end{aligned} \tag{A.27}
$$

Since $\tilde{\eta}_1$ and $\tilde{\eta}_n$ do not appear in this inverse map, we must look for them in the fermionic delta function when extracting this component. Therefore, we can simply replace the fermionic delta function by $\langle n, 1 \rangle^4$ and consider the component $(\tilde{\eta}_{n-j})^4 \ldots (\tilde{\eta}_{n-1})^4$ of the simpler quantity

$$
\left. \frac{\langle n, 1 \rangle^4}{\langle 1, 2 \rangle \ldots \langle n, 1 \rangle} M_n^{\text{MHV loop}}(\lambda, \tilde{\lambda}) \mathcal{R}(\eta, Z) \right|_{\eta_j = \sum_{k=2}^{j-1} \langle k, j \rangle \tilde{\eta}_k} . \tag{A.28}
$$

In turn, this component is also straightforward to extract since it is another example of a saturation effect. More precisely, $\tilde{\eta}_{n-1}$ shows up only in η_n such that extracting four units of it is tantamount to taking four powers of η_n (times $\langle n-1, n \rangle^4$). Next, η_n is crossed out and $\tilde{\eta}_{n-2}$

shows up in η_{n-1} only and so on. All in all, we arrive at

$$\mathcal{A}_n[1^-, 2^+, ..., (n-j-1)^+, (n-j)^-, ..., n^-] = \tag{A.29}$$

$$= M_n^{\text{MHV loop}}(\lambda, \tilde{\lambda}) \frac{\langle n, 1 \rangle^4}{\langle 1, 2 \rangle \dots \langle n, 1 \rangle} \langle n-1, n \rangle^4 \dots \langle n-j, n-j+1 \rangle^4 \mathcal{R}_{(n)^4 \dots (n-j+1)^4} \,.$$

The right hand side of (A.24) can be treated similarly.[7] In the end, we conclude that

$$\frac{\langle n, 1 \rangle^4}{\langle 1, 2 \rangle \dots \langle n, 1 \rangle} \langle n-1, n \rangle^4 \dots \langle n-j, n-j+1 \rangle^4 \mathcal{R}_{(n)^4 \dots (n-j+1)^4}(Z)$$

$$= \frac{[n-j-2, n-j-1]^4}{[1, 2] \dots [n, 1]} [n-j-3, n-j-2]^4 \dots [2, 3]^4 \mathcal{R}_{(n-j-2)^4 \dots (3)^4}(W) \tag{A.30}$$

which gives precisely the ratio in (A.23) thus proving (3.36). This was the main goal of this appendix.

Other cases can be analyzed in a similar way. For instance, to establish an identity like $\mathcal{P}_{1234} \circ \dots \circ \mathcal{P}_{1234} \circ \mathcal{P}_{123} \circ \mathcal{P}_4 \circ \mathcal{P} \circ \dots \circ \mathcal{P} = \mathcal{P} \circ \dots \circ \mathcal{P} \circ \mathcal{P}_4 \circ \mathcal{P}_{123} \circ \mathcal{P}_{1234} \circ \dots \circ \mathcal{P}_{1234}|_{Z \to W}$ we start – on the amplitude side – with an amplitude that besides gluons also involves a positive helicity fermion ψ and one negative helicity fermion $\bar{\psi}$. However, the analysis becomes more and more cumbersome as we consider cases with pentagons that are further away from being maximally charged. It would be interesting to streamline this analysis and work out the general case in a clean way. A better understanding of (the space of) all possible inverse maps $\eta(\tilde{\eta})$ would probably be useful in this respect.

---

[7]When doing so it is convenient to note that the right hand side of (A.24) can be also written as $(\mathcal{A}_n[1^-, 2^+, ..., (j+3)^+, (j+4)^-, ..., n^-])^*_{i \to i-j-2}$. In this form, it is clear that we can simply recycle the result (A.29) with the obvious replacement of angle brackets by square brackets following from the conjugation.

Appendix B

Pentagon transitions and measures

In this appendix we summarize our knowledge about elementary transitions $P_{X|Y}$, with (X,Y) being any pair of flux tube excitations. Their general structure is

$$P_{X|Y}(u|v) = f_X(u)F_{XY}(u,v)f_Y(-v)$$
$$\times \exp\left[2(\kappa_X(u) - i\tilde{\kappa}_X(u))^t \cdot \mathcal{M} \cdot \kappa_Y(v) + 2i(\kappa_X(u) + i\tilde{\kappa}_X(u))^t \cdot \mathcal{M} \cdot \tilde{\kappa}_Y(v)\right], \quad \text{(B.1)}$$

where all the objects in the exponent were explicitly given in the appendix C of [23] for all sorts of excitations of the flux tube (with $\mathcal{M} = \mathbb{Q} \cdot \mathbb{M}$ in the notations of [23], see also [24]). We also found convenient to strip out the factor

$$\log f_X(u) = \int\limits_0^\infty \frac{dt}{t}(J_0(2gt) - 1)\frac{\frac{1}{2}J_0(2gt) + \frac{1}{2} - e^{-q_X t}e^{-iut}}{e^t - 1}, \quad \text{(B.2)}$$

for each excitation, with $J_0(z) = 1 + O(z^2)$ the Bessel function of the first kind and $q_X = -1/2, 0, 1/2, 1, \ldots$ for scalar, large fermion, elementary gluon, bound state of two gluons, etc. (Note that in the case of a small fermion, i.e. $X = \psi_S$ or $\bar{\psi}_S$, we have $f_X(u) = 1$ identically, see B.2 below.)

The factor (B.2) as well as the term in the exponent above are quite universal and, in particular, only depend on the absolute values of the $U(1)$ charges (e.g. they cannot distinguish between $(X,Y) = (\psi,\psi), (\psi,\bar{\psi}), (\bar{\psi},\psi)$, or $(\bar{\psi},\bar{\psi})$). As such, the function $F_{XY}(u,v)$ has the same conjugation property as its parent transition. Since all our transitions obey[1]

$$P_{X|Y}(u|v)^* = P_{\bar{Y}|\bar{X}}(v|u), \quad \text{(B.3)}$$

---

[1] We failed to find a reason for this simple property, but noticed that it is consistent both with the fundamental relation (4.11), since $S_{XY}(u,v)^* = S_{YX}(v,u) = S_{\bar{Y}\bar{X}}(v,u)$, and with the mirror equation (4.12). In the latter case, one needs to use that $u^{-\gamma}$ turns into $u^{+\gamma}$ upon conjugation and that (4.12) is equivalent to $P_{X|Y}(u|v^\gamma) = P_{Y|\bar{X}}(v|u)$.

upon complex conjugation (for real rapidities), with of course $\bar{\phi} = \phi$ for a scalar, $\bar{F}_a = F_{-a}$ for a gluon, etc., then the exact same relation holds true for the corresponding functions F.

It is also interesting to note that both $\log f_X$ and the exponent in (B.1) are of order $O(g^2)$ for small g. (This estimate is not uniform in the rapidities and holds only away from the locations of singularities, which are at imaginary half integer values at weak coupling.) The leading order weak coupling results can thus be directly obtained from the prefactors F_{XY}.

B.1   Summary of transitions

Knowing the transitions is equivalent to knowing the prefactors F in (B.1). For them, which as we just said are also all we need to know to leading order at weak coupling, we have the following lists. (Up to few exceptions involving gluonic bound states, all the transitions given below already appeared in [22–24, 28, 39, 51]. At the end of this subsection, we comment on the 'difference of normalizations' between our transitions here and those obtained in these series of papers.)

Transitions involving a gluon or a bound state of gluons

We start by the cases involving a gluon or a bound state of gluons.

The purely gluonic transitions are given by

$$
\begin{aligned}
F_{F_a F_b}(u, v) &= \sqrt{(x^{[+a]}y^{[-b]} - g^2)(x^{[-a]}y^{[+b]} - g^2)(x^{[+a]}y^{[+b]} - g^2)(x^{[-a]}y^{[-b]} - g^2)} \\
&\times \frac{(-1)^b \Gamma(\frac{|a|-|b|}{2} + iu - iv)\Gamma(\frac{|a|+|b|}{2} - iu + iv)}{g^2 \Gamma(1 + \frac{|a|}{2} + iu)\Gamma(1 + \frac{|b|}{2} - iv)\Gamma(1 + \frac{|a|-|b|}{2} - iu + iv)}, \quad \text{for } ab > 0, \\
F_{F_a F_b}(u, v) &= \frac{1}{\sqrt{(1 - \frac{g^2}{x^{[+a]}y^{[-b]}})(1 - \frac{g^2}{x^{[-a]}y^{[+b]}})(1 - \frac{g^2}{x^{[+a]}y^{[+b]}})(1 - \frac{g^2}{x^{[-a]}y^{[-b]}})}} \\
&\times \frac{\Gamma(1 + \frac{|a|+|b|}{2} + iu - iv)}{\Gamma(1 + \frac{|a|}{2} + iu)\Gamma(1 + \frac{|b|}{2} - iv)}, \quad \text{for } ab < 0,
\end{aligned}
\tag{B.4}
$$

and the mixed ones by

$$
F_{F_a \phi}(u, v) = F_{\phi F_a}(-v, -u) = \frac{\sqrt{x^{[+a]}x^{[-a]}}\,\Gamma(\frac{1}{2} + \frac{|a|}{2} + iu - iv)}{g\,\Gamma(1 + \frac{|a|}{2} + iu)\Gamma(\frac{1}{2} - iv)}, \tag{B.5}
$$

for any a, and by

$$F_{F_a\psi}(u,v) = F_{\psi F_a}(-v,-u) = -\frac{iy(x^{[+a]}x^{[-a]})^{3/4}\Gamma(\frac{a}{2}+iu-iv)\sqrt{(1-\frac{g^2}{x^{[+a]}y})(1-\frac{g^2}{x^{[-a]}y})}}{g^{3/2}\Gamma(1+\frac{a}{2}+iu)\Gamma(1-iv)},$$

$$F_{F_{-a}\psi}(u,v) = F_{\psi F_{-a}}(-v,-u) = \frac{(x^{[+a]}x^{[-a]})^{1/4}\,\Gamma(1+\frac{a}{2}+iu-iv)}{g^{1/2}\Gamma(1+\frac{a}{2}+iu)\Gamma(1-iv)\sqrt{(1-\frac{g^2}{x^{[+a]}y})(1-\frac{g^2}{x^{[-a]}y})}},$$

(B.6)

for $a > 0$. In all cases, we have $x = x(u)$, $x^{[\pm a]} = x(u\pm ia/2)$, $y = x(v)$, $y^{[\pm b]} = x(v\pm ib/2)$, $x(u) \equiv \frac{1}{2}(u+\sqrt{u^2-(2g)^2})$ and $\Gamma(z)$ the Euler Gamma function. Transitions involving $\bar{\psi}$ can be obtained by conjugating those with ψ, as in (B.3).

(Note that all the factors above are normalized such that the associated transitions are equal to 1 to leading order at strong coupling, in the perturbative regime, i.e. for excitations with momenta of the same order as their masses. This is the expected decoupling property of the gluons at strong coupling.)

Transitions involving only scalars or fermions

We proceed with the remaining set of functions F_{XY} involving scalars and fermions. They read

$$F_{\phi\phi}(u,v) = \frac{\Gamma(iu-iv)}{g\Gamma(\frac{1}{2}+iu)\Gamma(\frac{1}{2}-iv)},$$

$$F_{\phi\psi}(u,v) = F_{\phi\bar{\psi}}(u,v) = \frac{\sqrt{y}\,\Gamma\left(\frac{1}{2}+iu-iv\right)}{g\Gamma(\frac{1}{2}+iu)\Gamma(1-iv)},$$

$$F_{\bar{\psi}\psi}(u,v) = -F_{\psi\bar{\psi}}(u,v) = \frac{(xy)^{3/4}\Gamma(1+iu-iv)}{g^{3/4}\Gamma(1+iu)\Gamma(1-iv)\sqrt{xy-g^2}},$$

$$F_{\psi\psi}(u,v) = -F_{\bar{\psi}\bar{\psi}}(u,v) = \frac{i(xy)^{1/4}\Gamma(iu-iv)\sqrt{xy-g^2}}{g^{5/4}\Gamma(1+iu)\Gamma(1-iv)}.$$

(B.7)

(The branch choice for the mixed transitions above was mostly driven by the goal of getting the sign-free large (positive) v behaviours (B.20).)

The lists (B.4), (B.5), (B.6) and (B.7) cover all the pentagon transitions of the OPE program.

Comparison with the literature

As alluded to before, the pentagon transitions listed before already appeared in the literature. We found useful however to redefine some of them, still preserving the fundamental relation (4.11)

172

and the mirror axiom (4.12). For instance, comparing the scalar transition in (B.7) with the one appearing in [22], we find that

$$P_{\phi|\phi}(u|v)_{\text{here}} = g P_{\phi|\phi}(u|v)_{[22]} . \tag{B.8}$$

Clearly, such an innocent rescaling cannot alter the validity of (4.11) and (4.12). A slightly more involved redefinition is found when comparing our mixed transitions in (B.6) with those found in [39]. We get

$$P_{F|\psi}(u|v)_{\text{here}}^2 = -\frac{\sqrt{x^+ x^-}}{g} \times P_{F|\psi}(u|v)_{[39]}^2 ,$$

$$P_{F|\bar{\psi}}(u|v)_{\text{here}}^2 = -\frac{g}{\sqrt{x^+ x^-}} \times P_{F|\bar{\psi}}(u|v)_{[39]}^2 . \tag{B.9}$$

Nonetheless, here as well, both expressions fulfill the same axioms (4.11) and (4.12), and thus differ only by CDD factors. Along a somewhat similar vein,[2] we have

$$P_{\psi|\psi}(u|v)_{\text{here}} = i\frac{g^{3/4}}{(xy)^{1/4}} \times P_{\psi|\psi}(u|v)_{[23]} , \qquad P_{\psi|\bar{\psi}}(u|v)_{\text{here}} = -\frac{(xy)^{1/4}}{g^{3/4}} \times P_{\psi|\bar{\psi}}(u|v)_{[23]} , \tag{B.10}$$

and also

$$P_{\bar{\psi}|\bar{\psi}}(u|v)_{\text{here}} = -P_{\psi|\psi}(u|v)_{\text{here}} , \qquad P_{\bar{\psi}|\psi}(u|v)_{\text{here}} = -P_{\psi|\bar{\psi}}(u|v)_{\text{here}} , \tag{B.11}$$

while the convention of [23] was

$$P_{\bar{\psi}|\bar{\psi}}(u|v)_{[23]} = P_{\psi|\psi}(u|v)_{[23]} , \qquad P_{\psi|\bar{\psi}}(u|v)_{[23]} = P_{\bar{\psi}|\psi}(u|v)_{[23]} . \tag{B.12}$$

These are all the differences we could find. As we can see, they almost all relate to the choice of CDD factors, which (by definition) is the sole freedom left after imposing the bootstrap axioms.[3] This ambiguity is not without connection to the freedom we have to reshuffle factors in the definitions of the various elements of the POPE integrand, provided we have the same physical integrand once we multiply them together. This is precisely what happens when relating the integrands that we can produce here with those derived in [22,23,28,39,51] using slightly different transitions, measures, and, sometimes, rules for assigning form factors. Our conventions here have the slight advantage that no form factors are needed for MHV amplitudes; equivalently, they are normalized such that the relation between charged pentagons and zero momentum fermions is most straightforward. It is nonetheless clearly desirable to find a better handle on the ambiguities mentioned above. Additional constraints should, for instance, follow from the nonlinear nature of the anomalous mirror rotation for fermions and/or from certain fusion properties the various transitions could obey. It remains to work them out and see how much they can tell.

---

[2]In case of fermions, it is much harder to check which choice is better as far as the mirror property is concerned, since the mirror algebra is anomalous for fermions and thus harder to implement, see appendices of [22] for more details.

[3]In the conventions of [23] the fundamental axiom (4.11) for $\psi\bar{\psi}$ was not including a minus sign in front of the S-matrix; hence differences in transitions related to this sign are not strictly speaking of CDD type.

B.2 Analytic continuation to small fermions

It is also convenient to store the representation for small fermions. This one is obtained by direct analytical continuation, $x(v) \to x(\check{v}) = g^2/x(v)$, and it was thoroughly exemplified in [23]. The squared transitions, for instance, read as :

$$P_{\phi|\psi}(u|\check{v})^2 = -\frac{S_{\phi\psi}(u,\check{v})}{(u-v+\frac{i}{2})S_{\star\phi\psi}(u,\check{v})}\,,$$

$$P_{F|\psi}(u|\check{v})^2 = -\frac{g\sqrt{x^+x^-}y(u-v-\frac{i}{2})S_{F\psi}(u,\check{v})}{(x^+y-g^2)(x^-y-g^2)S_{\star F\psi}(u,\check{v})}\,,$$

$$P_{F|\bar{\psi}}(u|\check{v})^2 = -\frac{(x^+y-g^2)(x^-y-g^2)S_{F\bar{\psi}}(u,\check{v})}{g\sqrt{x^+x^-}y(u-v-\frac{i}{2})S_{\star F\bar{\psi}}(u,\check{v})}\,,$$

$$P_{\psi|\psi}(u|\check{v})^2 = -\frac{\sqrt{gxy}\,S_{\psi\psi}(u,\check{v})}{(xy-g^2)(u-v+i)S_{\star\psi\psi}(u,\check{v})}\,, \tag{B.13}$$

$$P_{\psi|\bar{\psi}}(u|\check{v})^2 = -\frac{(xy-g^2)S_{\psi\bar{\psi}}(u,\check{v})}{\sqrt{gxy}\,(u-v)S_{\star\psi\bar{\psi}}(u,\check{v})}\,,$$

$$P_{\psi|\psi}(\check{u}|\check{v})^2 = \frac{(xy-g^2)S_{\psi\psi}(\check{u},\check{v})}{\sqrt{gxy}\,(u-v)(u-v+i)S_{\star\psi\psi}(\check{u},\check{v})}\,,$$

$$P_{\psi|\bar{\psi}}(\check{u}|\check{v})^2 = \frac{\sqrt{gxy}\,S_{\psi\bar{\psi}}(\check{u},\check{v})}{(xy-g^2)S_{\star\psi\bar{\psi}}(\check{u},\check{v})}\,,$$

where, again, 'check marked' rapidities indicate analytical continuation to the small momentum sheet.

More explicitly, and including bound states as well, we can take all the transitions listed before and perform the continuation. The explicit form of the analytically continued transitions still preserves the structure (B.1), but the prefactors as well as the functions in the exponent are changed. The continuation of the exponent was explicitly worked out in [23] and here we provide once again only the expressions for the prefactors. We stress in particular that $f_{\psi_S}(u) \neq f_\psi(\check{u})$ and $F_{X\psi_S}(u,v) \neq F_{X\psi}(u,\check{v})$, since upon continuation of the *full* transition some extra terms are produced by the exponent in (B.1) and transferred to the prefactors. Instead, the correct analytic continuation produces $f_{\psi_S}(u) = 1$ and

$$F_{F_a\psi_S}(u,v) = F_{\psi_S F_a}(-v,-u) = -\frac{\sqrt{g}(u-v+ia/2)}{y(x^{[+a]}x^{[-a]})^{1/4}\sqrt{(1-\frac{g^2}{x^{[+a]}y})(1-\frac{g^2}{x^{[-a]}y})}}\,, \quad \text{for } a>0\,,$$

$$F_{F_a\psi_S}(u,v) = F_{\psi_S F_a}(-v,-u) = \frac{(x^{[+a]}x^{[-a]})^{1/4}}{\sqrt{g}}\sqrt{\left(1-\frac{g^2}{x^{[+a]}y}\right)\left(1-\frac{g^2}{x^{[-a]}y}\right)}\,, \quad \text{for } a<0\,, \tag{B.14}$$

and

$$F_{\phi\psi_S}(u,v) = 1/\sqrt{y}, \qquad\qquad F_{\psi_S\phi}(u,v) = 1/\sqrt{x},$$

$$F_{\psi\psi_S}(u,v) = \frac{g^{1/4}}{x^{1/4}y^{3/4}}\bigg/\sqrt{1 - \frac{g^2}{xy}}, \qquad F_{\psi\bar\psi_S}(u,v) = -\frac{1}{g^{1/4}}\left(\frac{x}{y}\right)^{1/4}\sqrt{1 - \frac{g^2}{xy}},$$

$$F_{\psi_S\psi}(u,v) = -\frac{g^{1/4}}{x^{3/4}y^{1/4}}\bigg/\sqrt{1 - \frac{g^2}{xy}}, \qquad F_{\psi_S\bar\psi}(u,v) = -\frac{1}{g^{1/4}}\left(\frac{y}{x}\right)^{1/4}\sqrt{1 - \frac{g^2}{xy}},$$ (B.15)

$$F_{\psi_S\psi_S}(u,v) = -\frac{(xy)^{1/4}}{g^{1/4}(u-v)}\sqrt{1 - \frac{g^2}{xy}}, \qquad F_{\psi_S\bar\psi_S}(u,v) = -\frac{g^{1/4}}{(xy)^{1/4}}\bigg/\sqrt{1 - \frac{g^2}{xy}}.$$

B.3   Measures

We recall that the measures are obtained from the direct transitions through

$$\text{Res}_{v=u} P_{X|X}(u|v) = \frac{i}{\mu_X(u)}.$$ (B.16)

They have the universal structure

$$\mu_X(u) = \frac{M_X(u)}{f_X(u)f_X(-u)} \exp\left[2\tilde\kappa_X(u)^t \cdot \mathcal{M} \cdot \tilde\kappa_X(u) - 2\kappa_X(u)^t \cdot \mathcal{M} \cdot \kappa_X(u)\right],$$ (B.17)

with

$$M_\phi(u) = \frac{\pi g}{\cosh(\pi u)},$$

$$M_\psi(u) = -i\frac{\pi g^{5/4}u}{\sqrt{x}\,\sinh(\pi u)\sqrt{x^2 - g^2}},$$ (B.18)

$$M_{F_a}(u) = \frac{(-1)^a g^2 \Gamma(1 + \frac{a}{2} + iu)\Gamma(1 + \frac{a}{2} - iu)}{\Gamma(a)(x^{[+a]}x^{[-a]} - g^2)\sqrt{((x^{[+a]})^2 - g^2)((x^{[-a]})^2 - g^2)}}, \quad \text{for } a > 0.$$

Moreover, we have that $\mu_{F_{-a}}(u) = \mu_{F_a}(u)$ and $\mu_{\bar\psi}(u) = -\mu_\psi(u)$. Upon analytical continuation to the small fermion sheet, we obtain

$$M_{\psi_S}(u) = i\frac{g^{1/4}\sqrt{x}}{\sqrt{x^2 - g^2}}.$$ (B.19)

B.4 Zero momentum limit

Given a transition $P_{\bar{\psi}|Y}(\check{u}|v)$ it is immediate to derive its scalings at $u = \infty$, i.e. for a zero momentum fermion. This one can be read directly from the function $F_{\bar{\psi}_S Y}(u, v)$ listed before, since the remaining factors in (B.1) all go to 1 in this limit. We get this way

$$
\begin{aligned}
P_{\bar{\psi}|\bar{\psi}}(\check{u}|v) &\sim \frac{g^{1/4}}{u^{3/4} y^{1/4}} \,, \\[4pt]
P_{\bar{\psi}|\phi}(\check{u}|v) &\sim \frac{1}{\sqrt{u}} \,, \\[4pt]
P_{\bar{\psi}|\psi}(\check{u}|v) &\sim \frac{1}{g^{1/4}} \left(\frac{y}{u}\right)^{1/4} \,, \\[4pt]
P_{\bar{\psi}|F_a}(\check{u}|v) &\sim \frac{\sqrt{g}}{(y^{[+a]} y^{[-a]})^{1/4}} \,, && \text{for } a < 0 \,, \\[4pt]
P_{\bar{\psi}|F_a}(\check{u}|v) &\sim \frac{(y^{[+a]} y^{[-a]})^{1/4}}{\sqrt{g}} \,, && \text{for } a > 0 \,,
\end{aligned}
\tag{B.20}
$$

where, again, $y = x(v)$ and $y^{[\pm a]} = x(v \pm i\frac{a}{2})$. This information was used to obtain the non-MHV form factors $h_{\bar{Y}}(v)$ of the excitation $Y(v)$ in the bulk of the paper, with help of the asymptotic behaviour of the Jacobian factor

$$
\sqrt{\frac{\Gamma_{\text{cusp}}}{2ig} \mu_{\bar{\psi}}(\check{u}) \frac{du}{dp_{\bar{\psi}}}(\check{u})} \sim \frac{u^{3/4}}{g^{3/8}} \,,
\tag{B.21}
$$

itself following from

$$
\mu_{\bar{\psi}}(\check{u}) \sim -\frac{ig^{1/4}}{\sqrt{u}} \,, \qquad \frac{dp_{\bar{\psi}}}{du}(\check{u}) \sim -\frac{\Gamma_{\text{cusp}}}{2u^2} \,.
\tag{B.22}
$$

Appendix C

The superconformal charge $\mathcal{Q}$ and the flux Goldstone fermion

In section 4.2.2 we used the realization of the superconformal generator $\mathcal{Q}_A$ as a zero momentum fermion. The precise relation is (4.24) and is repeated here for convenience

$$\mathcal{Q}|0\rangle = \sqrt{\frac{\Gamma_{\text{cusp}}}{2g}} \lim_{p \to 0} |p\rangle = \lim_{v \to \infty} \sqrt{\frac{\Gamma_{\text{cusp}}}{2gi} \frac{d\check{v}}{dp_{\bar{\psi}}} \mu_{\bar{\psi}}(\check{v})} \, |\bar{\psi}(\check{v})\rangle \,. \tag{C.1}$$

In this appendix we will derive this relation.

C.1 The zero momentum fermion

The non-trivial part of (C.1) is the factor dressing the zero momentum fermion state. To derive it, we should first fix the normalization of that flux-tube state $|\bar{\psi}\rangle$. It is instructive to do this in two steps. First we note that we have a well defined flux tube square measure μ, which allows us to overlap states in the flux Hilbert space. Using the supersymmetry algebra, this measure leads to a precise representation of the superconformal generators on the flux, that we denote by $\mathbb{Q}_A$. There is no reason however for this realization of the supercharge on the flux tube to be normalized in the same way as its realization on the generating function of amplitudes or equivalently, the super loop. Namely, the two may differ by an overall proportionality constant $\mathbb{Q}_A = c_0 \times \mathcal{Q}_A$.[1] We shall now first relate $\mathbb{Q}_A$ to a zero momentum fermion using the measure and the supersymmetry algebra. We will then fix the constant c_0 by demanding that pentagon NHMV amplitude is the same as the MHV one as appears in the generating function (4.14).

---

[1]See [16] for a very similar relation.

Consider first a delta-function normalized momentum states

$$\langle p(u)|\tilde{p}(v)\rangle = 2\pi\delta(p(u) - \tilde{p}(v)) \qquad \Rightarrow \qquad \langle p=0|\tilde{p}=0\rangle = 2\pi\delta(0) = \mathrm{Vol}(\sigma) \qquad (C.2)$$

where $\mathrm{Vol}(\sigma)$ is the infinite volume of the flux in the coordinate σ conjugate to p. These momentum states differ by a simple normalization factor (involving the measure $\mu_{\bar{\psi}}$) from the rapidity states, which we conventionally normalize as [22]

$$\langle v|u\rangle = \frac{2\pi}{\mu_{\bar{\psi}}(u)}\delta(v - u) \qquad \Rightarrow \qquad |p(u)\rangle = \sqrt{-i\frac{dv}{dp_{\bar{\psi}}}\mu_{\bar{\psi}}(u)}\,|u\rangle \qquad (C.3)$$

On the other hand, with respect to this square measure, we have

$$2||\mathbb{Q}_A|0\rangle||^2 = \langle 0|\{\mathbb{Q}_A, \bar{\mathbb{Q}}^A\}|0\rangle \qquad (C.4)$$

where $|0\rangle$ is the GKP vacuum, normalized so that $\langle 0|0\rangle = 1$. The commutator is a special conformal generator that can be written in terms of the symmetries of the square as

$$\sum_{A=1}^{4}\{\mathbb{Q}_A, \bar{\mathbb{Q}}^A\} = 2(\partial_\tau - i\partial_\phi) + \mathcal{C}\ , \qquad (C.5)$$

where the total helicity $\mathcal{C} = 0$ in our case and for simplicity, we have summed over the R-charged index, see section C.2. The GKP vacuum does not carry $U(1)$ charge while ∂_τ measures its energy. We conclude that

$$||\mathbb{Q}_A|0\rangle||^2 = \frac{1}{4}E_{\mathrm{GKP}}\langle 0|0\rangle = \frac{1}{4}\Gamma_{\mathrm{cusp}}\,\mathrm{Vol}(\sigma) \qquad (C.6)$$

where in the last step we used the interpretation of Γ_{cusp} as the energy density of the flux in the σ direction [48]. It then follows that

$$\mathbb{Q}|0\rangle = \sqrt{\frac{\Gamma_{\mathrm{cusp}}}{4}}\lim_{p\to 0}|p\rangle = \lim_{v\to\infty}\sqrt{\frac{\Gamma_{\mathrm{cusp}}}{4i}\frac{d\check{v}}{dp_{\bar{\psi}}}\mu_{\bar{\psi}}(\check{v})}\,|\bar{\psi}(\check{v})\rangle \qquad (C.7)$$

where the check over the fermion rapidity ($\check{v}$) indicates that it is on the so-called *small fermion sheet* where the zero momentum point is, see [23].

Next, we shall fix the proportionality constant c_0. This is done by demanding that the pentagon NHMV amplitude is the same as the MHV one. Translated to the POPE notations, this condition reads

$$1 = P(0|0)\overset{!}{=}P^{[4]}(0|0) \qquad (C.8)$$
$$= \frac{1}{c_0^4}\left(\frac{\Gamma_{\mathrm{cusp}}}{4}\right)^2\prod_{j=1}^{4}\lim_{v_j\to\infty}\sqrt{-i\frac{d\check{v}_j}{dp_{\bar{\psi}}}\mu_{\bar{\psi}}(\check{v}_j)}\times P_{\bar{\psi}^4|0}(\check{v}_1,\check{v}_2,\check{v}_3,\check{v}_4|0)\times(\texttt{matrix part}) = \frac{g^2}{4c_0^4}$$

178

where in the last step we used the large v behaviours quoted in B.4, together with

$$P_{\bar{\psi}|\bar{\psi}}(\check{v}|\check{u}) \sim \frac{(vu)^{\frac{1}{4}}}{g^{\frac{1}{4}}(u-v)} \, ,$$

that can be read from the expressions in B.2, and, finally, the expression for the matrix part (which is nontrivial in this case) given by [58]

$$\texttt{matrix part} = \frac{1}{\displaystyle\prod_{i>j}^{4}(v_i - v_j + i)} \, .$$

We deduce that $c_0 = \sqrt{g/2}$ and hence the relation (C.1). In the following subsection we elaborate on the commutation relation (C.5).

C.2   The commutator of superconformal charges

We shall now derive the relation relation (C.5) used above. For that aim, it is convenient to decompose any twistor in the basis of the square four twistors, (see for example appendix A of [22] for an explicit choice)

$$Z = z_b \, Z_{\text{bottom}} + z_t \, Z_{\text{top}} + z_r \, Z_{\text{right}} + z_l \, Z_{\text{left}} \, . \tag{C.9}$$

In this basis, the three symmetries of the square are generated by

$$\partial_\tau = z_b \partial_{z_b} - z_t \partial_{z_t} \, , \qquad \partial_\sigma = z_r \partial_{z_r} - z_l \partial_{z_l} \quad \text{and} \quad \partial_\phi = \frac{i}{2}\left(z_b \partial_{z_b} + z_t \partial_{z_t} - z_r \partial_{z_r} - z_l \partial_{z_l}\right) \, . \tag{C.10}$$

The relation (C.5) is an algebra relation between superconformal generators and therefore we can use any representation of the generators to test it. When acting on the generating function of helicity amplitudes, the supercharge is represented as $Q_A^\alpha = Z^\alpha \partial_\eta$. The operator $\mathcal{Q}_A$ is a specific component of the superconformal generator Q_A^α which was specified in [2]. To translate between (C.9) and the notations of [2] we may think of the square here as the bottom square of the j'th pentagon in the POPE decomposition. Then, equations (10)-(11) in [2] for the component of Q_A^α read

$$\mathcal{Q}_A = \partial_{\chi_j^A} \; \propto \; (Z_{j-1} \wedge Z_j \wedge Z_{j+1}) \cdot Z \partial_\eta \; \propto \; z_b \partial_{\eta^A} \tag{C.11}$$

where we used that $Z_j = Z_{\text{left}}$, $Z_{j-1} = Z_{\text{right}}$ and Z_{j+1} is a linear combination of Z_{right} and Z_{top}. Here, we drop the proportionality factors in (C.11) as it drops out in the commutator (C.5). We

179

can now use the conjugate operator in this representation to evaluate the commutator in (C.5). We find[2]

$$
\begin{aligned}
\sum_A \{\mathcal{Q}_A, \bar{\mathcal{Q}}^A\} &= \sum_A \{z_b \partial_{\eta^A}, \eta^A \partial_{z_b}\} = 4 z_b \partial_{z_b} + \sum_A \eta^A \partial_{\eta^A} \qquad\qquad \text{(C.12)} \\
&= 2(\partial_\tau - i\partial_\phi) + (z_b \partial_{z_b} + z_t \partial_{z_t} + z_r \partial_{z_r} + z_l \partial_{z_l}) + \sum_A \eta^A \partial_{\eta^A} \\
&= 2(\partial_\tau - i\partial_\phi) + \mathcal{C}
\end{aligned}
$$

Here, the summation over the R-charge index was done for simplicity. Otherwise, on the right hand side we would also had an R-charge generator. Alternatively to this derivation, (C.5) can be read from equation (3.9) in [32] by specifying to the corresponding component.

---

[2]Note that the commutation relation (C.12) is independent of the measure one uses to realise it and thus $\{\mathcal{Q}_A, \bar{\mathcal{Q}}^A\} = \{\mathbb{Q}_A, \bar{\mathbb{Q}}^A\}$.

Appendix D

A second example: $\mathcal{P}_1 \circ \mathcal{P}_2 \circ \mathcal{P}_{34}$

In this second example we analyse another heptagon component where the middle pentagon is charged, namely $\mathcal{P}_1 \circ \mathcal{P}_2 \circ \mathcal{P}_{34}$. We consider again the contribution from multiparticle states in both squares, this time a term proportional to

$$e^{-2\tau_1 - 3i\phi_1/2} \times e^{-2\tau_2 + i\phi_2} \,. \tag{D.1}$$

To find which processes contribute we first note that we need twist 2 states for both squares with helicities -3/2 and +1. Then we follow the same logic as in section 4.3.2 and see the implications of R-charge conservation. The first pentagon carries one unit of $R-$charge which enforces the state propagating in the first middle square to be in the anti-fundamental ($\bar{\mathbf{4}}$) representation of $SU(4)$. The second pentagon also possesses one unit of $R-$charge. This implies that the state in the second middle square should be in one of the two representations entering in the decomposition of $\bar{\mathbf{4}} \otimes \bar{\mathbf{4}} = \mathbf{6} \oplus \overline{\mathbf{10}}$. The state is finally projected onto the vector representation ($\mathbf{6}$) by the last pentagon that carries two units of $R-$charge. In the first square, the only option is the state formed by $\bar{\psi} F_{-1}$. In the second one we could either have ϕF_1 or $\psi\psi$; as the reader might guess, it is the second state which contributes at tree level given the small fermions behaviour. All we are left to do is study the process

$$\texttt{vacuum} \to \bar{\psi} \, F_{-1} \to \psi\psi \to \texttt{vacuum} \,. \tag{D.2}$$

We see that the R-charge index of the antifermion in the first middle square is fixed by the R-charge index of χ in the first pentagon. However, this is not the case for the two fermions in the second square. In other words the matrix part is not trivial in this case, but one can compute it in a straightforward way following the logic in [23] where the contribution of $(\psi\bar{\psi})$ was studied and the S-matrix of the fermions in the vector ($\mathbf{6}$) representation [28]. The full integrand is then

given by the product of the following parts

$$\texttt{dynamical part} \;=\; \hat{\mu}_{F_{-1}}(u)\,\hat{\mu}_{\bar{\psi}}(w_1)\,\hat{\mu}_{\psi}(w_2)\,\hat{\mu}_{\psi}(v) \tag{D.3}$$

$$\times \frac{P_{\bar{\psi}|F_1}(w_2|u)P_{\bar{\psi}|F_1}(v|u)P_{\bar{\psi}|\psi}(w_2|w_1)P_{\bar{\psi}|\psi}(v|w_1)}{P_{F_1|\psi}(u|w_1)P_{\bar{\psi}|F_{-1}}(w_1|u)P_{\psi|\psi}(w_2|v)P_{\bar{\psi}|\bar{\psi}}(v|w_2)}\,, \tag{D.4}$$

$$\texttt{form factors part} \;=\; \frac{1}{g^{\frac{5}{4}}}h_{\psi}(w_1)h_{\bar{\psi}}(w_1)h_{F_{-1}}(u)h_{\bar{\psi}}(w_2)h_{\bar{\psi}}(v)(h_{\psi}(w_2))^2(h_{\psi}(v))^2, \tag{D.5}$$

$$\texttt{matrix part} \;=\; \frac{2}{(v-w_2)^2+1}\,. \tag{D.6}$$

Given that the fermions can be small or large, one can split the process into the different contributions

$$\mathcal{W}_{\bar{\psi}\,F_{-1}\to\psi\psi} \;=\; \mathcal{W}_{\bar{\psi}_L\,F_{-1}\to\psi_L\psi_L} + \mathcal{W}_{\bar{\psi}_L\,F_{-1}\to\psi_S\psi_S} + 2\times\mathcal{W}_{\bar{\psi}_L\,F_{-1}\to\psi_S\psi_L} \tag{D.7}$$

$$+\,\mathcal{W}_{\bar{\psi}_S\,F_{-1}\to\psi_L\psi_L} + \mathcal{W}_{\bar{\psi}_S\,F_{-1}\to\psi_S\psi_S} + 2\times\mathcal{W}_{\bar{\psi}_S\,F_{-1}\to\psi_S\psi_L}\,, \tag{D.8}$$

where the factor of 2 accounts for the two equivalent ways of choosing which of the two fermions is small. At tree level only the last term contributes. One could expect that also the second to last term with two small fermions in the last square would also appear at tree level, but as explained in [23] this contribution vanishes[1]. Therefore we consider only the last term in (D.7) and the transition reads

$$\mathcal{W}_{\bar{\psi}\,F_{-1}\to\psi\psi} \;=\; 2\int_{\mathbb{R}}\frac{du}{2\pi}\int_{\mathbb{R}-i0}\frac{dv}{2\pi}\int_{\bar{\mathcal{C}}_{\mathrm{small}}}\frac{dw_2}{2\pi}\int_{\mathcal{C}_{\mathrm{small}}}\frac{dw_1}{2\pi}\,(\texttt{dynamical part})$$

$$\times (\texttt{form factors part})\times(\texttt{matrix part})\,, \tag{D.9}$$

where we use $-i\epsilon$ prescription for fermions in the top square and the opposite prescription for fermions in the bottom square. (Accordingly we use the lower half plane (half-moon) contour $\mathcal{C}_{\mathrm{small}}$ for the small fermion at the bottom and its conjugate $\bar{\mathcal{C}}_{\mathrm{small}}$ for the small fermion at the top.) We can now integrate out the two small fermions by picking the poles $w_2 = v+i$ coming from the pentagon transition $P_{\bar{\psi}F_{-1}}$ and $w_1 = u-i/2$ from the matrix part. Finally we integrate over u and v and find that the tree-level prediction is given by

$$\mathcal{W}_{\bar{\psi}\,F_{-1}\to\psi\psi} \;=\; \frac{e^{-2\tau_1-2\tau_2-3i\phi_1/2+i\phi_2}}{(e^{2\sigma_1}+1)^2\,(e^{2\sigma_2}+1)^2\,(e^{2\sigma_1}+e^{2\sigma_2}+e^{2\sigma_1+2\sigma_2})^3}$$

$$\times \big(e^{7\sigma_1} + 3e^{5\sigma_1+2\sigma_2} + 5e^{7\sigma_1+2\sigma_2} + 3e^{3\sigma_1+4\sigma_2} + 12e^{5\sigma_1+4\sigma_2}$$

$$+\,10e^{7\sigma_1+4\sigma_2} + e^{\sigma_1+6\sigma_2} + 5e^{3\sigma_1+6\sigma_2} + 10e^{5\sigma_1+6\sigma_2} + 6e^{7\sigma_1+6\sigma_2}\big)\,. \tag{D.10}$$

---

[1]This is because after integrating out the first small fermion there are no more singularities enclosed by the second integration contour. In colloquial words, one should have at least one large excitation to attach the fist small fermion (e.g. $F_1\psi_S\psi_S$ would have a non vanishing contribution).

To check this expression against data, we first relate $\mathcal{P}_1 \circ \mathcal{P}_2 \circ \mathcal{P}_{34}$ to a linear combination of super amplitude η-components [2]

$$
\begin{aligned}
\frac{\partial}{\partial\chi_1}\frac{\partial}{\partial\chi_2}\left(\frac{\partial}{\partial\chi_3}\right)^2\mathcal{W} &= \frac{(-\mathbf{1})_1\,((\mathbf{5})_3)^2}{(\mathbf{1})_2(\mathbf{2})_2(\mathbf{3})_2}\frac{\partial}{\partial\eta_{-1}}\left(\langle 1,2,3,-1\rangle\frac{\partial}{\partial\eta_{-1}} + \langle 1,2,3,0\rangle\frac{\partial}{\partial\eta_0}\right)\left(\frac{\partial}{\partial\eta_5}\right)^2\mathcal{W} \\
&= \frac{(-\mathbf{1})_1\,((\mathbf{5})_3)^2}{(\mathbf{1})_2(\mathbf{2})_2(\mathbf{3})_2}\left(\langle 1,2,3,-1\rangle\,\mathcal{W}^{(-1,-1,5,5)} + \langle 1,2,3,0\rangle\,\mathcal{W}^{(-1,0,5,5)}\right)(\text{D}.11)
\end{aligned}
$$

Then we extract the amplitude components in Mathematica and evaluate the full expression with the heptagon twistors. After expanding at large τ_1 and τ_2 and picking up the term proportional to (D.1) we find again a perfect match with the OPE result (D.10).

Appendix E

More on matrix part and formation of Bethe strings

In this Appendix we give more details on the evaluation of the matrix part of the POPE integrand and the formation of the Bethe strings. Let us start by explaining the overall symmetry factors. For one effective particle states, the symmetry factor S_n in (5.1) is given by $S_n = 1/(N_{\psi_s}! N_{\bar\psi_s}!)$ [1]. From the matrix part we also have an overall factor of $1/(K_1! K_2! K_3!)$. As mentioned in the main text, when choosing an order in which we take the residues for the auxiliary and small fermion rapidities $\{\mathbf{w}, \mathbf{v}, \bar{\mathbf{v}}\}$, we need to multiply by a combinatoric factor that takes into account all other possible orderings. This factor is simply given by the possible permutations between the different sets of rapidities over which we are integrating: $N_{\psi_s}! N_{\bar\psi_s}! \times K_1! K_2! K_3!$. As we can see, this factor exactly cancels the overall factors previously mentioned. Therefore the effective measure will be given by

$$\mu_\Phi(u) = \operatorname*{Res}_{\{\mathbf{w}, \mathbf{v}, \bar{\mathbf{v}}\} = \{\mathbf{w}^*, \mathbf{v}^*, \bar{\mathbf{v}}^*\}} \left[\Pi_{\mathrm{dyn}} \times \Pi_{\mathrm{FF}} \times \Pi_{\mathrm{mat}}^{(\mathrm{int})} \right] \tag{E.1}$$

where $\Pi_{\mathrm{mat}}^{(\mathrm{int})}$ is the integrand in (5.4) and $\{\mathbf{w}^*, \mathbf{v}^*, \bar{\mathbf{v}}^*\}$ are the positions of the rapidities in the patterns for integration discussed below.

Now let us see how we can determine the order in which we need to take the residues with two examples. The first one we shall study is the effective measure of the state $F_3 \psi_s (\psi_s \bar\psi_s)^n$. Recall that the relevant poles are contained only in the matrix part of the POPE integrand. Since we are redefining the pentagon transitions between gluon bound states and small fermions, we need to include a new function $h^b(u, \mathbf{v}) = \prod_j [(u - v_j)^2 + (\frac{b}{2})^2]$ in the matrix part integrand, which in

---

[1] This is trivial to see when the fundamental excitation is a gluon bound state or a scalar. When the fundamental excitation is a large fermion we have that $S_n = N_\psi/(N_\psi! N_{\bar\psi_s}!)$, where the numerator counts the possible cases in which fermion is large; since $N_\psi = N_{\psi_s} + 1$ we have that indeed $S_n = 1/(N_{\psi_s}! N_{\bar\psi_s}!)$.
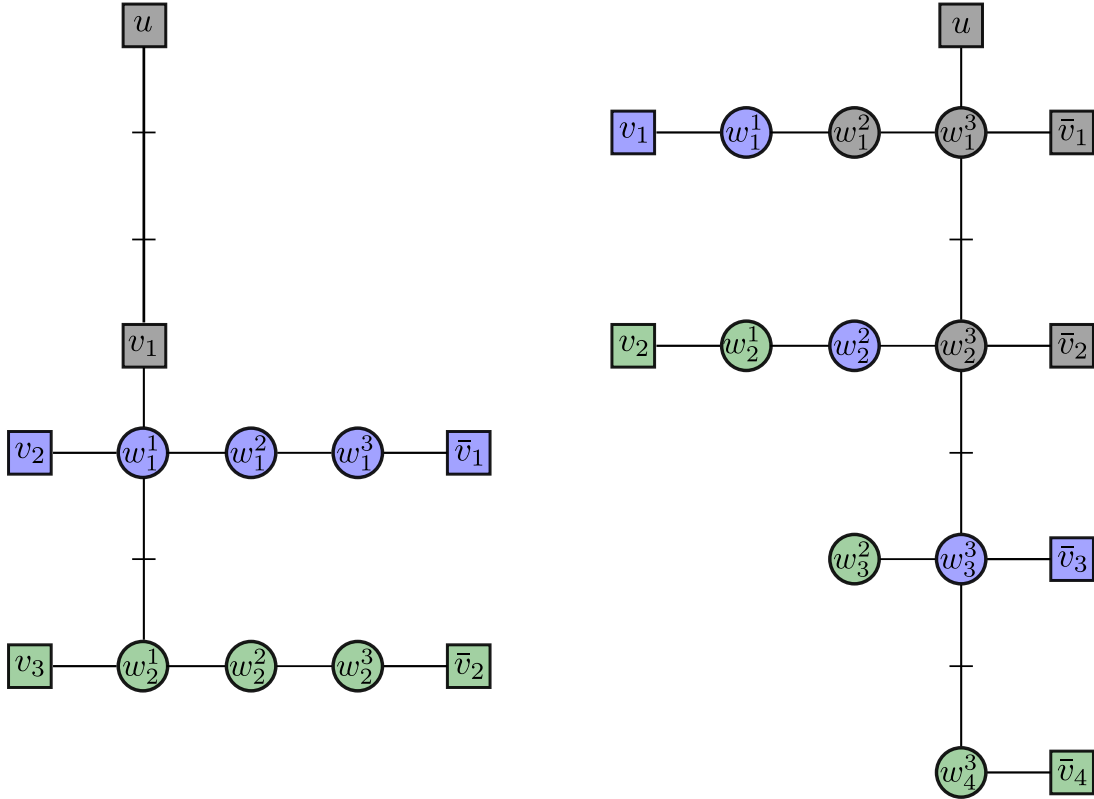
Figure E.1: Patterns for matrix part integration for the flux tube states $F_3\psi_s(\psi_s\bar{\psi}_s)^2$ (left) and $\bar{\psi}\bar{\psi}_s\bar{\psi}_s(\psi_s\bar{\psi}_s)^2$ (right). The top node corresponds to the fundamental excitation with rapidity u. The rest of the nodes are integrated out by taking residues at the positions $u - i\#/2$, where $\#$ is the number of line segments between the node we are integrating out and the fundamental one. The nodes forming the primary excitation are coloured in gray and in blue (green) the nodes that are added when we consider the first (second) descendant.

this case reads

$$\Pi^{(\text{int})}_{\text{mat}} = \frac{g(\mathbf{w}^1)g(\mathbf{w}^2)g(\mathbf{w}^3)}{f(\mathbf{w}^1,\mathbf{w}^2)f(\mathbf{w}^2,\mathbf{w}^3)f(\mathbf{w}^1,\mathbf{v})f(\mathbf{w}^3,\bar{\mathbf{v}})h^3(u,\mathbf{v})}\,. \tag{E.2}$$

For $n=0$ the integrand (E.2) reduces to $1/h^3(u,v)$ so that we only need to take the residue at $v_1 = u - i3/2$. This is shown in gray in figure E.1 with three line segments separating the u and v nodes (for a gluon of positive helicity b there will be b line segments separating the nodes).

For $n=1$ there is one auxiliary root of each type and only the functions f and h are present in the integrand. Some of the rapidities appear only once in the denominator so that we know immediately which residue we should take. For example, the small antifermion with rapidity $\bar{v}_1$ appears only in the function $f(w_1^3, \bar{v}_1)$ so we know that we should take the residue at $\bar{v}_1 = w_1^3 - i/2$, afterwhich we are in the same situation for w_1^3 and so on until we arrive at the structure in gray and blue in figure E.1. Of course, this is equivalent to take the following sequence of residues: $\{v_1 = u - i3/2,\ w_1^1 = u - i4/2,\ v_2 = u - i5/2,\ w_1^2 = u - i5/2,\ w_1^3 = u - i6/2,\ \bar{v}_1 = u - i6/2\}$.

For $n=2$ it is not as straightforward since each variable appears in more than one function so there are several options for which residues to take. The idea is to repeat the pattern found for $n=1$ for each new set of rapidities and unite each row with an effective link. If we integrate all the rapidities but w_1^1, w_2^1 in each row we get an effective pole $1/((w_1^1 - w_2^1)^2 + 1)$ so that –although at the beginning it was prohibited by the function $g(w_1^1, w_2^1)$– in the end we can take the residue at $w_2^1 = w_1^1 - i$. The same effective link between different rows is found for higher n and all other excitations. The pattern is summarized in the structure in the left of figure E.1. The order in which we take the poles is important. A simple way to get to right answer is to start from the top of the pattern and take the residues of the nodes closer to the fundamental excitation. This pattern gives rise to the first Bethe string in figure 5.5.

Considering other states, the number of auxiliary roots of each type might be different (in (5.5) we see that it depends exclusively on the representation and excitations of the flux tube state), so each level might not be "complete" as in the previous example. Rather, when we add a descendant we fill the node closer to the fundamental excitation. This is what is depicted the second pattern of integration in figure E.1 for the state $\bar{\psi}\bar{\psi}_s\bar{\psi}_s(\psi_s\bar{\psi}_s)^2$. In figure 5.5 it corresponds to the fourth Bethe string.

As we can see in these examples, the complexity of the patterns of integration increases with the number of excitations in the primary state. However, the maximum number of fermions we can have in a primary state is four, so the most complicated pattern is a slight modification of the example on the right in figure E.1.

Finally, since we are taking all residues in the lower half of the complex plane and the integrations over the auxliary rapidities w_i are over the real line, one has to multiply by an overall factor of $(-1)^{N_w}$, where N_w is the total number of auxiliary rapidities.

In practice, the residues were computed for the first few descendants of all the primary excitations in figure 5.1. From them we guessed the pattern for any n resulting in the proposals in the next section.

Appendix F

Measure prefactors at finite coupling

In this appendix we present the factors $M_\Phi(u)$ in (5.12) which are the most important functions at leading order in perturbation theory. Since we are dealing with somewhat lengthy equations, let us introduce the notation $[\circlearrowright] = x(u - i \circlearrowright)$ with the usual Zhukowsky variable $x(u) = \frac{1}{2}(u + \sqrt{u^2 - 4g^2})$. The prefactor $M_\Phi(u)$ can be conveniently factorized into two pieces, one which contains the contribution from the primary excitations in figure 5.1 and another one that takes into account its descendants. We identify an excitation by the parameter $\hat{r}$ which tells us in which $SU(4)$ representation it transforms[1] and the helicity a. The prefactors for the effective measures read

$$M_\Phi(u) = M_{\Phi_{\mathrm{plane}}}(u) \, \frac{1}{\Gamma(n+1)\,\Gamma\left(|a| + n + \frac{\hat{r}}{2}\right)} \times \tag{F.1}$$

$$\prod_{l=1}^{n} [l_+]^{2-\mathfrak{b}} [l_-]^{\mathfrak{b}} \frac{\sqrt{[l_-]^2 - g^2}}{\sqrt{[l_+]^2 - g^2}} \, \frac{\left([l_+][\mathfrak{a}] - g^2\right)\left([l_-][1-\mathfrak{a}] - g^2\right)\left([l_-][l_- + 1] - g^2\right)}{\left([l_-][\mathfrak{a}] - g^2\right)\left([l_+][1-\mathfrak{a}] - g^2\right)\left([l_+][l_- + 1] - g^2\right)} \,.$$

where $l_\pm = l + \frac{|a|}{2} + \frac{\hat{r}}{4} \pm \frac{|r_{12}|}{4}$, $\mathfrak{a} = \frac{a}{2} + \frac{\hat{r}}{4}$ and

$$\mathfrak{b} = \begin{cases} 0 & \text{singlet,} \\ \frac{1}{2} & \text{fundamental/antifundamental,} \\ 1 & \text{vector.} \end{cases}$$

The constants coming from the matrix part as well as the dynamical part, nicely combine into the two gamma functions shown in the first line of (F.1).

---

[1] Note that we are keeping $\hat{r}$ as for the tree level NMHV measures, but in general it does not necessarily correspond to the R-charge of one of the pentagons. For instance, the measures for the MHV component include excitations in the two singlet lines (first and last row in figure 5.1) but we keep using $\hat{r} = 4, 0$ or $(\hat{r} = 4, 0)$ to differentiate between the two.

Next we present the prefactors for the primary excitations. For excitations transforming in the vector SU(4) representation we have

$$M_\phi(u) = \frac{\pi g}{\cosh(\pi u)}, \tag{F.2}$$

$$M_{\psi\psi_s}(u) = -\frac{\pi g u}{\sinh(\pi u)} \frac{[1]}{[0]} \frac{1}{\sqrt{[0]^2 - g^2}\sqrt{[1]^2 - g^2}} \left([0][1] - g^2\right), \tag{F.3}$$

$$M_{F_b\psi_s\psi_s}(u) = -g(-1)^b \frac{\Gamma\left(iu + \frac{|b|}{2} + 1\right)\Gamma\left(-iu + \frac{|b|}{2} + 1\right)}{\Gamma(|b|)} \times \tag{F.4}$$

$$\times \frac{\left[\frac{|b|}{2} + 1\right]}{\left[-\frac{|b|}{2}\right]} \frac{1}{\sqrt{\left[-\frac{|b|}{2}\right]^2 - g^2}\sqrt{\left[\frac{|b|}{2} + 1\right]^2 - g^2}} \left(\left[-\frac{|b|}{2}\right]\left[\frac{|b|}{2} + 1\right] - g^2\right).$$

189

For particles in the fundamental SU(4) representation

$$M_{F_b\psi_s}(u) = ig^{5/4}(-1)^b \frac{\Gamma\left(iu + \frac{|b|}{2} + 1\right)\Gamma\left(-iu + \frac{|b|}{2} + 1\right)}{\Gamma(|b|)} \times$$

$$\times \frac{1}{\left[-\frac{|b|}{2}\right]^{1/2}\sqrt{\left[-\frac{|b|}{2}\right]^2 - g^2}}, \tag{F.5}$$

$$M_\psi(u) = i\frac{g^{5/4}\pi u}{\sinh(\pi u)}\frac{1}{[0]^{1/2}}\frac{1}{\sqrt{[0]^2 - g^2}}, \tag{F.6}$$

$$M_{\phi\bar{\psi}_s}(u) = -i\frac{g^{5/4}\pi}{\cosh(\pi u)}\left[\frac{3}{2}\right]^{3/2}\frac{1}{\sqrt{\left[\frac{3}{2}\right]^2 - g^2}}, \tag{F.7}$$

$$M_{\bar{\psi}\bar{\psi}_s\bar{\psi}_s}(u) = i\frac{g^{5/4}\pi u}{\sinh(\pi u)}\frac{[1]^{3/2}[2]^{3/2}}{[0]^{3/2}}\frac{1}{\sqrt{[0]^2 - g^2}\sqrt{[1]^2 - g^2}\sqrt{[2]^2 - g^2}} \times$$

$$\times \frac{([0][1] - g^2)([0][2] - g^2)}{([1][2] - g^2)}, \tag{F.8}$$

$$M_{F_{-b}\bar{\psi}_s\bar{\psi}_s\bar{\psi}_s}(u) = ig^{5/4}(-1)^b\frac{\Gamma\left(iu + \frac{|b|}{2} + 1\right)\Gamma\left(iu + \frac{|b|}{2} + 1\right)}{\Gamma(|b|)}\frac{\left[\frac{|b|}{2} + 1\right]^{3/2}\left[\frac{|b|}{2} + 2\right]^{3/2}}{\left[-\frac{|b|}{2}\right]^{3/2}} \times$$

$$\times \frac{1}{\sqrt{\left[-\frac{|b|}{2}\right]^2 - g^2}\sqrt{\left[\frac{|b|}{2} + 1\right]^2 - g^2}\sqrt{\left[\frac{|b|}{2} + 2\right]^2 - g^2}} \times \tag{F.9}$$

$$\times \frac{\left(\left[-\frac{|b|}{2}\right]\left[\frac{|b|}{2} + 1\right] - g^2\right)\left(\left[-\frac{|b|}{2}\right]\left[\frac{|b|}{2} + 2\right] - g^2\right)}{\left(\left[\frac{|b|}{2} + 1\right]\left[\frac{|b|}{2} + 2\right] - g^2\right)}.$$

The measures for the conjugate excitations in the antifundamental representation are given by the same expressions multiplied by (-1).

Finally, for excitations transforming in the singlet SU(4) representation we have

$$
M_{F_b}(u) = g^2(-1)^b \frac{\Gamma\left(iu + \frac{|b|}{2} + 1\right)\Gamma\left(-iu + \frac{|b|}{2} + 1\right)}{\Gamma(|b|)} \frac{1}{\sqrt{\left[-\frac{|b|}{2}\right]^2 - g^2}\sqrt{\left[\frac{|b|}{2}\right]^2 - g^2}} \times
$$

$$
\times \frac{1}{\left(\left[-\frac{|b|}{2}\right]\left[\frac{|b|}{2}\right] - g^2\right)}, \tag{F.10}
$$

$$
M_{\psi\bar\psi_s}(u) = \frac{g^2\pi u}{\sinh(\pi u)}[2]^2 \frac{1}{\sqrt{[0]^2 - g^2}\sqrt{[2]^2 - g^2}} \frac{1}{([0][2] - g^2)}, \tag{F.11}
$$

$$
M_{\phi\bar\psi_s\bar\psi_s}(u) = -\frac{g^2\pi}{\cosh(\pi u)}\left[\tfrac{3}{2}\right]^2\left[\tfrac{5}{2}\right]^2 \frac{1}{\sqrt{\left[\frac{3}{2}\right]^2 - g^2}\sqrt{\left[\frac{5}{2}\right]^2 - g^2}} \frac{1}{\left(\left[\frac{3}{2}\right]\left[\frac{5}{2}\right] - g^2\right)}, \tag{F.12}
$$

$$
M_{\bar\psi\bar\psi_s\bar\psi_s\bar\psi_s}(u) = \frac{g^2\pi u}{\sinh(\pi u)}\frac{[1]^2[2]^2[3]^2}{[0]^2} \frac{1}{\sqrt{[0]^2 - g^2}\sqrt{[1]^2 - g^2}\sqrt{[2]^2 - g^2}\sqrt{[2]^2 - g^2}} \times
$$

$$
\times \frac{([0][1] - g^2)([0][2] - g^2)([0][3] - g^2)}{([1][2] - g^2)([2][3] - g^2)([3][1] - g^2)}, \tag{F.13}
$$

$$
M_{F_{-b}\bar\psi_s\bar\psi_s\bar\psi_s\bar\psi_s}(u) = g^2(-1)^b \frac{\Gamma\left(iu + \frac{|b|}{2} + 1\right)\Gamma\left(iu + \frac{|b|}{2} + 1\right)}{\Gamma(|b|)} \frac{\left[\frac{|b|}{2} + 1\right]^2\left[\frac{|b|}{2} + 2\right]^2\left[\frac{|b|}{2} + 3\right]^2}{\left[-\frac{|b|}{2}\right]^2} \times
$$

$$
\times \frac{1}{\sqrt{\left[-\frac{|b|}{2}\right]^2 - g^2}\sqrt{\left[\frac{|b|}{2} + 1\right]^2 - g^2}\sqrt{\left[\frac{|b|}{2} + 2\right]^2 - g^2}\sqrt{\left[\frac{|b|}{2} + 3\right]^2 - g^2}} \times \tag{F.14}
$$

$$
\times \frac{\left(\left[-\frac{|b|}{2}\right]\left[\frac{|b|}{2} + 1\right] - g^2\right)\left(\left[-\frac{|b|}{2}\right]\left[\frac{|b|}{2} + 2\right] - g^2\right)\left(\left[-\frac{|b|}{2}\right]\left[\frac{|b|}{2} + 3\right] - g^2\right)}{\left(\left[\frac{|b|}{2} + 1\right]\left[\frac{|b|}{2} + 2\right] - g^2\right)\left(\left[\frac{|b|}{2} + 2\right]\left[\frac{|b|}{2} + 3\right] - g^2\right)\left(\left[\frac{|b|}{2} + 3\right]\left[\frac{|b|}{2} + 1\right] - g^2\right)},
$$

and the same for the conjugate excitations.

Appendix G

Details on momentum integration

In this section we present the relevant functions for the resummation of general POPE components. For clarity, let us rewrite (5.25)

$$P^{[r_1]} P^{[r_2]} = \delta_{|r_1 - r_2|, 4} + \frac{g^{[r_1, r_2]}(t^\star)}{|f'(t^\star)|} \sum_a \left[e^{-\tau - \sigma}(t - 1) \right]^{|a|} e^{ia\phi} + r^{[r_1, r_2]} + \mathcal{O}(g^2) \,, \qquad \text{(G.1)}$$

where $f(t) = 2\sigma - \ln[(1-t)(1+e^{-2\tau} t)/t]$ and the other functions depend on the POPE component we are considering.

Although for the case studied in the main text there was a symmetry between positive and negative helicity states, this is in general not the case. This can be seen from (5.19) where the integrand depends explicitly on $\hat{r}$. This means that for each component we have two different functions depending on the value of $\hat{r}$

$$
\begin{aligned}
g^{[4,0]([0,4])} &= \begin{cases} \dfrac{t^2 e^{-2\tau}}{(1-t)^2(1+te^{-2\tau})}\,, & \hat{r} = 4, \\[4mm] \dfrac{1}{t(1-t)(1+te^{-2\tau})^2}\,, & \hat{r} = 0\,. \end{cases} \\[6mm]
g^{[3,1]([1,3])} &= \begin{cases} \dfrac{t^{5/4} e^{-3\tau/2}}{(1-t)^{7/4}(1+te^{-2\tau})^{5/4}}\,, & \hat{r} = 3, \\[4mm] -\dfrac{e^{-\tau/2}}{t^{1/4}(1-t)^{5/4}(1+te^{-2\tau})^{7/4}}\,, & \hat{r} = 1\,. \end{cases} \qquad \text{(G.2)} \\[6mm]
g^{[2,2]} &= -\dfrac{t^{1/2} e^{-\tau}}{(1-t)^{3/2}(1+te^{-2\tau})^{3/2}}\,, & \hat{r} = 2,
\end{aligned}
$$

The other relevant functions $r^{[r_1,r_2]}$ arise when performing the analytical continuation in a. For the component $P^{[4]}P^{[0]}(P^{[0]}P^{[4]})$ the function comes from taking the residue of the integrand in (5.19) at $u = i$ with $a = 0$ and at $u = i/2$ with $a = -1(+1)$

$$r^{[4,0]}(\sigma, \tau) \;=\; e^{-2(\sigma+\tau)}\left(-1 + \frac{e^{\sigma+\tau-i\phi}}{e^{2\tau}+1}\right), \tag{G.3}$$

$$r^{[0,4]}(\sigma, \tau) \;=\; e^{-2(\sigma+\tau)}\left(-1 + \frac{e^{\sigma+\tau+i\phi}}{e^{2\tau}+1}\right). \tag{G.4}$$

For $P^{[3]}P^{[1]}(P^{[1]}P^{[3]})$ the residues are taken at $u = i$ with $a = -\frac{1}{2}(+\frac{1}{2})$ and at $u = i$ with $a = \frac{1}{2}(-\frac{1}{2})$ and the functions read

$$r^{[3,1]}(\sigma, \tau) \;=\; e^{-2\sigma-\tau-\frac{i\phi}{2}}\left(-\frac{e^{\sigma-\tau}}{e^{-2\tau}+1} + e^{i\phi}\right), \tag{G.5}$$

$$r^{[1,3]}(\sigma, \tau) \;=\; -e^{-2\sigma-\tau+\frac{i\phi}{2}}\left(-\frac{e^{\sigma-\tau}}{e^{-2\tau}+1} + e^{-i\phi}\right). \tag{G.6}$$
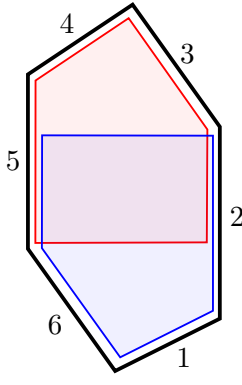
Note that these functions are the same (up to a sign) after we make the replacement $\phi \to -\phi$. For completeness we rewrite $r^{[2,2]}$ which is found by taking the residue at $u = i/2$ with $a = 0$

$$r^{[2,2]}(\sigma, \tau) = \frac{1}{2}e^{-\sigma}\mathrm{sech}(\tau). \tag{G.7}$$

Appendix H

Hexagon twistors

In this appendix we review how the kinematical data enters in the POPE approach. We shall use momentum twistors which are very useful variables since they trivialize momentum conservation and on-shellness. They are four components vectors (spinors of $\mathbb{R}^{2,4}$) defined up to rescaling $Z \simeq tZ$. Each twistor Z_i is associated to an edge i of the polygon. For example, for the hexagon we have

$$
\begin{pmatrix} Z_1 \\ Z_2 \\ Z_3 \\ Z_4 \\ Z_5 \\ Z_6 \end{pmatrix} = \begin{pmatrix} e^{\sigma - \frac{i\phi}{2}} & 0 & e^{\tau + \frac{i\phi}{2}} & e^{\frac{i\phi}{2} - \tau} \\ e^{\sigma - \frac{i\phi}{2}} & 0 & 0 & 0 \\ -1 & 0 & 0 & 1 \\ 0 & 1 & -1 & 1 \\ 0 & 1 & 0 & 0 \\ 0 & e^{-\sigma - \frac{i\phi}{2}} & e^{\tau + \frac{i\phi}{2}} & 0 \end{pmatrix} \tag{H.1}
$$

The hexagon twistors are constructed by acting with the symmetries of the middle square on the bottom of the polygon as explained in appendix A of [22]. The variables τ, σ and ϕ parametrize the three conformal symmetries that the middle square preserves [21] and play the role of flux tube time, space and angle coordinates. They can be related to the three cross ratios $\{u_1, u_2, u_3\}$ of the hexagon (see again [22] for the explicit relations).

As mentioned in the main text, the tree level and one loop NMHV components can be extracted from the package [36]. For instance, to extract the component $P^{[2]}P^{[2]}$ at tree level and evaluate with the above twistors, we simply write

```
evaluate@superComponent[{1,2},{},{},{3,4},{},{}]@treeAmp[6,1]
```

and multiply the result by the appropriate weights defined in [2] which in this case combine to ± 1.

APPENDICES PART II

Appendix I

Numerical Implementation

In section 7.2.3 we introduced the dispersion relation which takes into account the crossing symmetry and analytic properties of the S-matrices. We rewrite equation (7.11) here for convenience

$$\mathbf{S}(s) = \mathbf{S}(2) + \sum_{n=1}^{n_{BS}} \Big(\mathbf{pole}_n(s) + \mathrm{d} \cdot \mathbf{pole}_n(4-s) \Big) + \int_{4m^2}^{\infty} \frac{(s-2)}{(x-2)} \left[\frac{\boldsymbol{\rho}(x)}{x-s} - \mathrm{d} \cdot \frac{\boldsymbol{\rho}(x)}{x-4+s} \right] dx \,,$$

$$\mathbf{pole}_n(s) = \frac{s-2}{m_n^2 - 2} \frac{g_n^2}{s-m_n^2} (\delta_{\mathrm{singlet},\mathrm{rep}_n}, -\delta_{\mathrm{anti},\mathrm{rep}_n}, \delta_{\mathrm{sym},\mathrm{rep}_n})^{\mathsf{T}} \,. \tag{I.1}$$

In order to use this dispersion relation in a numerical context, it is necessary to discretize the function $\boldsymbol{\rho}(x)$ parametrizing the discontinuity across the branch cuts. To this end we define a grid of points $x_1, \ldots, x_M$ and make a linear interpolation for $\boldsymbol{\rho}(x)$. That is, in the interval $x \in [x_m, x_{m+1}]$ we set

$$\boldsymbol{\rho}(x) = \boldsymbol{\rho}_m \frac{x - x_{m+1}}{x_m - x_{m+1}} + \boldsymbol{\rho}_{m+1} \frac{x - x_m}{x_{m+1} - x_m} \,, \tag{I.2}$$

where $\boldsymbol{\rho}_m \equiv \boldsymbol{\rho}(x_m)$. For the last interval $x \in [x_M, \infty)$ we assume logarithmic decay

$$\boldsymbol{\rho}(x) = \boldsymbol{\rho}_M \frac{\log x_M}{\log x} \,. \tag{I.3}$$

Now we can simply perform the integrals in (I.1), so that each $\boldsymbol{\rho}_m$ comes with a coefficient:

$$
I_{m<M}(s) = \int_{x_{m-1}}^{x_m} \frac{(s-2)(x-x_{m-1})\,dx}{(x-2)(x_m-x_{m-1})(x-s)} + \int_{x_m}^{x_{m+1}} \frac{(s-2)(x-x_{m+1})\,dx}{(x-2)(x_m-x_{m+1})(x-s)} \tag{I.4}
$$

$$
= \frac{(x_{m-1}-s)\log(s-x_{m-1})}{x_m-x_{m-1}} + \frac{(x_{m-1}-2)\log\left(\frac{x_m-2}{x_{m-1}-2}\right)}{x_m-x_{m-1}} +
$$

$$
\frac{(x_{m+1}-x_{m-1})(s-x_m)\log(s-x_m)}{(x_m-x_{m-1})(x_{m+1}-x_m)} +
$$

$$
\frac{(x_{m+1}-s)\log(s-x_{m+1})}{x_{m+1}-x_m} + \frac{(x_{m+1}-2)\log\left(\frac{x_m-2}{x_{m+1}-2}\right)}{x_{m+1}-x_m} , \tag{I.5}
$$

and for the last interval (I.3) we have

$$
I_M(s) = \int_{x_{M-1}}^{x_M} \frac{(s-2)(x-x_{M-1})\,dx}{(x-2)(x_M-x_{M-1})(x-s)} + \int_{x_M}^{\infty} \frac{(s-2)(\log x_M)\,dx}{(x-2)(\log x)(x-s)} , \tag{I.6}
$$

where the second integration is performed numerically. The discretized dispersion relation $\mathbf{S}^d(s)$ with a finite set of parameters is therefore:

$$
\mathbf{S}^d(s) = \mathbf{S}(2) + \sum_{n=1}^{n_{BS}} \left(\mathbf{pole}_n(s) + \mathbb{d} \cdot \mathbf{pole}_n(4-s) \right) + \sum_{m=1}^{M} \boldsymbol{\rho}_m I_m(s) . \tag{I.7}
$$

Since we are giving the bound state masses m_n as an input, the parameters in the dispersion relation are: $\mathbf{S}(2)$[1], g_n, and $\boldsymbol{\rho}_m$. Finally, we choose a grid $s_{j=1,\ldots J}$ (it can be different from the discretization grid x_m) in which we impose the unitarity constraints $|\mathbf{S}^d(s_j)|^2 \leq 1$ and maximize one (or a combination) of the parameters in the dispersion relation. The maximization can be straightforwardly performed with the function `FindMax` in Mathematica or using SDPB [71] with the positive semidefinite condition of (8.1) for unitarity.

---

[1]Recall that the crossing condition $\mathbf{S}(2) = \mathbb{d} \cdot \mathbf{S}(2)$ fixes one of the subtraction constants in function of the other two.

Appendix J

Fixing parameters in analytic solution

In this appendix we explain how to compute the parameters μ_i and ζ in the analytic solution (7.37). For this, it is convenient to look at the product $S_{\text{anti}}(\theta)S_{\text{anti}}(\theta + i\pi)$ which has a much simpler analytic structure. In particular one can compute explicitly the second infinite product in (7.37) and get

$$
\begin{aligned}
S_{\text{anti}}(\theta)S_{\text{anti}}(\theta + i\pi) &= \left[\prod_{i=1}^{\infty}\frac{\mu_i^2 + \theta^2}{\mu_i^2 + (\theta + i\pi)^2}\right]\frac{\theta^2 + (\pi - \lambda)^2}{(\theta - i\lambda + 2i\pi)(\theta + i\lambda)} \times \\
&\quad \times \frac{\Gamma\left[\frac{\nu}{\pi^2}(-i\pi + \zeta - \theta)\right]\Gamma\left[\frac{\nu}{\pi^2}(i\pi + \zeta + \theta)\right]}{\Gamma\left[\frac{\nu}{\pi^2}(\zeta - \theta)\right]\Gamma\left[\frac{\nu}{\pi^2}(\zeta + \theta)\right]}.
\end{aligned}
\tag{J.1}
$$

Using $\mathbf{S}(0) = (1, 1, -1)^{\mathsf{T}}$, one can then compute the values of $\mathbf{S}(i\pi n)$ $(n \in \mathbb{Z})$ using crossing and unitarity to derive

$$
S_{\text{anti}}(i\pi n)S_{\text{anti}}(i\pi(n+1)) = \frac{\cosh[n\,\nu]}{\cosh[(n+1)\nu]}.
\tag{J.2}
$$

Evaluating the product (J.1) at $\theta = i\pi n$, one can rearrange terms in (J.2) and arrive at a more suggestive form, reminiscent of Bethe equations for μ_i:

$$
\left[\prod_{i=1}^{\infty}\frac{\mu_i^2 - \pi^2 n^2}{\mu_i^2 - \pi^2(n+1)^2}\right]h(n, \zeta) = 1,
\tag{J.3}
$$

199

where we have defined $h(n, \zeta)$ by

$$h(n, \zeta) = \frac{(\lambda - (n+1)\pi)(\lambda + (n-1)\pi)}{(\lambda - (n+2)\pi)(\lambda + \pi n)} \frac{\Gamma\left[\frac{(\zeta - i(n+1)\pi)\nu}{\pi^2}\right] \Gamma\left[\frac{(i\pi(n+1)+\zeta)\nu}{\pi^2}\right]}{\Gamma\left[\frac{(\zeta - in\pi)\nu}{\pi^2}\right] \Gamma\left[\frac{(i\pi n + \zeta)\nu}{\pi^2}\right]} \frac{\cosh[\nu(n+1)]}{\cosh(\nu n)} . \quad (\text{J.4})$$

Given $N = 2 \cosh \nu$ and a bound state mass m_{sing} (or equivalently λ), there is an infinite number ($n \in \mathbb{Z}$) of coupled equations (J.3) for infinite variables μ_i and ζ. In practice, we can truncate the number of parameters and equations, assuming that the remaining μ's are spaced by π. That is, we truncate the infinite product in (J.3) to some i_{max} and assume $\mu_{i+1} - \mu_i = \pi$ for $i \geq i_{\text{max}}$. This approximate spacing is observed numerically and can be understood from the fact that as we go further away from the physical strip we have more zeros and poles corresponding to previous μ's and less space between these and the boundary of the of the corresponding strip (see for example the $\theta \in i[3\pi, 4\pi]$ strip in figure 7.16). The truncation leads to the simple modification

$$\left[\prod_{i=1}^{i_{\text{max}}} \frac{\mu_i^2 - \pi^2 n^2}{\mu_i^2 - \pi^2 (n+1)^2}\right] \frac{\mu_{i_{\text{max}}} + \pi(n+1)}{\mu_{i_{\text{max}}} - \pi n} h(n, \zeta) = 1 . \quad (\text{J.5})$$

Now we only need to consider $i_{\text{max}} + 1$ different values of n to solve the system of equations. The values obtained in table 7.3 were found by evaluating the effective equations (J.5) for $n = 1, \ldots, 5$ and $i_{\text{max}} = 4$. We performed this exercise for various m_{sing} and N and found always perfect agreement with the position of zeros and poles in our numerics.